Understanding and controlling lipid membrane dynamics with external agents

Yusuf Qutbuddin

München 2024

Understanding and controlling lipid membrane dynamics with external agents

Yusuf Qutbuddin

Dissertation
an der Fakültät für Physik
der Ludwig–Maximilians–Universität
München

vorgelegt von
Yusuf Qutbuddin
aus Jabalpur, Indien

München, den 14th November 2024

Erstgutachter: Prof. Dr. Petra Schwille
Zweitgutachter: Prof. Dr. Don C. Lamb
Tag der mündlichen Prüfung: 3rd February 2025

میری جان کے نام

میرے والدین اور میرے بھائی کے نام

Zusammenfassung

Synthetische Zellen benötigen, genau wie lebende Zellen, eine dynamische Grenze, die das Innere vom Äußeren trennen kann. Lipidmembranen sind aufgrund ihrer eleganten Chemie und ihrer dynamischen, neu entstehenden Eigenschaften nach wie vor die besten Kandidaten für lebende und synthetische Zellen. Lipidmembranen faszinieren Chemiker und Physiker nach wie vor und beschäftigen sie, um ein wirklich ganzheitliches Verständnis ihres Verhaltens zu entwickeln. In lebenden Zellen sind Lipidmembranen an vielen entscheidenden Prozessen beteiligt, die die Zelle für ihren Erhalt und ihre Vermehrung benötigt. Wenn diese Lipidmembranen jedoch zur Kompartimentierung isoliert werden, in der Hoffnung, synthetisches Leben zu schaffen, behalten sie ihr dynamisches Potenzial, verlieren jedoch die Wirkstoffe, die die Membranen manipulieren. Biologen und Biophysiker setzen dann verschiedene Zellmaschinerien ein, um die Membranen wie gewünscht zu manipulieren. Die Rekonstitution von Proteinmaschinerie in Lipidmembranen ist ein umfangreiches Thema, und ein großer Vorteil, der die Lipidsysteme in die synthetische Welt bringt, ist die tatsächliche Nutzung der technologischen Fortschritte der synthetischen Chemie.
In dieser Arbeit habe ich mich auf die Verwendung und Entwicklung von Strategien zur Manipulation von Modellmembranen mit den Werkzeugen konzentriert, die synthetischen Chemikern zur Verfügung stehen. Diese externen Wirkstoffe können passiv sein, wie Makromoleküle, die sich spontan in Lipidmembranen einbetten und komplexe Wechselwirkungen mit der Doppelschicht aufweisen. Im Gegensatz dazu können sie auch aktive Wirkstoffe sein, die Energie auf die Lipiddoppelschichten übertragen, ohne dass ein biologisches Arsenal erforderlich ist. Mein Ziel war es, diese chemischen Werkzeuge einzusetzen, um ein grundlegendes Verständnis dafür zu entwickeln, wie sie auf Lipidmembranen wirken und welche Folgen diese Wechselwirkungen aus der Perspektive der Doppelschicht haben. Dies erweitert nicht nur unser Wissen über Lipiddoppelschichten, sondern legt auch den Grundstein für zukünftige Forscher, um bessere Werkzeuge für gewünschte Ergebnisse zu entwickeln.
Die Projekte in dieser Arbeit untersuchen sowohl passive als auch aktive externe Wirkstoffe, um morphologische Übergänge in Modellmembranen zu induzieren. Fluoreszenzmikroskopie und -spektroskopie, einschließlich Fluoreszenzlebensdauerspektroskopie und Fluoreszenzkorrelationsspektroskopie, erweisen sich als wesentliche Methoden zur Untersuchung von Modellmembranen. Ich habe mich auch darauf konzentriert, verfügbare Techniken wie die Elektrodenbildung von Vesikeln zu komplexeren Systemen weiterzuentwickeln, um ihre Verwendung in Studien zu synthetischen Zellen zu optimieren.
Diese Arbeit führte die Welt der Rotationsmotoren systematisch in Lipid-Doppelschichten ein, und photoaktive Verbindungen sind vielversprechende, entscheidende Wegbereiter für synthetische Zellen. Darüber hinaus würden synthetische Zellen mit besseren Oberflächen-veredelungs- und Beschichtungsstrategien auch für den Einsatz in der Arzneimittelabgabe und in der pharmazeutischen Industrie praktikabler werden. Diese Arbeit zeigt auch die Grenzen der aktuellen Technologie auf und wirft wichtige offene Fragen und potenzielle zukünftige Unternehmungen auf. Die rasanten Fortschritte in der synthetischen Chemie, den Fluoreszenztechniken und der Rechenleistung versprechen, die Forscher zur Entwicklung *echter* synthetischer Zellen zu führen.

Abstract

Synthetic cells, just like living cells, require a dynamic boundary that can separate what is inside and outside. Lipid membranes remain the most deserving candidates for both living and synthetic cells owing to their elegant chemistry and their dynamic emergent properties. Lipid membranes continue to fascinate and employ chemists and physicists to truly develop a holistic understanding of their behavior. In living cells, lipid membranes are involved in a lot of crucial processes that the cell requires for sustenance and proliferation. However, whenthese lipid membranes are isolated for use in compartmentalization, in hopes of creating synthetic life, they retain their dynamic potential but lose active agents that manipulate the membranes. Biologists and biophysicists then employ various cell machinery to attempt manipulation of the membranes as desired. Reconstitution of protein machinery in lipid membranes is a vast topic, and a major advantage that bring the lipid systems into the synthetic world is to truly utilize the technological advancements of synthetic chemistry.

In this thesis, I have focused on using and developing strategies of manipulating model membranes with the tools accessible to synthetic chemists. These external agents can be passive like macromolecules which spontaneously embed into lipid membranes and exhibit complex interactions with the bilayer. Contrarily, they can be active agents that transfer energy to the lipid bilayers without the need of biological arsenal. I aimed to employ these chemical tools to develop a fundamental understanding of how they act on lipid membranes and the consequences of these interactions from the perspective of the bilayer. It not only accentuates our knowledge on lipid bilayers, but also lays groundwork for future researchers to design better tools for desired outcomes.

The projects in this thesis explore both passive and active external agents to induce morphological transitions in model membranes. This work utilizes both supported and free-standing lipid bilayers to systematically characterize the effects of external agents on the mechanical properties of the membrane. Fluorescence microscopy and spectroscopy, including fluorescence lifetime spectroscopy and fluorescence correlation spectroscopy prove to be essential methodologies for studying model membranes. I also focused on advancing available techniques like electrodeformation of vesicles to more complex systems for optimizing their use in synthetic cell studies.

This work systematically introduced the world of rotary motors to lipid bilayers, and photoactive compounds hold great promise for being crucial game-changers in synthetic cells. Furthermore, with better surface-engineering and coating strategies, synthetic cells would also become more viable for being used in drug delivery and pharmaceutical industries. This work also highlights the limitations in current technology, posing important open questions and potential future endeavors. Rapid advances in synthetic chemistry, fluorescence techniques and computational power promise to lead researchers to the development of *true* synthetic cells.

Publications and Manuscripts

Publications and Manuscripts Included in this Thesis

Qutbuddin Y[†], Guinart A[†], Gavrilović S, Al Nahas K, Feringa BL, Schwille P. Light-Activated Synthetic Rotary Motors in Lipid Membranes Induce Shape Changes Through Membrane Expansion. *Adv Mater. 2024* (see section 6.1)

Guinart A[†], **Qutbuddin Y**[†], Ryabchun A, Krohn J, Schwille P, Feringa BL. Elucidating the physicochemical processes of light activated rotary motors embedded in lipid membranes. *under review, Chem Cell-Press. 2024* (see section 6.2)

Guinart A[†], Doellerer D[†], **Qutbuddin Y**, Zivkovic H, Hrebik D, Briggs J, Schwille P*, and Feringa B*. Photoswitchable molecular motor phospholipid: synthesis, characterization and integration into lipid vesicles. *Langmuir. 2025* (see section 6.3)

Qutbuddin Y[†], Krohn J[†], Brüggenthies G, Stein J, Gavrilović S, Stehr F, Schwille P. Design Features to Accelerate the Higher-Order Assembly of DNA Origami on Membranes. *The Journal of Physical Chemistry B. 2021* (see section 7.1)

Qutbuddin Y[†], Terracciano R[†], Bassi G, Aleksanyan M, Huband S, Gavrilović S, Yilmaz G, Dimova R, Schwille P, Becer R. Mimicking glycolipids and glycoproteins to create "fuzzy" membranes. *to be submitted, Biomacromolecules. 2024* (see section 8.1)

Pegoraro C, Karpova E, **Qutbuddin Y**, Sanchis E, Dimitrijevs P, Huck-Iriart C, Gavrilović S, Arsenyan P, Schwille P, Felip-León C, Duro-Castaño A, Conejos-Sánchez A*, and Vicent M*. Polyproline-polyornithine diblock copolymers with inherent mitochondria tropism. *Adv Mater. 2025* (see section 8.2)

Additional Publications and Manuscripts

Guinart A, **Qudbuddin Y**, Schwille P*, Feringa B*. Photoisomerization In Biological Membranes *Review under preparation. 2024*

Kanwa N, Gavrilović, Brüggenthies G, **Qutbuddin Y**, Schwille P. Inducing Lipid Domains in Membranes by Self-Assembly of DNA Origami. *Adv. Mater. Interfaces 2023* (see section 7.1)

Kaletta N, Burick S, **Qudbuddin Y**, Schwille P*. Designing tunable DNA condensates to control membrane transformation in synthetic cells. *under review, Advanced Science. 2025*

María Reverte-López, Kanwa N, **Qutbuddin Y**, Jasnin M, Schwille P*. Self-organized spatial targeting of contractile actomyosin rings for synthetic cell division. *Nature Comm. 2024*

Krohn J-H, Babl L, Isnel L, **Qutbuddin Y**, Schwille P*. Measuring Partition Coefficients of In Vitro Biomolecular Condensates Using Fluorescence Correlation Spectroscopy. *Bacterial Chromatin. Methods in Molecular Biology, vol 2819. 2024*

[†] These authors contributed equally to this work

Contents

Part I

Scientific Context

1
Cellular Membranes

1.1 A brief history

In the context of life, a crucial distinction lies in what is living, and what is not. When considering the smallest unit of life, a cell, it is important to distinguish the subject from its surroundings. Cellular membranes perform this critical role of separating the cellular contents from the external environment. Whatever is within the confines of these membranes is life, and thus membranes become the first point of contact for life to the outside world. This means that the membranes must permit the flow of essential nutrients into the cell and facilitate the passage of waste products out of the cell, while simultaneously acting as a barrier protecting from the outside and confining the inside. The first indication of the existence of such a membrane surface on cells was a result of the discovery of osmosis. It was in the second half of the 19th century, when Wilhelm Pfeffer, sometimes regarded as the father of the membrane theory, proposed that the protoplasm of the cells are surrounded by a thin layer. [1,2] Another important role that the membranes perform is maintaining the shape and integrity of the cell. Nature has equipped biological membranes to fulfill these essential requirements by exploiting the physico-chemical properties of the molecules that make up these membranes.

Cellular membranes are primarily constituted of lipids, which have a hydrophilic end (usually referred as the head) and a hydrophobic end (referred as the tail) (see Figure 1.1B). Such surfactants pose an important impediment to nature as no solvent can truly satiate the energy minimization requirements of the head and tail. Nature deals with this by the introduction of "self-assembly", a phenomenon of *emergence*, where the cooperative aggregates of these molecules "emerge" with novel physical and chemical properties not inherent in the individual molecules themselves. These lipid molecules are not chemically bonded to each other in their self-assembled state, introducing a range of dynamics and energetics that equip them to fulfill the requirements demanded by a cell.

Even though the presence of membranes surrounding cells seem intuitive now, the history behind this realization has led to important breakthroughs in the fields of physics and chemistry. Starting out from the observations of an amateur scientist in 1867 [3], membrane theory has been recognized since the mid-nineteenth century, from the observation of osmosis across the inside and outside of cells, to indication of the lipid nature of these membranes based on the correlation between rates at which particles permeate through plant cells and their partition coefficients between water

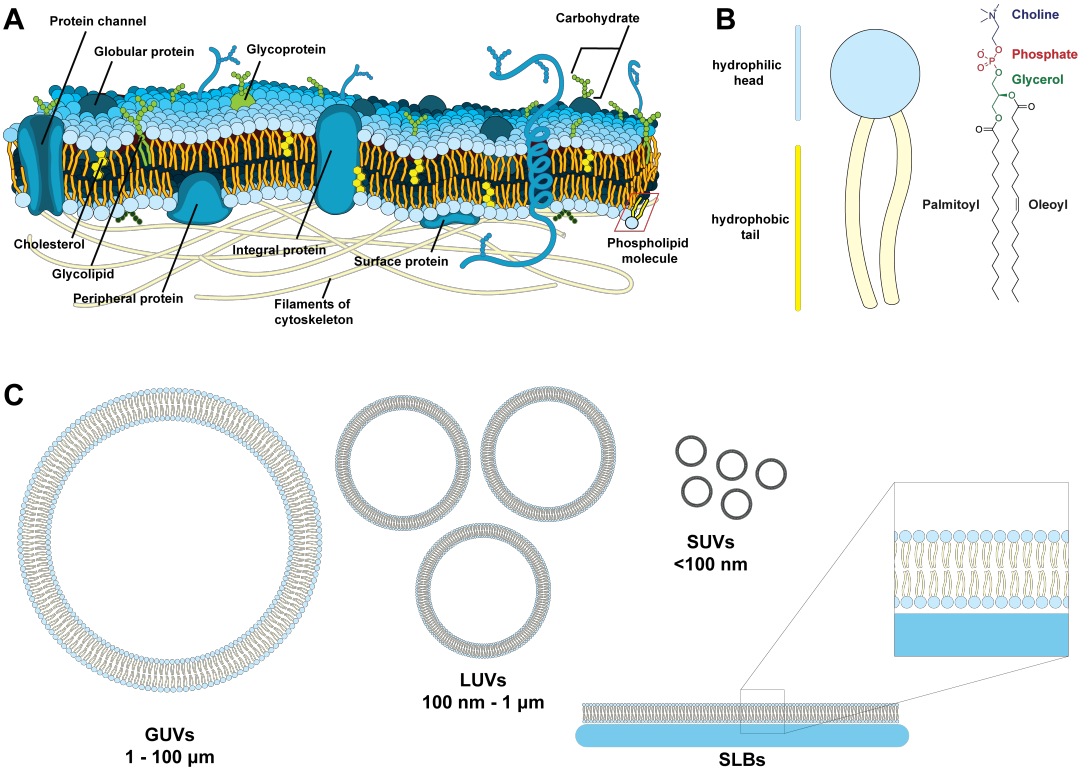

Figure 1.1. Lipid membrane. A) Schematic of a cellular membrane showing all the components including the glycocalyx, proteins, cytoskeleton, and phospholipids. B) (left) Schematic of a phospholipid with a hydrophilic head and hydrophobic tails. (right) 1-palmitoyl-2-oleoyl-sn-glycero-3-phosphocholine (POPC) chemical structure. C) Schematic of different kinds of model membranes, including giant unilamellar vesicles (GUVs), large unilamellar vesicles (LUVs), small unilamellar vesicles (SUVs), and supported lipid bilayers (SLBs).

and oil studied by Overton in 1895. [4,5] After the development of the Langmuir apparatus [6] for studying monolayers at the air-water interface, Gorter and Grendel experimentally investigated the surface area of the lipids extracted from red blood cells in acetone. [7] They found that the surface area of the monofilms was twice that of what they measured through microscopic images, and concluded that cellular membranes are a "bilayer" of these lipids. Although, this simplistic (and certainly correct) picture describes how the membranes look like, it almost entirely fails to account for the diverse functions performed by cellular membranes. Advancement of technology and understanding of the cellular membranes progressed in close proximity. With the observation of adsorbed proteins on the lipid bilayers, there was a new "paucimolecular" or otherwise known as Davson-Danielli model of the cell membranes. [8] Again, as electron microscopy progressed, Robertson described a picture of the cellular membranes as a three-layered structure with two protein layers adsorbed to either side of the bilayer. [9] As X-ray crystallography led the next revolution in understanding biological macro-molecules, the discovery of high α-helical contents in membrane proteins, [10] and the observation of isolated spot formations in electron micro-graphs of labeled proteins led to the "fluid-mosaic model" of the lipid membrane. [11] The "fluid-mosaic mode" with refinements over the last half-century is re-

garded as the best description of the cellular membranes. [12–17] The proposition of the fluid-mosaic model was paralleled by important experimental developments that gave further insight into the dynamics of these membranes. Spin-labeled lipids and steroids were employed to probe the lateral diffusion in the bilayer, [18,19] indicating the diffusion constants to be in the order of $\mu m\, s^{-2}$. Simultaneously, the observations of shape transitions of red blood cells and the consideration of elastic properties of lipid bilayers led to the inference of membranes being 2D fluids. [20, 21]. The *fluidity* of lipid bilayers imply that understanding the structure of these thin membranes around the cell must be complemented with a deeper insight into their dynamics.

Lipid membranes have successfully attracted the attention of physicists since its realization and advanced experimental techniques have displayed that the mechanical properties of the membranes control the functionality of these membranes at the cellular level. Physicists brought with them the ability to simplify complex systems to study them bottom-up, and thus started the era of model membranes. On one hand, such model membranes could be controlled in complexity to understand the underlying physical principles behind biological processes, and on the other, such nanoscopic and microscopic entities could be used as a tool for therapeutics and other applications. In the last few decades, extensive theoretical models have been developed and refined to study the curvature elasticity of biological membranes, [22–25] lateral diffusion, [26, 27] permeability [28] and shape transformations. [25, 29] These membranes have thus become an essential field of research, as a deeper understanding of how they function helps us come closer to understanding the processes of life, and lets us build better bio-inspired materials for chemical and biological applications. Coming from the times of discovering that cells are surrounded by a thin membrane, understanding its structure, realizing its dynamics, and formulating synthetic models, we are now entering the era of controlling the mechanical properties of these self-assembled entities. In the following sections, we will see how these model membranes are formulated, what experimental implications occur with their method of productions, and how can they be physically characterized in terms of their mechanical properties and dynamics.

1.2 How are membranes modeled?

Lipid vesicles or liposomes have been present in experimental laboratories for at least over a century. [30,31] As early as the late nineteenth century, experiments were performed to hydrate lecithin lipids to form what were known as myelin figures. [32] Bangham showed, with the help of light micro-graphs and an electron microscope that these swollen phospholipid particles are self enclosed and are semi-permeable to monovalent ions. These giant liposomes greatly varied in size and lamellarity and soon after a much more reproducible vesicle system was produced by sonicating these liposomes to generate smaller and uniformly sized unilamellar vesicles. [33] Small unilamellar vesicles have been heavily used in pharmaceutical and medical applications in the past. [34–36] Giant unilamellar vesicles on the other hand have gained popularity in the field of membrane physics, and with further development of reliable formation techniques and reconstitution of biological components, giant vesicles became physiologically relevant micro-reactors. [37–39] Over the course of the last century, many different model membrane systems have been established to study

the various properties of the lipid bilayer. These include solid substrate supported membranes, tethered membranes, pore spanning black lipid membranes, small and giant unilamellar vesicles that each offer a benefit over the other for studying specific processes. [40, 41] In the following sections, I will describe in detail the model membrane systems and their characterization techniques that were extensively used in my work.

1.2.1 Can we see what we cannot see?

Small unilamellar vesicles (SUVs) are defined as the vesicles with diameters less than $100\,\mathrm{nm}$, whereas large unilamellar vesicles (LUVs) range between $100\,\mathrm{nm}$ to $1000\,\mathrm{nm}$ (see Figure 1.1C). These vesicles have been extensively used for studying membrane-protein binding and interactions, although their sizes limit them from observation of the membrane dynamics. The diffraction-limit prevents their direct visualization by conventional optical techniques, and similar to how these small vesicles were observed for the first time, scientists rely on electron microscopes for imaging them. On the other hand, the simplicity of their production methods and the near-arbitrary control over their sizes and composition make them extremely useful for measurements requiring large statistical ensembles. Additionally, preparation of these nano-compartments usually require apparatus that are commonly available in biochemistry or biophysics laboratories.

Lipids are amphiphilic molecules that are stable and soluble in organic solvents such as chloroform. When introduced in aqueous environments, lipids self-assemble in giant aggregates to form bilayer structures. [42] When dried lipid films are hydrated and mixed thoroughly they form vesicles that are heterogeneous in size and lamellarity. These multilamellar vesicles (MLVs) are then mechanically forced to transform into the desired size and lamellarity. Sonication of these MLVs result in the formation of SUVs, these SUVs can be less than $50\,\mathrm{nm}$ in diameter and this results in them being meta-stable. The high curvature energies for these lipid bilayers are released by fusion among them resulting in larger SUVs. To accurately measure the size of these small particles, either electron microscopy or dynamic light scattering (DLS) is employed. An important caveat, using DLS for small vesicles ($< 50\,\mathrm{nm}$) falsely yields diameters around $100\,\mathrm{nm}$ as smaller sizes are near the detection limit of the device. [43]

With fluorescence based techniques, researchers can decipher a myriad of membrane properties and lipid-particle interactions with large ensembles of liposomes. Recently, advances have also been made towards developing high-throughput measurement techniques for studying the content and properties of nano-particles, including but not limited to liposomes. [44] Presently, solvatochromic membrane dyes are the most promising tools to measure the biophysical properties of the model membranes. [45] They are highly sensitive to their local environment within the vesicle bilayer, and their lipophilicity offers an efficient incorporation in the bilayer. Laurdan and Prodan, and their derivatives have been developed for improving the performance of these dyes in the lipid bilayer. [46,47] Similarly, Nile Red and its derivatives have been widely used due to its operation range at longer wavelengths resulting in reduced photo-toxicity. [48] Mechanosensitive push-pull probes have also been developed, which planarize upon increased physical compression due to their environment, resulting in an increased fluorescence lifetime τ. [49, 50] One such push-pull

probe is "Flipper-TR" which has been developed recently, and has been used for sensing the membrane tension of model membranes and cells. [51] Flipper reports on the membrane tension by sensing the *order* of the lipids and can thus be also used to detect lipid domains. Fluorescence lifetime spectroscopy is used to measure the change in fluorescence lifetime of Flipper, incorporated in SUVs/LUVs of desired lipid composition. [52] This can be used to observe the effect of interaction of active agents on or within the lipid membranes.

1.2.2 Supported bilayers have their own fixed place

Lipid mono- or bilayers supported on the surface of solid substrates are a widely used model membrane system which offers great advantages such as high stability and environmental control. Various substrate coating continuous membrane systems have been used in the past, including supported lipid bilayers (SLBs), bilayers on polymeric cushions, and supported bilayers tethered on solid substrates (t-SLBs). [53, 54] Since these supported membranes are "fixed" to the substrate, they provide an absolute control over solvent exchange and manipulation without a further necessity of immobilization. In addition to the mechanical stability, supported membranes can also be be used for studying specific geometries by patterning the desired geometries on the solid substrates. Numerous studies have made use of the advancing technologies in nano-printing to achieve this, and such printed nano-structure patterned substrates are now commercially available. [55–59]

Conventionally, supported lipid bilayers (SLBs) are made by deposition of SUVs on solid substrates and lipid-substrate and lipid-lipid interactions cause fusion of these vesicles into a continuous supported bilayer. Divalent cations like Ca^{2+} and Mg^{2+} act as fusogens and promote the formation of SLBs. [23] Additionally, substrates are activated either by etching with piranha solution or plasma cleaning to promote SLB formation. Treatment of the substrate surface, lipid composition and charge, pH of the solution, presence of divalent cations and temperature of formation, all play important roles in the formation and stability of these supported lipid bilayers. Additionally, different approaches have also been developed for the formation of supported bilayers. [60] It is important to consider that the mechanical stability of supported bilayers comes with a price, close proximity of the substrate means that the membrane fluidity is dependent on the roughness of the solid substrate. The substrate also affects the bending energy of the lipid membrane, and thus great care must be taken while drawing inferences about the mechanical effects of interacting particles when studying supported lipid membranes.

A variety of microscopy and spectroscopy techniques have been combined with the use of supported lipid bilayers to decipher the interactions at the membrane surface and to shine light on some membrane properties. Atomic force microscopy (AFM) is a scanning probe microscopy technique which uses specialized cantilevers used for force measurement and topographic imaging of samples with a spatial resolution up to a fraction of nm. [61] AFM has been widely employed to study various membrane properties of supported lipid bilayers, including liquid-liquid phase separation behavior of membranes, stretching modulus using force spectroscopy, homogeneity and thickness of the membrane. [62–64] As a combination, SLBs are the optimal model membrane when combined with AFM imaging to study processes occurring on the surface of the membrane. Similarly, for fluorescence imaging of such

supported membranes, employing total internal reflection fluorescence microscopy (TIRF-M) is advantageous because of the high optical sectioning, improving fluorescence imaging at the surface. [65] Furthermore, fluorescence correlation spectroscopy (FCS) can measure the lateral diffusion coefficients of the membrane with the use of lipid conjugated dyes. The general idea of the correlation technique has resulted in various iterations/forms of the FCS technique which targets specific parameters, such as surface integrated FCS (SI-FCS) and localization based FCS (lbFCS) for measuring the binding kinetics of particles to the surface and single particle counting, *calibration free* techniques such as z-scan FCS, and scanning FCS. [66–68]

1.2.3 Towards bigger vesicle pictures

Liposomes in the size range of $1\,\mu m$ to $100\,\mu m$ appropriately called giant unilamellar vesicles (GUVs) are arguably more accurate mimics of the cellular membrane as compared to other model membranes. [69] They are free standing membranes that encapsulate an aqueous lumen which can be used for reconstituting specific cellular machinery to observe their behavior with the lipid membrane. The size of these GUVs make them suitable for optical microscopy observations and membrane physics has seen tremendous technological development in the invention of optical methods for studying membrane mechanics using giant vesicles. Unlike emulsions, the shape of these vesicles are not purely driven by the interfacial energy, especially since the outside and inside are both aqueous environments. This renders vesicle shapes an exciting and important field of study, and has been the focus of theoretical physicists. On the other hand, every living cell requires shape transformations for essential processes of life such as motility, division, endocytosis, exocytosis and apoptosis. [70]

There are many commonly used formulation techniques for producing giant vesicles, great care should be taken to consider the nuances of different methodologies as they also affect the formed vesicles. Some common techniques are gel-assisted swelling, [71, 72] electroformation, [73] and emulsion transfer [74, 75] through an interface. These techniques produce giant vesicles reliably but are less controllable in terms of size distributions. On the other hand, other high-throughput methods have also been developed with microfluidics like octanol assisted liposome assembly (OLA) and continuous droplet interface crossing encapsulation (c-DICE). [76, 77] Ironically, there is no perfect method developed to generate desired GUVs, the method of choice depends on solubility of the desired lipids in solvents, lipid charge, acyl chain saturation, cholesterol content, compositional complexity, phase behavior, temperature as more intrinsic parameters. [37, 78] Additionally, it also depends on more extrinsic parameters as total time of production, purity, and the content that requires to be encapsulated. Consequently, the method of production also affects the properties of the lipid bilayer in the giant vesicles. [79–81] Microfluidic methods rely on the dewetting process of oils to transform from a double emulsion droplet to a lipid bilayer. The benefit of large yields and homogeneity in size is contrasted by the presence of oil as a continuous phase and time taken for production of appropriate volume of samples. Inverted emulsion transfer also carries the drawbacks of presence of oil in the system, but is a faster method to actively encapsulate desired content in less time, with little control over the sizes. Swelling methods like gel-assisted swelling or electroformation (where alternating electric fields are used to assist the swelling process) enjoy purely aqueous environments, encapsulation is only possible

passively with the requirement of purification or dialysis afterwards. [39] With the swelling methods, there is little empirical control over the sizes, and charges on the lipid head-groups or high ionic content in the sample pose as challenges for electric field assisted swelling. Emulsion transfer methods are the most widely used in *in vitro* reconstitution studies of peripheral membrane proteins to study the dynamics of lipid membranes under action. In contrast, when cleaner samples are needed for more quantitative mechanical studies on the membrane, there is a preference towards electroformation of GUVs. [80]

Even though the methods to produce them might not be perfect yet, GUVs themselves are the perfect models for studying membrane dynamics and mechanical properties. Particularly, membrane bending elasticity, lateral diffusive fluidity, membrane tension and stretching elasticity are common mechanical parameters measured using various techniques. [82] Fluorescence correlation spectroscopy (FCS) and its derivatives offer precise measurements of long-term diffusion constants of the lipids and any associated proteins or particles embedded in the membrane. [66, 83] Common environment sensing dyes and probes are also used for semi-quantitative (or comparative) measurement of membrane tension, fluidity and lipid order. [45, 49] Moreover, mechanical techniques such as bead pulling with optical tweezers and micro-pipette aspiration are used for measuring the stretching modulus and bending rigidity of the bilayers. [84] Additionally, other non-contact techniques have also been developed to measure the bending rigidity of the membranes including fluctuation spectroscopy and electrodeformation, where thermal fluctuations in the lipid membranes are accessed through osmotic deflation. Other properties such as permeability and phase-separation are also extensively studied with optical techniques. Additionally, computational scientists have been on their toes, performing coarse grained and atomistic molecular dynamic (MD) simulations on lipid membranes to further our knowledge about these self-assembled bilayers. [85]

1.3 Model membranes in the context of synthetic biology

As has been the case with most scientific achievements in the field of Physics, we need to answer the fundamental questions to gain insight on universal mechanisms. In our universe, everything is made up of atoms, which obliges science to understand atoms before it can understand "things". For that, the universe offered physicists the simplest atom, with one proton, one electron and a unit molar mass. Understanding the hydrogen atom revolutionized our understanding of the universe. [86] It begs the questions, can we do the same in biology? Cells are the smallest unit of life, but as is apparent just by looking at a cell, they are far too complex and convoluted to function as the unit entity which can function as a foundation upon which scientists can extrapolate. Such an absolute minimal unit cell is what scientists have previously described as "the hydrogen atom of biology", and we currently don't have such protocells provided by nature. [87,88] The bottom-up approach of synthetic biology is to build a minimal cell from the least components necessary which can perform basic functionalities of life. [89] One crucial element of which is having a well-defined and transformable boundary around what would be an artificial cell. [90] Lipid membranes are the obvious choice for building the compartmentalization for synthetic cells due to their dynamic ability and role in real-life cells. Thus, understanding and

developing the ability to transform membranes is imperative. [91]

In the last couple of decades, majority of scientific groups working towards building a synthetic cell have used lipid membranes in conjugation with specific protein machinery, [38, 92, 93] DNA nanotechnology, [94, 95] organic polymers, [96–98] and polypeptides [99] to form synthetic cells. All of these components act towards modulating the lipid bilayers through peripheral interactions or transmembrane insertions. The energy is driven by either chemical processes such as ATP-ase activity or by spontaneous reactions that minimize the energy of the system. Scientists have also developed systems which respond to external factors that could be triggered on demand, for example synthetic molecular motors activated by light have been used in polymersomes to release encapsulated drugs. [100] Studying the lipid membrane with these reconstituted machinery serves as a dual-edged sword, firstly it helps to understand how the cells use these specific macromolecules in their processes, and secondly how they can be used in the context of synthetic cells for a desired application.

2

Light-triggered dynamics in lipid bilayers

2.1 Membrane dynamics

In nature, the dynamical properties of the lipid membrane is a result of application of force either by peripheral or transmembrane proteins, polymers or external chemical or electrical stimuli and the inherent properties of the bilayer. [101] The interaction between proteins and lipid membranes has been found to play a crucial role in facilitating membrane remodeling events, which are essential for various cellular processes, including endocytosis and cell division. Membrane remodeling is a complex process that involves the interplay of various cellular components, including the cytoskeleton, extracellular matrix, and membrane-associated proteins. [102, 103] The formation of structural scaffolds by these components can exert external forces on lipid membranes, inducing membrane deformation. This process is also mediated by the recruitment and insertion of cytosolic proteins at specific membrane sites, which can change the spontaneous curvature and facilitate membrane budding. [104, 105] Additionally, the intrinsic properties of the bilayer can be modulated through reorganization of lipids, changes in lipid composition, regulation of sterols, and the activity of transmembrane proteins. [106–109] Scientists have also developed synthetic systems that mimic these behaviors to remodel membranes in response to external stimuli. In one of the earliest examples, Käs and Sackmann experimentally realized shape deformations as a result of increase in temperature due to the differing volume expansivity of water and area expansivity of the lipid bilayers. [110] Thermal undulations of the lipid bilayers can also be observed by introducing hyperosmotic conditions, and the magnitude of these undulations are then dependent on the bending modulus of the membrane and the temperature. [111] These thermal fluctuations of the lipid bilayer can relax into membrane tubes or buds, depending on the physical properties of the membranes and their interactions with the environment. Structurally, these lipid bilayers act as a capacitor and thus are responsive to electric fields. Researchers have used alternating electric fields at varying frequencies and field strengths to measure different mechanical and electrical properties of the membrane. [112, 113] Additionally, at certain frequencies, excess surface area of the vesicles can be "pulled" by these electric fields to induce morphological deformations into prolate and oblate spheroids. [114] Local pH gradients across the bilayer have been used to generate cristae-like membrane invaginations. [115] Other mechanical and invasive force applications have also been extensively studied, including mi-

cropipette aspiration, [116] membrane tube pulling with optical tweezers, [117] and microfluidic shear with mechanical traps. [118,119]

2.2 Lights. Camera. Action!

Various synthetic light-responsive molecules ranging from photoisomerizing switches, rotary molecular motors, and photosensitizers have been employed in the context of lipid membranes. I will briefly describe these light-responsive molecules, their interactions with lipid membranes and their applications.

2.2.1 Photosensitizers

Photosynthetic reactions in cells which require absorption of light produce significant amounts of reactive oxygen species (ROS) which result in the oxidative damage of biological systems. [121] Lipid membranes in cells are greatly affected by photooxidation and thus it is crucial for scientists to understand the mechanisms of photooxidation to develop methods for prevention against the ROS. Model membranes such as GUVs have been used to study this phenomenon by decorating the vesicles with anchored or embedded photosensitizers or by immersing the vesicles in water soluble photosensitizers. [122] These possibilities also allow the selective localization of the photosensitizers in the lipid bilayer. Various photosensitizers have been employed, and it has been observed that high level of oxidation can disrupt the lipid bilayers resulting in membrane rupture. It has been shown that upon continuous irradiation of the photosensitizers, giant vesicles show membrane fluctuations and shape transformations (including budding, membrane tubes, etc.) as a result of the membrane area increase. [123–125] The hydroperoxides of the unsaturated lipids have a higher area per lipid as compared to their non-oxidised counterparts, but also the membrane thickness decreases with the peroxidized lipids. [126,127]

Various techniques have been employed to measure the excess surface area produced by the peroxidation of the lipids in a bilayer. [123,125,126] Micropipette aspiration proves out to be the most effective method, as one can access the excess surface area while avoiding the stretching regime. [128] The membrane bending rigidity and stretching modulus have been measured to decrease with increasing amounts of hydroperoxidized lipids as the hydrophobicity of the bilayer decreases with the insertion of the peroxides in the hydrophobic core. Membrane permeability results from the formation of truncated lipids. Light triggered permeability, morphological transitions and induced changes in mechanical properties due to lipid oxidation has also attracted attention from the field of synthetic cells. [129] Recently, by embedding a photosensitizer into the lipid membrane of a synthetic cell, researchers triggered cargo-loading and release with light irradiation, and induced light-triggered division of a vesicle. [130]

2.2.2 Photoswitches

Molecular photoswitches are a class of chemical compounds that can change their structure in response to light. These compounds typically consist of two or more isomers that can be converted into each other through exposure to light (see Figure 2.1B). Photoswitches have been widely studied and include a variety of compounds,

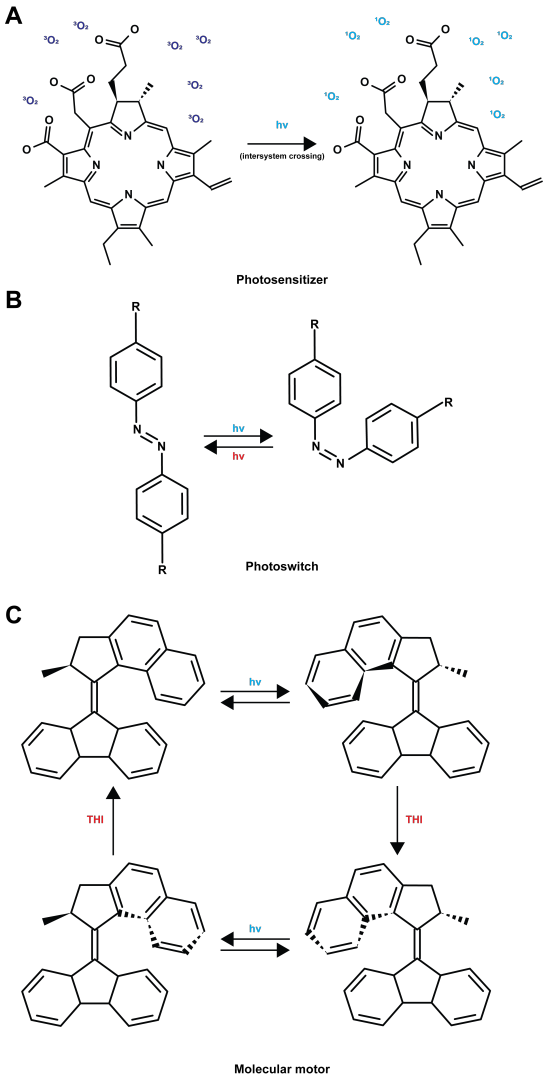

Figure 2.1. Light-responsive molecules. A) Chemical structure of photosensitizer Chlorin-E6. After light absorption, Chlorin-E6 excites to the singlet excited state, when the singlet excited state transitions to a triplet state through intersystem crossing, the photosensitizer can interact with triplet oxygen to produce singlet oxygen. Adapted from [120] with permission from American Chemical Society, Copyright (2023). B) Chemical structure of an azobenzene based photoswitch. Photoswitches absorb light to photoisomerize between *trans* and *cis* forms. C) Structure of a light-activated rotary motor. Rotation cycle of a molecular motor about the central double bond.

particularly (hetero)-aryl azo dyes have garnered attraction for their wide-range of implications in model membranes.

Morphological changes in lipid aggregates due to the presence of photoisomerizing chromophores has been known for more than half a century. [131] Researchers have also seen that these photoswitches that are expected to embed in the hydrophobic region of the lipid bilayers, can also be optically triggered to affect the electrochemical behavior of the lipid membrane. [132, 133] Further studies have shown that such reversible photoswitching of molecules embedded in the lipid bilayer results

in alteration of the membrane surface area which can induce morphological changes in the vesicle shapes. [134, 135] These studies systematically calculated the surface area change in the lipid bilayers, comparing it with the expected morphological transition as expected from vesicle shape equations. [136] In recent years, water soluble azobenzene derivatives have been used to trigger morphological deformations in lipid vesicles. [137] Additionally, dramatic shape changes have been induced *in vivo* in red blood cells with photoisomerization of such azobenzene derivatives, showing a reversible shape switching between discocytes and echinocytes. [138, 139]

Morgan et. al. reported the synthesis and application of one of the first photoresponsive lipid **Azo-PC**, with an azobenzene moiety incorporated in one of the acyl chains of phosphatidylcholine lipid. [140] Eventually, different variants of the Azo-PC were synthesized with selective positions of the azobenzene (palmitoyl-AzoPC and oleoyl-AzoPC) and with azobenzene on both the acyl chains (bis-AzoPC). Large surface area changes were observed in the Langmuir monolayers of these synthetic lipids as they isomerized from the *trans* to *cis* state. [141, 142] Recently, induced membrane deformations and the changes in mechanical properties of the membrane due to Azo-PC isomerization has been probed in detail. Morphological changes in giant vesicle shapes have been observed upon transitioning to the *cis* state using dark field microscopy. [143] It has also been shown that in its *trans* state the azobenzenes form *H-aggregates* in the lipid bilayer that would have interesting consequences on the mechanical properties of the membrane. [144] Consequently, the membrane mechanical properties were studied in more detail for both *trans* and *cis* state of Azo-PC at varying concentrations of the synthetic lipid. Small angle X-ray scattering (SAXS) and atomic force microscopy (AFM) showed an increase in membrane thickness in the *trans* state as compared to the *cis* state. [145, 146] Electrodeformation was employed to measure the changes in surface area of vesicles upon irradiation with UV-A (*trans* to *cis* transition). With the use of fluctuation spectroscopy, it was found that when Azo-PC is in the *trans* state, it increases the rigidity of the membrane and in the *cis* state the membrane rigidity goes down. Fluorescence recovery after photobleaching (FRAP) measurements on supported lipid bilayers (SLBs) composed of Azo-PC show corroborative evidence in their fluidity, with *cis* state being more fluid (having a higher diffusion coefficient) as compared to the *trans* state. Further studies on the atomic scale have also been undertaken to understand the mechanism of action of the Azo-PC lipid. [147] In all the cases the molar ratio of Azo-PC defines the magnitude of change that occurs upon isomerization.

Azo-PC lipid offers a controllable switch as part of the lipid bilayer that can be switched with light to achieve two different states affecting the morphological, mechanical, and electrical properties of the membranes. Such a control has allowed scientists to show its potential use, including in *in vitro* assays to deliver drugs to a cell culture and triggering and ceasing the release with light. [148] Furthermore, azobenzenes have been incorporated in sphingolipids and glycolipids and have proven to be effective agents to modulate the mechanical properties and the phase behavior of lipid membranes. [149–151]

2.2.3 Light-activated rotary motors

Overcrowded alkene-based rotary molecular motors are a sophisticated class of molecular machines that are derived from chiroptical molecular switches (see Figure 2.1C).

[152] These molecules were first introduced in 1999 and have since undergone significant research and development. [153] The motion of these molecular motors is driven by the consumption of light energy, involving a sequence of photochemical and thermal steps, resulting in a repetitive $360°$ rotation between four distinct molecular states. The development of overcrowded alkene-based rotary molecular motors has led to a deeper understanding of the underlying mechanisms and has enabled the design of more sophisticated molecular machines. The light-induced isomerization of these molecular motors has a profound impact on their fundamental characteristics, including their polarity, morphology and electronic properties. This ability to alter the properties of the molecule through photo-induced isomerization makes them highly versatile and has significant implications for their potential applications in biological systems. [154]

These rotary motors benefit from their unidirectionality, and by design maintain a dynamic out-of-equilibrium state in contrast with the photoswitches that are bidirectional and have two equilibrium states. One of the first applications of these molecular motors in lipid membranes showed up in 2017, when molecular motors with rotational speeds of $2\,\mathrm{MHz}$ to $3\,\mathrm{MHz}$ were used with lipid vesicles and living cells. [155] UV irradiation of these molecular motors showed dye release from the lipid vesicles and an accelerated necrosis displaying signs that these molecular motors could "drill" holes in the lipid bilayers. Subsequently, researchers also questioned the contributions of photo-oxidation of the lipid bilayer that would result from reactive oxygen species (ROS) produced by the molecular motors. [156]

These early works opened an avenue for the use of light-activated rotary molecular motors with cellular membranes, although the understanding on their mechanism of action remained unclear. Photoswitches had been extensively studied in the context of membranes, primarily due to their interesting and controllable effects on the lipid membrane. As is the ultimate desire of entropy, systems need to be driven out-of-equilibrium, which rotary motors are more equipped for than photoswitchable molecules. On the other hand, this intrinsic property also makes rotary motors extremely difficult to control. A systematic characterization of how molecular motors function in lipid bilayers was wanting, and such a study was taken place and can be found in Chapter 6 of this thesis.

3
Membrane interactions with macromolcules

Cells have a high abundance of macromolecules, ranging from small particles to polymers, that interact with the cellular membranes and are responsible for various processes necessary for the survival of the cell. [157] These macromolecules affect both the mechanical properties of the lipid bilayer, and alter the environment that the membrane experiences. These molecules can have various tendencies and preferences with respect to lipid bilayers depending on their structure, size, hydrophobicity, and charge. [158] They can embed inside the bilayer, adsorb on the membrane, or be engulfed by the lipid membrane depending on their properties. Structurally, their size as compared to the membrane thickness also plays an important role in their behavior. Many macromolecular processes also use the cellular membranes as a platform for reactions benefitting from the bilayer's ability to create a confinement at two dimensions. Additionally, biomembranes usually consist of a lot of macromolecules within their architecture, including carbohydrates, membrane proteins, peptides, DNA and RNA. For example, nuclear membranes host a myriad of DNA associated processes. [159] These macromolecules thus have a variety of effects that they produce on and within lipid bilayers, and understanding these interactions help us understand the particular molecule's biology. Moreover, reconstituting or mimicking these macromolecules allow scientist to replicate the effects in user-defined systems, especially when creating artificial cells. In this chapter, I will discuss the current knowledge in membrane-polymer interactions, brief theoretical framework, and how synthetic polymers can be studied and developed for pharmaceutical use.

3.1 Theoretical framework of membrane-polymer interactions

The state of a polymer in three-dimensional solvent is dependent on the interactions of the monomers among themselves and with the solvent or environment. A more detailed description of the discussions to follow can be found in ref. [160]. When the polymers interact with a membrane, they see the membrane as an interface, and depending on particular conditions, this interface can be penetrable, impenetrable, attractive or replulsive. The membranes can be treated theoretically as a boundary condition introducing a surface potential $U_s(r)$, if we assume the surface is perpendicular to the z-axis, and the interface is at z = 0, impenetrable membrane condition would be represented by a surface potential $U_s(z) = \infty$ for $z \leq 0$. Further the behaviour of the surface potential $U_s(z)$ for $z > 0$ will be dependent on the attraction of

the polymer to the surface. In the case where $U_s(z) = 0$ for $z > 0$, the molecules will be depleted from the interface. On the contrary, if there are attractive forces present between the polymer and the interface (H-bonding for example), then the surface potential is given by $U_s(z) = -\epsilon\delta(z-b)$ for $z > 0$ where ϵ is the strength of the attraction and b is the distance (from the interface) at which the force is experienced. For all the above cases, if the interface is penetrable with an energy cost, then $U_s(z) = U_o$ for $z \leq 0$ and adsorbing polymers can be present on both sides of the interface. [160] Lastly, for end-grafted chains, where there is a covalent interaction between at least one end of the polymer with the interface, $U_s(z) = -\infty$ at $z = 0$. Then the state of the polymers are described by their intractions with other end-grafted polymers. For a low surface density σ, such that $\sigma \ll R_F^{-2}$, where R_F is the Flory radius, the polymer state is described by the monomer-monomer and monomer-surface interactions. This case is known as the "mushroom" regime. Conversely, when $\sigma \gg R_F^{-2}$, or the "brush" regime, there is a strong interaction between the chains.

When polymer-membrane interactions are studied, polymer states are not possible to measure with optical techniques, so it is far more efficient to measure the contribution of the polymer to the behavior of the membrane. It has been shown that macromolecules when interacting with lipid membranes result in the bending of the lipid bilayers, resulting in a variety of shape deformations and transitions. For an arbitrary planar shape, the membrane energy density associated with the curvature can be written using the spontaneous curvature model

$$e(C_1, C_2) = \frac{\kappa}{2}(C_1 + C_2 - 2C_{spo})^2 + \bar{\kappa}C_1C_2$$

where C_1 and C_2 are the local principal curvatures, C_{spo} is the spontaneous curvature that accounts for the asymmetry in the membrane leaflets, κ is the bending rigidity and $\bar{\kappa}$ is the Gaussian rigidity that contributes to the topology of the membrane. Energy density for a spherical membrane with a radius R in a solution is given by

$$\Delta e = e(R) - e(\infty) = -\frac{4\kappa C_{spo}}{R} + \frac{2\kappa + \bar{\kappa}}{R^2}.$$

The excess surface energy due to the introduction of the macromolecules on the membranes are described by an expansion in powers of $\frac{1}{R}$ for $R \ll 1$. [136] These excess surface energies result in a change in the spontaneous curvature, bending rigidity and the Gaussian rigidity of the membrane. I will briefly go through some important and interesting cases which have been developed theoretically in refs. [161–163].

When describing a membrane in a non-ionic polymer solution which adsorbs at the mean-field level, reversible adsorption is described by an energy density which is a functional of the local monomer volume fraction was defined. [161] In the limit of weak adsorption, it was calculated $\Delta\kappa \propto -c^{-1/2}$ and for strong adsorption $\Delta\kappa < 0$ is independent of the bulk polymer concentration. [163, 164] For both these cases $\Delta\kappa < 0$ and $\Delta C_{spo} < 0$ which results in the softening of the membrane and the membrane bends towards the solution of the polymer. For end-grafted polymers, the experimental and theoretical results show $\Delta\kappa > 0$ and $\Delta C_{spo} > 0$ indicating that the membrane bends away from the solution of the polymers. [165–167] Initial studies in the case of irreversible adsorption showed that the magnitudes of both $\Delta\kappa$ and ΔC_{spo} are decreased but the signs are not changed, which was at odds to the

intuition as one would imagine an irreversibly adsorbed polymer to be the same as an end-grafted polymer. [168] An interesting theoretical consequence that was discussed by Skau and Blokhuis; when the desorption kinetics are assumed to be slow and irreversible adsorption is fixed to a value greater than the equilibrium adsorption value (i.e. the polymers are forced on the membrane), the magnitude of rigidity change and spontaneous curvatures decrease, and can also lead to a change in sign. [162] These considerations become an important benchmark for understanding the interactions of macromolecules studied in this thesis in the context of lipid membranes. Furthermore, the experimental evidence in this thesis, combined with the previously known therotical framework, will be paramount to develop controllable synthetic macromolecules for future applications.

3.2 Sweet polymers on lipid membranes

The glycocalyx, a complex carbohydrate-based coating on the surface cellular membranes, plays a crucial role in modulating cellular behavior and intercellular communication. [169] This dynamic structure is composed of polysaccharides, proteins, and lipids with covalently attached sugars. This "sweet" coating influences cellular behavior through different mechanisms, including regulating glycan-related gene expression, secretory pathway activity, and metabolic processes. Recently, the glycocalyx's significant contribution to shaping plasma membrane architecture and facilitating effective cellular interaction with the environment has been thoroughly investigated. An advancement in characterization techniques have enabled a more detailed probing of glycocalyx structure, revealing its involvement in vesicle budding and intercellular bridge formation (see Figure 3.1A). [170] Intercellular communication, which involves the transfer of nucleic acids and proteins, is mediated by extracellular vesicles (EVs) that bud directly from the plasma membrane. Glycocalyx polymers, such as mucins, podocalyxin, and hyaluronic acid (HA), trigger this process, which can occur through tip budding from tubular protrusions and membrane instabilities generated by glycopolymers. [171]

Cellular adhesion is an extremely complex and important focus of cell biologists, where it has been known that the glycans play a crucial role because of their binding with lectins. [173] Furthermore, the glycan's primary structure, density and distribution all play a crucial role in their biochemical activity. [174] Molecular studies of the glycosylated structures on the cell membranes prove to be extremely difficult due to the heterogeneous nature of the surface. Biophysicists and chemists, always overzealous to break down complex processes into bite-sized problems, approach understanding of these processes by mimicking a cellular membrane surface, embedded with synthetic carbohydrates. [175] The glyco-functionalization approach requires the glycan of interest to be conjugated with a hydrophobic anchor and incubating with either model cell membranes or cultured cells. Bertozzi et. al. showed an example of non-covalent cell surface engineering using synthetic mucin mimics on cell surfaces (see Figure 3.1B). [172] In their previous work, they developed the synthetic mucin mimicking polymers to decorate supported lipid bilayers. [176] Additionally, researchers started looking into the molecular orientation of these glycopolymers when decorated on bilayers, which opened new questions on the effect of the glycopolymers on lipid membranes. [177]

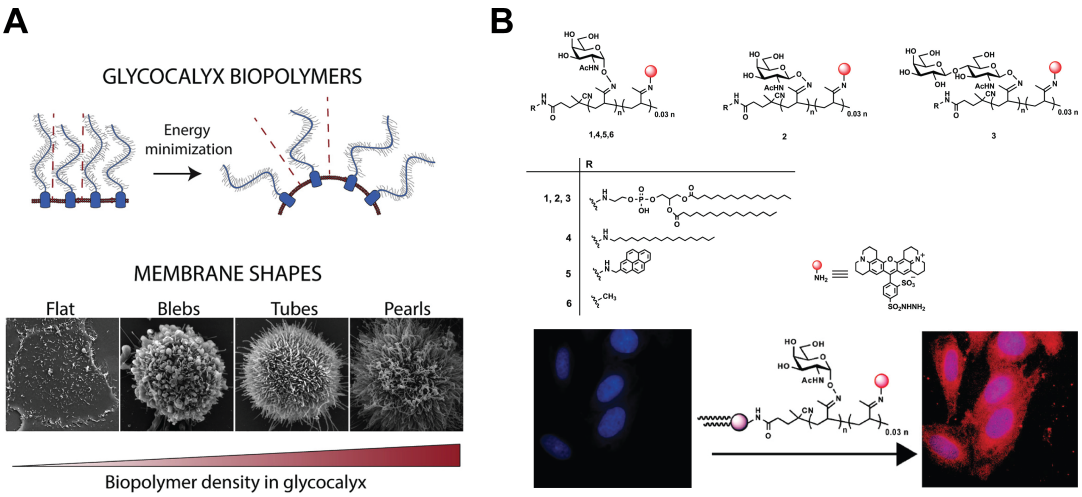

Figure 3.1. Effects of glycocalyx crowding and glycoengineering. A) Increasing density of glycopolymers such as mucin and hyaluronan (HA) leads to changing membrane morphology as a result of crowding. Reprinted from [170] with permission from Elsevier, Copyright (2019). B) Chemical structures of bioactive mucin mimic glycopolymers and their incorporation into the cellular membrane. Reprinted from [172] with permission from American Chemical Society, Copyright (2008).

Recently, biophysical characterizations on the membrane properties and a observations into the effect of surface crowding and density were made with polysachharides and glycomacromolecules on model lipid membranes. [98, 178] Dendritic cells decorated with glycopolymers were shown to improve cell-adhesion and thus enhancing the T-cell activation. [179] This implies that glycoengineering holds great promise for the development of glycopolymer associated drug delivery systems and also to understand the complex mechanisms of the glycocalyx on cellular surfaces and their effects on the lipid membrane of the cell.

3.3 Functionalizing cellular membranes with DNA nanotechnology

Back in 1982, Nadrian Seeman foresaw the use of DNA's ability to self-assemble into double helical structures would be useful for building arbitrary 2D or 3D structures. [180, 181] Later, Paul Rothemund made use of a viral DNA vector as a scaffold for designing 2D and 3D DNA origami (see Figure 3.2). [182] This extraordinary ability of DNA to self-assemble into desirable (and customizable) structures and its nativity to the cellular environments makes it an excellent candidate as an exogenous candidate for targeting lipid membranes. A wide range of biophysical and biochemical research has been dedicated to the development of such nanodevices, with the focus of the studies ranging from developing membrane functionalization strategies, to designing structures for biosensing and imaging applications. [183]

The choice of membrane anchoring strategy is crucial as it has a major influence on the interactions with the lipid bilayer. The most straightforward option is with conjugation of hydrophobic tags, such as cholesterol or fatty acids, with the DNA for insertion into the bilayer. Albeit offering biorthogonality, this results in a homogeneous distribution of the nanostructures and cannot be used for selective targeting.

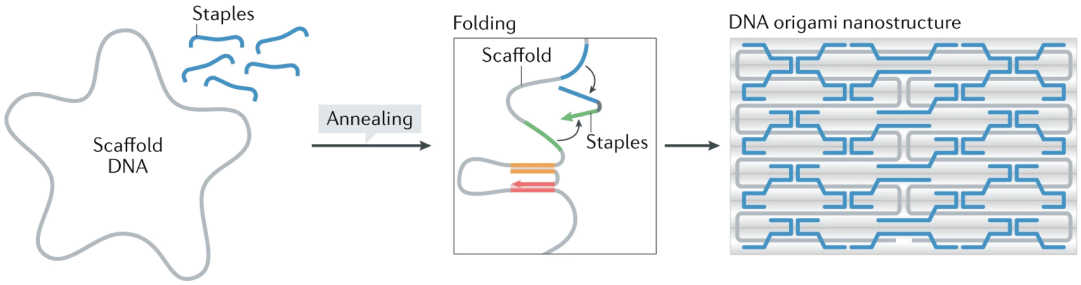

Figure 3.2. Principle of DNA origami. Large scaffold ssDNA are annealed with smaller staple ssDNA sequences which have complementary bases, designed to fold the structure in the desired 2D or 3D shape. Reprinted from [184] with permission from Springer Nature, Copyright (2021).

Cholesterol as a membrane anchor is the most common sight for DNA nanostructures being used in synthetic cells. [185] Another alternative is to make use of chemical crosslinking to the protein of interest, or using biotin-streptavidin binding to anchor the DNA structures. [185]

DNA origami offers high selectivity, are customizable both in geometry and functionalization, as is evident from its use with model membranes. They have been used to mimic the BAR domain to sculpt model membranes driving defined curvatures. [186] Kerstin Göpfrich and colleagues have extensively used double-crossover DNA tiles as nanotubes to synthesize DNA based cytoskeleton that can contract on demand, and deform giant vesicles. [187–189] It has been shown that DNA hybridization can be manipulated by the use of photo-cleavable moieties to trigger aggregation with the use of light, making DNA a bioorthogonal photoresist. [190] Many studies have also employed membrane spanning DNA origami as pores for transport of macromolecules across the bilayer. [191, 192] DNA has thus shown a great potential to be manipulated for desired results with cellular membranes for the goal of achieving controllable synthetic cells, in Chapter 7, I will discuss how this thesis contributes and applies to this field.

4
Fluorescence and optical techniques

The invention of fluorescence microscopy has revolutionized the field of biological and biophysical science, enabling researchers to visualize and study complex biological systems with unprecedented precision. [193, 194] Fluorescence microscopy has allowed researchers to acquire images, and achieve an excellent contrast between the object of interest and the background. [195] This specificity is provided by the ability to label the object of interest with fluorescent labels, thus retaining the object of interest in the foreground. The development of a wide range of fluorescent labels and probes has further expanded the capabilities of fluorescence microscopy, enabling the simultaneous imaging of multiple targets and the study of dynamic biological processes. [196] Especially, with the development of fluorescent proteins like green fluorescent protein (GFP) and mCherry, life scientists can tag proteins of interest in living cells. [197, 198] Significant advancements have also been accomplished on the engineering of superior fluorescence microscopy techniques, from confocal microscopy significantly increasing spatial resolution to super-resolution techniques that overcome diffraction-limited spatial resolution. Simultaneously, various techniques have been developed to attempt to study dynamics on the micro- and nanoscale. This thesis greatly relies on these fluorescence techniques among others which have been heavily used for observations, and I will briefly describe them in the following sections.

4.1 Fluorescence

Fluorescence refers to the absorption of a photon by a molecule and subsequent emission of a photon with lower energy. Jablonski diagram is a good visual representation of all the processes involved when electromagnetic radiation is absorbed by a molecule. Upon absorption of light with a suitable wavelength, the molecule can transition from the electronic ground state to a higher excited state. The molecule can then relax back to the ground state by various processes with different probabilities. Fluorescence is when the molecule relaxes to the ground state in a radiative manner, resulting in the emission of a photon. At the higher excited state, the molecule can also lose energy due to thermal and vibrational relaxation, resulting in the emitted radiative photon to have a lower energy (or a higher wavelength). This shift of wavelength, known as the Stokes shift, allows the spectral separation of the emitted photons from the excitation source with the use of optical filters. The process of flu-

orescence thus also offers a high selectivity and contrast, as the optical filters can be tuned for specific spectra rendering everything that is not of interest to be "dark". Another important aspect of fluorescence is the average fluorescence lifetime of a fluorophore, i.e. the time taken for the total fluorescence intensity of an ensemble of fluorophores to decay to $1/e$ of its initial value. On a molecular level the fluorescence lifetime τ corresponds to the average time a molecule spends in the excited state. Then τ can be described by the rates of radiative and non-radiative transition rates as

$$\tau = \frac{1}{k_r + \sum k_{nr}}$$

where k_r is the rate constant for radiative decay and $\sum k_{nr}$ is the sum of all non-radiative decay constants. Since the non-radiative decay is sensitive to the micro-environment of the molecule, the fluorescence lifetime can be used as an environment probing technique. Finally, since all fluorophores have a limited "photon budget" after which the fluorophores end up in a permanent dark state, a process known as photobleaching.

4.2 Fluorescence microscopy

I will briefly describe some microscopy techniques that were used in this thesis, and discuss their benefits for studying lipid membrane dynamics.

4.2.1 Total internal reflection fluorescence microscopy (TIRF-M)

Snell's law describes the refraction of light as it traverses from a medium of refractive index n_1 to a medium of refractive index n_2. If θ_1 is the angle of incidence at the interface between the two media, and θ_2 is the angle of refraction, then Snell's law is given by

$$n_1 sin\theta_1 = n_2 sin\theta_2.$$

If $n_1 > n_2$, then if the angle of incidence is increased such that $\theta_1 < 90°$, at a certain critical angle θ_c one would obtain

$$n_1 sin\theta_c = n_2$$

and for a typical fluorescence setup with aqueous solution on a glass coverslip, with $n_1 = 1.52$ and $n_2 = 1.33$ we get $\theta_c = 61.05°$. Above this critical angle, light will be reflected back from such an interface, resulting in total internal reflection. The reflected light generates an evanescent field in the lower refractive index media with its field intensity decaying as an exponential, such that

$$I(r) = I_o exp(-r/r_0)$$

where r is along an arbitrary axis and r_o is the distance along this axis when the evanescent field drops to $\frac{1}{e} * I(0)$. This decay constant can be calculated as

$$r_o = \frac{\lambda}{4\pi\sqrt{n_1^2 sin^2\theta_1 - n_2^2}}$$

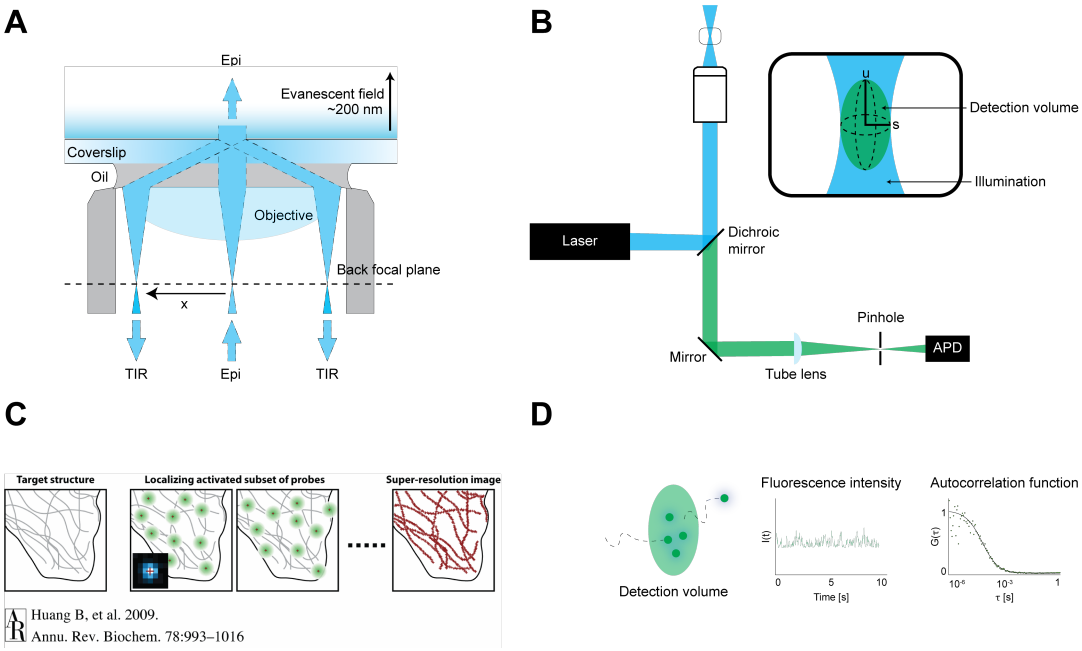

Figure 4.1. Fluorescence techniques. A) Schematic of objective-type total internal reflection fluorescence microscopy. The collimated laser beam is focused on the back focal plane and deflected by a distance x to achieve critical angle, oil matches the refractive index of glass and the total internal reflection takes place at the glass-water interface. Reprinted and adapted from [199] with permission from Springer Nature Methods, Copyright (2008). B) Schematic of a confocal microscope. The emission light is focused through a pinhole before collecting with an avalanche photodiode detector. Inset shows the confocal volume with the PSF radius as s and PSF aspect ratio u/s. C) Principle of single molecule localization microscopy. In SMLM, each frame has a small group of fluorophores emitting, producing diffraction limited images. (inset) Gaussian approximation on the image from single fluorophores can give the coordinate for each fluorophore. Post acquisition reconstruction results in a super-resolved image of the target structure. Reprinted with permission from Annual Reviews, Inc. [200], Copyright (2009). D) Principle of fluorescence correlation spectroscopy. Brownian motion of the fluorophores result in intensity fluctuations in the fluorescence signal. Correlation analysis of the fluorescence intensity give the autocorrelation curves which can be fitted to attain the diffusion coefficients and average number of particles in the detection volume.

and for $\theta_1 = 65° > \theta_c$ with $\lambda = 639nm$ we get the exponential decay constant to be r_o $141nm$. TIRF microscopy uses this phenomenon to achieve excitation of the sample which is close to the surface of the glass, and since these evanescent field is in the order of $200nm$, this technique renders high spatial resolution in the z-axis. [201] TIRF-M then becomes particularly powerful when imaging close to the surface, and the volume above the surface needs to be treated as background. Particularly, for supported lipid membranes, which are formed on surfaces, interactions with proteins, and other macromolecules can be visualized with high spatial resolution (see Figure 4.1A).

4.2.2 Confocal Microscopy

Confocal microscopy is a widely used technique that overcomes the limitations of traditional wide-field microscopy by eliminating out-of-focus light and providing high-resolution images of thick specimens. The design of a confocal microscope introduces a physical pinhole in front of the detector in an optically conjugate plane to eliminate the out-of-focus fluorescence, and thus creating a femtoliter detection volume (see Figure 4.1B). This also ensures that light at or very close to the focal plane is allowed to enter the detector, significantly increasing the optical resolution of the image, improving the signal-to-noise ratio, while reducing the signal intensity as most of the light is blocked out. [195] The light after the pinhole is recollimated and optical filters are used for spectral selection before acquiring the signal on the detectors. The development of effective photomultiplier tubes (PMT) and avalanche photodiodes (APD) detectors, fast objective scanners (galvo-scanners), sample scanners (piezo-scanners), lasers and fast computation have made confocal microscopy the golden standard for imaging in life sciences. [202, 203] The Abbe limit for diffracton limited resolution gives minimum lateral resolvable distance r_{lat} as

$$r_{lat} = \frac{0.61\lambda}{NA}.$$

For confocal microscopy, the size of the pinhole can be changed to achieve higher lateral or axial resolution while simultaneously sacrificing the number of photons collected by the detector. A point source through an objective would produce a point spread function (PSF) at the image plane, which is described by an Airy pattern. The Airy pattern at the plane of the pinhole is given by

$$d_{Airy} = \frac{1.22\lambda}{NA} * M$$

where M is the total magnification of the system, and the optimal size of the pinhole should be equal to or slightly greater than the d_{Airy}.

4.2.3 Single molecule localization microscopy (SMLM)

For conventional fluorescence microscopy, all excited fluorophores simultaneously emit fluorescence light which is received by the detector, producing a diffraction-limited image. Any two fluorophores positioned closer than the diffraction limit, will be unresolvable in this image. SMLM overcomes the diffraction limit by employing a stochastic strategy, such that a subset of the total fluorophores emit during acquisition of an image. In this way, if a large set of these images are acquired, their average would be the same as a conventional fluorescence diffraction-limited image where all the fluorophores are emitting simultaneously. In SMLM, this large set of images are individually processed to fit a gaussian distribution on single emitters to attain their precise location, and with all the images, one could reconstruct a super-resolved image from a set of diffraction-limited images (see Figure 4.1C). This stochastic "on and off" driving of the fluorophores have been achieved by various means including the photoactivity of the fluorophores and external chemical cues. This has led to the development of various super-resolution techniques such as Photoactivated Localization Microscopy (PALM), [204, 205] Stochastic Optical Reconstruction

Microscopy (STORM), [206] and Points Accumulation for Imaging in Nanoscale Topography (PAINT). [207] Furthermore, this "blinking" of the emitters has also been achieved by the use of fast hybridization kinetics of single stranded DNA molecules (termed as DNA-PAINT). [208] In this technique, the particles of interest are tagged with a binder DNA strand and complementary imager strands are available in bulk. An additional advantage of DNA-PAINT is the near infinite bulk of imager strands and the constant turnover results in extremely high "photon budget" which is convenient for SMLM which requires imaging thousands of frames over a large period of time.

4.3 Fluorescence correlation spectroscopy (FCS)

Fluorescence correlation spectroscopy (FCS) is a fluorescence based technique that extracts information from the fluctuations in fluorescence intensity by the use of correlation mathematics. The correlation in the time-domain fluctuations in the fluorescence intensity provides information about the processes that are responsible for this fluctuation (see Figure 4.1D). Many descriptions of this are available in literature and this technique has seen extensive advancements in both technology and its theory. [185, 209–217] FCS has been used heavily in this thesis, and this has led to an explanation of the principle of FCS to various collaborators from diverse scientific backgrounds. I will briefly describe this approach here, as more *accurate* and detailed description of the principle of FCS can be found elsewhere. [196, 215, 218–220]

Let's consider a large ensemble of particles undergoing Brownian motion, with five particles in the detection volume, and each particle emits a single photon in a unit time. Average fluorescence intensity from this measurement would thus give a fluorescence intensity of 5 arbitrary units (5 AU). Since these particles are diffusing due to Brownian motion, the fluorescence intensity would fluctuate due to the particles entering or exiting the detection volume. If a particle enters, the intensity goes up by 1 AU and *vice versa* if a particle leaves. This would mean that the rate of change of fluorescence intensity would then contain the information on how fast or slow the particles diffuse in and out of the detection volume. Thus, the temporal dependence of the fluctuations would encode the diffusivity of the particles under observation. Now, imagine if we increase the total ensembe of particles and at any point we have a hundred particles in the detection volume. The average intensity would be given as 100 AU. If a particle enters or leaves the volume, the change in intensity would still be 1 AU. The fluctuations would still encode the diffusivity of the particles, and this will remain the same as the particles are the same. Although, the magnitude of fluctuation as compared to the average intensity would be much smaller. Similarly, if there were 1000 particles in the detection volume, this fluctuation magnitude would become even smaller. This also convinces us that the fluctuations not only encode the diffusivity of the particles, but also the number of particles in the detection volume, and the magnitude of fluctuations are inversely proportional to the number of particles in the detection volume on average. Now, correlation analysis is the tool which can extract this *clearly* available information from the intensity fluctuations. An autocorrelation funcion on the intensity is given by

$$G(\tau) = \frac{\langle I(t)I(t+\tau)\rangle}{\langle I(t)\rangle^2} = 1 + \frac{\langle \delta I(t)\delta I(t+\tau)\rangle}{\langle I(t)\rangle^2}$$

where $I(t)$ is the fluorescence intensity at time t, τ is an infinitesimal time increment, and $\delta I(t) = I(t) - \langle I(t) \rangle$. The PSF for a confocal microscope can be approximated by a 3D gaussian, for a freely diffusing particle in 3D we get the autocorrelation function

$$G(\tau) = \frac{1}{2\sqrt{2}\langle N \rangle}[1 + \tau/\tau_D]^{-1}[1 + \kappa^{-2}\tau/\tau_D]^{-1/2} + 1$$

where τ_D is the diffusion time of the particles, $\langle N \rangle$ is the average number of particles in the detection volume, and κ is the PSF aspect ratio which is measured during calibration of the setup. Similarly, for diffusion of particles in 2D

$$G(\tau) = \frac{1}{2\langle N \rangle}[1 + \tau/\tau_D]^{-1} + 1$$

which is a good description for diffusion of lipids in a membrane or particles diffusing in the bilayer.

Fluidity of the membranes play an important role in their morphology, and their interactions with their environment. Ability to probe this mechanical property of the membrane makes FCS one of the most vital techniques in membrane biophysics, [66, 83, 221–224] and has been utilized extensively in this thesis.

5
Contents of this thesis

Lipid membranes are ubiquitous in biology and their *emergent* properties are extremely intriguing from a fundamental point of view. Inching towards the creation of synthetic cells, it is important to develop technology to control and manipulate membrane based encapsulations. Various protein machinery is employed to mimic basic aspects of a cell, in an attempt to duplicate the activities of a living cell. We focused on finding and implementing external agents that could alter the mechanical properties of the lipid membranes. Lipid membranes of different compositions are well studied, and they show a well defined mechanical trend based on the chemistry of the lipids that make the bilayer. Our aim was to functionalize the membranes with agents which could dynamically change the composition of the bilayer, such that we could induce membrane deformations. With collaborations with material scientists and chemists, we focused on two strategies:

1. How would an energy-driven system incorporated within the bilayer affect the thermodynamics of the lipid membrane? We chose light-activated synthetic rotary motors, owing to their hydrophobic nature, they incorporate in the core of the bilayer. We systematically investigated the action of rotary motors inside lipid membranes, further observed their correlation with the chemical structure, aggregation properties and rotation dynamics of the motors.

2. How would functionalized macromolecules change the mechanical properties of the membrane? An extensive theoretical framework is available for polymer-membrane interactions, and with increasing complexity of synthetic polymers, we needed fundamental experimental studies to probe their behavior with lipids.

The investigations in this thesis were focused on model membranes, for creating controllable experimental scenarios with measurable parameters to probe the changes. The systems used in this thesis could be extended to synthetic cell formulations with *in vitro* reconstitution of protein machinery. Additionally, these systems also have interesting implications in bilayers formed of synthetic copolymers. The objective of this thesis was to study and characterize strategies to manipulate the dynamics of lipid membranes. The work in this thesis has been made possible because of the exceptional collaborators and their excellent work.

Part II

Results and Discussion

6
Rotary motors in lipid membranes

In the pursuit of answering a simple question, "What happens if we have rotating synthtic motors inside the lipid bilayer?", we stumbled upon some interesting consequences. I will present a series of projects in this chapter which explore the effects of these light-activated rotary motors. The research presented in this chapter was conducted in close collaboration with Ainoa Guinart Planellas (then PhD student at the group of Prof. Ben Feringa). Previously being reported as molecules which could "drill" holes in the membrane of living cells, these rotary motors stood out as promising candidates for modulation of membrane dynamics. There was a clear lack of systematic investigation of what these motors could be capable of, or their mechanism of action when it came to their use in lipid membranes. Drawing inspiration from the decade long studies of azobenzene based photoswitches in lipid bilayers, we embarked on a journey to investigate the consequences of a unidirectional motion in membranes. We employed various quantitative and optical techniques to systematically investigate how these inherently contiguous machines can drive lipid membranes out of equilibrium. Furthermore, we investigated how rotary motors with different chemical and structural properties would affect this process. Finally, with these investigations showing promising potential, rotary motor conugated phospholipids were studied in lipid bilayers to achieve membrane building units that could be driven out of equilibrium with light.

6.1 P1. Light-Activated Synthetic Rotary Motors in Lipid Membranes Induce Shape Changes Through Membrane Expansion

This work provides a systematic investigation into the impact of light-activated molecular rotary motors on well-defined biological membranes. It was noted that the molecular motors induce significant mechanical transformations in lipid bilayers upon irradiation. Crucial factors such as the concentration of the embedded motors, lipid composition, and more prominently, the fluidity of the membrane, were found to have substantial influence over this phenomenon. It was observed that under continuous irradiation, the membranes perpetually stay in an out-of-equilibrium state with continued deformations. This study focuses on the characterization of these machines, and subsequently offers an in-depth inquiry into their operation within membranes. Importantly, the surrounding lipid environment was identified to have a distinct impact on the rotation cycle of the molecular motors. Using giant unilamel-

lar vesicles (GUVs) as a model system, the study examined how molecular motors induce a change in the mechanical properties of the membrane. Notably, a broad array of shape transitions were observed, corroborating the key role of the motors as dynamic agents contributing to the increase in the surface area of lipid bilayers. Upon irradiation, these vesicles demonstrated pronounced membrane fluctuations. Some of them further went through consequential morphological alterations under extended irradiation. Surface area and volume calculations from volumetric images of these vesicles, before and after irradiation, clearly demonstrated that the shape transformations were a consequence of area expansion. Despite such considerable morphological transformations, vesicles did not get permeable to small molecules (in this case, Alexa488). This observation was at odds with what was observed when these motors were added to living cells, which also motivated this study to consider and carefully investigate photo-oxidation effects. Upon termination of the $405\,\mathrm{nm}$ excitation, membrane fluctuations were seen to gradually decrease with the vesicles ultimately reverting to their quasi-spherical or spherical shapes. Overall, this study provides profound insights into the complex dynamics governing the interaction of molecular rotary motors with biological membranes. The study has identified that the continual activation of the motors results in a dynamic alteration of the surface area of the lipid membrane. These crucial insights advance our understanding of the functions of molecular rotary motors within the context of lipid membranes. The findings set the stage for future investigations into the promising applications of these molecules in chemical biology and various other fields.

Light-Activated Synthetic Rotary Motors in Lipid Membranes Induce Shape Changes Through Membrane Expansion

Yusuf Qutbuddin, Ainoa Guinart, Svetozar Gavrilović, Kareem Al Nahas, Ben L. Feringa,* and Petra Schwille*

Author contributions:

Y.Q. and A.G. contributed equally. **Y.Q.**, A.G., P.S., and B.F. conceived this study. **Y.Q.** and A.G. performed all the experiments. **Y.Q.** and A.G. designed the experiments. **Y.Q.** performed the FCS experiments and analysis. A.G. performed experiments with SLBs and analysis. **Y.Q.** performed experiments with GUVs and analysis. **K.A.N** designed the microfluidic traps and produced the chips. S.G. and **Y.Q.** performed and analyzed the AFM experiments. **Y.Q.**, A.G., B.F., and P.S. wrote the manuscript. All authors discussed and revised the manuscript.

Y. Qutbuddin, A. Guinart, S. Gavrilović, K. Al Nahas, B. L. Feringa, P. Schwille, Light-Activated Synthetic Rotary Motors in Lipid Membranes Induce Shape Changes Through Membrane Expansion. Adv. Mater. 2024, 36, 2311176.
https://doi.org/10.1002/adma.202311176

published in

Advanced Materials (2024)

RESEARCH ARTICLE

ADVANCED MATERIALS
www.advmat.de

Light-Activated Synthetic Rotary Motors in Lipid Membranes Induce Shape Changes Through Membrane Expansion

Yusuf Qutbuddin, Ainoa Guinart, Svetozar Gavrilović, Kareem Al Nahas, Ben L. Feringa, and Petra Schwille**

Membranes are the key structures to separate and spatially organize cellular systems. Their rich dynamics and transformations during the cell cycle are orchestrated by specific membrane-targeted molecular machineries, many of which operate through energy dissipation. Likewise, man-made light-activated molecular rotary motors have previously shown drastic effects on cellular systems, but their physical roles on and within lipid membranes remain largely unexplored. Here, the impact of rotary motors on well-defined biological membranes is systematically investigated. Notably, dramatic mechanical transformations are observed in these systems upon motor irradiation, indicative of motor-induced membrane expansion. The influence of several factors on this phenomenon is systematically explored, such as motor concentration and membrane composition., Membrane fluidity is found to play a crucial role in motor-induced deformations, while only minor contributions from local heating and singlet oxygen generation are observed. Most remarkably, the membrane area expansion under the influence of the motors continues as long as irradiation is maintained, and the system stays out-of-equilibrium. Overall, this research contributes to a comprehensive understanding of molecular motors interacting with biological membranes, elucidating the multifaceted factors that govern membrane responses and shape transitions in the presence of these remarkable molecular machines, thereby supporting their future applications in chemical biology.

1. Introduction

Cells are the most efficient chemical laboratories known to exist, simultaneously performing and maintaining thousands of parallel processes that are key to and essential for life.[1] Reconstituting a pertinent set of these procedures, such as metabolism, homeostasis, and replication, in bottom-up approaches will be crucial to address fundamental questions related to the origin of life.[2] This is the reason why there has been an increasing interest over the last years in engineering and controlling artificial cellular systems able to replicate lifelike functions.[3] To harbor the abovementioned, compartmentalization is one of the fundamental features of living systems. This simple concept holds a pivotal role due to its ability to create isolated microenvironments, concentrate molecules, protect structures, and foster chemical communication.[4] Primarily composed of lipids, cellular membranes spontaneously arrange into bilayers due to their amphipathic properties, effectively segregating polar environments. Membrane-bound structures possess the unique ability to confine different compartments while still allowing for exchange and interaction with the environment and supporting their own dramatic transformation in the replication process. Mechanistically understanding and controlling the emergence, fusion, budding, and division of membranous organelles is therefore of great importance. In nature, membrane deformations are driven by a combination of external and internal mechanical forces acting on the membrane. These forces are often generated by dynamic protein networks in a direct interplay with membrane lipids. For instance, proteins can integrate into the membrane or form large assemblies on the membrane surface and thereby apply lateral pressure, inducing local changes in membrane curvature and membrane budding. However, to execute large-scale membrane transformations as required for cell division, the cell is thought to invest chemical energy, e.g., by engaging force-inducing motor proteins or cytomotive filaments fueled by NTP hydrolysis.[5] The natural mechanisms for membrane deformation have been previously discussed,[6] and remodeling of membrane topology and shape has been thoroughly studied.[7]

Y. Qutbuddin, S. Gavrilović, K. Al Nahas, P. Schwille
Cellular and Molecular Biophysics
Max Planck Institute of Biochemistry
82152 Martinsried, Germany
E-mail: schwille@biochem.mpg.de

A. Guinart, B. L. Feringa
Stratingh Institute for Chemistry
University of Groningen
Groningen 9747 AG, The Netherlands
E-mail: b.l.feringa@rug.nl

The ORCID identification number(s) for the author(s) of this article can be found under https://doi.org/10.1002/adma.202311176

DOI: 10.1002/adma.202311176

ADVANCED SCIENCE NEWS
www.advancedsciencenews.com

ADVANCED MATERIALS
www.advmat.de

In the context of investigating the mechanics of cellular processes, diverse external stimuli have been employed to artificially introduce membrane deformations. Among these, various methods including temperature gradients,[8,9] osmotic stress,[10,11] electric fields,[12,13] chemical reactions,[14] or pH variations[15] have been applied. But also, membrane components themselves may be used to induce deformations. Photoswitches, molecules capable of reversible interconversion between distinct states upon exposure to light, and photosensitizers have been incorporated into lipid bilayers as an additional strategy for membrane remodeling.[16–19] An even more innovative approach involves directly modifying the membrane building blocks by attaching a light-responsive molecule, e.g., by introducing it to one of the acyl tails of the phospholipids.[20] Photoswitchable lipids have been explored for altering membrane properties such as controlling and modifying domain sizes in supported lipid bilayers (SLBs),[21,22] increasing fluidity of planar membranes,[23] transient pore formation in giant vesicles,[24] and facilitating fusion,[25] among others. However, most of these systems only function under UV light, which can severely damage lipid membranes.[26,27] An important aspect to be considered when using photoswitches is the interconversion between two different states in contrast to a unidirectional continuous movement. These systems are interesting for many applications, where switching between an "on" and "off" state is required. In contrast, here we present a novel approach to push lipid systems out of equilibrium by using a continuous remodeling process.

Emerging from chiroptical molecular switches, a more controlled motion can be achieved by the so-called overcrowded alkene-based rotary molecular motors.[28] These molecules were first reported by Feringa et al. in 1999 and represented a breakthrough in the field of molecular machines because of their repetitive, photochemically driven unidirectional rotation around a carbon–carbon double bond.[29] They fulfill the three basic requirements of a motorized machine: a complete 360° unidirectional rotation, repetitive motion, and energy consumption. Extensive reviews about the design of light-driven rotary molecular motors have been published since then.[28,30] Because of their continuous unidirectional rotation when irradiated with the appropriate wavelength of light, Feringa motors have garnered substantial interest in biological applications. As recently shown by the Feringa group, these remarkable machines can be used to promote on-demand delivery from polymersomes in cancer cells.[31] Notably, the amphiphilic polymer employed in the study differs strongly in its mechanical characteristics from phospholipids. A lower molecular mass, membrane thickness and elasticity were found to be critical for the system to break under motor action. The spectacular functions of protein motors found in nature have inspired chemists to integrate synthetic machines into similar media, from simple synthetic lipid bilayers to living cellular systems with the goal to modulate and control biological functions in the microscopic world. Pioneering work of this kind appeared in 2017 by the Tour group.[32] Their studies reported induction of cellular death in both mammalian cancer cells and bacterial organisms by the application of light-activated rotary motors to their membranes.[33–35] Tour's proposed hypothesis regarding the interaction between motors and membranes is based on the concept of light-activated mechanical motion inducing membrane disruption, or citing textually, "drilling holes" into the lipid membranes.[32] More recently, an alternative mechanism was introduced by Antonenko et al. according to which photodynamic activity rather than mechanical action was responsible for membrane permeability.[36] In a different study, Wang et al. showed that light-driven molecular motors can boost selective ion transport through phospholipid bilayers.[37] One should emphasize that both studies were carried out using a laser-scanning confocal microscope to activate the molecular motor. This method of illuminating the sample point-by-point with a high-energy laser has been proven to also induce localized heating effects and cellular damage using many kinds of photoresponsive molecules.[38]

GUVs offer a unique platform for visualizing membrane responses to external stimuli.[39] They can be imaged using phase-contrast techniques to observe the overall effects on the membrane induced by various processes. Additionally, their sizes of typically many tens of micrometers allow for imaging with fluorescent labels incorporated into the membrane. GUVs have served as valuable tools in the investigation of diverse light-triggered membrane responses. Notable examples include photosensitizers that induce oxidation-related structural changes in the membrane,[18,40] photoswitches that enable controlled regulation of membrane channels,[41–43] and photoswitchable lipids and molecules capable of triggering membrane deformations[44–46] among others. Furthermore, such light-controllable molecules have been employed to induce reversible changes in the membrane area of red blood cells.[47] Light triggered plasmon resonance gold nanoparticles have also been employed to heat lipid membranes locally to reversibly control current across lipid membranes.[48] These advances hold significant promise for manipulating synthetic cell membranes. In all the systems mentioned above, light-triggered activity is reversible and shifts between two equilibrium states.

In contrast, we here revisit the question of how photoactive rotary motors, an out-of-equilibrium system, may dynamically trigger responses of well-controlled membranes in synthetic cells. Our primary objective is to enhance our mechanistic understanding of the interactions between light-driven molecular machines and biological membranes. To this end, we employed the simplest unfunctionalized molecular motor and investigated its behavior within both, supported and free-standing membrane systems. Our pioneering investigation considers the influence of the lipid environment on various features of molecular machine dynamics, such as rotational speed, quantum yield of photoisomerization, and solvent-dependent degradation. Additionally, we explore the impact of rotary motor activity on the mechanical properties of the membrane, such as shape and fluidity. We discovered that these molecular machines possess a remarkable capability to induce multiple shape transitions and membrane modulation in GUVs, however, without affecting the permeability of the membrane as has been suggested. Furthermore, we achieve significant changes in the reduced volume of our vesicles under light exposure, enabling membrane deformation over time. Moreover, we present a comprehensive quantitative analysis on SLBs, where we systematically investigate the effects of motor concentration, membrane order, local heating, and photooxidation to the lipid systems.

ADVANCED SCIENCE NEWS
www.advancedsciencenews.com

ADVANCED MATERIALS
www.advmat.de

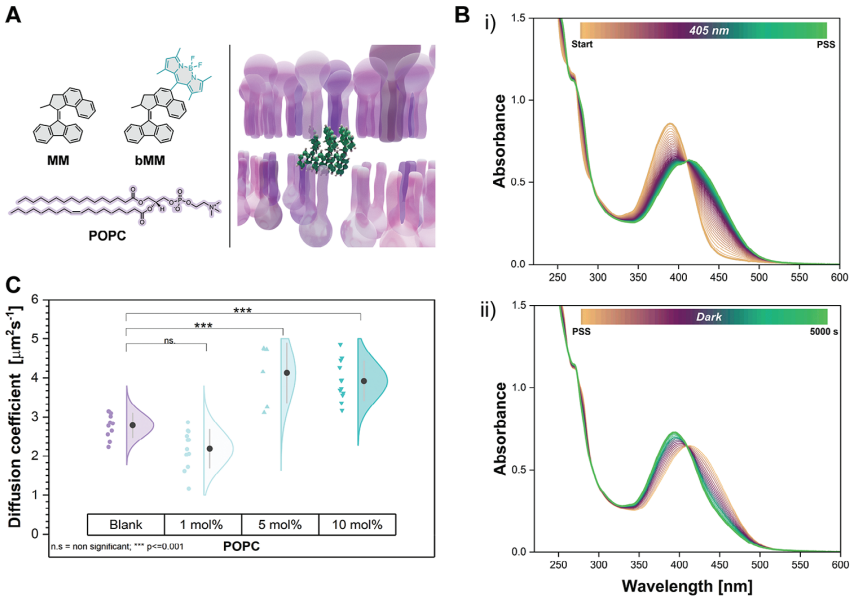

Figure 1. Molecular motor and lipid membrane interactions. A) Chemical structures of **MM** (upper left), **bMM** (upper right), and POPC (bottom). B) UV–vis absorption spectra of $\mathbf{MM}_S$ in a POPC vesicle (400 nm diameter in MiliQ). Total concentration photoactive molecule concentration 50 μm representing 10 mol.% of total lipid content. i) Change of absorption spectra under light irradiation to photostationary state (PSS, 405 nm, 25 °C). ii) Change of absorption spectra after PSS under dark conditions, THI process. C) The diffusion coefficient of lipid membranes changes upon incorporation of **MM** in different concentrations. Measurements were performed using FCS in POPC SLBs at 25 °C. The graph shows the mean ± SD of independent experiments. Statistically significant data (*** equivalent to a $P \leqslant 0.001$). Non significant statistical data (ns).

2. Results and Discussion

2.1. Molecular Motor Incorporation Into Lipid Membranes

A light-driven molecular motor (**MM**) was employed in our study as the photoresponsive membrane intercalator. The general design of our molecular machines is shown in **Figure 1**a and consists of an overcrowded alkene molecular motor able to undergo unidirectional rotation across the central double bond when irradiated with blue light.[49] For tracking purposes, and when indicated explicitly, we took advantage of our recent discovery, an analogous molecular motor conjugated to a BODIPY molecule (**bMM**) able to undergo unidirectional rotation and photoluminescence synergistically when the appropriate wavelength is employed.[50] These molecules have been fully characterized and analyzed previously, whereas the focus of this study is to understand their integration and operation into lipid systems. We first focused on their successful incorporation into both supported and free-standing phospholipid systems prepared as described in the experimental section with 1-palmitoyl-2-oleoyl-sn-glycero-3-phosphocholine (POPC) as a reference lipid. Figure 1b i) shows the absorbance change upon irradiation with 405 nm light, corresponding to the photoisomerization $\mathbf{MM}_{stable} \rightarrow \mathbf{MM}_{metastable}$ incorporated in a POPC vesicle. Similar transitions with the different systems studied in this work can be found in Figure S3 (Supporting Information). Figure 1b ii) shows the change in the absorption spectra after reaching the photostationary state (PSS) under dark conditions, corresponding to the thermal helix inversion (THI) process. The maximum absorbance of $\mathbf{MM}_{stable}$ is located at 400 nm and is directly proportional to its concentration.[51] Quantitative uptake efficiencies for the different environments can be found in Figure S2 and Table S1 (Supporting Information). Incorporation was also evaluated qualitatively using **bMM** fluorescence in both SLBs and GUVs. Figure S1a (Supporting Information) shows an SLB imaged with total internal reflection fluorescence (TIRF) microscopy with **bMM** incorporated. Notice the non-uniform distribution of the fluorescence intensity of **bMM** (green), which appears to concentrate in denser regions ("hot spots") of the lipid membrane (magenta). The reasoning behind this observation can be attributed to the preference of our molecular machines to form small aggregates within the hydrophobic pocket of the membranes. This preference is attributed to the aromaticity of our compounds, which promotes π–π stacking interactions. Incorporation in GUVs can also be validated using **bMM** fluorescence (Figure S1b, Supporting Information). We did not observe any phase separation, in agreement with previous works where domain formation occurred only for ternary mixtures with photoswitchable lipids.[22,52] Intuitively, the addition of an external molecule also influences the ordering of the lipid membrane. Fluidity measurements using fluorescence correlation spectroscopy (FCS) revealed an increase in the diffusion coefficient of the membranes when introducing any of our compounds (Figure 1c; Figure S4, Supporting Information).

ADVANCED SCIENCE NEWS
www.advancedsciencenews.com

ADVANCED MATERIALS
www.advmat.de

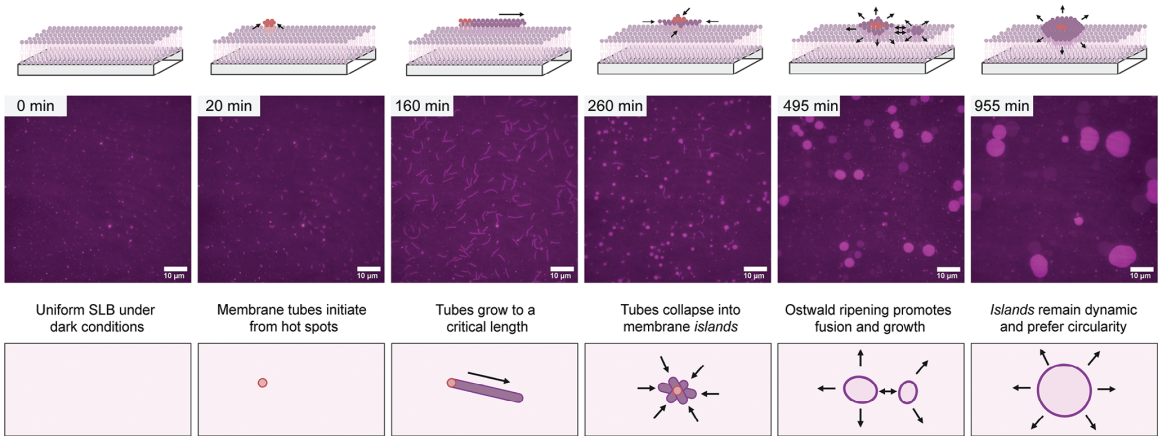

Figure 2. Molecular motor action in an SLB. TIRF microscopy images of the step-wise process of the induced effects of a POPC SLB with 10 mol.% **MM** under irradiation and explanatory schematics of the observed process. The images show different time points of the same spot in the SLB sample during the continuous irradiation using 405 nm @1.5% (**MM** action), 642 nm@0.1% (lipid imaging), 3 s interval time-lapse, during a 16h experiment.

2.2. Lipid Environment Influences the Rotation Cycle

We next investigated how the lipid environment impacts the rotation cycle of our molecular motors. Extensively documented in the literature by the Feringa group, these molecules can undergo a 360° rotation cycle, accomplished through four sequential steps in a unidirectional manner.[53] In the case of symmetric motors like **MM**, this process involves two equivalent photochemical *E-Z* isomerizations, each followed by a THI step, resulting in continuous unidirectional motion along the central axis. This movement persists as long as the system is exposed to photons of the appropriate wavelength. The full rotation cycle of **MM** in dodecane, to simulate the lipid environment, along with the corresponding molecular states revealed by ^{1}H-NMR studies, is illustrated in Figure S5 (Supporting Information). During the study, it was observed that the peak intensity of the protons corresponding to the stable state of the motor decreases after irradiation. In contrast, new absorption peaks emerged, attributed to the metastable isomer of the motor. At 5 °C and after 60min of constant irradiation at 405 nm, a photostationary state (PSS) was reached, with a stable-to-metastable isomer ratio of 60:40. Removing the light source led to the complete recovery of the stable state after 175min in the dark. Once we confirmed the rotary function of **MM** in a solvent simulating the lipid environment, we proceeded to investigate its optical properties using steady-state UV/vis absorption spectroscopy. In addition to the dodecane solution, we examined the motor in toluene, serving as a reference organic solvent, and embedded in the membrane of small unilamellar vesicles (SUVs) of the different lipids used later in the study. To compare with previous work by Tour and coworkers, we also prepared the samples in water + 1% DMSO solution. **Figure 2b** and Figure S3 (Supporting Information) display the corresponding absorption spectra at the stable state (orange line) with absorption band maxima at ≈400 nm. Despite the different media, no significant changes in the shape of the absorption spectra were observed. To assess the photochemically driven isomerization of **MM** in these environments, we subjected each sample to irradiation with a 405 nm light-emitting diode (LED) and monitored the changes in the absorption spectra until reaching PSS (green line), enabling us to quantify the quantum yield (QY) of the process, which corresponds to 8.2% in dodecane (Table S2 and Figure S6, Supporting Information). Notably, a substantial decrease (around half) in the QY of the photoisomerization process was observed when **MM** was confined within the lipid membrane. Specifically, the QY was found to be 3.8%, 4.2%, and 2.4% in POPC, DOPC, and DPPC vesicles, respectively. This effect is proven to be correlated with the fluidity of the membrane, being less intense in unsaturated more flexible lipids like DOPC and more pronounced (≈fourfold decrease) when using rigid saturated lipids like DPPC. These results, in concordance with previous studies on solvent-viscosity effects,[54] indicate how a crowded environment hinders the molecule's isomerization process and will strongly influence the remodeling capabilities of **MM** as it will be shown in the following sections. A decrease in the QY could also be explained by the previously mentioned "hot spots", where **MM** tends to form small aggregates due to $\pi-\pi$ interactions. The aggregation state may impede the isomerization step, which involves a large conformational change, leading to the observed reduction in QY. Interestingly, when the sample is prepared in a water + 1% DMSO solution the QY is the most affected, indicating possible aggregation and degradation of the sample. Once the light source is removed and the sample is kept in dark, the metastable isomer can undergo THI to the second, chemically identical, stable isomer. This transformation completes a unidirectional 180-degree rotation and represents the rate-determining step of the process.[53] Kinetic studies determined the thermodynamic parameters of this process in the different conditions studied (half-life of 139 s in dodecane at 25 °C, see Table S3, Supporting Information). In essence, no significant differences in rotation speed were observed when comparing the motor's behaviour in a lipid environment and in solution (116, 121, and 107 s for POPC, DOPC, and DPPC, respectively). However, a general trend indicates a faster rotation speed (≈30 s decreases in half-life) when **MM** is embedded in a membrane system. This observation can be attributed to

ADVANCED SCIENCE NEWS
www.advancedsciencenews.com

ADVANCED MATERIALS
www.advmat.de

a considerably smaller conformational change between the THI and photoisomerization steps, along with a higher preference of the motor to undergo THI favouring intermolecular interactions. It is important to note a substantial decrease (ten-times fold) in the motor's speed when the sample is prepared in a water + 1% DMSO solution, with no clear isosbestic point in the THI process, indicating degradation and/or aggregation of the motor (Figure S8, Supporting Information). As a result, this condition was discarded in the subsequent experiments. Overall, these results indicate that ordered environments of lipid bilayers reduce the efficiency of the photochemical step but speed up the thermal relaxation of **MMs**.

2.3. Motor Activity Induces Membrane Remodeling in Supported Lipid Bilayers

In contrast to a vesicle, where the lipid bilayer forms a closed shell, SLBs are planar structures that rest on a solid support. This arrangement offers a significant advantage in terms of stability and enables the use of a greater number of characterization tools. As a result, it becomes possible to achieve a more reliable quantification of the destabilization process induced by the molecular motors. SLBs were formed via vesicle fusion with 10 mol.% of **MM** and using a single phospholipid composition primarily consisting of POPC unless otherwise specified. The analysis was carried out using a TIRF microscope which offers several advantages when studying SLBs. This technique provides exceptional spatial resolution in the z-axis, allowing us to visualize dynamic processes occurring at the SLB surface with high optical sectioning, making it suitable for long-term imaging. TIRF microscopy also offers advantages for irradiation experiments. The microscope's 405 nm laser enables widefield illumination of the entire sample, in contrast to scanning confocal microscopy, where the sample is irradiated one confocal point at a time. This leads to a noteworthy decrease in the required power for activating the motors (600mW cm^{-2} when used at 10%). Throughout the experiment, the microscopy chamber was consistently maintained at 25 °C. The effect of irradiation was methodically assessed under diverse conditions with respect to motor concentration, membrane order influenced by cholesterol insertion, lipid composition, thermal contribution, and the influence and generation of reactive oxygen species (ROS).

2.3.1. Effect of Molecular Motor Rotation on SLBs

We started by evaluating the integrity and homogeneity of the membranes, which were found to be satisfactory under all tested conditions. Throughout the entire duration of the subsequent experiments, no presence of domains or membrane holes was observed (Figure S9, Supporting Information). The photoresponsivity and ability of **MMs** to deform SLBs was assessed by conducting a 16h experiment involving simultaneous irradiation and imaging of the sample (405 nm @0.5% (**MM** action), 642 nm @0.1% (lipid imaging), 10 s interval time-lapse). In membranes lacking **MMs**, no light-induced effects were detected (Figure S9, Supporting Information). In contrast, SLBs containing **MMs** exhibited a step-wise remodeling process (Figure 2; Video S1, Supporting Information). At the outset of irradiation, membrane tubes began to form and continued growing from one end until they reached a saturation length of (4.3±0.9) µm (Figure S10, Supporting Information). After 160min of irradiation, some of these tubes started collapsing into star-shaped structures while remaining attached to the membrane. This process occurred for all observed tubes, and after 260min of irradiation, all the tubes collapsed. Subsequently, the star-shaped membrane underwent a rapid transformation into circular-shaped membrane "islands" through an Ostwald ripening process, and their size increased as long as the irradiation persisted. Notably, even after 16h of constant irradiation, these "islands" remained dynamic and capable of further remodeling, as long as the light source stayed on. It is essential to mention that the time scale of this process is dependent on the irradiation method. The remodeling process can be accelerated by increasing the laser power or reducing the time between subsequent irradiations (time-lapse intervals). The so-formed "islands" were characterized by evaluating their fluorescence intensity profile and height. Atomic force microscopy (AFM) measurements revealed the 3D structure of the "islands" as their height corresponds to two or three times the bilayer height (4 nm) (**Figure 3a**; Figure S11, Supporting Information). These membrane exclusions that end up as "islands" are indicative of a response to area expansion in the lipid bilayer. In reaction to such an area increase, the membrane expels lipid tubes since the total area of the supported membrane is confined. These tubes above a certain size flatten out to form patches of membrane on top. Similar tubulations have been observed as a result of lipid peroxidation-induced area expansion.[55] Notably, when SLBs with 10 mol.% **bMM** were observed under irradiation, the tubes and patches exhibited a signal for both the channels corresponding to the membrane and **bMM**. Lipowsky has explained in the context of supported bilayers why tubes growing from SLBs are energetically favorable as compared to vesicles.[56] These observations confirm the effect of **MM** irradiation on membrane remodeling and how this is linked to the lipid membrane accommodating new space created by the molecular motor action.

2.3.2. Effect of Molecular Motor Concentration on Membrane Remodeling

Once the remodeling process was characterized, the irradiation setup was adjusted to speed up the "islands" formation to a more convenient timescale (405 nm @1.5% (**MM** irradiation) 642 nm@0.1% (lipid imaging), 3 s interval time-lapse). This ensured the formation of membrane "islands" within 60min of irradiation. To quantify the deformation, the percentage of area occupied by "islands" was evaluated at the beginning and after 1h of irradiation, using 10 × 10 tiles (600µ m^2) of at least three independent samples (See Experimental Section for details and Figures S12 and S13, Supporting Information). Changing the **MM** concentration from 1 to 25 mol.% demonstrated a linear effect on "islands" formation, and this linearity persisted even after 6h of irradiation (Figure 3b). Additionally, the growth rate of the "islands" was found to be concentration-dependent, with higher concentrations (10–25 mol.%) accelerating the process, while lower concentrations (1–5 mol.%) exhibited a slower growth speed, especially during the first 30min of irradiation (Figure S14, Supporting Information). These results confirm the direct

ADVANCED SCIENCE NEWS
www.advancedsciencenews.com

ADVANCED MATERIALS
www.advmat.de

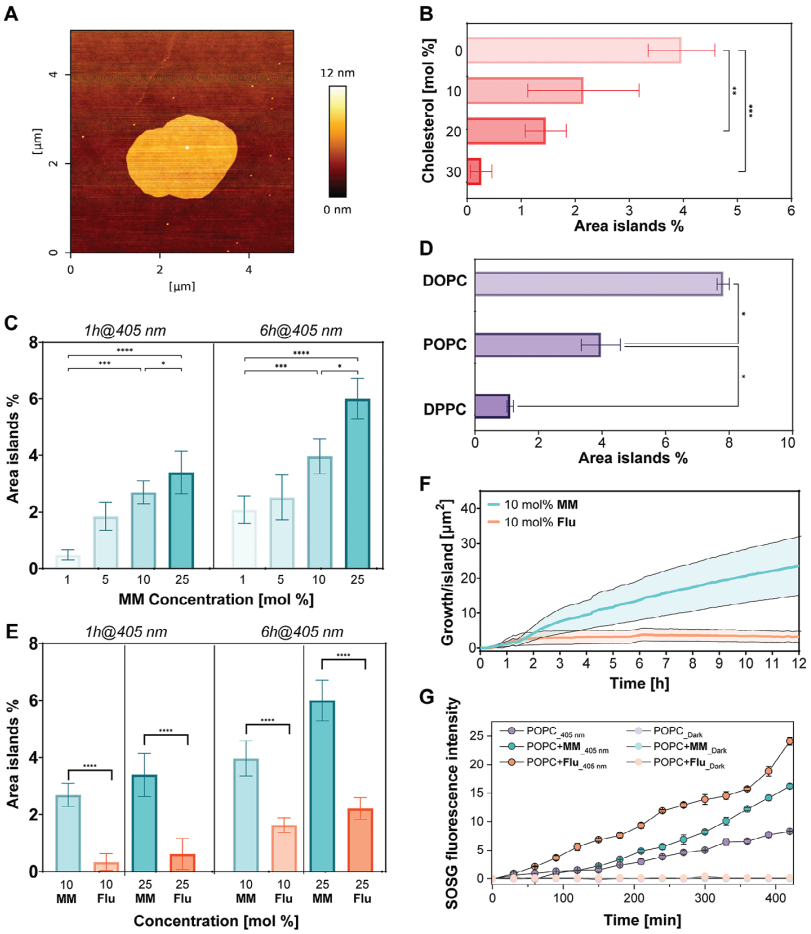

Figure 3. Factors influencing molecular motor remodeling process. A) Atomic force microscopy image of a membrane island created due to **MM** irradiation. The image shows a POPC SLB sample with 10mol.% **MM** which was irradiated for 1h with 405 nm@1.5%. B) Effect of cholesterol addition on the % of area deformation in POPC SLBs with 10 mol.% **MM** (Samples irradiated for 1h with 405 nm@1.5%). C) Percentage of membrane island deformation in POPC SLBs with increasing concentrations of **MM** (1 to 25 mol.%) after 1 or 6h of irradiation 405 nm@1.5%. D) Membrane fluidity effect on the % of area deformation in SLBs using different lipids and 10 mol.% of **MM** (Samples irradiated for 1h with 405 nm@1.5%). E) Thermal contribution in the SLB deformation. **MM** ■ and **Flu** ■ at 10 mol.% in POPC SLBs irradiated for 1 or 6h with 405 nm@1.5%. F) Long-term thermal contribution. Deformation effect on POPC SLBs containing **MM** and **Flu** at 10 mol.% in POPC irradiated for 16h with 405 nm@0.5% and 10 s interval. G) Fluorescence intensity from SOSG probe (total concentration 1µM) measured at 525 nm during 420min in SUVs samples containing plain POPC ■, 10 mol.% **MM** ■, or 10 mol.% **Flu** ■. Samples were constantly irradiated with a 400 nm LED between measurements. For all SLB samples irradiations were performed with 3 s interval (unless stated differently) and with 642 nm@0.1% for imaging purposes. The graph shows the mean ± SD of three independent experiments. Statistically significant data (****, ***, **, * equivalent to a $P \leqslant 0.0001$, $\leqslant 0.001$, $\leqslant 0.01$, and $\leqslant 0.05$, respectively).

relationship between molecular motor concentration and the membrane remodeling process when irradiated with blue light.

2.3.3. Effect of Membrane Order and Fluidity on Membrane Remodeling by Molecular Motors

The influence of cholesterol (Chol) on membrane order has been extensively investigated.[57] Particularly in POPC membranes, cholesterol exhibits a strong affinity to interact and pack tightly with the acyl chains of lipids, leading to reduced lipid mobility, an increase in overall membrane order, and a decrease in fluidity (Figure S16, Supporting Information). This structural effect contributes to the formation of a more rigid and compact lipid bilayer. Consequently, exploring the impact of cholesterol on membrane order is of great significance for understanding membrane processes and their functionality. Herein, we evaluated the effect of adding 10, 20, and 30 mol.% of cholesterol to POPC membranes containing 10 mol.% of **MM**. As shown in (Figure 3c; Figures S15 and S16, Supporting Information), increasing concentrations of cholesterol linearly inhibited membrane remodeling by **MM**, eventually suppressing it at high concentrations

ADVANCED SCIENCE NEWS
www.advancedsciencenews.com

ADVANCED MATERIALS
www.advmat.de

(30 mol.% Chol). This effect also influences the growth rate of the "islands" (Figure S17, Supporting Information), which can be attributed to cholesterol filling up the spaces between phospholipids and hindering the membrane expansion by the motor action. We also previously observed that decreasing the fluidity of lipid membranes has a direct effect on reducing the photochemical step of the motors. To further investigate the impact of membrane fluidity on the motor's ability to deform membranes, we designed SLBs using two different types of phospholipids: DOPC (1,2-dioleoyl-sn-glycero-3-phosphocholine) and DPPC (1,2-dipalmitoyl-sn-glycero-3-phosphocholine) introduced early in the study. These lipids share the same polar head group as POPC but differ in their degree of unsaturation, which significantly affects their membrane fluidity. The model lipid, POPC, contains one unsaturated acyl chain (oleoyl) and one saturated acyl chain (palmitoyl). This combination of saturated and unsaturated acyl chains provides POPC with an intermediate level of fluidity.[58] DOPC, with two unsaturated acyl chains, introduces kinks in the lipid tails, which prevents tight packing, resulting in a higher degree of fluidity compared to POPC. Conversely, DPPC has two fully saturated acyl chains, allowing for closer packing and leading to a more ordered and less fluid membrane. In agreement with the previous results on the molecular motor quantum yield, the % area excluded on DOPC membranes after 1h of irradiation was significantly higher than when using POPC. Conversely, the opposite was observed when using DPPC (Figure 3d; Figures S18 and S19, Supporting Information). These lipids have been extensively studied, and their structural parameters have been both theoretically calculated and experimentally measured.[59–62] The low amount of membrane exclusion in DPPC membranes can be associated with its higher area compressibility modulus at $T < T_M$ (k_A[MD] = 310mN m^{-1})[63]) as compared to DOPC (k_A[all-atomistic FF] = (282±34)mN m^{-1})[64]) or POPC (k_A[MD] = 230mN m^{-1})[63]). We propose that the membrane exclusion is inversely related to the area expansivity (α_A) of the lipid membranes ((α_{POPC} = 0.0037K^{-1}) and (α_{DOPC} = 0.0029K^{-1}) at 303K),[65] which results in more membrane exclusion in the case of DOPC membrane as it facilitates less expansion as compared to POPC membranes. These findings reinforce our argument that the motor remodeling process is linked to the membrane's ability to accommodate surface expansion.

2.3.4. Heat Generation and Thermal Contribution

Any molecule capable of absorbing light also possesses the ability to emit light back or to dissipate heat. In the case of molecular motors, when excited to higher energy levels, they undergo different relaxation processes; photoisomerization, leading to motor rotation, radiative relaxation pathways, such as fluorescence (fluorescence quantum yield is extremely low for **MM**), and non-radiative relaxation pathways, resulting in heat dissipation. To investigate the impact of thermal dissipation on the observed membrane remodeling, we introduced fluorenone (**Flu**) molecules under the same experimental conditions used for studying **MMs**. The fluorenone molecules and the molecular motors used in this study present comparable absorption coefficients and spectra (Figure S3, Supporting Information). However, the **Flu** lacks the ability to undergo double bond rotation, ensuring that all absorbed energy is dissipated in a non-radiative manner. We conducted identical procedures as those performed with **MMs** on samples containing 10 and 20 mol.% **Flu**. Qualitative observation of the SLBs using TIRF microscopy indicated a similar incorporation pattern as that observed with **MMs**, displaying the characteristic "hot spots", which suggests comparable $\pi-\pi$ stacking behavior (Figure S20, Supporting Information). When illuminating the samples for 1h, we observed a different membrane deformation without the formation of pulled-out membrane tubing, but the emergence of small membrane "islands" (Figures S21 and S22, Supporting Information). A comparison between membrane deformation caused by **Flu** and **MMs** revealed a heat contribution of ≈15% after 1h of irradiation with a remarkably slower growing rate (Figure S23, Supporting Information). However, when we examined SLBs behavior during longer irradiation times (16h, using 405 nm light at 1.5% intensity for **MM** irradiation and 642 nm light at 0.1% intensity for lipid imaging, with 10s interval time-lapse), we observed significantly less deformation produced by **Flu** compared to samples containing the same amount of **MMs** (Figure 3e; Figure S21, Supporting Information). By calculating the growth rate of the "islands", we found a saturation of thermal effects after a few hours of irradiation, with a constant contribution at longer irradiation times (Figure 3f). These results confirm a temperature-dependent effect on the action of **MMs**, which cannot be neglected and exhibits a significant but substantially lower contribution during short irradiation times that can be regarded as constant during longer illumination times. We further discuss the dissipative heat contribution in the Section S2.1 (Supporting Information).

2.3.5. Photooxidation Contribution and Singlet Oxygen Production

We next investigated the photodynamic activity of **MMs** in lipid membranes. Similarly, to what was discussed before, photoactive compounds can also play a role in generating reactive oxygen species (ROS). Among them, singlet oxygen ($^1O_2$) is a highly reactive and short-lived compound with potent oxidative properties. The photodynamic effect on lipid membranes triggers peroxidation of unsaturated lipids, leading to the formation of deeper oxidation products and eventually damage to the membrane structure.[66] To assess the photodynamic contribution to the observed membrane deformations, we employed an oxygen scavenger system that effectively removes any present oxygen radical from the media. The pyranose oxidase and catalase (POC) system has proven to be an efficient oxygen scavenging system that can operate at varying buffer strengths and pH levels.[67] This system has been previously validated for super-resolution microscopy applications where the elimination of ROS is critical.[68] To assess the impact of singlet oxygen on motor activity, we compared the % area deformation after 1h of SLB irradiation, with and without the addition of the POC system. Our results indicated no significant differences between the studied samples (Figures S24– S26, Supporting Information). These findings suggest that the presence of ROS might not exert a significant influence on motor activity; notice that % area seems to slightly increase when the POC system is present. We hypothesized that

ADVANCED SCIENCE NEWS
www.advancedsciencenews.com

ADVANCED MATERIALS
www.advmat.de

these results might be linked to oxygen scavengers slowing down possible motor degradation due to photooxidation.

We were still intrigued by the ability of **MMs** to produce singlet oxygen and act as a photosensitizer, as this feature may hold critical implications for future biological applications. For this reason, we quantified the amount of singlet oxygen using a fluorescent probe Singlet Oxygen Sensor Green (SOSG) which has been proven to be highly specific in singlet oxygen detection.[69] In the presence of $^1O_2$, SOSG can react to produce SOSG endoperoxides (SOSG-EP) that emits strong green fluorescence. The change in fluorescence at 525 nm was monitored for samples containing just POPC SUVs, SUVs containing 10 mol.% of **MM**, and SUVs containing 10 mol.% of **Flu**. A positive control using a known photosensitizer, Rose Bengal, was also used to compare our results. The samples were constantly irradiated up to 420min using an equivalent photon flux as the one used for the SLB experiments, and the fluorescence was monitored every 30min. Upon irradiation, all samples showed an increase in green fluorescence, representing the generation of $^1O_2$ (Figure 3g). SUVs containing 10 mol.% of **Flu** exhibited the highest fluorescence, followed by **MM** and plain POPC vesicles. When comparing the fluorescence intensity of our samples with our reference photosensitizer, we could calculate a contribution of 15%, 7%, and 4% from **Flu**, **MM**, and POPC, respectively (after 240min of irradiation, Figure S27, Supporting Information). Figure S28 (Supporting Information) shows the normalized fluorescence intensity at 525 nm for our samples compared to the reference control. These results confirm the ability of molecular motors to act as weak photosensitizers and generate singlet oxygen species; however, this seems not to be the main contribution to our membrane deformation effects.

2.4. Membrane Deformation of Free-Standing Membranes in Giant Unilamellar Vesicles

Next, we examined the impact of irradiated motors on GUVs primarily composed of POPC. GUVs provide a unique platform for exploring the influence of active processes on lipid bilayers through advanced imaging techniques. The **MMs** were introduced into the lipid mixture in chloroform before bilayer formation, resulting in their integration into the bilayers. Given their hydrophobic nature, we anticipated their localization within the acyl chains of the lipid molecules. Their presence in the acyl region could potentially alter the bilayer's properties. To prepare the GUVs for experimentation, we employed PVA-assisted swelling in a 300 mM aq. sucrose solution, followed by dilution in a 300 mM glucose solution, achieving a final concentration that was 10–20 times diluted compared to the initial mixture (see the Experimental Section). During image acquisition, the sample underwent irradiation with a 405 nm laser. This was done using Spinning Disk confocal microscopy which offers the possibility to acquire thin optical sections in a high-speed fashion while illuminating the whole sample volume. Notably, the entire formation process was meticulously conducted in the dark to prevent ambient light from triggering the motors. The signal from bMMs was distributed homogeneously across the vesicle and we did not observe the $\pi-\pi$ stacked "hot spots" from the fluorescence signal, owing to an order of magnitude higher diffusion in vesicles as compared to SLBs.

2.4.1. Vesicle Shape Deformation Under Exposure

As discussed in the preceding sections, **bMM** fluorescence revealed a homogeneous distribution of molecular motors within the free-standing membranes. Following the generation of GUVs, it was observed that, in the absence of light irradiation, the majority of GUVs assumed a spherical shape. Consistent with the previously discussed fluorescence correlation spectroscopy (FCS) measurements performed on SLBs comprising the same lipid composition and molecular motor concentration, the incorporation of MMs into the bilayer correlated with an increase in the diffusion coefficient of fluorescent-tagged lipids. Moreover, a few GUVs exhibited deformed shapes or excessive membrane tubulations prior to irradiation. However, in all cases, these deformations exhibited shape dynamics upon blue light exposure. Notably, we observed substantial alterations in GUV membrane geometry when imaging at the equatorial plane. Initially, we investigated GUV samples composed solely of lipids, in which no significant changes in spherical GUV geometry were noted (see **Figure** 4a) i). This observation suggests that our experimental conditions did not induce noticeable photooxidation effects on the lipids. In the case of GUV membranes containing molecular motors, upon exposure to the 405 nm laser, most vesicles within the field of view displayed membrane fluctuations (see Figure 4a) ii, c), with some expelling membrane tubes either outward or inward. Subsequently, they underwent morphological transitions upon extended irradiation (see Figure S32, Supporting Information). To comprehensively assess these deformations, we acquired 3D volumetric data over time. This analysis revealed pronounced flattening of the GUVs during irradiation (see Figure S30, Supporting Information).

Unless otherwise specified, GUV recordings were captured as z-stacks with a 100ms exposure time per frame. We employed a 405 nm laser for triggering motor activity, and 488 and 640 nm laser lines for imaging **bMM** and the membrane, respectively. There was a 30 s interval between the initiation of each new stack acquisition, with varying total acquisition times depending on the field of view, ranging from 30min to 4h. The GUVs began losing their spherical shape within 5min of 405 nm exposure, and after 15min, major shape transformations could be observed. These observations refurbish our hypothesis of motor activity-induced area expansion of the lipid membrane as we had seen in the preceding sections for SLBs.

2.4.2. Effect of the Molecular Motors on the Permeability of Vesicles

Several studies have demonstrated that the isomerization of photoswitchable lipids in vesicles can induce transient pore formation, allowing free dye to leak out through these pores.[70] Given that **MMs** also undergo isomerization cycles, we conducted experiments to investigate whether similar transient pore formation could be observed. To this end, we designed experiments with a 10μM concentration of free Alexa-Fluorophore 488

ADVANCED SCIENCE NEWS
www.advancedsciencenews.com

ADVANCED MATERIALS
www.advmat.de

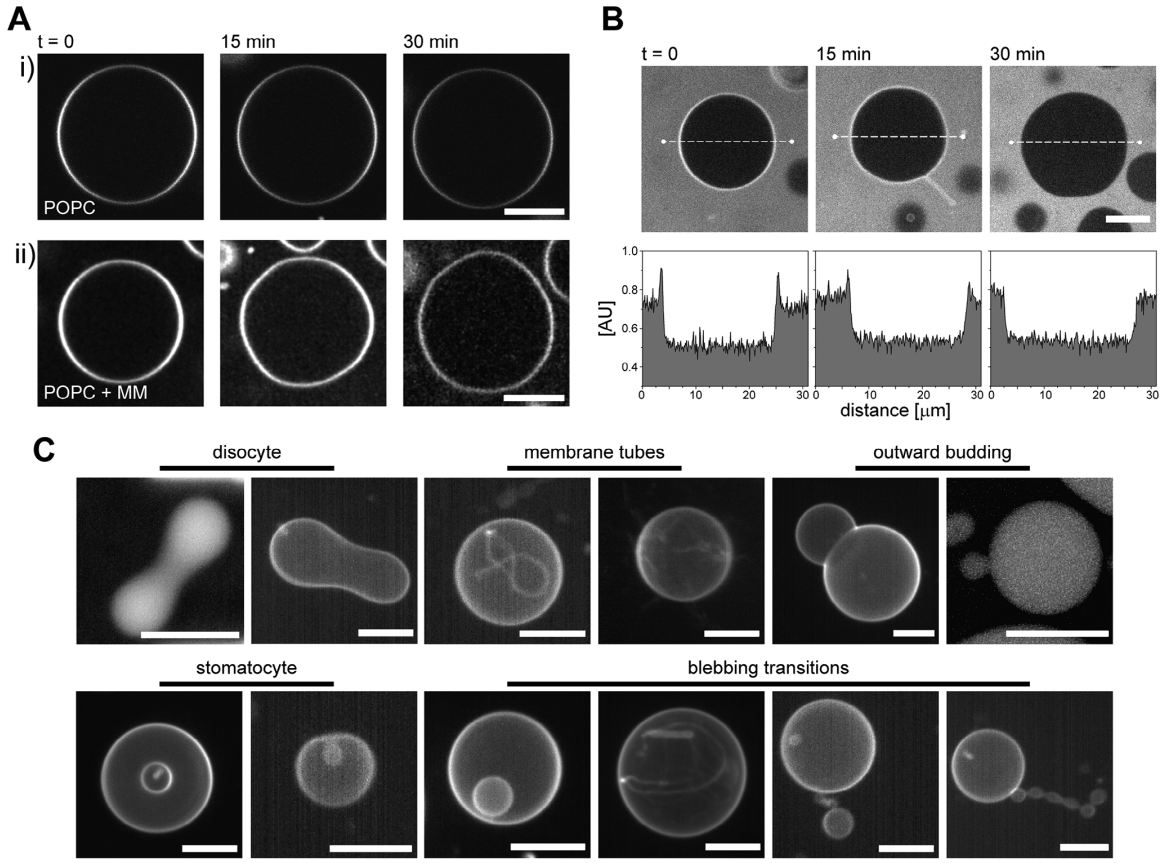

Figure 4. Molecular motor action on GUVs. a) Irradiation of GUVs (labeled with 0.05 mol.% Atto655-DOPE) with 405 nm laser over time for vesicles i) containing POPC, and ii) POPC + 10 mol.% MM (lower). b) No occurrence of AlexaFluor 488 leaking into the membrane as membrane deformation takes place with exposure. Normalized fluorescence curves show no change in fluorescence inside the vesicles. c) Representative images of different shape transitions observed after irradiation with 405 nm laser. The shape transitions are consistent with what is theoretically expected when area expansion happens in the membrane. **Scale bar: 10 μm**

(AF488) in the glucose solution, which was present outside the vesicles. Notably, we observed no signal corresponding to the green channel within the GUV lumen in the absence of irradiation. This observation aligns with results obtained from vesicles composed solely of lipids. The absence of green signal accumulation inside the GUVs, even as their membranes underwent deformation over time, confirms that the continuous dynamics driven by **MMs** prevent the formation of transient pores (see Figure 4b; Figure S33, Supporting Information). This is in contrast to photoswitchable lipids, which undergo abrupt isomerization-induced area changes resulting in discrete shifts in the total membrane area. In the case of **MMs**, their unidirectional and continuous rotation avoids discrete changes and instead leads to a constant, albeit continuous, remodeling of the bilayer. This phenomenon is further underscored by the fact that GUVs do not reach a "final" shape during deformation, as they would if they were attaining an equilibrium state (see Figure S35, Supporting Information). The absence of transient pore formation also provides an explanation for the observed shape transitions in GUVs, as they undergo changes in surface area with relatively minimal alteration in volume.

2.4.3. Shape Transitions Into Non-Spherical Geometries

Shape transformations have been achieved and thoroughly theoretically studied in the past.[71] These transformations have been induced through various means, including osmotic shocks, gradual heating of the bilayers,[72] and lipid peroxidation. Osmotic shocks, for instance, are a well-established method for altering the shape of lipid vesicles by introducing changes in the internal and external osmotic pressures. Gradual heating of the bilayers is another approach, where the temperature increase leads to asymmetric thermal expansions of the leaflets, resulting in shape transitions. Additionally, lipid peroxidation, which involves oxidative damage to lipid molecules, can also instigate morphological changes in vesicles. In all these cases, the underlying principle is the creation of additional surface area within the lipid bilayer.

ADVANCED SCIENCE NEWS
www.advancedsciencenews.com

ADVANCED MATERIALS
www.advmat.de

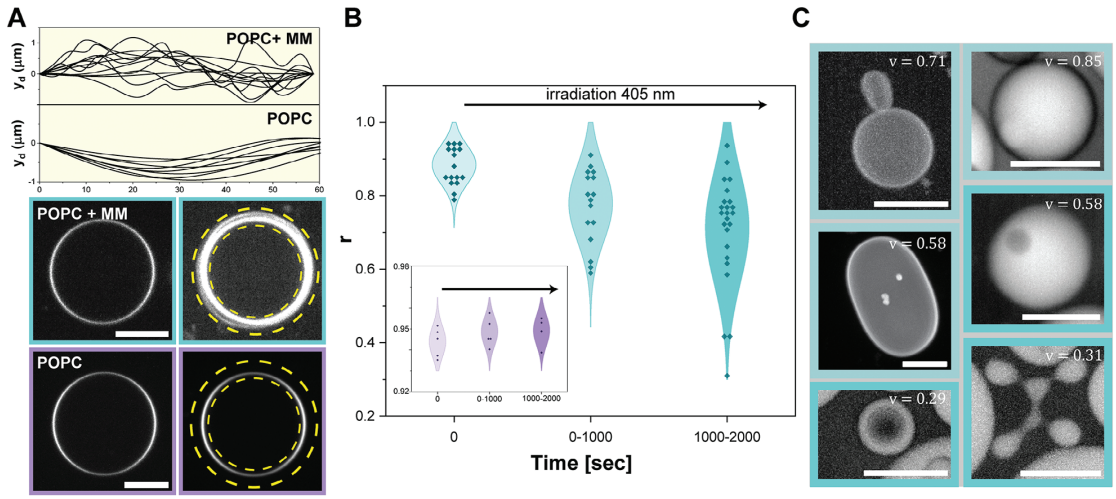

Figure 5. Reduced volume changes in GUVs upon exposure. A) Confocal images of GUV consisting of POPC and POPC with 10 mol.% **MM** at the start of irradiation (bottom left) with 405 nm, a projection of time points after drift correction on a single image to show flickering of the membrane (bottom right), GUVs with POPC show no flickering while those with **MM** do when irradiated with 405 nm. The flickering profile is flattened with a 45 px wide circle and the membrane is plotted for both cases (top). B) Spread in the reduced volumes of different GUVs with time for vesicles consisting of 10 mol.% **MM** and the case with vesicles consisting of only POPC (inset). C) Representative deformed GUVs with different reduced volumes. **Scale bar: 10 µm**

MMs, in this context, also function as an agent that contributes to an increase in surface area. In this study, we demonstrate a diverse array of **MM**-induced shape transformations in GUVs (see Figure 4c; Videos S2–S4, Supporting Information for a 3D reconstruction of these deformed vesicles). We observed a remarkable variety of shape transitions for different GUVs: disocytes, stomatocytes, outward/inward budding transitions, membrane tubes, and pear-shaped transitions. In our investigation, we focus on the distinct role of **MMs** as dynamic agents capable of actively modulating the surface area of lipid bilayers. By triggering GUVs containing **MMs**, we showcase a range of shape transformations, adding to the repertoire of techniques for achieving dynamic alterations in vesicle morphology. These transformations are of particular interest due to their relevance in understanding the influence of **MMs** on lipid membrane dynamics and their potential applications in various synthetic systems as membrane modulators as a complement to different force mechanisms.

2.4.4. Membrane Area Changes with Activation of Molecular Motors

In the case of photoswitchable lipids, it has been well-documented that a trans-to-cis transition leads to an increase in membrane area due to the larger spatial requirements of the cis isomer compared to the trans isomer. In the case of **MMs**, there is a continuous unidirectional motion that results in an ongoing and simultaneous transition between different isomers. This perpetual change in the physical space occupied by the motor dynamically alters the surface area of the lipid membrane. The initial presence of perfectly spherical vesicle membranes observed when the **MMs** are maintained in a non-irradiated state, suggests that in their non-activated configuration, the motors occupy the smallest possible area, likely attributable to $\pi - \pi$ stacking interactions. Following the initiation of motor rotation, photoisomerization occurs, and they occupy a larger surface area, which is not fixed due to the continuous nature of the rotation. To visualize the local fluctuations occurring at the membrane, we projected the equatorial plane of a GUV (after drift correction to mitigate particle movement) containing 10 mol.% **MM** and compared it to a GUV composed exclusively of lipids (see **Figure** 5a). Subsequently, we flattened the lipid membrane using a 45-pixel width (as indicated by a representative yellow circle) and traced the local fluctuations over time, relative to the lipid-only GUVs (see Section S1.20, Supporting Information). These local fluctuations indicate an increase in surface area from the initial state, although the new surface area also exhibits temporal variability. Importantly, our observation of an absence of leakage allowed us to assume negligible changes in the volume of deforming vesicles over time. Consequently, we quantified the total surface area of the evolving shapes formed by these membranes, using 3D segmentation as described in the Experimental section (see Figure S31, Supporting Information).

Our analysis, in accordance with our assumption, also revealed minimal variation in the measured volume of a vesicle over time. To illustrate the degree of deformations with increasing exposure time, we calculated reduced volumes, defined as $r = \frac{3V}{\sqrt{4\pi A^3}}$, a dimensionless parameter that is independent of vesicle size. Notably, purely lipid vesicles exhibited consistently reduced volumes over time (see Figure 5b inset). In contrast, vesicles containing 10 mol.% **MM** exhibited high variance in their reduced volumes over time (see Figure 5b), as further exemplified by representative vesicles shown in Figure 5c, where smaller r corresponds to higher deformations.

ADVANCED SCIENCE NEWS
www.advancedsciencenews.com

ADVANCED MATERIALS
www.advmat.de

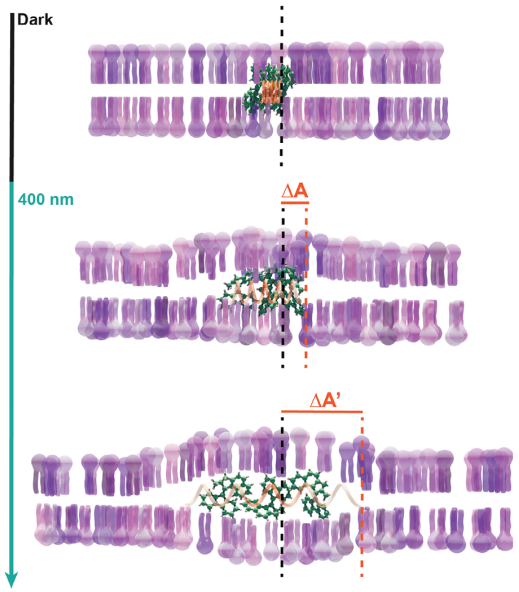

Figure 6. Schematic representation of surface area modulated by the rotation of molecular motors.

The continuous remodeling of the membrane, originating from an initially uniform spherical shape and resulting in a broadening range of reduced volumes, suggests that although the total surface area increases, it does not maintain a constant value. This conforms well with intuition when one considers the communal **MM** motion as that of a lateral spring in the bilayer that can expand and contract (see **Figure 6**). We hypothesize that at any point during irradiation, the ratio of the population of different isomeric states changes to mimic the contraction and expansion of a spring. An additional noteworthy observation is that in many instances, even highly deformed GUVs continued to exhibit floppiness when further exposed to blue light irradiation. We observe that upon terminating the 405 nm excitation, we see a gradual reduction in the membrane fluctuations and the vesicles returning back to the quasi-spherical or spherical shapes (see Figure S38, Supporting Information). These results confirm a continuous action of **MM** when remodeling lipid membranes as long as they are exposed to the appropriate wavelength.

3. Conclusion

In this study, we conducted an extensive examination of the interactions between artificial molecular motors, specifically, overcrowded alkenes referred to as **MMs**, and lipid membranes. Our investigation revealed intriguing insights into how these rotary motors and membranes influence each other. For **MMs**, we observed that the lipid environment significantly impacts the quantum yield of photoisomerization, while the speed of motor rotation remains unaffected. We proposed that small clusters or "*hotspots*" of **MMs** form within the lipid membranes due to favorable $\pi-\pi$ stacking interactions. This dynamic aggregation state appears to hinder substantial conformational changes required for photoisomerization but has minimal effect on small rearrangements necessary for thermal helix inversion.

Furthermore, our research demonstrated how the presence of molecular motors influences the properties of the lipid membrane, as evident with fluorescence correlation spectroscopy (FCS) measurements on supported lipid bilayers (SLBs). At concentrations exceeding 5 mol.%, molecular motors increased membrane fluidity. We conducted a quantitative analysis of motor-induced deformations in SLBs, revealing that concentration and membrane order play pivotal roles in determining the extent of membrane remodeling. Local heating effects were significant at short irradiation times, contributing consistently during prolonged irradiation periods.

Additionally, we explored singlet oxygen generation within these systems to investigate its contribution toward molecular motor-induced membrane alterations. We found that molecular motors are able to generate singlet oxygen species and act as photosensitizers. However, when using an oxygen scavenger system, the deformation effects in the membranes persist, indicating that peroxidation is not the primary reason for **MM**'s action. Based on these experiments it is evident that only limited contributions from local heating and singlet oxygen generation to membrane remodeling are observed.

Our investigation extended also to free-standing membranes, where we noticed a diverse range of shape transitions in giant unilamellar vesicles (GUVs). We observed various shape transitions such as discocytes, stomatocytes, pear-shaped, dumbbell-shaped, and abrupt tether-forming vesicles with 1-palmitoyl-2-oleoyl-sn-glycero-3-phosphocholine (POPC) vesicles. We show that high membrane deformations could be achieved with a relatively low concentration requirement of an external agent when using **MMs**. Unlike membranes composed of photoswitchable lipids, our molecular motor system induces continuous membrane area modulation, remaining in a dynamic out-of-equilibrium state during the timescale of exposition by blue light.

Overall, this research provides a novel and comprehensive understanding of how artificial molecular machines influence and interact with lipid membranes. We could not reproduce any kind of membrane opening by motor activity, in contrast to what has been found in cell membranes. On the other hand, the motor-induced membrane expansion that leads to "island" formation on supported membranes and dramatic shape changes in GUVs appears to be a so far unparalleled effect compared to other light-activated membrane effectors. Their significant and progressive change in reduced volume prepares the vesicle for large-scale transformations that could eventually even result in fission. For the complete division of a spherical vesicle at conserved volume, i.e., without any leakage, membrane expansion of up to 26% would be required. This does not seem to be impossible to reach with high concentrations of motors and ideal membrane compositions. Thus, molecular rotary motors may present an ideal tool for future applications in more complex artificial cell systems, but also for natural cell applications when light-induced membrane remodeling is desired.

4. Experimental Section

Reagent and Chemicals: Unless specified otherwise, chemicals were purchased from Sigma–Aldrich/Merck. All reactions involving air-sensitive

ADVANCED SCIENCE NEWS
www.advancedsciencenews.com

ADVANCED MATERIALS
www.advmat.de

reagents were performed under an N_2 atmosphere. Solvents were degassed by purging with N_2 for a minimum of 30min or by three freeze-pump-thaw cycles. Reagents were purchased from Sigma–Aldrich, Fluorochem, or TCI Europe and were used without further purification. Anhydrous solvents were obtained from a solvent purification system (MBraun SPS-800). Flash column chromatography was performed on silica gel (Merck, type 9385, 230–400 mesh) or on a Büchi Reveleris purification system using Büchi silica cartridges. Thin-layer chromatography (TLC) was carried out on aluminum sheets coated with silica gel 60 F254 (Merck). All the lipids were purchased from Avanti Polar Lipids.

Photoactive Compounds Synthesis: Detailed synthesis of **MM** is extensively described in reference [49]. See reference [50] for **bMM**. See Supporting Information for more details.

SLB Preparation: SLBs were prepared as described elsewhere,[73] with the required lipid and molecular motor composition. Briefly, suspensions of small vesicles were deposited onto the cover glass in the presence of 5 mM $CaCl_2$ and incubated for 5min at 40 °C. Subsequently, the sample was rinsed with SLB buffer supplemented with 5 mM EDTA to chelate excess calcium ions (Ca^{2+}), followed by slow cooling down to room temperature by leaving them on the bench.

GUV Preparation: Giant Unilamellar Vesicles (GUVs) were prepared through a PVA-assisted swelling method, following established procedures.[74] Briefly, a 100µL solution of polyvinyl alcohol (PVA, MW 145 000, Merck KGaA, Darmstadt, Germany) was dissolved in Milli-Q water at a concentration of 5% (w/v). This PVA solution was deposited onto a plasma-cleaned coverslip (ϕ 30mm, #1.5). After a 5min incubation, the excess PVA solution was removed, and the coverslip was then dried in a 60 °C oven for 15min. Using a spin-coating device (Schaefer Technologie GmbH, Germany), a 50µL solution of the desired lipids and photoactive materials mixture, prepared at a concentration of 1mg mL^{-1}, was deposited onto the coverslip. The deposition was conducted at a rotation speed of five revolutions per second (rps) for a duration of 55 s. Subsequently, the coverslips were placed in a desiccator for 15min. To initiate the formation of GUVs, 1mL of a sucrose buffer with a concentration of 300 mM was deposited onto the coverslip and allowed to swell the vesicles in the dark for 1h. All experiments were conducted after ensuring that the osmolality of the inner aqueous solution was 5% higher than the osmolality of the outer aqueous solution.

Total Internal Reflection Fluorescence Microscopy: TIRF imaging was performed on a Zeiss Elyra 7 system, using 405, 488, and 641 nm laser lines. For the TIRF images alpha Plan-Apochromat 63x/1.46 Oil Korr M27 Var2 (Carl Zeiss, Germany) oil objective was used. The images were acquired on pco.edge sCMOS cameras (pco.edge 4.2 CLHS) at 100ms exposure time.

Spinning Disk Confocal Microscopy: Spinning disk confocal imaging was performed on a Nikon/Yokogawa CSU-W1 spinning disk confocal microscope, using 405, 488, and 641 nm laser lines. The 50 µ m pinhole spinning disk was used at 4000 rpm. The sample was illuminated through a Nikon Apo TIRF 60x Oil DIC N2 immersion oil objective and the images were acquired in pco.edge sCMOS cameras (pco.edge 4.2 LT USB) at 100ms exposure time. For z-stack imaging, the desired optical sectioning was set at 0.2 µ m. Due to the refractive index-mismatched system (oil immersion and aq. sample), the non-uniform translation along the z-axis was corrected as described here.[75] The median correction factor for axial distortion was used, $\frac{d\prime}{d} = \frac{\tan(\sin^{-1}\frac{0.5NA}{n_1})}{\tan(\sin^{-1}\frac{0.5NA}{n_2})}$ where $d\prime$ is the actual z-sectioning and d is the set z-sectioning.

UV–Vis Spectroscopy: UV–vis spectroscopy was used for quantification of molecular motor uptake, evaluation of molecular motor performance, thermodynamic studies of molecular motor speed and quantum yield determination of molecular motor photoisomerization. See Supporting Information for specific details on these sections. Briefly, samples containing free-standing lipid systems or molecular motor solutions were measured using an Agilent 8453 UV–vis Diode Array System, equipped with a Quantum Northwest Peltier controller. If specified, irradiations were done using a built-in setup coupled to an LED. Solutions were prepared and measured using a quartz cuvette. UV–vis absorbance measurements of SLBs were prepared in 96-well plates with flat glass-bottom and measured in a TECAN plate reader (Tecan Group Ltd., Mannedorf, Switzerland) at room temperature.

Singlet Oxygen Detection: A sample containing 3 mL of SUVs with a concentration of 50 µM of photoactive compound (if specified) and 5 µM of SOSG (S36002, Thermo Fisher, USA) was constantly irradiated up to 420min with a 405 nm LED (530 nm for Rose Bengal positive control). The exhibited emission fluoresence spectra was measured every 30min using a JASCO FP6200 spectrofluorometer (Jasco, USA) in a 10 mm pathlength quartz cuvette (101-QS, Hellma, Germany). Excitation was performed at 500 nm. The emission spectra was recorded keeping the slit widths constant at 5 nm from 505 to 650 nm.

Statistical Analysis: Pooled data was presented as mean ± s.d. unless otherwise indicated. Information regarding sample size, error bars and statistical analysis used was described in each figure legend. P values for statistical analysis of three experimental groups or for multiple comparisons were calculated using GraphPad Prism 10 (https://www.graphpad.com). Statistical significance was assessed using 1-way/2-way ANOVA (Turkey's multiple comparisons test), Brown-Forsythe and Welch ANOVA (Dunnett's T3 multiple comparisons test), Kruskal-Wallis test (Dunn's multiple comparisons test) or unpaired two-tailed t-test depending on the experiment. The linearity of the data was tested using Simple linear regression, Non-linear fit (Malthusian) and Non-linear fit (Goempertz). Significance is reported following American Psychological Association (APA) guidelines ($^{*}P \leq 0.05$, $^{**}P \leq 0.01$, $^{***}P \leq 0.001$, $^{****}P \leq 0.0001$).[76] Detailed statistical analysis and raw data are available (contact the authors).

Supporting Information

Supporting Information is available from the Wiley Online Library or from the author.

Acknowledgements

Y.Q. and A.G. contributed equally to this work. The authors acknowledged Prof. Wiktor Szymanski and Dr. Henri Franquelim for valuable feedback and suggestions. The authors thank Prof. Jan van Hest for his suggestion for the singlet oxygen probe. The authors would like to acknowledge Jan-Hagen Krohn for the help with fluorescence microscopy infrastructure. The authors would like to thank Adrian Merino and Dr. Nishu Kanwa for the insightful discussions. The authors acknowledged Sigrid Bauer for lipid and buffer preparations. The authors would like to thank MPIB Imaging Facility for help with data analysis. Y.Q. and A.G. received funding from the European Union's Horizon 2020 research and innovation programme under the Marie Skłodowska-Curie grant agreement no. 859416. The authors gratefully acknowledged financial support from the Ministry of Education, Culture and Science of the Netherlands (Gravitation Program no. 024.001.035 to B.L.F). Y.Q. and S.G. acknowledged support from the International Max Planck Research School for Molecules of Life (IMPRS-ML). S.G. was part of the ONE MUNICH Project supported by the Federal Ministry of Education and Research (BMBF), as well as the Free State of Bavaria under the Excellence Strategy of the Federal Government and the Länder. K.A.N. acknowledged support from the Max Planck-Bristol Centre for Minimal Biology. P.S. acknowledged support from Center for NanoScience (CeNS). The schematic for Figure 2 was created with BioRender.com.

Open access funding enabled and organized by Projekt DEAL.

Conflict of Interest

The authors declare no conflict of interest.

Data Availability Statement

The data that support the findings of this study are available from the corresponding author upon reasonable request.

ADVANCED SCIENCE NEWS
www.advancedsciencenews.com

ADVANCED MATERIALS
www.advmat.de

Keywords

GUV (Giant Unilamellar Vesicle) shape transitions, membrane area expansion, membrane biophysics, membrane deformation, molecular motors

Received: October 25, 2023
Revised: December 16, 2023
Published online: January 18, 2024

[1] C. GM, *The Cell: A Molecular Approach, 2nd edition. Chapter 2, The Chemistry of Cells*, Sunderland: Sinauer Associates, MA, USA **2000**.
[2] M. Preiner, S. Asche, S. Becker, H. C. Betts, A. Boniface, E. Camprubi, K. Chandru, V. Erastova, S. G. Garg, N. Khawaja, G. Kostyrka, R. Machné, G. Moggioli, K. B. Muchowska, S. Neukirchen, B. Peter, E. Pichlhöfer, Á. Radványi, D. Rossetto, A. Salditt, N. M. Schmelling, F. L. Sousa, F. D. K. Tria, D. Vörös, J. C. Xavier, *Life* **2020**, *10*, 3.
[3] H. Jia, P. Schwille, *Curr. Opin. Biotechnol.* **2019**, *60*, 179.
[4] N. A. Yewdall, A. F. Mason, J. C. M. van Hest, *Interface Focus* **2018**, *8*, 20180023.
[5] J. Löwe, L. A. Amos, *Int. J. Biochem. Cell Biol.* **2009**, *41*, 323.
[6] K. Farsad, P. De Camilli, *Curr. Opin. Cell Biol.* **2003**, *15*, 372.
[7] R. Lipowsky, *Adv. Biol.* **2021**, *6*, 1.
[8] H. G. Döbereiner, J. Käs, D. Noppl, I. Sprenger, E. Sackmann, *Biophys. J.* **1993**, *65*, 1396.
[9] J. Käs, E. Sackmann, *Biophys. J.* **1991**, *60*, 825.
[10] M. Yanagisawa, M. Imai, T. Taniguchi, *Phys. Rev. Lett.* **2008**, *100*, 148102.
[11] K. Oglecka, J. Sanborn, A. Parikh, R. Kraut, *Front. Physiol.* **2012**, *3*, https://doi.org/10.3389/fphys.2012.00120(?PMU?).
[12] P. Peterlin, *J. Biol. Phys.* **2010**, *36*, 339.
[13] R. Dimova, K. A. Riske, S. Aranda, N. Bezlyepkina, R. L. Knorr, R. Lipowsky, *Soft Matter* **2007**, *3*, 817.
[14] P. G. Petrov, J. B. Lee, H.-G. Döbereiner, *Europhys. Lett.* **1999**, *48*, 435.
[15] N. Khalifat, N. Puff, S. Bonneau, J.-B. Fournier, M. I. Angelova, *Biophys. J.* **2008**, *95*, 4924.
[16] A. A. Beharry, G. A. Woolley, *Chem. Soc. Rev.* **2011**, *40*, 4422.
[17] Y. Suzuki, K. H. Nagai, A. Zinchenko, T. Hamada, *Langmuir* **2017**, *33*, 2671.
[18] K. A. Riske, T. P. Sudbrack, N. L. Archilha, A. F. Uchoa, A. P. Schroder, C. M. Marques, M. S. Baptista, R. Itri, *Biophys. J.* **2009**, *97*, 1362.
[19] N. L. Mutter, J. Volarić, W. Szymanski, B. L. Feringa, G. Maglia, *J. Am. Chem. Soc.* **2019**, *141*, 14356.
[20] C. Pernpeintner, J. A. Frank, P. Urban, C. R. Roeske, S. D. Pritzl, D. Trauner, T. Lohmüller, *Langmuir* **2017**, *33*, 4083.
[21] P. Urban, S. D. Pritzl, D. B. Konrad, J. A. Frank, C. Pernpeintner, C. R. Roeske, D. Trauner, T. Lohmüller, *Langmuir* **2018**, *34*, 13368.
[22] J. A. Frank, H. G. Franquelim, P. Schwille, D. Trauner, *J. Am. Chem. Soc.* **2016**, *138*, 12981.
[23] P. Urban, S. D. Pritzl, M. F. Ober, C. F. Dirscherl, C. Pernpeintner, D. B. Konrad, J. A. Frank, D. Trauner, B. Nickel, T. Lohmueller, *Langmuir* **2020**, *36*, 2629.
[24] S. D. Pritzl, P. Urban, A. Prasselsperger, D. B. Konrad, J. A. Frank, D. Trauner, T. Lohmüller, *Langmuir* **2020**, *36*, 13509.
[25] H. A. Scheidt, K. Kolocaj, D. B. Konrad, J. A. Frank, D. Trauner, D. Langosch, D. Huster, *Biochim. et Biophys. Acta (BBA) - Biomembr.* **2020**, *1862*, 183438.
[26] Y. Matsumura, H. N. Ananthaswamy, *Toxicol. Appl. Pharmacol.* **2004**, *195*, 298.
[27] I. M. Welleman, M. W. H. Hoorens, B. L. Feringa, H. H. Boersma, W. Szymański, *Chem. Sci.* **2020**, *11*, 11672.
[28] J. C. M. Kistemaker, A. S. Lubbe, B. L. Feringa, *Mater. Chem. Front.* **2021**, *5*, 2900.
[29] N. Koumura, R. W. J. Zijlstra, R. A. van Delden, N. Harada, B. L. Feringa, *Nature* **1999**, *401*, 152.
[30] D. R. S. Pooler, A. S. Lubbe, S. Crespi, B. L. Feringa, *Chem. Sci.* **2021**, *12*, 14964.
[31] A. Guinart, M. Korpidou, D. Doellerer, G. Pacella, M. C. A. Stuart, I. A. Dinu, G. Portale, C. Palivan, B. L. Feringa, *Proc. Natl. Acad. Sci.* **2023**, *120*, e2301279120.
[32] V. García-López, F. Chen, L. G. Nilewski, G. Duret, A. Aliyan, A. B. Kolomeisky, J. T. Robinson, G. Wang, R. Pal, J. M. Tour, *Nature* **2017**, *548*, 567.
[33] C. Ayala Orozco, D. Liu, Y. Li, L. B. Alemany, R. Pal, S. Krishnan, J. M. Tour, *ACS Appl. Mater. Interfaces* **2020**, *12*, 410.
[34] D. Liu, V. García-López, R. S. Gunasekera, L. Greer Nilewski, L. B. Alemany, A. Aliyan, T. Jin, G. Wang, J. M. Tour, R. Pal, *ACS Nano* **2019**, *13*, 6813.
[35] T. Galbadage, D. Liu, L. B. Alemany, R. Pal, J. M. Tour, R. S. Gunasekera, J. D. Cirillo, *ACS Nano* **2019**, *13*, 14377.
[36] A. M. Firsov, J. Pfeffermann, A. S. Benditkis, T. I. Rokitskaya, A. S. Kozlov, E. A. Kotova, A. A. Krasnovsky, P. Pohl, Y. N. Antonenko, *J. Photochem. Photobiol., B* **2023**, *239*, 112633.
[37] W.-Z. Wang, L.-B. Huang, S.-P. Zheng, E. Moulin, O. Gavat, M. Barboiu, N. Giuseppone, *J. Am. Chem. Soc.* **2021**, *143*, 15653.
[38] T. Bernas, M. Zarebski, J. W. Dobrucki, P. R. Cook, *J. Microsc.* **2004**, *215*, 281.
[39] R. Dimova, *Annu. Rev. Biophys.* **2019**, *48*, 93.
[40] G. Weber, T. Charitat, M. S. Baptista, A. F. Uchoa, C. Pavani, H. C. Junqueira, Y. Guo, V. A. Baulin, R. Itri, C. M. Marques, A. P. Schroder, *Soft Matter* **2014**, *10*, 4241.
[41] H. Erkan-Candag, D. Krivic, M. A. F. Gsell, M. Aleksanyan, T. Stockner, R. Dimova, O. Tiapko, K. Groschner, *Biomolecules* **2022**, *12*, 799.
[42] J. Pfeffermann, B. Eicher, D. Boytsov, C. Hannesschlaeger, T. R. Galimzyanov, T. N. Glasnov, G. Pabst, S. A. Akimov, P. Pohl, *J. Photochem. Photobiol., B* **2021**, *224*, 112320.
[43] A. Kocçer, M. Walko, W. Meijberg, B. L. Feringa, *Science* **2005**, *309*, 755.
[44] M. Aleksanyan, A. Grafmüller, F. Crea, V. N. Georgiev, N. Yandrapalli, S. Block, J. Heberle, R. Dimova, *Adv. Sci.* **2023**, *10*, 31.
[45] V. N. Georgiev, A. Grafmüller, D. Bléger, S. Hecht, S. Kunstmann, S. Barbirz, R. Lipowsky, R. Dimova, *Adv. Sci.* **2018**, *5*, 1800432.
[46] C. Pernpeintner, J. A. Frank, P. Urban, C. R. Roeske, S. D. Pritzl, D. Trauner, T. Lohmüller, *Langmuir* **2017**, *33*, 4083.
[47] F. Höglsperger, B. E. Vos, A. D. Hofemeier, M. D. Seyfried, B. Stövesand, A. Alavizargar, L. Topp, A. Heuer, T. Betz, B. J. Ravoo, *Nat. Commun.* **2023**, *14*, 1.
[48] P. Urban, S. R. Kirchner, C. Mühlbauer, T. Lohmüller, J. Feldmann, *Sci. Rep.* **2016**, *6*, 22686.
[49] J. Vicario, A. Meetsma, B. L. Feringa, *Chem. Commun.* **2005**, 5910, https://doi.org/10.1039/B507264F.
[50] R. Toyoda, N. V. Hoang, K. G. Moghaddam, S. Crespi, D. R. S. Pooler, S. Faraji, M. S. Pshenichnikov, B. L. Feringa, *Nat. Commun.* **2022**, *13*, 5765.
[51] D. F. Swinehart, *J. Chem. Educ.* **1962**, *39*, 333.
[52] P. Urban, S. D. Pritzl, D. B. Konrad, J. A. Frank, C. Pernpeintner, C. R. Roeske, D. Trauner, T. Lohmüller, *Langmuir* **2018**, *34*, 13368.
[53] D. R. Pooler, A. S. Lubbe, S. Crespi, B. L. Feringa, *Chem. Sci.* **2021**, *12*, 14964.
[54] M. Klok, L. P. B. M. Janssen, W. R. Browne, B. L. Feringa, *Faraday Discuss.* **2009**, *143*, 319.
[55] A. M. Baxter, L. R. Jordan, M. Kullappan, N. J. Wittenberg, *Langmuir* **2021**, *37*, 5753.
[56] R. Lipowsky, *Faraday Discuss.* **2013**, *161*, 305.
[57] S.-T. Yang, A. J. B. Kreutzberger, J. Lee, V. Kiessling, L. K. Tamm, *Chem. Phys. Lipids* **2016**, *199*, 136.
[58] N. Kahya, P. Schwille, *J. Fluoresc.* **2006**, *16*, 671.

ADVANCED SCIENCE NEWS
www.advancedsciencenews.com

ADVANCED MATERIALS
www.advmat.de

[59] J. Pan, S. Tristram-Nagle, N. Kučerka, J. F. Nagle, *Biophys. J.* **2008**, *94*, 117.
[60] J. F. Nagle, S. Tristram-Nagle, *Biochim. et Biophys. Acta (BBA) - Rev. Biomembr.* **2000**, *1469*, 159.
[61] R. M. Venable, F. L. Brown, R. W. Pastor, *Chem. Phys. Lipids* **2015**, *192*, 60.
[62] M. Doktorova, M. V. LeVine, G. Khelashvili, H. Weinstein, *Biophys. J.* **2019**, *116*, 487.
[63] D. Drabik, G. Chodaczek, S. Kraszewski, M. Langner, *Langmuir* **2020**, *36*, 3826.
[64] J. P. M. Jämbeck, A. P. Lyubartsev, *J. Chem. Theory Comput.* **2012**, *8*, 2938.
[65] Z.-J. Wang, M. Deserno, *New J. Phys.* **2010**, *12*, 095004.
[66] T.-G. Nam, *Toxicol. Res.* **2011**, *27*, 1.
[67] M. Swoboda, J. Henig, H.-M. Cheng, D. Brugger, D. Haltrich, N. Plumeré, M. Schlierf, *ACS Nano* **2012**, *6*, 6364.
[68] J. Kwon, M. S. Elgawish, S.-H. Shim, *Adv. Sci. (Weinh)* **2022**, *9*, 2101817.
[69] A. Prasad, M. Sedlářová, P. Pospíšil, *Sci. Rep.* **2018**, *8*, 13685.
[70] S. D. Pritzl, P. Urban, A. Prasselsperger, D. B. Konrad, J. A. Frank, D. Trauner, T. Lohmüller, *Langmuir* **2020**, *36*, 13509.
[71] U. Seifert, K. Berndl, R. Lipowsky, *Phys. Rev. A* **1991**, *44*, 1182.
[72] J. Käs, E. Sackmann, *Biophys. J.* **1991**, *60*, 825.
[73] Y. Qutbuddin, J.-H. Krohn, G. A. Brüggenthies, J. Stein, S. Gavrilovic, F. Stehr, P. Schwille, *J. Phys. Chem. B* **2021**, *125*, 13181.
[74] A. Weinberger, F.-C. Tsai, G. H. Koenderink, T. F. Schmidt, R. Itri, W. Meier, T. Schmatko, A. Schröder, C. Marques, *Biophys. J.* **2013**, *105*, 154.
[75] E. E. Diel, J. W. Lichtman, D. S. Richardson, *Nat. Protoc.* **2020**, *15*, 2773.
[76] American Psychological Association, *APA style numbers and statistics guide, p.2*, APA Publication Manual Sections **2022**, pp. 6.32-6.35.

6.2 P2. Elucidating the physicochemical processes of light activated rotary motors embedded in lipid membranes

Having established that light driven rotary motors could render lipid membranes out of equilibrium, we followed up by trying to decipher how differing structural and chemical properties of the molecular motors would affect these dynamic mechanisms. This study focuses specifically on nine alkene-based molecular motors, to compare how their chemical differences map on the lipid bilayer. Such an investigation would also be beneficial as it would highlight which kinds of motors to choose for specific future applications. Upon incoporation in POPC bilayers, we compare the uptake efficiencies, aggregation types, molecular orientation, rotational speed and photoisomerization quantum yield of the molecular motors. Simultaneously, we correlated these with the membrane tension and fluidity of POPC bilayers composing of these molecular motors without being activated. We further observed the effects of irradiation for all the cases on the surface area modulation of POPC vesicles. Analysis confirmed that molecular motors 7 and 9 (named MM7 and MM9 respectively) have their double bonds aligned perpendicular to the membrane normal, in contrast with the other seven motors that have their double bonds aligned parallel to the membrane normal. In conclusion, the research emphasizes the key role of structure, orientation, and interaction parameters of light-driven rotary molecular machines within lipid membranes. The profound insights offered in the study lay vital groundwork to pave the way for the deployment of these molecular machines in various biological applications. Importantly, the research underscores the need for in-depth characterization of each molecular system when considering their application in complex biological environments, ensuring a more targeted and prediction-based approach to practical applications.

Elucidating the physicochemical processes of light activated rotary motors embedded in lipid membranes

Ainoa Guinart, Yusuf Qutbuddin, Alexander Ryabchun, Jan-Hagen Krohn, Petra Schwille*, and Ben L. Feringa*

Author contributions:

B.L.F., P.S., A.G., and **Y.Q.**, designed the study. A.G., characterized the compounds investigated, performed NMR and UV-Vis measurements of the rotation cycle, quantum yields and thermodynamic processes. A.G., performed DFT calculations., A.R., performed linear dichroism measurements. **Y.Q.**, performed studies on membrane tension and diffusion coefficients. J.K., and **Y.Q.**, developed acquisition and analysis macros. A.G., and **Y.Q.**, carried out all measurements and analysis on molecular motors embedded in lipid systems. B.L.F and P.S., supervised the work and acquired funding. A.G. and **Y.Q.**, wrote the manuscript. All authors discussed and commented on the manuscript.

under review

Chem - Cell Press (2024)

Elucidating the physicochemical processes of light activated rotary motors embedded in lipid membranes

Ainoa Guinart [1,3], Yusuf Qutbuddin [2,3], Alexander Ryabchun [1], Jan-Hagen Krohn [2], Petra Schwille [2] *, and Ben L. Feringa [1,4] *

[1] Stratingh Institute for Chemistry, University of Groningen, 9747AG Groningen, The Netherlands.

[2] Cellular and Molecular Biophysics, Max Planck Institute of Biochemistry, 82152 Martinsried, Germany

[3] These authors contributed equally

[4] Lead contact

* Correspondence. E-mail: b.l.feringa@rug.nl

SUMMARY

The integration of light-driven molecular machines with lipid membranes holds significant interest for advancing biological applications, necessitating a comprehensive understanding of the underlying biophysical mechanisms. Here, we report the incorporation of nine alkene-based molecular rotary motors with diverse chemical compositions into synthetic lipid membranes and establish a set of experimental tools to probe their behavior. Through molecular-scale characterizations, including motor positioning, orientation, aggregation, and uptake efficiency, as well as analysis of rotation cycle dynamics under membrane confinement, we elucidate the complex interactions between these molecular machines and lipid membranes. Moreover, we investigate the influence of motor incorporation on the biophysical properties of the membrane, such as fluidity and membrane tension. Additionally, we examine light-triggered membrane deformations and area expansion using electrodeformation of giant vesicles. Our findings reveal significant differences in how molecular-rotary motors interact with biological membranes, providing a comprehensive framework for future applications of synthetic molecular machines in biological contexts.

INTRODUCTION

Life, as we understand it, emerges from the complex interactions of multiple independent components, which synergistically give rise to properties that distinguish living systems from non-living ones. In vivo, many cellular elements influence the spatiotemporal dynamics of the whole, including the transport of metabolites, maintenance of homeostasis, and modification of cell size and shape during division, among other processes. To gain a better understanding of living systems, engineering principles such as bottom-up approaches are used to construct individual cellular parts, module by

module, and to study their function in isolation[1]. Compartmentalization is a fundamental feature of these systems, playing a crucial role by creating isolated microenvironments and concentrating chemical molecules[2]. Phospholipids, naturally form bilayers due to their amphiphilic properties, where these bilayers can be classified as two-dimensional fluids. These bilayers confine polar environments while allowing some exchange and interaction with the surroundings, as well as supporting significant processes dependent on shape. Such shape transformations allow for essential functions including cell division[3], endo- and exo-cytosis[4], membrane trafficking[5], and cellular movement[6]. In nature, dynamic protein networks drive these membrane transformations through intrinsic interactions within the membrane and through their peripheral activity on the bilayers[7,8]. To induce these forces, the cell needs to invest chemical energy, for example, in the form of NADPH reduction or ATP hydrolysis[9]. When creating cell-like mimicking systems, lipid membranes are produced using assemblies of natural or synthetic lipids[10]. Model membranes with varying compositions and structures are used today, ranging from supported lipid membranes to free standing vesicles of different sizes[11]. In bottom-up approaches, light can be converted into mechanical energy through the use of photoresponsive molecules, providing a controllable and precise source of energy[12] and triggering a (mechanical) response. A key advantage of light-induced processes is the high spatiotemporal control over the targeted system, allowing for regulation of exposure wavelength, time, and intensity[13]. Photo-induced processes enable the conversion of active molecules, referred to as photoswitches, between low-energy, thermodynamically favorable states, and high-energy metastable states[14]. Taking inspiration from biological motors like the membrane- bound ATP-ase rotary motor, pioneering studies on overcrowded alkene-based molecular motors demonstrated how they can be used to achieve a more controlled mechanical action[15]. These molecules complete a recurrent 360° unidirectional rotation through the consumption of light energy[16,17]. Because of their continuous nanoscopic operation and ease of functionalization, these remarkable molecular machines have garnered substantial interest towards biological applications. From attaching them to a surface and triggering mechano-sensitive channels in living cells[18], promoting on-demand drug delivery in systems[19], to incorporation into synthetic bilayers to simulate transmembrane ion-transport[20,21], these molecular machines have been used to reveal a fascinating range of potential applications in biological environments. Recently we showed how rotary molecular motors can be used to induce shape transformations in artificial membrane systems by systematically investigating the factors governing this process in both supported and free-standing lipid bilayers[22]. In the present study, we aim to develop a toolbox of experiments to elucidate key parameters to support future work involving molecular rotary machines in the context of biological membranes. By studying nine different alkene-based molecular rotary motors with diverse chemical composition (functional groups, upper or lower half modifications) and physical properties (polarity, rotation speed, etc.), we explore the substantial differences in their interaction with model membranes. Small (~ 100 nm in diameter) and giant (~ 20 µm in diameter) vesicles of 1-palmitoyl-2-oleoyl-sn-glycero-3-phosphocholine (POPC), a synthetic model lipid used for producing lipid bilayers, were used throughout this work. Characterizations at the molecular scale, such as position and orientation of the motors in the bilayer, aggregation and uptake efficiency of the light-

active compounds in membranes was performed using linear dichroism, and UV-Vis spectroscopy techniques supported by DFT calculations.

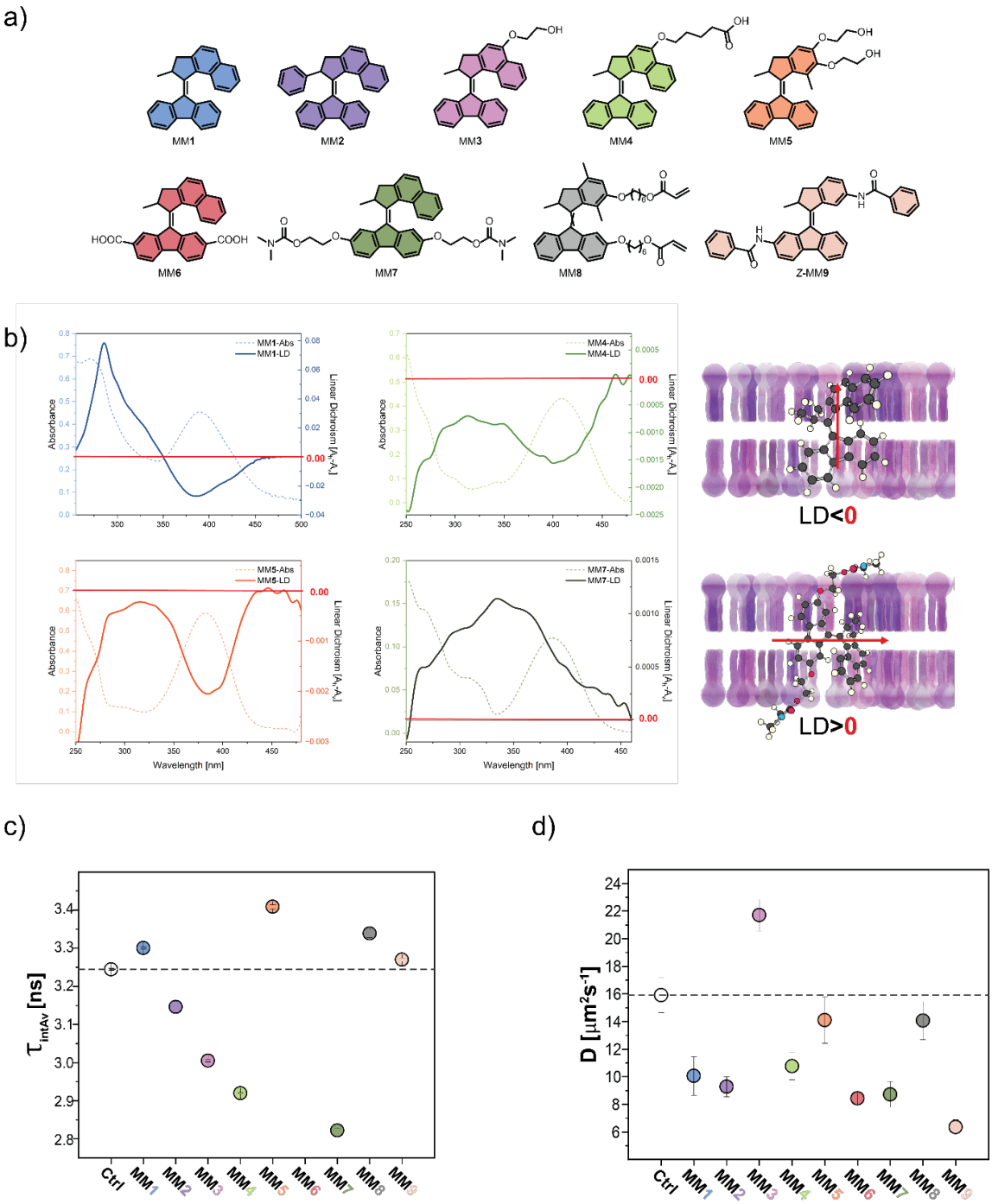

*Figure 1. a) Molecular motors used in the study. b) Absorption spectra and linear dichroism measurements of MM**1**, MM**4**, MM**5** and MM**7** in membrane environments (left) with a scheme of preferential membrane alignment depending of the LD signal (right). c) Flipper lifetime average values obtained for lipid membranes containing MM**1-9**. d) Diffusion coefficient average values obtained for*

*fluidity measurement of lipid membranes containing MM**1-9**. All lipid environments reported here corresponding to POPC SUVs +10 mol% MM**X**.*

Changes in membrane biophysical properties (fluidity, tension, etc.) were investigated through fluorescence correlation spectroscopy, a solvatochromic fluorescent probe and electrodeformation of giant unilamellar vesicles (GUVs). Furthermore, we investigated the influence of membrane confinement on the mechanical performance of the different molecular machines, analyzing the photochemical and thermodynamic steps of the rotation cycle. Finally, we characterized membrane deformations when the active molecules were under light irradiation using optical microscopy and semi-quantitative analysis of the membrane area change. Together, these results highlight remarkable differences between these compounds' interplay with biological membranes, and identifying the molecular motors that exert the most distinctive effects for future applications in chemical biology.

RESULTS AND DISCUSSION

Description of molecular motors and lipid systems studied

In this study, we systematically investigate a set of nine light-driven rotary molecular motors based on overcrowded alkene structures as photoresponsive membrane-intercalating agents. These compounds have been previously described by the Feringa group and others , and their synthesis and full characterization can be found elsewhere (see supplemental information). This research focuses on their incorporation in model membrane systems. All the studies were performed for lipid membranes composed of POPC, with 0.1 mol% of lipid conjugated dye Atto655-DOPE where fluorescence imaging was used. This lipid presents a phosphatidylcholine polar head group as well as one unsaturated (oleoyl) and one saturated (palmitoyl) acyl chain. We conducted a thorough investigation focusing on potential future uses in biomedical, biophysical, and biomechanical research as well as biomimetic materials. Molecular machines, among them, light-driven rotary motors, provide an unprecedented control of motion at the molecular scale, overcoming Brownian motion[23]. The study pivots around second-generation molecular motors due to their suitability for biological applications in terms of actuation in the visible spectrum and convenient rotation dynamics (more about this and other types of molecular motors can be found in ref's[17,24,25]. These motors are characterized by distinct upper and lower halves and bear a single stereogenic center.

Molecular motors **1**-**9** (MM**1**-**9,** Figure 1a) present the same core chemical structure that allows for broad functionalization: two five-membered carbon rings connected through a double bond (rotational axis). Briefly, MM**1** represents a non-functionalized reference compound and has been previously the main subject of study on lipid membrane remodeling[22]. MM**2** bears a bulkier phenyl ring, yielding a nonplanar structure of the tetrasubstituted central akene, which translates into a broader and higher absorption band, as well as slower rotational speed compared to MM**1**. MM**3**,

MM**4**, and MM**5** include flexible chains in their upper halves terminated with either alcohol or carboxylic acid groups to explore the influence of such substituents on membrane action. On the other hand, MM**6** and MM**7** present functional groups on their bottom halves: terminating carboxylic acids and carbamate groups, respectively, with two different chain lengths. Finally, MM**8** and MM**9** combine both upper- and lower-half modifications with propyl acrylate and benzamide groups, respectively. Note that MM**8** was used as a mixture of *E* and *Z* isomers, while MM**9** was used purely in its *Z*-form. Unless specified otherwise, tests were conducted using 10 mol% of MM**X** incorporated into the POPC membranes.

	Uptake%	*Lipophilicity log[$P_{o/w}$]*	*LD signal*	*Type aggregates*	*Dif. Coef. [$\mu m^2 s^{-1}$]*	*Flipper-TR lifetime [ns]*	*$\Delta G^{\ddagger}_{Lipid}$/ $\Delta G^{\ddagger}_{EtOH}$*	*QY_{Lipid}/QY_{EtOH}*
MM**1**	**91** ± 0.9	**0.86** ± 0.29	-	J	**10.1** ± 1.4	**3.301** ± 0.003	**0.992** ± 0.009	**0.6** ± 0.20
MM**2**	**96** ± 0.9	**1.44** ± 0.04	-	J	**9.3** ± 0.7	**3.146** ± 0.015	**0.973** ± 0.005	**0.4** ± 0.04
MM**3**	**93** ± 1.6	**0.95** ± 0.27	-	H	**21.7** ± 1.1	**3.005** ± 0.003	**0.997** ± 0.008	**1.0** ± 0.08
MM**4**	**88** ± 1.0	**1.01** ± 0.39	-	J	**10.8** ± 1.0	**2.920** ± 0.002	**0.982** ± 0.009	**0.1** ± 0.01
MM**5**	**86** ± 2.3	**0.82** ± 0.16	-	J	**14.1** ± 1.7	**3.409** ± 0.005	**0.981** ± 0.004	**0.6** ± 0.05
MM**6**	**91** ± 1.9	**1.1** ± 0.1	-	J	**8.4** ± 0.4	nmo	**0.983** ± 0.006	**0.1** ± 0.01
MM**7**	**75** ± 3.9	**0.48** ± 0.18	+	J	**8.7** ± 0.9	**2.822** ± 0.006	**1.020** ± 0.025	**0.4** ± 0.08
MM**8**	**91** ± 2.2	**1.05** ± 0.44	-	J	**14.1** ± 1.4	**3.339** ± 0.011	**0.996** ± 0.011	**0.6** ± 0.06
MM**9**	**64** ± 0.8	**0.59** ± 0.31	+	J	**6.4** ± 0.5	**3.270** ± 0.005	**1.027** ± 0.020	**0.3** ± 0.02

Table 1. ***Measurement on molecular motor organization and membrane properties.*** *Depicted values for model membranes of POPC incorporating 10 mol% of MM**X**. Linear dichroism (LD), diffusion coefficient (Dif. Coef.), quantum yield photoisomerization (QY), no measurement obtained (nmo).*

Uptake analysis of molecular motors embedded in lipid membranes

The hydrophobic nature of most organic aromatic compounds makes them excellent membrane intercalators[26]. Their lipophilic nature mostly ensures optimal incorporation into the hydrophobic region of lipid bilayers when both systems are mixed in organic solution prior to self-assembly in aqueous environments. However, slight differences in their chemical structure can lead to significant variances in their incorporation efficiency. To better understand the behavior of molecular motors in phospholipid bilayers, the partition coefficient (*n*-octanol/water) was determined using the shake flask

method[27]. This technique allows for easy estimation of the partition coefficient of organic compounds in membranes using a value ($logP_{O/W}$) that represents the solute distribution between the aqueous and membrane phases[28–30].

A high $logP_{O/W}$ value (>1) indicates greater lipophilicity of a compound, and thus, better membrane intercalation efficiency. Results on $logP_{O/W}$ values of MM**1-9** range from 0.48 ± 0.18 (MM**7**) to 1.44 ± 0.04 (MM**2**) (Table 1, Table S4, and Figure S11), indicating varying degrees of hydrophilicity to lipophilicity. Despite some fluctuations, these values show a consistent trend when correlated with uptake efficiencies (Figure S12). MM**7** and MM**9**, with the lowest $logP_{O/W}$ values and larger dipole moments (Table S1), also exhibit the lowest uptake efficiencies (75% and 65%, respectively). Conversely, MM**2**, with the biggest lipophilic character, demonstrates the highest incorporation uptake (96%) in POPC bilayers. These results suggest that while most molecular motors are effective membrane intercalators, special attention is required when incorporating highly polar compounds or those with water-soluble groups.

Studies on molecular motor orientation inside lipid membranes

To further test the hypothesis that small structural differences in the motor can lead to significant mismatches in their interaction with lipid membranes, we investigated how the molecules align within the bilayer. For this purpose, small unilamellar vesicles (SUVs) composed primarily of POPC and containing 10 mol% of MM**X** were subjected to shear flow, to distort the vesicles into an ellipsoidal form using Couette flow chambers[31,32], before recording linear dichroism (LD) measurements. By employing light polarized horizontal and vertical to the shear force, we measured the energy absorption along different axes of the molecule, providing insights into its orientation[33]. Molecules in solution that are not bound to the lipid membrane do not contribute to the LD signal. The positive or negative sign of the LD (determined by the equation $LD = A_h - A_v$) signal reports on the orientation of the electronic transition of the molecule, in this case, the electronic transition along the double bond. A_h and A_v represent the absorption of light polarized horizontally and vertically to the shear force respectively. Therefore, a negative LD value indicates that the electronic transition dipole moment of the motor is perpendicular to the applied force, i.e., parallel to the membrane normal. Conversely, a positive LD value indicates a parallel orientation to the shear force, suggesting an orthogonal orientation to the former. We calculated the electronic transition moment associated with the photoisomerization transition ($S^0 \rightarrow S^1$) using time-dependent density functional theory (TD-DFT) to gain further insights into the membrane positioning of MM**1-9** (Table S1). In all the studied molecular motors, the vector is oriented along the double bond with slight angular variations, providing a rough estimate of the molecules' alignment within the lipid bilayer (Figure S1). Interestingly, all motors exhibited a negative LD signal except MM**7** and MM**9** (Figure 1b, Figure S2). These findings indicate a preferential orientation for MM**1**, MM**2**, MM**3**, MM**4**, MM**5**, MM**6**, and MM**8**

parallel to the membrane normal, whereas MM**7** and MM**9** show orientation perpendicular to the membrane normal.

These results suggest that polar compounds with long-chain functional groups, bearing partially soluble water compounds, require the molecular motors to adopt a transmembrane structure conformation within the lipid bilayer. These findings are crucial for applications of such light-activated rotary motors in conjunction with ion-channels and scramblases.

Aggregation state of molecular motors within in lipid membranes

In the absence of light, the absorbance spectra of MM**1-9** were recorded in ethanol as a reference organic solvent, in octanol to mimic membrane-like conditions (surrounded by alkane groups) in solution, and in conjunction with phospholipids (POPC) forming SUVs in water. The absorption spectra display a red-shift in the absorption peak when transitioning from solution to self-assembled environments (Figure S7). Generally, changes in the absorption spectra are indicative of variations in intermolecular interactions, electronic environments, and structural organization when going to a self-assembled state. The observed bathochromic shift likely reflects enhanced π- π stacking interactions among the motor molecules, which reduces the energy gap between the ground state and excited states. An even more intriguing effect was observed when examining the change in absorbance spectra with increasing concentrations of MM**1-9** in POPC. Upon assembly in the bilayer, an exponential change in absorption maxima was observed for concentrations ranging from 1 to 25 mol% of MM**1-9**. This phenomenon has been previously observed with other photoactive compounds embedded in lipid membranes and is attributed to the formation of H/J-aggregates[34–37].

In essence, these shifts directly indicate the coupling strength between the molecules and provide information about their density and intermolecular distance. A hypochromic shift is associated with the formation of H-aggregates, where molecules align parallel to each other in a face-to-face conformation. In contrast, bathochromic shifts correspond to J-aggregates, where molecules adopt a head-to-tail aggregation state. In our case, all motors except MM**3** (which exhibited a blue shift indicative of H-aggregation) presented a red-shift in absorption maxima with increasing concentrations in the bilayer, indicating the formation of J-aggregates (Figure 2a, Table 1, Figure S9). The magnitude of the spectral shift in both H and J-aggregates offers qualitative information about the strength of molecular interactions, as well as size, density and stability of the formed aggregates. On the other hand, the exponential growth rate of such aggregates allows for a qualitative assessment of their aggregation propensity. When examining the values corresponding to our MM**1-9** aggregates (Table S2), we observed that MM**4** showed a large spectral shift (~13 nm) combined with a fast exponential growth (t-fit ~0.7±0.1), indicating strong molecular interactions and tightly packed aggregates. In contrast, MM**9** exhibited a small bathochromic shift (~3 nm) and slow exponential growth (t-fit ~ 8±2.5), suggesting the formation of smaller or more loosely packed aggregates. Notably, MM**3**, the only molecular motor that shows face-to-face aggregation, presented the fastest growth with a t-fit value of 15±3.4 and a small spectral shift of ~4 nm.

These results likely indicate that MM**3** aggregates form rapidly but have relatively weak interactions, with no significant alteration of the electronic environment. In the following sections we will explore how the observations regarding the organization of molecular motors within lipid membranes are corroborated by the influence on both the surrounding lipid environment and the intrinsic rotation parameters.

Changes in lipid membrane tension from molecular motor incorporation

As explained in the previous sections, MM**1-9** show different orientations and aggregation states in the model lipid membranes. Preferential orientation of such molecular motors would affect the membrane order of the bilayer, moreover, H- and J-aggregation states would also affect the mechanical properties of the membrane. To investigate the effect on the membrane order, we employed the recently developed solvatochromic fluorescent membrane tension probe, Flipper-TR[38], henceforth called Flipper. The fluorescence lifetime of Flipper reports on the local environment of the dye, higher fluorescence lifetimes correspond to a higher membrane tension and vice versa, as was shown in a recent study where Flipper lifetime can effectively probe the effect of cholesterol in model membranes[39]. To probe changes in membrane tension induced by the presence of MM**1-9**, we prepared SUVs of POPC containing 10 mol% of MM**X**, which were labeled with Flipper, by incubating the sample with $1\ \mu M$ of the dye in solution. Results on the reported fluorescence lifetime are shown in Figure 1c and Figure S5. An increase in fluorescence lifetime was observed for MM**1** ($\Delta\tau = 0.06\ ns$), MM**5** ($\Delta\tau = 0.16\ ns$), MM**8** ($\Delta\tau = 0.10\ ns$), and MM**9** ($\Delta\tau = 0.03\ ns$). Whereas MM**2** ($\Delta\tau = -0.10\ ns$), MM**3** ($\Delta\tau = -0.24\ ns$), MM**4** ($\Delta\tau = -0.33\ ns$), and MM**7** ($\Delta\tau = -0.42\ ns$) show a decrease in the membrane tension (Figure 2c, and Figure S5). Membranes imbedding MM**5** showed the highest increase in membrane order, indicating a high affinity to aggregation in ordered configurations within lipid membranes. On the other hand, MM**7** showed the highest decrease in fluorescence lifetime, and thus membrane tension, when compared to a pure POPC membrane. The contrasting membrane tension between membranes composing of MM**7** and MM**9** show that the induced membrane tension by molecular motors with similar orientations along the membrane are dependent on the functional groups attached to the aromatic rings. Samples with **MM6** repeatedly showed a low photon count, and were thus excluded from our calculations. It has been reported that H/J-aggregation can result in the quenching of fluorophores through energy transfer[40–42]. Supplementary video S1 shows that such quenching effects were observed when combining our model lipid membranes containing molecular motors and a membrane fluorophore. Since fluorescence quenching reduces the fluorescence lifetime of the dye, fluorescent probes alone cannot account for the correct estimation of the membrane properties in the case of molecular motors.

Effects on lipid membrane fluidity after molecular motor incorporation

The dynamics of membrane interactions and remodeling rely heavily on their inherent fluidity, a crucial mechanical property. Conducting fluidity measurements after peripheral interaction or exogenous molecule incorporation can provide key insights into the interplay between the studied compounds and lipid membranes. Moreover, the importance of modulating bilayer fluidity is essential in devising applications involving membranes. We investigate the effects of incorporation of MM**1-9** on the fluidity of supported lipid bilayers, specifically, POPC membranes which constitute 10 mol% MM**X** and 0.002 mol% lipid conjugated dye A655-DOPE.

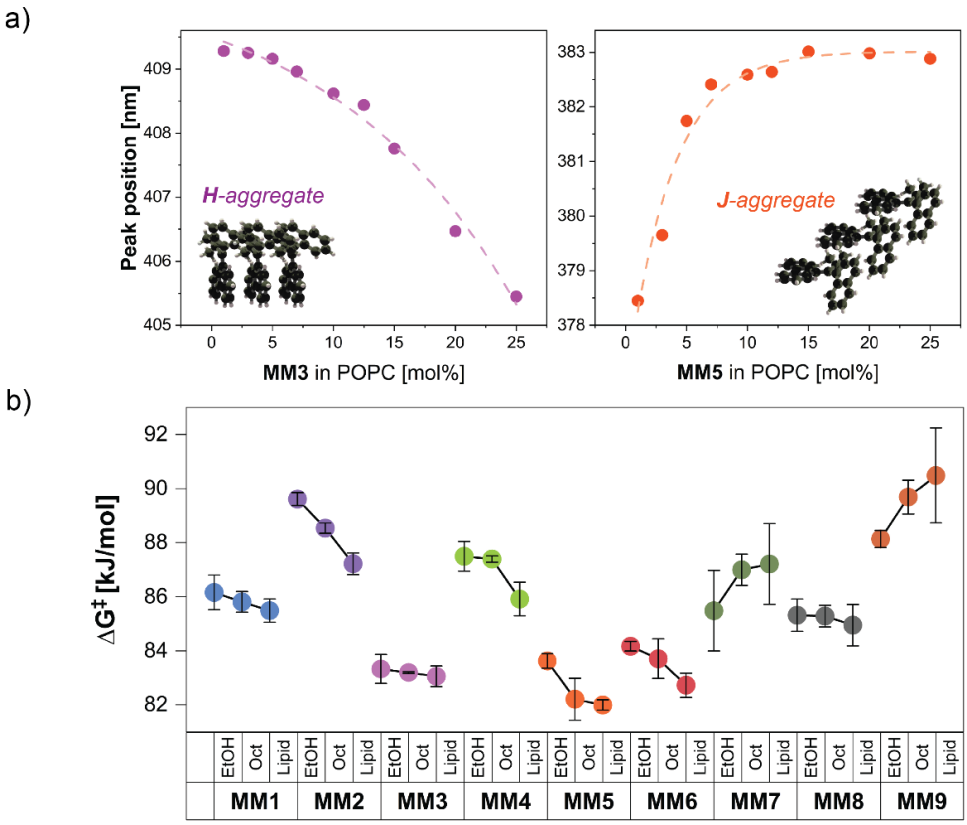

*Figure 2. a) H/J aggregate formation for MM**3** (left) and MM**5** (right) shown by characteristic absorbance peak displacement with increasing concentration of molecular motor inside lipid membrane. b) Energy barrier for the THI step of MM**1-9** in different environments. All lipid environments reported here corresponding to POPC SUVs +10 mol% MM**X**.*

We employed Fluorescence Correlation Spectroscopy (FCS) to analyze the diffusion coefficient of the lipid-conjugated dye A655-DOPE within supported lipid bilayers imbedding MM**1-9**. To mitigate against the overestimation of diffusion times resulting from imperfect focal position or membrane undulations, we adopted Z-scan FCS. This method involves performing measurements at varied focal positions along the membrane normal, followed by calculation of autocorrelation curves specific to each position. Figure S3 depicts representative autocorrelation curves at different focal positions along

the membrane, and calculated diffusion times for the calculation of true diffusion times in the membrane (refer to supplemental information, section 4). Figure 1d shows that as compared to pure POPC membranes, incorporation of all molecular motors with the exception of MM**3** ($D = 21.7 \pm 1.1\ \mu m^2 s^{-1}$) induced a reduction in the fluidity of the membrane. This difference could be linked to the formation of H-aggregates by MM**3**, in contrast to the preferred J-aggregation of the other molecular motors. Remarkably, MM**2**, MM**4**, and MM**7** show seemingly contradictory behavior. Despite presenting lower diffusion coefficients than the standard POPC membranes, the environmental probe Flipper indicates a decrease in membrane order. This further indicates that environment sensing fluorescent probes could be largely affected by the photophysics of molecular motors. These results denote the ability of molecular motors, depending on their structures, to alter the viscosity of lipid membranes on demand. The effect of H/J-aggregation on the resulting fluidity of the membrane can be further investigated in the future with molecular motors that display a strong H- or J-aggregation behavior. We will also show how higher affinity for ordered conformations affect the dynamics of molecular motor interactions in lipid membranes (see following sections).

Lipid environment and molecular motors rotation cycle: Photochemical isomerization step

We next investigated how the rotation cycle of MM1-9 was affected by membrane confinement. The first and third steps of the 360º rotation cycle of the studied molecular motors involve a photochemical E-Z isomerization (equivalent for symmetric motors) when the systems are irradiated with the appropriate wavelength of light (more about the rotation of molecular motors can be found in [17]). First, ^{1}H-NMR studies were carried out to confirm the ability of MM**1-9** to perform unidirectional rotation and characterize their photostationary distribution ratio in solution (supplemental information section 6, and Figure S6) As expected, the peak intensity of characteristic protons corresponding to the stable state of the motors decreased during irradiation. On the contrary, new absorption peaks emerged, attributed to the metastable isomers of the motors. When the photostationary state (PSS) was reached, the light source was removed and the systems were allowed to recover back to the stable isomer in the dark (corresponding to the second and fourth steps of the rotation cycle, the thermal helix inversion (THI)). To further investigate the photoisomerization properties, MM**1-9** were studied using UV-Vis spectroscopy in the previously described scenarios (EtOH, *n*-octanol, and SUVs composed of POPC and 10 mol% of MM**1-9** in water). Monitoring the changes of the absorption spectra under appropriate irradiation until reaching PSS allowed us to calculate the photoisomerization quantum yields (QY) of the process (Table 1, Tables S3 and S5, Figure S10). Comparisons of the QY values for the same molecules in both ethanol and octanol solutions reveled an interesting trend. For those motors with high polarity (MM**7** and MM**9**), a decrease in the QY can be observed when moving to a less polar environment, compared to a slight increase for the others. On the other hand, as previously reported for similar systems, a decrease in QY can be observed for all the molecular motors when confined inside a self-assembled lipid system. It is believed that this decrease relates to the aggregation state of the systems inside the membranes, impeding the isomerization step which in turn involves a large

conformational change[22]. This effect is also known to be strongly dependent on the fluidity of the media[43]. Furthermore, in a previous study where MM**1** was tested in different lipid systems the QY decrease proved to correlate to the fluidity of the membrane system[22]. Indeed, the only motor that seems to not have an effect on its QY regardless of the lipid environment is MM**3**, which in turn is the only that reported an increase in the fluidity of the lipid membranes as well as weak H-aggregates formation. We want to remark that some of the molecules studied (i.e., MM**4**, MM**6**, or MM**9**) show a significant decrease on their QY of photoisomerization, raising the importance of proper characterization of the rotation dynamics of each system every time it is applied to a new set of conditions (specifically highly crowded biological systems) to avoid misinterpretations of the obtained results.

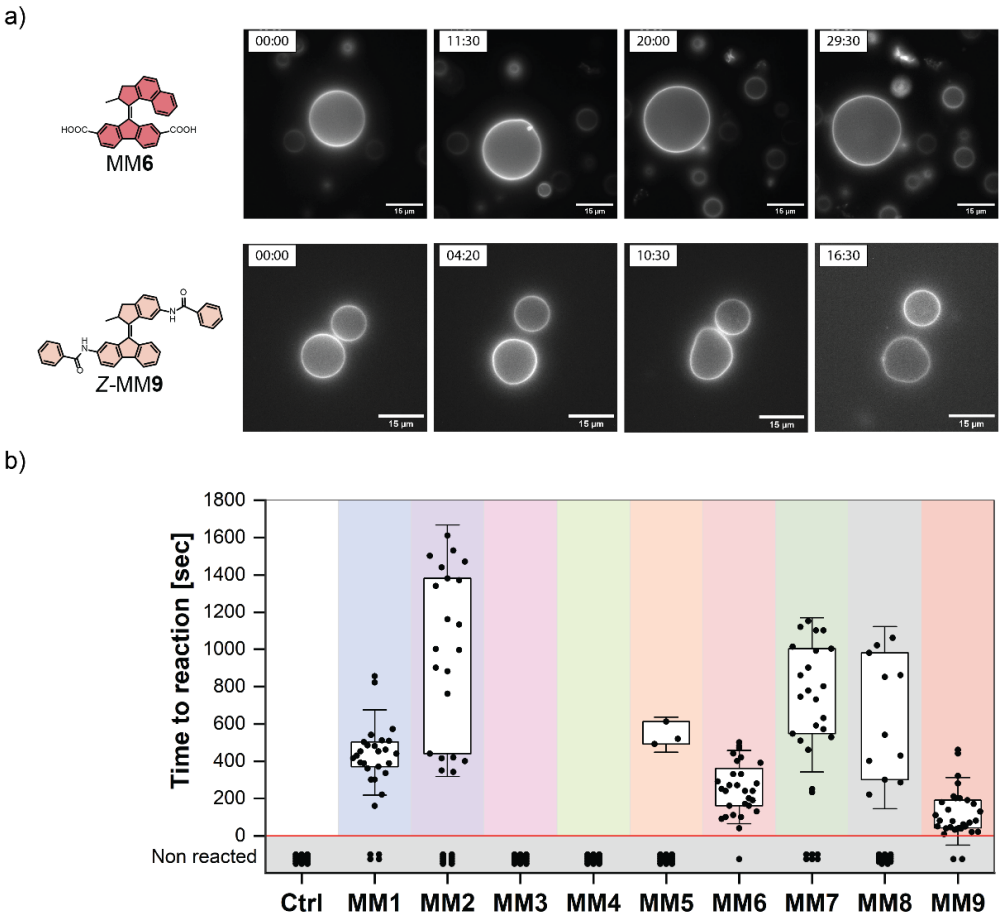

*Figure 3. Molecular motor induced fluctuations in giant unilamelar vesicles. a) Representative time-lapse images of MM6 and MM9-induced membrane deformations under 405 light exposure. b) Reported times for initiated membrane fluctuations in giant vesicles incorporating MM**1-9**. All lipid environments reported here corresponding to POPC SUVs + 0.1 mol% Atto655-DOPE (fluorescent imaging) + saturation concentration of MM**X**.*

Lipid environment and molecular motor rotation cycle: Thermal helix inversion step

Following our investigation into the rotation cycle, we looked at the THI step. This transformation occurs at a slower rate compared to the photochemical step (which has a timescale of nanoseconds) and is known as the rate-determining step of our systems. Thermodynamic studies of motors **1-9** determined the kinetic parameters of this process in the previously mentioned environments (EtOH, *n*-octanol, and SUVs) (Figure 2b, Figure S13 and supplemental information section 7f for details). An interesting trend could be observed when analyzing the results from the Eyring analysis in these environments. Specifically, a decrease in the activation barrier (faster rotational speed) was observed for those molecular motors that showed a preferential vertical alignment inside a lipid environment compared to the same molecules in solution. In contrast, MM**7** and MM**9**, which showed positive LD signal and thus a perpendicular orientation with respect to the lipid tails, were the only molecules that manifested an increase in their activation energy barrier (slower rotational speed). We also noted a positive entropy change only for these latter motors during the thermodynamic step. While we do not yet have a detailed explanation for these observations, they appear to correlate significantly with the orientation of the motors within the membrane systems, potentially influencing intermolecular interactions involved in the THI process. Further studies in this area should focus on a comprehensive exploration of all thermodynamic parameters and their interactions within biological systems. Overall, these results point out once more the importance of properly characterizing our molecular motor systems when applying them in specific biological applications.

Molecular motor action on membrane remodeling: fluctuation reaction times

Next, we examined the impact of *in situ* irradiation of molecular motors under fluorescence microscopy using GUVs. For GUV preparation, we employed PVA-assisted swelling in a 300 mM sucrose solution, followed by 10x to 30x dilution in equimolar glucose solution (see supplemental information section 8). Once diluted and stabilized in a temperature-controlled chamber, samples were irradiated with the respective laser lines in epifluorescence mode. The samples were irradiated every second and lasted an average of 30 min (up to 60 min in the case of non-reacting samples). At least 30 vesicles were analyzed for each molecular motor. GUVs with diameters less than 20 μm or those which showed perturbations (fluctuations, tubulations, and budding) prior to sample irradiation were excluded from the analysis. Examples of analyzed videos are provided in Figure 3a and Supplementary video S2. The start of perturbation was considered as the first visible fluctuation for each vesicle. GUVs which did not show any fluctuations during the acquisition time were considered as non-reactive. Results for pure POPC vesicles (Ctrl) and vesicles containing saturation concentrations of MM**1-9** are depicted in Figure 3b. Despite similarities in molecular motor sizes and rotational speed samples containing MM**3** and MM**4** showed no visible effect, while MM**5** had little influence on membrane remodeling. On the other hand, MM**1**, MM**6** and MM**9** exhibited fast and uniform reaction times, compared to a wider distribution of values for MM**2**, MM**7**, and MM**8**. Here, we are only considering the starting time of visible fluctuations and not their magnitude. Interestingly, the ability to induce deformations in lipid

membranes does not appear to be related to motor orientation (systems that are both parallel and perpendicular to the membrane normal showed the ability to deform GUVs membranes), rotation speed (MM**9** and MM**6** exhibited the fastest reaction times while being one of the slowest and fastest motors, respectively), and/or photoisomerization quantum yield. In the following section, we qualitatively assess the magnitude of membrane deformations when they are irradiated while being stretched in alternating electric fields.

Area expansion on lipid membranes triggered by molecular motor action

Observations on the fluctuations of lipid membranes due to the irradiation of molecular motors can be error prone due to a large number of different transformations that are induced for each system. To obtain a more detailed understanding, we measured the surface area changes of the giant unilamellar vesicles with deformation of vesicles under an AC electric field[44]. This method has been recently employed for observing changes in membrane surface area of vesicles containing photoswitchable Azo-PC upon photoisomerization[44]. Briefly, an alternating current (AC) electric field is applied to pull out excess area stored in thermal fluctuations. We worked under specific conductivity and frequency conditions where the vesicles acquire a prolate shape upon application of the electric field[22,45]. After the start of irradiation, changes in the vesicle area can be calculated through the geometric changes in the major and minor axes of the prolate spheroid. We applied 10 kV/m electric fields at 200 to 500 kHz to attain a prolate shape for our GUVs imbedding MM**1-9** and assessed the change in surface area after actuation of the molecules (Figure 4a, Figure S14 and S15, supplemental information section 8). Since the distribution of the molecular motors across the leaflets, and their orientation along the membrane is expected to result in different non-zero spontaneous curvatures during irradiation, we qualitatively analyzed the change in absolute area of the vesicle upon irradiation. The measurements were performed while irradiating with a 405 nm laser line to activate the molecular motors. In accordance with previous observations of area modulation with MM**1**, we similarly observed shape transformations for most molecular motors. A summary of the average absolute area change after 400 sec is presented in Table 2. Notably, most vesicles composing of MM**X** show initial tubulation upon dilution in hypertonic solutions, needed to release thermal fluctuations for electrodeformation. This can be due to possible leaflet asymmetry caused by the orientational preference of the molecular motors which would result in either positive or negative spontaneous curvatures. The obtained results for absolute area change over irradiation time for each of MM**1-9** is reported in Figure S15. In short, MM**3** and MM**4** displayed negligible area modulation upon irradiation under an electric field, corroborating the lack of response observed without electric field (see next section and Figure 3b). Interestingly, GUVs composing MM**3** also showed little response to the electric field frequencies applied. MM**5** shows expulsion of outward tubes and budding upon extended irradiations, thus inducing positive spontaneous curvature on the membrane (Figure S14). MM**1** and MM**6** show both inward and outward tubes, indicating heterogeneous preferential spontaneous curvature changes (Figure 4d and Figure S15). Conversely, MM**2**, MM**7**, MM**8** and MM**9** all show

inward tubes, thus inducing negative spontaneous curvatures upon extended irradiation (Figure 4b, 4c, Figure S14, Supplementary Video S3). Interestingly, MM**9** which showed a ~2-fold decrease in membrane fluidity, induced the quickest and largest shape deformation of GUVs with eventual expulsion of inward membrane tubes (see Supplementary Video S4). Similarly, MM**6** and MM**7**, which rigidify the membrane before irradiation, show large area modulations upon irradiation. The increase in viscosity of the membrane for such molecular motors without irradiation indicate their high affinity to ordering into aggregates. Upon irradiation, the change in motor conformations would thus disrupt these aggregations resulting in remodeling of the membrane. Less significant decrease in fluidity in the case of MM**4** and MM**5** also correlate well with the smaller deformations induced when irradiated. For all the molecular motors that induce deformations in the membrane, the resulting area change or modulation is heterogeneously distributed (see Figure 4b, 4c, 4d, and Figure S15).

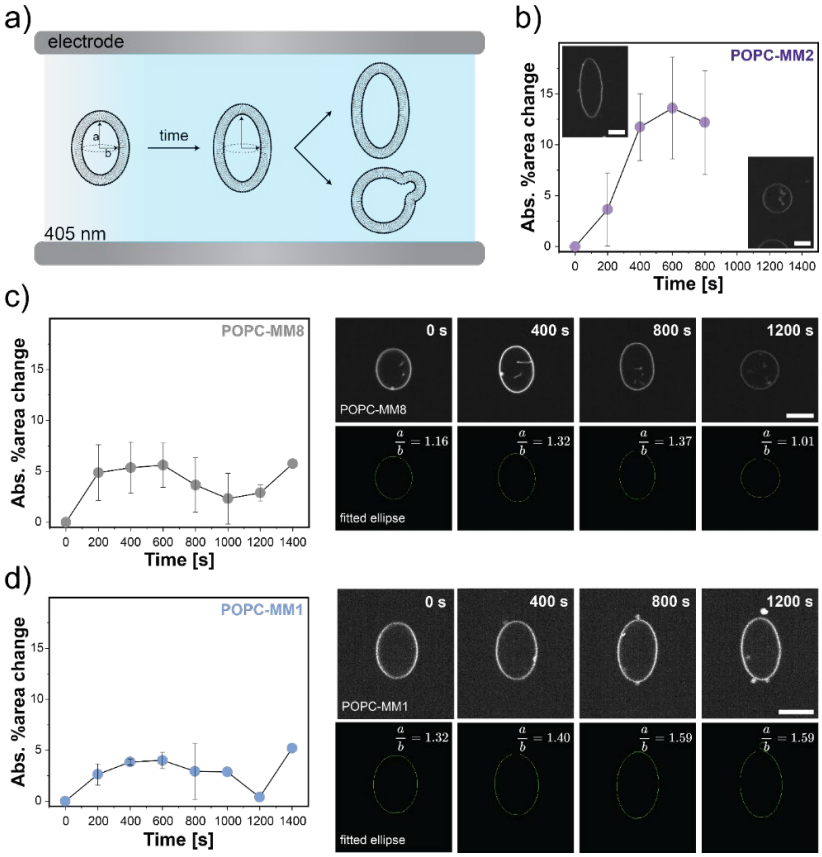

*Figure 4. Measurement of total surface area of giant unilamelar vesicles containing MM**1-9** with vesicles under an AC field a) schematic representation of area change after application of electric field and illumination of the samples. b) Absolute %area change for vesicles containing MM**2** (insets: representative vesicles at 0s and 1200s after illumination) c) Absolute %area change for vesicles containing MM**8** and representative vesicle with illumination time showing negative spontaneous curvature. d) Absolute %area change for vesicles containing MM**1** and representative vesicle with illumination time showing positive spontaneous curvature. All lipid environments reported here*

*corresponding to POPC GUVs + 0.1 mol% Atto655-DOPE (fluorescent imaging) + saturation concentration of MM**X**. Scale bar: 10 µm.*

Upon extended irradiation times, the vesicles tend to relax into spherical geometries with the excess surface area stored in membrane tubes or buds. This allows us to further assess the total surface area of membrane stored in the vesicle. Additionally, the preferential spontaneous curvature generation from these molecular motor irradiations can be estimated by looking at the prevalence of inward or outward tubes while the vesicle is held under constant stress due to the electric field. These results indicate that depending on the structure, orientational preference, functional groups, and aggregation preference; molecular motors can drive lipid membranes out of equilibrium while offering partial control over the mechanical properties of the membrane.

	Absolute %area change (400 sec)			*Number of vesicles analyzed*
MM**1**	3.19	±	1.15	3
MM**2**	11.74	±	3.29	4
MM**3**	1.85	±	0.15	2
MM**4**	2.27	±	0.4	2
MM**5**	1.99	±	1.22	4
MM**6**	7.47	±	4.89	7
MM**7**	3.29	±	0.66	3
MM**8**	5.36	±	2.5	4
MM**9**	4.89	±	2.9	5

*Table 2. Summary of absolute area changes observed after 400 sec of illumination with 405 nm for giant vesicles containing molecular motors **1-9** and number of vesicles analyzed.*

CONCLUSIONS

In this work we present a systematic investigation of nine distinct light-driven rotary molecular machines as photoresponsive membrane-intercalating agents for future applications in biology. We explored their structural organization in model lipid membranes in terms of incorporation efficiency, orientation in the bilayer, distribution and aggregation state. We found the large influence of compound polarity and chemical structure on the different membrane arrangements. These preferential organizations proved to be directly correlated to changes in the biophysical properties of

the lipid bilayers such as membrane fluidity and tension. Remarkably, the individual supramolecular organization of the different compounds studied proved to be strongly related to their rotational performance inside the membrane environment. In particular, we observed how an increase or decrease in membrane fluidity is directly related to the photoisomerization quantum yield in our molecular motors' rotation cycle. In addition, a preferential perpendicular or parallel alignment of the light-sensitive compounds, to the membrane normal, determines a decrease or increase in their rotation speed, respectively. Through this study we also examined the light-induced membrane deformations due to molecular motor action. These include analysis of membrane fluctuations and dynamic alterations of giant unilamelar vesicles as well as quantitative studies on absolute area changes using electrodeformation of GUVs. We proved how induced changes in the membrane mechanical properties are dependent on motors' chemical structure and show preferential spontaneous curvature changes. Overall, our study shows how differences in the chemical structure of light-activated rotary molecular motors translate into substantial divergence in their organization inside a biological membrane, which in turn transforms into significant changes in the motor performance as well as preferential remodeling of the membranes. This work will provide a clear pathway for future molecular motor applications into biological systems in addition to highlighting the importance of exhaustive characterization of each molecular system when used in a complex biological environment.

EXPERIMENTAL PROCEDURES

Full experimental procedures can be found in the supplemental information.

Resource availability

Lead contact

Further information and requests for resources should be directed to and will be fulfilled by the lead contact, Prof. Ben L. Feringa (b.l.feringa@rug.nl).

Materials availability

All unique reagents generated in this study are available from the lead contact upon reasonable request.

Data and code availability

All data supporting the findings of this study are included within the manuscript and its supplemental information and are also available from the authors upon request. This study did not generate any datasets.

SUPPLEMENTAL INFORMATION

Supplemental information can be found online at ...

ACKNOWLEDGMENTS

We gratefully acknowledge financial support from the Ministry of Education, Culture and Science of the Netherlands (Gravitation Program No. 024.001.035 to B.L.F). Y.Q. acknowledges support from the International Max Planck Research School for Molecules of Life (IMPRS-ML). P.S. acknowledges support from Center for NanoScience (CeNS). The authors gratefully acknowledge Pieter van der Meulen for guidance with NMR measurements. We thank the Centre for Information Technology of the University of Groningen for their support and for providing access to the Peregrine (now Hábrók) high performance computing cluster. We thank Dr. Rumiana Dimova for assistance in setting up the electrodeformation technique at MPI-B.

AUTHOR CONTRIBUTION

B.L.F., P.S., A.G., and Y.Q., designed the study. A.G., characterized the compounds investigated, performed NMR and UV-Vis measurements of the rotation cycle, quantum yields and thermodynamic processes. A.G., performed DFT calculations., A.R., performed linear dichroism measurements. Y.Q., performed studies on membrane tension and diffusion coefficients. J.K., and Y.Q., developed acquisition and analysis macros. A.G., and Y.Q., carried out all measurements and analysis on molecular motors embedded in lipid systems. B.L.F and P.S., supervised the work and acquired funding. A.G. and Y.Q., wrote the manuscript. All authors discussed and commented on the manuscript.

DECLARATION OF INTERESTS

The authors declare no competing interests.

REFERENCES

1. Jia, H., and Schwille, P. (2019). Bottom-up synthetic biology: reconstitution in space and time. Curr Opin Biotechnol *60*, 179–187. https://doi.org/10.1016/J.COPBIO.2019.05.008.
2. Amy Yewdall, N., Mason, A.F., and Van Hest, J.C.M. (2018). The hallmarks of living systems: towards creating artificial cells. Interface Focus *8*. https://doi.org/10.1098/RSFS.2018.0023.
3. Ong, J.Y., and Torres, J.Z. (2019). Dissecting the mechanisms of cell division. J Biol Chem *294*, 11382–11390. https://doi.org/10.1074/JBC.AW119.008149.

4. Wu, L.G., Hamid, E., Shin, W., and Chiang, H.C. (2014). Exocytosis and endocytosis: modes, functions, and coupling mechanisms. Annu Rev Physiol *76*, 301–331. https://doi.org/10.1146/ANNUREV-PHYSIOL-021113-170305.
5. Akinwunmi, O.A. (2023). Membrane Trafficking Mechanisms and Their Biological Relevance. Arch Razi Inst *78*, 1397–1412. https://doi.org/10.22092/ARI.2023.78.5.1397.
6. Ananthakrishnan, R., and Ehrlicher, A. (2007). The forces behind cell movement. Int J Biol Sci *3*, 303–317. https://doi.org/10.7150/IJBS.3.303.
7. Farsad, K., and De Camilli, P. (2003). Mechanisms of membrane deformation. Curr Opin Cell Biol *15*, 372–381. https://doi.org/10.1016/S0955-0674(03)00073-5.
8. Lipowsky, R. (2022). Remodeling of Membrane Shape and Topology by Curvature Elasticity and Membrane Tension. Adv Biol *6*, 2101020. https://doi.org/10.1002/ADBI.202101020.
9. Alberts, B., Bray, D., Johnson, A., Lewis, J., Raff, M., Roberts, K., and Walter, P. (2018). Cells: The Fundamental Units of Life. Essential Cell Biolog, 1–38. https://doi.org/10.1201/9781315815015-1/CELLS-FUNDAMENTAL-UNITS-LIFE-BRUCE-ALBERTS-DENNIS-BRAY-ALEXANDER-JOHNSON-JULIAN-LEWIS-MARTIN-RAFF-KEITH-ROBERTS-PETER-WALTER.
10. Podolsky, K.A., and Devaraj, N.K. (2021). Synthesis of lipid membranes for artificial cells. Nature Reviews Chemistry 2021 5:10 *5*, 676–694. https://doi.org/10.1038/s41570-021-00303-3.
11. Marquardt, D., Geier, B., and Pabst, G. (2015). Asymmetric Lipid Membranes: Towards More Realistic Model Systems. Membranes 2015, Vol. 5, Pages 180-196 *5*, 180–196. https://doi.org/10.3390/MEMBRANES5020180.
12. Di Martino, M., Sessa, L., Diana, R., Piotto, S., and Concilio, S. (2023). Recent Progress in Photoresponsive Biomaterials. Molecules 2023, Vol. 28, Page 3712 *28*, 3712. https://doi.org/10.3390/MOLECULES28093712.
13. Emiliani, V., Entcheva, E., Hedrich, R., Hegemann, P., Konrad, K.R., Lüscher, C., Mahn, M., Pan, Z.H., Sims, R.R., Vierock, J., et al. (2022). Optogenetics for light control of biological systems. Nature Reviews Methods Primers 2022 2:1 *2*, 1–25. https://doi.org/10.1038/s43586-022-00136-4.
14. Pianowski, Z.L. (2022). Molecular Photoswitches: Chemistry, Properties, and Applications, 2 Volume Set. Molecular Photoswitches: Chemistry, Properties, and Applications, 2 Volume Set *1–2*, 1–1112. https://doi.org/10.1002/9783527827626.
15. Koumura, N., Zijistra, R.W.J., Van Delden, R.A., Harada, N., and Feringa, B.L. (1999). Light-driven monodirectional molecular rotor. Nature 1999 401:6749 *401*, 152–155. https://doi.org/10.1038/43646.
16. Kistemaker, J.C.M., Lubbe, A.S., and Feringa, B.L. (2021). Exploring molecular motors. Mater Chem Front *5*, 2900–2906. https://doi.org/10.1039/D0QM01091J.
17. Pooler, D.R.S., Lubbe, A.S., Crespi, S., and Feringa, B.L. (2021). Designing light-driven rotary molecular motors. Chem Sci *12*, 14964–14986. https://doi.org/10.1039/D1SC04781G.
18. Zheng, Y., Han, M.K.L., Zhao, R., Blass, J., Zhang, J., Zhou, D.W., Colard-Itté, J.R., Dattler, D., Çolak, A., Hoth, M., et al. (2021). Optoregulated force application to cellular receptors using molecular motors. Nature Communications 2021 12:1 *12*, 1–10. https://doi.org/10.1038/s41467-021-23815-4.

19. Guinart, A., Korpidou, M., Doellerer, D., Pacella, G., Stuart, M.C.A., Dinu, I.A., Portale, G., Palivan, C., and Feringa, B.L. (2023). Synthetic molecular motor activates drug delivery from polymersomes. Proc Natl Acad Sci U S A *120*, e2301279120. https://doi.org/10.1073/PNAS.2301279120/SUPPL_FILE/PNAS.2301279120.SAPP.PDF.
20. Wang, W.Z., Huang, L.B., Zheng, S.P., Moulin, E., Gavat, O., Barboiu, M., and Giuseppone, N. (2021). Light-Driven Molecular Motors Boost the Selective Transport of Alkali Metal Ions through Phospholipid Bilayers. J Am Chem Soc *143*, 15653–15660. https://doi.org/10.1021/JACS.1C05750/ASSET/IMAGES/LARGE/JA1C05750_0005.JPEG .
21. Yang, H., Yi, J., Pang, S., Ye, K., Ye, Z., Duan, Q., Yan, Z., Lian, C., Yang, Y., Zhu, L., et al. (2022). A Light-Driven Molecular Machine Controls K+ Channel Transport and Induces Cancer Cell Apoptosis. Angewandte Chemie International Edition *61*, e202204605. https://doi.org/10.1002/ANIE.202204605.
22. Qutbuddin, Y., Guinart, A., Gavrilovi´c, G., Al Nahas, K., Feringa, B.L., Schwille, P., Qutbuddin, Y., Gavrilovi´c, S.G., Al Nahas, K., Schwille, P., et al. (2024). Light-Activated Synthetic Rotary Motors in Lipid Membranes Induce Shape Changes Through Membrane Expansion. Advanced Materials *36*, 2311176. https://doi.org/10.1002/ADMA.202311176.
23. Mazo, R.M. (2009). Brownian Motion: Fluctuations, Dynamics, and Applications (The International Series of Monographs on Physics). 304.
24. Roke, D., Wezenberg, S.J., and Feringa, B.L. (2018). Molecular rotary motors: Unidirectional motion around double bonds. Proc Natl Acad Sci U S A *115*, 9423–9431. https://doi.org/10.1073/PNAS.1712784115/ASSET/E8C10520-22F8-4BCA-93A6-C4AD51C83E45/ASSETS/GRAPHIC/PNAS.1712784115FIG10.JPEG.
25. Vicario, J., Meetsma, A., and Feringa, B.L. (2005). Controlling the speed of rotation in molecular motors. Dramatic acceleration of the rotary motion by structural modification. Chemical Communications, 5910–5912. https://doi.org/10.1039/B507264F.
26. Hamacher, K.A., Kaiser, H., Kulasekere, R., and Worcester, D.L. (1995). Intercalation of organic compounds in lipid bilayers. Materials Research Society Symposium - Proceedings *376*, 297–302. https://doi.org/10.1557/PROC-376-297/METRICS.
27. Test No. 107: Partition Coefficient (n-octanol/water): Shake Flask Method (1995). https://doi.org/10.1787/9789264069626-EN.
28. Dearden, J.C., and Bresnen, G.M. (1988). The Measurement of Partition Coefficients. Quantitative Structure-Activity Relationships *7*, 133–144.
29. Finizio, A., Vighi, M., and Sandroni, D. (1997). Determination of n-octanol/water partition coefficient (Kow) of pesticide critical review and comparison of methods. Chemosphere *34*, 131–161. https://doi.org/10.1016/S0045-6535(96)00355-4.
30. Ong, S., Liu, H., and Pidgeon, C. (1996). Immobilized-artificial-membrane chromatography: measurements of membrane partition coefficient and predicting drug membrane permeability. J Chromatogr A *728*, 113–128. https://doi.org/10.1016/0021-9673(95)00837-3.
31. Dorrington, G., Chmel, N.P., Norton, S.R., Wemyss, A.M., Lloyd, K., Praveen Amarasinghe, D., and Rodger, A. (2018). Light scattering corrections to linear dichroism spectroscopy for liposomes in shear flow using calcein fluorescence and modified Rayleigh-Gans-Debye-Mie scattering. Biophys Rev *10*, 1385–1399. https://doi.org/10.1007/S12551-018-0458-8/FIGURES/9.

32. Rodger, A., Rajendra, J., Marrington, R., Ardhammar, M., Nordén, B., Hirst, J.D., Gilbert, A.T.B., Dafforn, T.R., Halsall, D.J., Woolhead, C.A., et al. (2002). Flow oriented linear dichroism to probe protein orientation in membrane environments. Physical Chemistry Chemical Physics *4*, 4051–4057. https://doi.org/10.1039/B205080N.
33. Tukova, A., and Rodger, A. (2021). Spectroscopy of model-membrane liposome-protein systems: complementarity of linear dichroism, circular dichroism, fluorescence and SERS. Emerg Top Life Sci *5*, 61–75. https://doi.org/10.1042/ETLS20200354.
34. Kuiper, J.M., and Engberts, J.B.F.N. (2004). H-Aggregation of Azobenzene-Substituted Amphiphiles in Vesicular Membranes. Langmuir *20*, 1152–1160. https://doi.org/10.1021/LA0358724/ASSET/IMAGES/LARGE/LA0358724F00018.JPEG.
35. Song, X., Perlstein, J., and Whitten, D.G. (1997). Supramolecular aggregates of azobenzene phospholipids and related compounds in bilayer assemblies and other microheterogeneous media: Structure, properties, and photoreactivity. J Am Chem Soc *119*, 9144–9159. https://doi.org/10.1021/JA971291N/ASSET/IMAGES/LARGE/JA971291NF00015.JPEG.
36. Kawai, T., Umemura, J., and Takenaka, T. (1989). UV Absorption Spectra of Azobenzene-Containing Long-Chain Fatty Acids and Their Barium Salts in Spread Monolayers and Langmuir—Blodgett Films. Langmuir *5*, 1378–1383. https://doi.org/10.1021/LA00090A020/ASSET/LA00090A020.FP.PNG_V03.
37. Urban, P., Pritzl, S.D., Konrad, D.B., Frank, J.A., Pernpeintner, C., Roeske, C.R., Trauner, D., and Lohmüller, T. (2018). Light-Controlled Lipid Interaction and Membrane Organization in Photolipid Bilayer Vesicles. Langmuir *34*, 13368–13374. https://doi.org/10.1021/ACS.LANGMUIR.8B03241/SUPPL_FILE/LA8B03241_SI_001.MPG.
38. Colom, A., Derivery, E., Soleimanpour, S., Tomba, C., Molin, M.D., Sakai, N., González-Gaitán, M., Matile, S., and Roux, A. (2018). A fluorescent membrane tension probe. Nature Chemistry 2018 10:11 *10*, 1118–1125. https://doi.org/10.1038/s41557-018-0127-3.
39. Ragaller, F., Sjule, E., Urem, Y.B., Schlegel, J., El, R., Urbancic, D., Urbancic, I., Blom, H., and Sezgin, E. (2024). Quantifying Fluorescence Lifetime Responsiveness of Environment-Sensitive Probes for Membrane Fluidity Measurements. Journal of Physical Chemistry B *128*, 2154–2167. https://doi.org/10.1021/ACS.JPCB.3C07006/ASSET/IMAGES/LARGE/JP3C07006_0005.JPEG.
40. Pritzl, S.D., Morstein, J., Kahler, S., Konrad, D.B., Trauner, D., and Lohmüller, T. (2022). Postsynthetic Photocontrol of Giant Liposomes via Fusion-Based Photolipid Doping. Langmuir *38*, 11941–11949. https://doi.org/10.1021/ACS.LANGMUIR.2C01685/SUPPL_FILE/LA2C01685_SI_006.AVI.
41. Harbron, E.J. (2013). Fluorescence Intensity Modulation in Photochromic Conjugated Polymer Systems. Isr J Chem *53*, 256–266. https://doi.org/10.1002/IJCH.201300016.
42. Chevalier, A., Renard, P.Y., and Romieu, A. (2017). Azo-Based Fluorogenic Probes for Biosensing and Bioimaging: Recent Advances and Upcoming Challenges. Chem Asian J *12*, 2008–2028. https://doi.org/10.1002/ASIA.201700682.
43. Jones, R.A.L., Sen, A., Ibele, M., Hong, Y., Velegol, D., Parnell, A.J., Tzokova, N., Topham, P.D., Adams, D.J., Adams, S., et al. (2009). The influence of viscosity on the

functioning of molecular motors. Faraday Discuss *143*, 319–334. https://doi.org/10.1039/B901841G.

44. Aleksanyan, M., Grafmüller, A., Crea, F., Georgiev, V.N., Yandrapalli, N., Block, S., Heberle, J., and Dimova, R. (2023). Photomanipulation of Minimal Synthetic Cells: Area Increase, Softening, and Interleaflet Coupling of Membrane Models Doped with Azobenzene-Lipid Photoswitches. Advanced Science *10*, 2304336. https://doi.org/10.1002/ADVS.202304336.
45. Aranda, S., Riske, K.A., Lipowsky, R., and Dimova, R. (2008). Morphological transitions of vesicles induced by alternating electric fields. Biophys J *95*, L19–L21. https://doi.org/10.1529/biophysj.108.132548.

6.3 P3. Photoswitchable molecular motor lipid: synthesis, characterization and integration into lipid vesicles

Inching towards the molecular motor equivalent of Azo-PC (phosphatidylcholine with an azobenzene conjugated to one of the acyl chains), this study reports the design, synthesis, and characterization of two novel photoswitchable lipids based on molecular rotary motors, MM1-PC and MM2-PC. Our collaborators investigated the photochemical and thermodynamic properties of these compounds in different solution and self-assembled environments, including their rotation cycle, photoisomerization behavior, and thermodynamic parameters. My major contribution in this work is the integration of these photo-responsive lipids into giant unilamellar vesicles (GUVs), and deciphering the effects upon photoactivation. We demonstrated that the incorporation of MM1-PC and MM2-PC into GUVs allows for the control of membrane opening and release of contents upon light irradiation. Specifically, the authors found that the incorporation of MM1-PC into GUVs leads to a significant reduction in fluorescence lifetime of the membrane dye, which would indicate the quenching effects associated with molecular motor aggregation. Upon irradiation with $405\,\mathrm{nm}$ light, the fluorescence signal on the GUVs increase significantly, followed by an explosion of the vesicle and fragmentation into smaller daughter vesicles. We proposed that the degradation of MM1-PC upon irradiation results in the generation of reactive oxygen species (ROS), which interact with sucrose present inside the vesicles, leading to an increase in the osmotic pressure and eventual membrane rupture. This mechanism is supported by the observation that the degradation of MM1-PC can be slowed down by reducing the concentration of MM1-PC incorporated into the membrane. The ability to control the opening of GUVs using light provides a new tool for the study of membrane dynamics and the development of controlled release systems. We suggest that this system could be used to design GUVs that can be triggered to release their contents on demand, without the need for light-sensitive molecules to be present inside the lumen. This study also highlights the challenges of synthesizing motor conjugated lipids, but indicate that these super-molecules could be revolutionary for pharmaceutical applications.

Photoswitchable molecular motor lipid: synthesis, characterization and integration into lipid vesicles

Ainoa Guinart†, Daniel Doellerer†, Yusuf Qutbuddin, Henry Zivkovic, Dominik Hrebik, John Briggs, Petra Schwille*, and Ben L. Feringa*

Author contributions:

B.L.F. and P.S. conceptualized the idea. A.G. and D.D. contributed equally to this work. D.D. synthesized the motor conjugated lipids. A.G. performed the photochemical characterizations. **Y.Q.** and A.G. performed the imaging and analysis of GUVs. **Y.Q.** performed the membrane tension experiments and analysis. **Y.Q.** performed the fluorescence lifetime measurements and analysis. A.G. performed the absorbance assays. A.G., D.D., and **Y.Q.** wrote the manuscript. All authors commented on the manuscript. B.L.F. and P.S. acquired funding.

Ainoa Guinart, Daniel Doellerer, Yusuf Qutbuddin, Henry Zivkovic, Cristina Branca, Dominik Hrebik, Petra Schwille, and Ben L. Feringa Langmuir 2025, XXXX, XXX, XXX-XXX.
https://doi.org/10.1021/acs.langmuir.4c04173

published in

Langmuir (2025)

LANGMUIR

pubs.acs.org/Langmuir Article

Photoswitchable Molecular Motor Phospholipid: Synthesis, Characterization, and Integration into Lipid Vesicles

Ainoa Guinart,‖ Daniel Doellerer,‖ Yusuf Qutbuddin, Henry Zivkovic, Cristina Branca, Dominik Hrebik, Petra Schwille,* and Ben L. Feringa*

Cite This: https://doi.org/10.1021/acs.langmuir.4c04173 Read Online

ACCESS | Metrics & More | Article Recommendations | Supporting Information

ABSTRACT: Lipid membranes are essential for cellular function, acting as barriers and platforms for major cellular and biochemical activities. The integration of photoisomerizable units into lipid structures allows for tunable membrane properties, offering insights into major membrane-related processes. In this study, we present the first molecular-motor-conjugated phospholipid system. The synthesis of two phosphatidylcholine derivatives is reported, where one acyl chain is replaced with a light-responsive molecular rotary motor moiety. We explore the photochemical and thermodynamic behaviors of these compounds in solution and as self-assembled systems, demonstrating their rotation cycles under illumination and their dynamic properties in combination with lipid molecules. Additionally, giant unilamellar vesicles with these compounds are formed to investigate the mechanisms of the photoinduced responses in synthetic lipid membranes. Our findings show that molecular motor-based lipids can operate in aqueous solution and with natural phospholipids, maintaining photoisomerization properties and enabling oxidation-driven release within giant lipid vesicles.

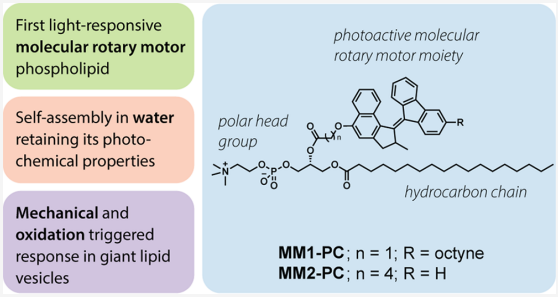

INTRODUCTION

The study of lipid membranes is crucial to understanding many biological processes and their underlying mechanisms. Lipid membranes play an essential role in cellular function, serving as barriers that compartmentalize and protect cellular contents, as well as platforms to carry out most biochemical activities in our body.[1] One of the key features of lipid membranes is the ability of their components to self-assemble into organized structures, driven by the amphipathic nature of their constituent molecules. Amphipathic molecules, such as phospholipids, readily form organized arrays by self-assembly in aqueous environments. Their cooperative behavior is strongly influenced by the length and degree of unsaturation of their acyl chains, as well as their headgroup composition.[2] For a given headgroup and fixed chain length, *cis*-unsaturation leads to bending in the acyl chain, due to packing effects derived by bond fixation. In contrast, *trans*-compounds exhibit more cooperative phase transitions.[3] The introduction of isomerizable units into the lipid structure offers the possibility to control membrane physical behavior, opening the door to tunable membrane characteristics such as fluidity,[4] packing area,[5] order,[6] and lipid rafts[7] among others. This regulation is highly relevant for studying the effects of bilayer physics and biochemistry in areas such as ion transport, membrane-bound enzyme activity, and membrane mechano-sensitivity. By modulating the structural properties of the membrane, we can gain insights into how different lipid compositions influence biological functions. Naturally occurring photoisomerization of phospholipids only happens at rather short wavelengths, which often involves photochemical decomposition.[8] In recent years, several photoisomerizable phospholipid analogs have been developed, highlighting the potential for controlled manipulation of membrane properties through photoisomerizing mechanisms.[9−11] Most of these examples are based on azobenzene photoswitches conjugated to a phospholipid backbone in one or both of its acyl chains. Studies report light-triggered changes in membrane properties[12−15] as well as fluidity[16,17] and lipid domain reorganization.[18,19] One of the recent studies demonstrated the dose-dependent function of an azobenzene-derived analog of palmitoyl-oleoylphosphatidylcholine (POPC) in constructing artificial photoswitchable cell mimetics. The authors provide a quantitative link between material properties and membrane parameters such as changes in area and thickness, morphology, elastic and electrical properties, and their relation to

Received: October 21, 2024
Revised: January 21, 2025
Accepted: January 29, 2025

https://doi.org/10.1021/acs.langmuir.4c04173
Langmuir XXXX, XXX, XXX−XXX

organization and restructuring at the molecular level.[5] Molecular photoswitches, such as azobenzenes, are compounds that interconvert between two different isomer states when irradiated at the appropriate wavelength. These systems hold promise for numerous applications, especially when a transition between two differentiated states is required. Similar to molecular photoswitches, a higher control of molecular motion can be achieved by the so-called overcrowded-alkene molecular rotary motors.[20] These molecules based on chiroptical molecular switches were first reported in 1999 and are able to perform repetitive, photochemically driven unidirectional motion involving four different molecular states.[21] Briefly, the rotation cycle is described by the sequential isomerization of the molecule that enforced a unidirectional motion as opposed to a randomized Brownian motion.[22] In the case of the molecular motors used in this study, this process is characterized by two photochemical *E*-*Z* isomerizations, each followed by a thermal helix inversion (THI) step that brings the system back to the initial state, resulting in continuous motion as long as there is a photon supply (for more details on molecular motor rotation dynamics see ref 20). We envision that combining such systems with a phospholipid backbone will achieve a higher degree of nanoscale control in self-assembled systems such as membranes, increasing the number of possible molecular states, together with a repetitive, out-of-equilibrium mechanical motion. Here we report the first molecular motor-phospholipid systems (**MM-PC**) to our knowledge. We discuss the synthesis of two distinct phosphatidylcholine derivatives, where one hydrophobic acyl chain has been replaced by a molecular rotary motor moiety. Investigations of the photochemical and thermodynamic behavior of the novel compounds both in solution and in self-assembled systems are presented. We also provide evidence of their rotation cycle under appropriate illumination as well as studies of the self-assembled behavior in combination with lipid molecules and their light-induced dynamic properties. Finally, we formed giant unilamellar vesicles (GUVs) with our **MM-PC** compounds and their phospholipid analog and explored the possible mechanisms of photoinduced responses in synthetic lipid membranes. In this study, we proved that molecular motor-based lipids can be operated in pure water and in vesicles when combined with natural phospholipids, with increased stability, retaining their photoisomerization properties. Such systems were integrated into giant lipid vesicles to promote cargo release via an unprecedented opening procedure.

EXPERIMENTAL SECTION

Synthesis and Characterization of MM1-PC and MM2-PC. *Chemicals.* All chemicals were purchased from commercial sources, by name Sigma-Aldrich, Fluorochem, TCI, and BLDpharm, and used without further purification. Dry solvents were obtained from Acros Organics and Alfa Aesar or from a solvent purification system (MBraun SPS-800).

Synthesis and Procedures. If not stated otherwise, all reactions were carried out in oven-dried glassware under a nitrogen atmosphere by using standard Schlenk techniques. Solids were added in a counter flow of nitrogen or before crimping the vials and cycled three times between vacuum and nitrogen before the addition of liquids. Solutions and reagents were added to nitrogen-flushed disposable syringes/needles. Analytical thin layer chromatography (TLC) was performed on silica gel 60 G/UV265 aluminum sheets from Merck (0.25 mm). Flash column chromatography was performed on a silica gel Davisil LC60A (Merck type 9385, 230−400 mesh) or a Biotage Selekt system (MPLC) using the indicated solvents. NMR spectra were recorded on a Varian Mercury-Plus 400, a Varian Unity Plus 500, or a Bruker 600 MHz NMR spectrometer at 298 K unless stated otherwise. High-resolution mass spectra (HRMS) were recorded on an LTQ Orbitrap XL spectrometer.

In Situ Irradiation Sudies. A solution (2.5 mM) of either **MM1-PC** or **MM2-PC** was prepared in methanol-d_4 and transferred into an NMR tube, which was subsequently fitted with a glass optic fiber for in situ irradiation studies. The sample was placed in a Varian Unity Plus 500 MHz NMR and cooled to −15 °C. ^{1}H NMR spectra were recorded before irradiation while irradiating with 405 nm until reaching PSS and during the THI step until completed.

UV−Vis Spectroscopy. UV−Vis spectroscopy was used for the determination of molecular motor photoisomerization quantum yield determination and thermodynamic studies (see Supporting Information for details). Briefly, samples containing free-standing lipid systems or molecular motor solutions were measured using an Agilent 8453 UV−vis Diode Array System, equipped with a Quantum Northwest Peltier controller. If specified, irradiations were done using a built-in setup coupled to an LED. Solutions were prepared and measured using a quartz cuvette with a 1 cm optical path.

Fluorescence Lifetime Spectroscopy. MicroTime200 (PicoQuant GmBH, Germany), equipped with a dual SPAD detection unit and a MultiHarp 150 TCSPC unit, was used to measure the fluorescence lifetime of A655-DOPE present in the membrane. SUVs were prepared with the desired concentration of the **MM1-PC** and 0.002 mol % A655-DOPE with a final lipid concentration of 2 mM. The SUVs were deposited on a #1.5 coverslip and excited with a 641 nm laser line, and the emission was collected through a 50 μm pinhole. Single photon counting histograms were collected for 180 s for each measurement. SymphoTime64 was used to analyze and fit the decay curves and obtain the fluorescence lifetime for each case.

Cryo-Electron Microscopy. Three μL of SUVs prepared at 2.5 mg/mL were applied on a glow-discharged Quantifoil 1.2/1.3 holey carbon grid, Cu 300 mesh (Quantifoil Micro Tools GmbH, Germany), and blotted for 3.5 s in 100% humidity at 20 °C and immediately plunge-frozen into an ethane-propane 1:1 mixture using the Leica EM GP2 (Leica, Germany). Grids were then loaded into a Titan Krios G4 transmission electron microscope operated at 300 kV, equipped with a Falcon4i direct detector camera, Selectris X energy filter, and CFEG electron source (ThermoFisher Scientific, USA).

Small Unilamellar Vesicles (SUVs) Preparation. 1-palmitoyl-2-oleoyl-*sn*-glycero-3-phosphocholine (POPC) purchased from Avanti Polar Lipids (Alabaster, USA) was used as the single phospholipid composition. For SUV preparation, the desired lipids and photoactive molecules were combined in chloroform at the specified molar ratio. The resulting mixture was transferred to a glass vial, and the solvent was removed using a stream of N_2 gas, followed by vacuum drying in a desiccator to ensure complete removal of residual solvents. To initiate hydration, Milli-Q water was added to the lipid film, achieving a final lipid concentration of 10 mM. This was followed by vigorous vortexing to create a suspension of multilamellar vesicles. Subsequently, these suspensions were further diluted if necessary (CryoEM samples were diluted to 2.5 mM). To promote vesicle homogenization and size reduction, the samples underwent three freeze−thaw cycles following sonication for 15 min.

Confocal Imaging of GUVs. GUVs were prepared through electroformation with Pt electrodes (see Supporting Information). Spinning disk confocal imaging was performed on a Nikon/Yokogawa CSU-W1 spinning disk confocal microscope using 405, 488, and 641 nm laser lines. The 50 μm pinhole spinning disk was used at 4000 rpm. The sample was illuminated through a Nikon Apo TIRF 60x Oil DIC N2 immersion oil objective, and the images were acquired in pco.edge sCMOS cameras (pco.edge 4.2 LT USB) at 100 ms exposure time. For z-stack imaging, the desired optical sectioning was set to 0.2 μm.

https://doi.org/10.1021/acs.langmuir.4c04173
Langmuir XXXX, XXX, XXX−XXX

Scheme 1. General Scheme for the Final Step Synthesis Step, a Yamaguchi Esterification between the Phospholipid Chain (PC) and the Photoactive Molecular Motor Moiety (MM1 and MM2)[a]

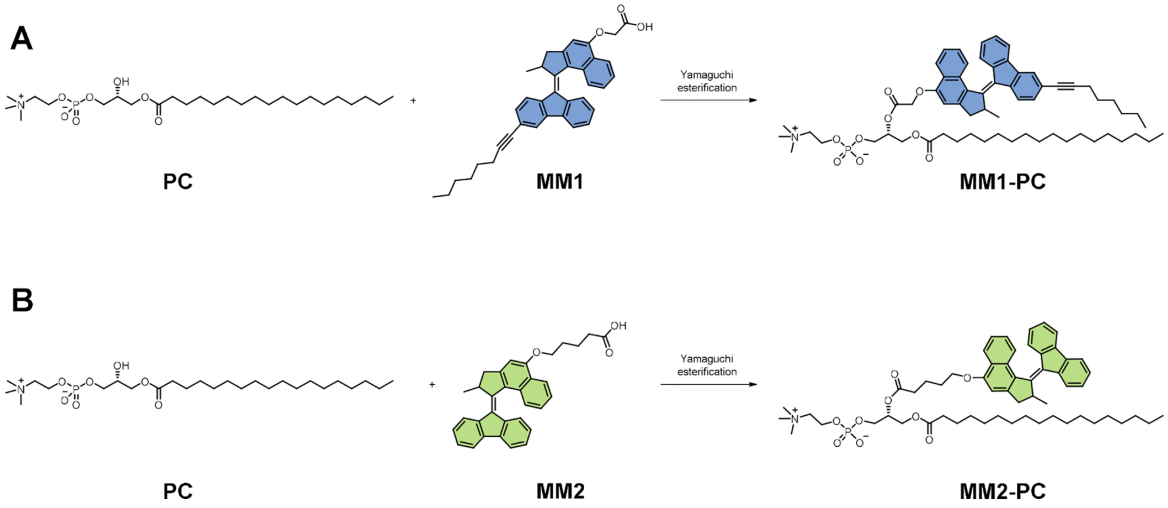

[a](A) For **MM1-PC**. (B) For **MM2-PC**.

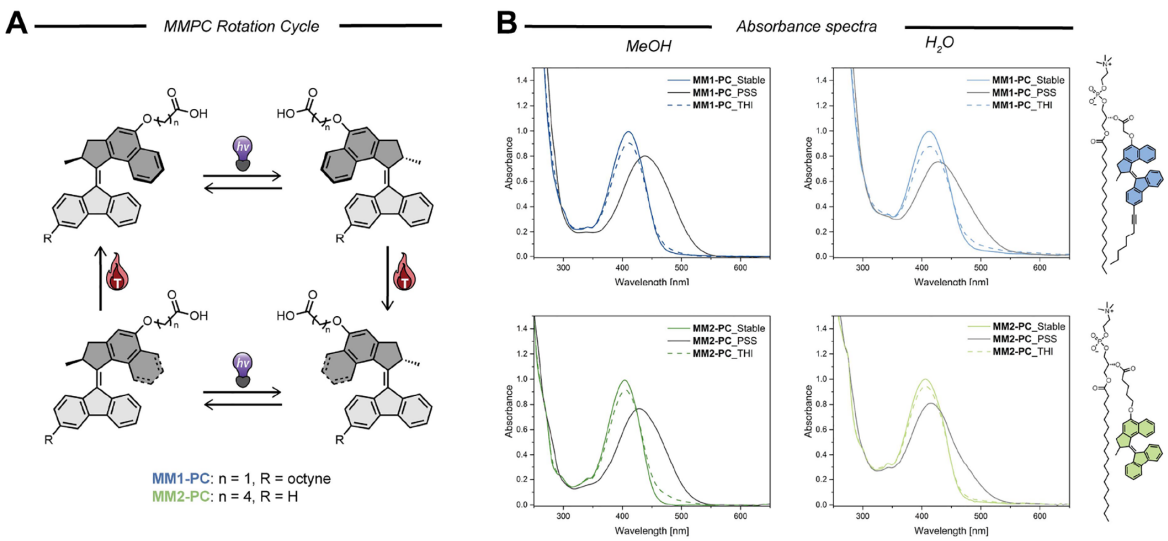

Figure 1. (A) **MMPC** rotation cycle. (B) Absorption spectra of pure **MM1-PC** (top, blue) and **MM2-PC** (bottom, green) in MeOH (left column) or self-assembled in aq solution (right column). Colored lines show the spectra before irradiation with 405 nm light, black lines represent the spectra for each compound after reaching PSS, and dotted colored lines indicate the recovered absorption spectra after THI under dark conditions.

RESULTS AND DISCUSSION

Compound Synthesis. Molecular motors **MM1** and **MM2** were used as building blocks to synthesize the desired molecular motor-modified phospholipids **MM1-PC** and **MM2-PC** using modifications of established procedures (Supporting Information Scheme S1 and ESI for detailed conditions). In short, **1** was synthesized by reacting 1-methoxynaphthalene with methacrylic acid in polyphosphoric acid (PPA) following a Friedel–Crafts acylation mechanism and a Nazarov cyclization.[23] A Williamson ether synthesis was performed on phenolic version **2**, which was obtained by deprotection of **1** with pyridine hydrochloride,[24] followed by ether bond formation using the respective bromoalkylate and potassium carbonate as the base, yielding substituted ketones **3a** and **3b**. Next, **3a**/**3b** were transformed into the respective thioketones **4a**/**4b** using Lawesson's reagent in toluene. To obtain the diazo compounds **6a** and **6b** for the coupling, the corresponding fluorenone derivative was transformed using hydrazine monohydrate to generate hydrazones **5a** and **5b**, and consecutively oxidized with manganese dioxide yielding **6a** and **6b**.[25] With both, the thioketone (**4a**/**4b**) and the diazo (**6a**/**6b**) compound in hand, a Barton-Kellogg coupling reaction was performed, using hexamethylphosphorous triamide as a desulfuration agent, resulting in molecular motors **7a** and **7b**. A

https://doi.org/10.1021/acs.langmuir.4c04173
Langmuir XXXX, XXX, XXX−XXX

Sonogashira cross-coupling between motor **7a**, containing a shorter spacer at the top part than **7b**, and 1-octyne, using *N*,*N*-diisopropylethylamine (DIPEA) as a base, dimethylformamide as a solvent, and CuI and $Pd(PPh_3)Cl_2$ as catalysts, yielded the octyne-substituted motor **8** in an *E*/*Z* mixture. It should be emphasized that triethylamine as a base and tetrahydrofuran (THF) as a solvent at 60 °C did not show any sign of product formation. The last step before the formation of the photoactive phospholipids was a saponification of compounds **7b** and **8** with sodium hydroxide, generating the free acid-containing molecules **MM1** and **MM2** (Scheme 1). The phospholipid precursor, containing a hydrocarbon chain and polar headgroup, was synthesized by reacting (*R*)-2,3-dihydroxypropyl (2-(trimethylammonio)-ethyl) with stearoyl chloride in the presence of dibutyltin oxide and triethylamine, catalyzing a selective reaction at the primary alcohol.[16] The photoactive phospholipids **MM1-PC** and **MM2-PC** were formed via Yamaguchi esterification under the exclusion of light. 2,4,6-Trichlorobenzoyl chloride was employed to form a mixed anhydride with **MM1** or **MM2**, which further reacted with the secondary alcohol moiety of **PC** and 1-methylimidazole as a base to form esters **MM1-PC** and **MM2-PC** (Scheme 1A and 1B, respectively).[16]

Observation of the Rotation Cycle. A schematic representation of the rotation cycle is depicted in Figure 1A. The photochemical properties of **MM1-PC** and **MM2-PC** were investigated by using UV−vis absorption spectroscopy under different conditions. Methanol was used as a reference organic solvent for lipid solutions.[26] Self-assembled samples in aq solution composed of pure **MM-PCs** or in combination with different fractions of POPC were also studied. Measurements were performed on the stable isomers of each compound. All spectra showed broad absorption bands with the maxima corresponding to the double bound isomerization transition ($S_0 \rightarrow S_1$) centered between 404 and 418 nm, tailoring into the visible region (up to 550 nm, colored line Figure 1B). We found that **MM1-PC** is slightly red-shifted compared to **MM2-PC** which can be attributed to the 3-position of the bottom half conjugated octyne moiety to the double bound. This effect is translated into a red-shift of the maximum absorption wavelength of around 5 nm (Table 1).

Table 1. Position of Absorbance Maxima [nm] of the Double Bound Transition for the Stable Isomer of MM1-PC and MM2-PC in Different Environments

compound	MeOH	H_2O	50 mol % inPOPC	25 mol %in POPC	10 mol % in POPC
MM1-PC	410	415	416	417	418
MM2-PC	404	409	411	412	412

Interestingly, all compounds showed a slight bathochromic shift for the self-assembled systems. Changes in the absorption spectra of a molecule when going from solution to a self-assembled state typically indicate variations in its structural organization and intramolecular interactions.[27] This effect is more pronounced for the self-assembled systems in conjugation with POPC molecules and seems to increase with the amount of POPC present in the assembly (Table 1, Figure S4). A similar effect has been previously described for azobenzene-modified phospholipids and is attributed to the formation of H/J-aggregates.[16,28] These molecules tend to organize by forming small aggregates in the lipid bilayer, favoring face-to-face noncovalent $\pi-\pi$ interactions.

Irradiation of the stable isomer of **MM1-PC** and **MM2-PC** with a 405 nm LED at 20 °C produced a change in the absorption spectra with a clear isosbestic point (dark line in Figures 1, S5, and S6). The resulting steady-state spectrum corresponds to the partial formation of the metastable isomer at the photostationary state (PSS). In accordance with previously reported second-generation molecular motors with five-membered upper and lower halves, the metastable form of **MM1-PC** and **MM2-PC** is significantly red-shifted compared to the stable isomer.[20] This is attributed to a decrease in the HOMO−LUMO gap of the metastable form based on earlier computational calculations in similar molecular motor structures.[29,30]

A detailed analysis of the rotation cycle of **MM1-PC** and **MM2-PC** was performed using low-temperature ^{1}H NMR spectroscopy (Figures 2 and S1−S3). Irradiations were carried out in situ directly in the NMR probe, using a glass fiber optic cable connected to a 405 nm LED at −15 °C in MeOD, for solubility reasons. For both compounds, constant irradiation of the stable isomer led to a decrease in the peak intensity of the protons corresponding to the stable state isomer, and a new set of signals appeared at the same rate, which were assigned to the metastable isomer, showing a selective isomerization profile (Figure 2). After 30 min of constant irradiation at 405 nm, a photostationary state was reached with a stable-to-metastable isomer ratio of 51:49 and 22:78 for **MM1-PC** and **MM2-PC**, respectively. Removing the light source led to a complete recovery of the stable state signals after overnight in the dark.

Analysis of the Photoisomerization Behavior and Thermodynamic Parameters. The quantum yield of the photoisomerization was also determined in all the previously studied systems (MeOH, H_2O, and in conjugation with POPC molecules) using the method outlined by Stranius and Börjesson[31] which follows the evolution of both components of the photostationary distribution (PSD) when irradiated at a known concentration. This method has been extensively used for molecular motors to determine their quantum yields of photoisomerization.[32,33] To assess the photochemically driven isomerization of **MM1-PC** and **MM2-PC**, we subjected each sample to irradiation with a 405 nm LED and monitored the changes in the absorption spectra at the irradiation wavelength until the PSS was reached. For **MM1-PC** and **MM2-PC**, this process corresponded to quantum yields of 3.2 ± 0.19 and 5.81 ± 0.12%, respectively.

When the same measurements were carried out in self-assembled systems, a drop in the quantum yield value was expected, as seen in previous studies of molecular motors embedded into crowded lipid environments, hindering the photoisomerization process.[34] Indeed, both **MM1-PC** and **MM2-PC** showed a sequential decrease in their quantum yield values with increasing concentrations of the molecules in POPC self-assembled systems (Table S1). Interestingly, the pure system in water showed the lowest quantum yield value for **MM1-PC** but just a small decrease for **MM2-PC** (Table S1). We envision that these results might be related to different self-assembled structures for the two compounds in water.

Eyring analysis of the studied compounds was performed to determine the activation parameters of the thermal isomerization step corresponding to the metastable to the stable transition of **MM1-PC** and **MM2-PC**. The rate of the THI step was determined by following the decay in the absorbance

https://doi.org/10.1021/acs.langmuir.4c04173
Langmuir XXXX, XXX, XXX−XXX

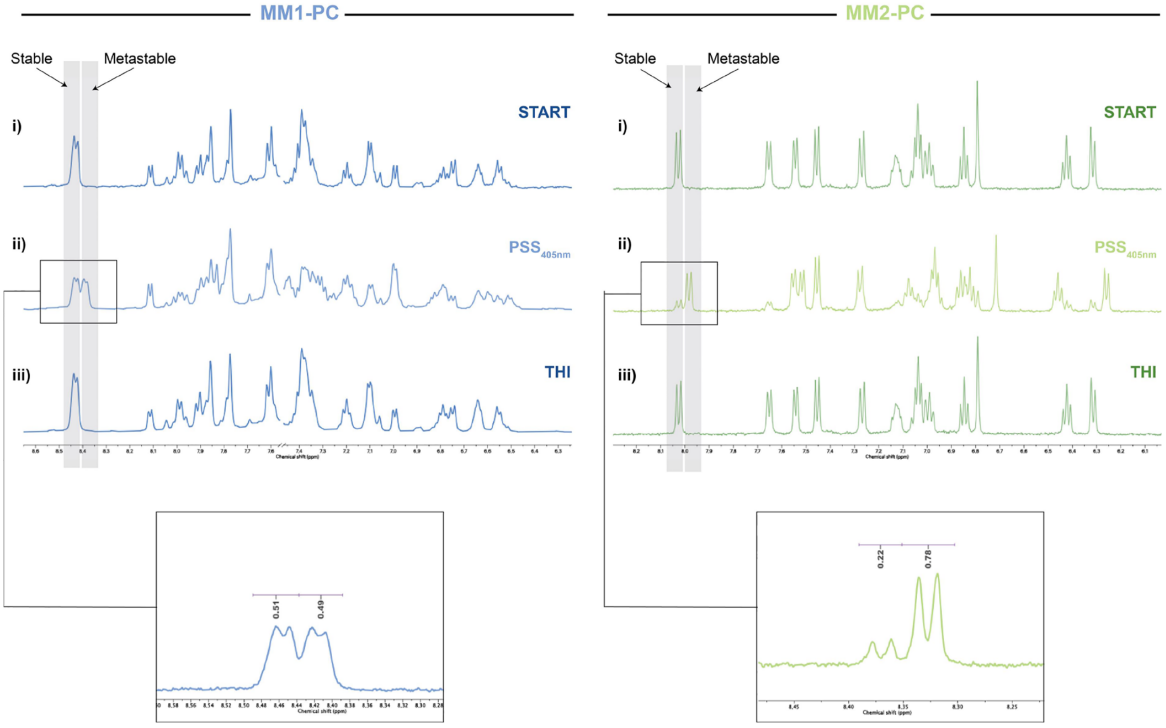

Figure 2. ^{1}H NMR irradiation studies (methanol-d_4, c = 2.5 mM, 15 °C) of **MM1-PC** (left) and **MM2-PC** (right). Starting from its stable form (i), spectra change under 405 nm irradiation in situ irradiation of the stable isomer until reaching PSS (ii) and after undergoing THI under dark conditions (iii). The inset corresponds to the stable/metastable distribution at PSS.

at 450 nm. The exponential decay was followed at three different temperatures (15, 20, and 25 °C) in all MeOH, H_2O, and lipid solutions. To calculate the activation parameters of the thermal barrier, the rate constants of the exponential decay function are obtained for each temperature and fitted using the linearized Eyring equation (Table S3, Figures S8 and S9). The calculated experimental barriers of both **MM1**- and **MM2-PC** were found to increase when going from a solution in methanol to the self-assembled structures in water (ESI Table S2). This effect was more pronounced with increasing concentrations of the motor compounds in POPC self-assemblies in water, reaching its maxima with the pure compound in water for **MM1-PC** ($t_{1/2}$ of 192 and 528 s in MeOH and H_2O, respectively). Interestingly, a similar behavior was found for increasing concentrations of **MM2-PC** in conjugation with POPC; however, the compound exhibited a sharp decrease of the activation barrier for the pure water condition ($t_{1/2}$ of 162 and 58 s in MeOH and H_2O, respectively). The differences in the half-lives of **MM1**- and **MM2-PC** between the two solvents can be attributed to the formation of more (in the case of **MM2-PC**) or less (in the case of **MM1-PC**) favorable self-assembled structures in water for the THI step.

Fatigue Resistance in Aqueous Environment. As the ultimate application of a lipid molecular motor requires their functioning in an aqueous environment, further studies were carried out under these conditions. First, the stability of the nonirradiated compounds in water was assessed during 1 week using UV−vis spectroscopy, and no sign of degradation was observed (Figure S7). However, upon prolonged 405 nm irradiation, apparent degradation by a general decrease in absorption over the whole spectrum was observed for both **MM1**- and **MM2-PC** in pure water. Fatigue studies of sequential PSS/THI processes over 5 cycles show a decrease in the 405 nm absorbance of around 5% for **MM1-PC** and 2.5% for **MM2-PC** after each cycle (Figure 3, left). This degradation has been reported in the past for water-soluble molecular motors and is attributed to a twisted and polarized conformation of the central double bound of the photogenerated intermediate which makes it more vulnerable to water addition.[34] Interestingly, in all cases, the unstable isomer thermally isomerizes back to the stable form in a clean process if the irradiation is halted. This phenomenon has also been reported for other compounds such as dihydroquinolines.[35] Remarkably, we could solve the issue of reduced stability (fatigue) in water by combining the vulnerable molecules within lipid environments due to some kind of hydrophobic shielding effect.[36] We were pleased to observe that the incorporation of 25 mol % of **MM1-PC** and **MM2-PC** in POPC systems retained the stability of the compounds under illumination (Figure 3, right), and fatigue resistance studies over 5 cycles show a major increase in the retention of the absorbance spectra at 405 nm irradiation. These results indicate the improved performance of the molecules in conjugation with phospholipid environments, and these combinations were used for the subsequent studies (vide infra).

Self-Assembly and Incorporation into GUVs. The ability of **MM1-PC** and **MM2-PC** to self-assemble in water was investigated by determining their critical aggregation

https://doi.org/10.1021/acs.langmuir.4c04173
Langmuir XXXX, XXX, XXX−XXX

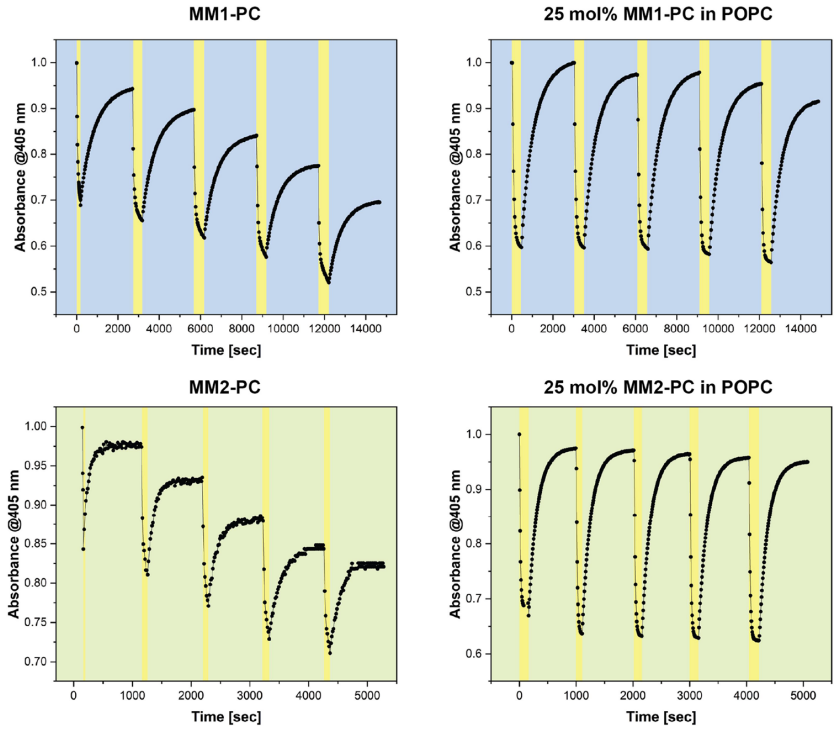

Figure 3. Changes in the absorbance for fatigue studies of **MM1-PC** and **MM2-PC** over the course of five successive PSS/THI processes under 405 nm irradiation.

concentration (CAC) using a Nile Red fluorescence assay (see ESI for details). The results revealed CAC values of 24.4 and 0.78 μM for **MM1-PC** and **MM2-PC**, respectively, before irradiation of the samples. Interestingly, after 1 min of irradiation with a 405 nm LED, the CAC value decreased more than 3-fold for **MM1-PC** (7.56 μM) and slightly for **MM2-PC** (0.58 μM) (Table S4, Figure S12). SUVs of 50 mol % of **MM1-PC** together with POPC were prepared and imaged using cryo-electron microscopy (see Supporting Information for details). The images were classified and averaged to evaluate their membrane before and after illumination with 405 nm light (see Figure S11). No significant changes were observed in the membrane thickness.

Next, we examined the incorporation of **MM1-PC** and **MM2-PC** to GUVs (~20 μm in diameter) composed of different ratios of **MM1-PC** and **MM2-PC**, POPC, and 1 mol % of Atto655-DOPE (for fluorescent imaging). To prepare the GUVs for experimentation, we employed the electroformation method (see ESI for details). Image acquisition was performed using spinning disk confocal microscopy, which allows for rapid acquisition via acquiring thin optical sections and illumination of the whole sample volume. As soon as the imaging started, we noticed a decrease in the expected fluorescent intensity (sample of only POPC with 1 mol % Atto655-DOPE). Examining the literature for similar compounds based on azobenzene-modified lipids, we found that these compounds are well-known dark quenchers for certain fluorophores.[37] In the case of azobenzene photoswitches and in our **MMPCs,** a photochemical isomerization at the central double bound is the preferred pathway to deactivate the electronic excited state back to the ground state in a nonradiative manner. Consequently, these molecules are usually weakly fluorescent or nonfluorescent compounds. Thus, in specific molecular systems where these systems are in close proximity to molecular dyes with certain characteristics, an effective Förster resonance energy transfer (FRET) can occur.[38] In this scenario, **MM1-PC** and **MM2-PC** can act as acceptors, dissipating energy through nonradiative pathways. As a consequence, the fluorescent donor, Atto655-DOPE in our case, is turned off as long as the FRET process occurs. In a FRET event, energy transfer from the excited donor to the acceptor takes place, leading to the quenching of the donor's fluorescence. Consequently, the fluorescence lifetime, defined as the average time a molecule remains in its excited state before emitting a photon, would decrease. This is because the added FRET acceptor provides an additional nonradiative pathway for the excited state of the donor to relax, accelerating the overall decay process. We observed a significant reduction in the fluorescence lifetime of A655-DOPE with increasing concentrations of **MM1-PC** in lipid membranes (see Figure S10). Interestingly, when we started irradiating with 405 nm light, a slow but significant increase of the fluorescence could be observed. In the case of photoswitchable lipids based on azobenzene, it is well documented how the quenching of the fluorophores is significantly stronger for the *cis* isomer compared to the *trans* one.[39,40] In our scenario, the molecular motor keeps a continuous unidirectional rotation between the different states, which most likely uninterruptedly remodels the phospholipid distribution inside the membrane. Based on this observation, we decided to form GUVs with **MM1-PC** and study them under optical microscopy. We observed that the fluorescence intensity of the membrane dye slowly increases

https://doi.org/10.1021/acs.langmuir.4c04173
Langmuir XXXX, XXX, XXX−XXX

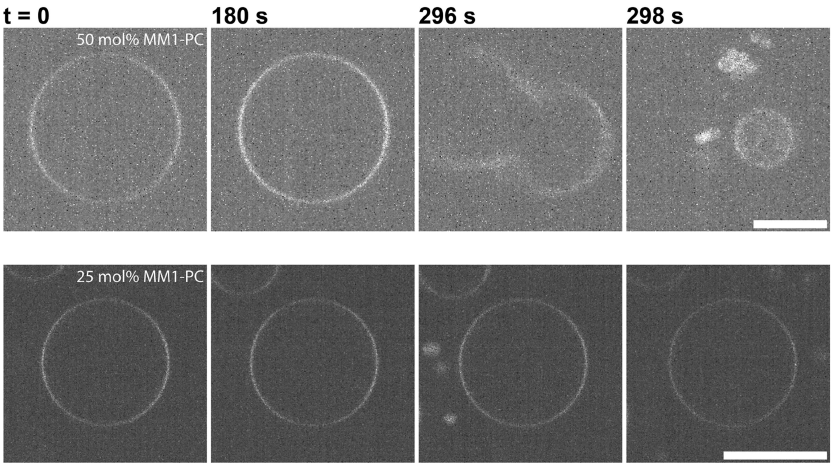

Figure 4. (top) Explosion of GUVs composed of POPC:**MM1-PC** (1:1) upon irradiation with 405 nm laser. (bottom) GUVs composed of POPC:**MM1-PC** (3:1) upon irradiation with 405 nm laser do not show any explosion. Scale bar: 10 μm.

upon irradiation under 405 nm. Following an increase in fluorescence intensity, vesicles do explode and fragment into smaller daughter vesicles (see Figure 4). The absence of membrane fluctuations rules out the possibility of over extension of the membrane due to area expansion. Such light-triggered vesicle explosions have been previously reported[41,42] where the generation of ROS increased the osmotic pressure inside the vesicle resulting in membrane rupture. As reported in previous sections, we propose that the degradation of **MM1-PC** upon irradiation results in the generation of ROS (hydroxyl radicals), which could interact with sucrose present inside the vesicles. It has been shown that sucrose can act as a hydroxyl radical scavenger,[43] where the radical attacks at the glucose moiety creating a scission at the glycosidic bond resulting in a fructose and a glucose radical. This would effectively increase the osmolarity in the lumen of the membrane. Degradation of the **MM1-PC** can be slowed down with a lower concentration of **MM1-PC** incorporated in the membrane, as has been shown by fatigue resistance studies (see Figure 3). However, the light-triggered vesicle explosions observed in our study present a unique mechanism distinct from those of previously reported processes involving ROS generation. While ROS production, such as the generation of hydroxyl radicals during the partial degradation of **MM1-PC**, plays a role, our findings suggest that the explosion mechanism involves a combination of ROS and mechanical effects. Lipid vesicle explosions driven by commonly reported photosensitizers such as chlorin e6 or methylene blue occur in a notably different sequence of morphological changes.[44,45] Photosensitizer-induced photodynamic damage typically involves distinct phases, including violent membrane fluctuations caused by lipid oxidation, surface area expansion, and repetitive swell-burst cycles.[46,47] In contrast, the gradual process in our study lacks such a behavior.

Given the extensive knowledge acquired over the past decades regarding the control of molecular motor rotation dynamics and parameters, we suggest that unprecedented control over the release from lipid systems can be achieved using similar molecules. This would offer a unique ability to design GUVs composed of homogeneous lipid systems, which could be triggered on demand to explode and release their contents without changing the headgroup composition of the membrane and without the need for light-sensitive molecules to be present inside the lumen. At lower ratios of **MM1-PC** in the membrane (see Figure 4 (bottom)), we do not observe vesicle explosion, which indicates a combination effect of ROS production and the mechanical effect of the motors. Studies with Langmuir monolayers would be essential to accurately estimate the mechanical effect of **MM1-PC** in the future.[48]

It is important to clarify that the conformational change observed after switching off the irradiation source is primarily attributed to a THI rather than an *E-Z* thermal back isomerization. While both processes are theoretically possible, the THI is the most likely dominant mechanism in our case. This is due to the significantly lower energy barrier for helix inversion compared to that required for *E-Z* isomerization, which is typically considered a nonreversible process. These energies and preferred isomerization pathways unequivocally demonstrate the rotatory process that has been extensively studied previously in the parent motors **MM1** and **MM2**, and substituted analogs prove the unidirectionality of the rotation cycle. This suggests that their underlying mechanism remains unaffected after the incorporation of an acyl chain. In contrast, if the molecules were to undergo back isomerization instead of the expected four-step rotation cycle, the resulting molecules would reassemble photoswitchable lipids, which are known to induce dramatic changes in the conformation of GUVs. However, our experiments show a distinct behavior for GUVs in the presence of **MM1-PC** and **MM2-PC**, similar to previously reported unidirectional molecular motors in lipid membranes,[34] which we attribute to the continuous four-step rotation cycle of the motors, producing gradual conformational changes across all states, rather than switching between two well-defined states. Thus, while we cannot provide direct proof of the THI, the available evidence and ample precedence in related substituted second-generation motors strongly support its role as the predominant process in these systems.

CONCLUSIONS

In this study, we report the first two photoswitchable lipids based on molecular rotary motors. The synthesis and characterization of two molecular motor-modified phospholi-

https://doi.org/10.1021/acs.langmuir.4c04173
Langmuir XXXX, XXX, XXX−XXX

pids (**MM1-PC** and **MM2-PC**) are described, and the analysis of their light-driven rotation cycle in solution and aqueous self-assembled environments is provided by means of UV−vis and low-temperature NMR spectroscopy. We observe a decrease in their photoisomerization quantum yield in self-assembled systems, which we attribute to the constraints of a more restricted environment. The thermodynamic parameters and activation energy profiles of **MM1-PC** and **MM2-PC** suggest distinct structural arrangements in aqueous solutions. We further explored their self-assembly behavior, measuring the CAC, which notably decreased upon irradiation. Fatigue resistance studies under aqueous conditions revealed the susceptibility of both molecules to degradation under prolonged irradiation, which is a common limitation for water-soluble molecular motors. However, embedding these motors within lipid environments significantly enhanced their stability and fatigue resistance, underscoring the protective role of the phospholipid assemblies. These findings point to **MMPCs** combined with phospholipid vesicles as promising candidates for biological applications. A key distinction observed in this study lies in the behavior of GUVs in the presence of these molecules, which contrasts with the behavior of traditional photoswitchable lipids. Specifically, the incorporation of **MM1-PC** triggered a light-induced increase in membrane fluorescence, followed by vesicle fragmentation. This phenomenon is attributed to the unique four-step rotary cycle of **MM1-PC** under illumination, resulting in sustained conformational changes, as opposed to a binary switching mechanism, combined with the generation of reactive oxygen species. This interplay between molecular motor activity and membrane integrity highlights the importance of the active compound's concentration in dictating system behavior.

In summary, this proof-of-concept study introduces the first photoswitchable lipids integrating molecular rotary motors and demonstrates their functionality within lipid systems. These findings open avenues for diverse applications in biomedical, biochemical, and synthetic cell research, paving the way for future advancements in light-responsive lipid systems.

■ ASSOCIATED CONTENT

Supporting Information

The Supporting Information is available free of charge at https://pubs.acs.org/doi/10.1021/acs.langmuir.4c04173.

Additional information on the synthetic procedures, materials, methods, and supporting data (PDF)

■ AUTHOR INFORMATION

Corresponding Authors

Petra Schwille − *Cellular and Molecular Biophysics, Max Planck Institute of Biochemistry, 82152 Martinsried, Germany*; orcid.org/0000-0002-6106-4847; Email: schwille@biochem.mpg.de

Ben L. Feringa − *Stratingh Institute for Chemistry, University of Groningen, 9747AG Groningen, The Netherlands*; orcid.org/0000-0003-0588-8435; Email: b.l.feringa@rug.nl

Authors

Ainoa Guinart − *Stratingh Institute for Chemistry, University of Groningen, 9747AG Groningen, The Netherlands*

Daniel Doellerer − *Stratingh Institute for Chemistry, University of Groningen, 9747AG Groningen, The Netherlands*

Yusuf Qutbuddin − *Cellular and Molecular Biophysics, Max Planck Institute of Biochemistry, 82152 Martinsried, Germany*; orcid.org/0000-0003-0054-0608

Henry Zivkovic − *Cellular and Molecular Biophysics, Max Planck Institute of Biochemistry, 82152 Martinsried, Germany*

Cristina Branca − *Stratingh Institute for Chemistry, University of Groningen, 9747AG Groningen, The Netherlands*; orcid.org/0009-0007-8495-4774

Dominik Hrebik − *Cell and Virus Structure, Max Planck Institute of Biochemistry, 82152 Martinsried, Germany*

Complete contact information is available at: https://pubs.acs.org/10.1021/acs.langmuir.4c04173

Author Contributions

‖A.G. and D.D. contributed equally to this work.

Notes

The authors declare no competing financial interest.

■ ACKNOWLEDGMENTS

A.G. and Y.Q. received funding from the European Union's Horizon 2020 research and innovation program under the Marie Skłodowska-Curie grant agreement no. 859416. Cryo-electron microscopy was performed in the Department of Cell and Virus Structure at the Max Planck Society. We thank John A.G. Briggs for support and discussion. We gratefully acknowledge financial support from the Ministry of Education, Culture and Science of The Netherlands (Bonus Incentive Scheme and Gravitation Program No. 024.001.035 to B.L.F) and the Zernike Institute for Advanced Materials at the University of Groningen. Y.Q. acknowledges support from the International Max Planck Research School for Molecules of Life (IMPRS-ML). P.S. acknowledges support from the Center for NanoScience (CeNS).

■ REFERENCES

(1) Van Meer, G.; Voelker, D. R.; Feigenson, G. W. Membrane Lipids: Where They Are and How They Behave. *Nat. Rev. Mol. Cell Biol.* **2008**, *9* (2), 112.

(2) Quinn, P. J.; Chapman, D.; Keith, A. D. The Dynamics of Membrane Structure. *CRC Crit Rev. Biochem* **1980**, *8* (1), 1−117.

(3) Ladbrooke, B. D.; Chapman, D. Thermal Analysis of Lipids, Proteins and Biological Membranes. A Review and Summary of Some Recent Studies. *Chem. Phys. Lipids* **1969**, *3* (4), 304−356.

(4) Urban, P.; Pritzl, S. D.; Ober, M. F.; Dirscherl, C. F.; Pernpeintner, C.; Konrad, D. B.; Frank, J. A.; Trauner, D.; Nickel, B.; Lohmueller, T. A Lipid Photoswitch Controls Fluidity in Supported Bilayer Membranes. *Langmuir* **2020**, *36* (10), 2629−2634.

(5) Aleksanyan, M.; Grafmüller, A.; Crea, F.; Georgiev, V. N.; Yandrapalli, N.; Block, S.; Heberle, J.; Dimova, R. Photomanipulation of Minimal Synthetic Cells: Area Increase, Softening, and Interleaflet Coupling of Membrane Models Doped with Azobenzene-Lipid Photoswitches. *Adv. Sci.* **2023**, *10* (31), No. 2304336.

(6) Doroudgar, M.; Morstein, J.; Becker-Baldus, J.; Trauner, D.; Glaubitz, C. How Photoswitchable Lipids Affect the Order and Dynamics of Lipid Bilayers and Embedded Proteins. *J. Am. Chem. Soc.* **2021**, *143* (25), 9515−9528.

(7) Frank, J. A.; Franquelim, H. G.; Schwille, P.; Trauner, D. Optical Control of Lipid Rafts with Photoswitchable Ceramides. *J. Am. Chem. Soc.* **2016**, *138* (39), 12981−12986.

https://doi.org/10.1021/acs.langmuir.4c04173
Langmuir XXXX, XXX, XXX−XXX

(8) Catalá, A. Lipid Peroxidation of Membrane Phospholipids Generates Hydroxy-Alkenals and Oxidized Phospholipids Active in Physiological and/or Pathological Conditions. *Chem. Phys. Lipids* **2009**, *157* (1), 1−11.
(9) Morgan, C. G.; Thomas, E. W.; Yianni, Y. P.; Sandhu, S. S. Incorporation of a Novel Photochromic Phospholipid Molecule into Vesicles of Dipalmitoylphosphatidylcholine. *Biochim Biophys Acta - Biomembr* **1985**, *820* (1), 107−114.
(10) Sandhu, S. S.; Yianni, Y. P.; Morgan, C. G.; Taylor, D. M.; Zaba, B. The Formation and Langmuir-Blodgett Deposition of Monolayers of Novel Photochromic Azobenzene-Containing Phospholipid Molecules. *Biochim Biophys Acta - Biomembr* **1986**, *860* (2), 253−262.
(11) Morgan, C. G.; Yianni, Y. P.; Sandhu, S. S.; Mitchell, A. C. LIPOSOME FUSION AND LIPID EXCHANGE ON ULTRAVIOLET IRRADIATION OF LIPOSOMES CONTAINING A PHOTOCHROMIC PHOSPHOLIPID. *Photochem. Photobiol.* **1995**, *62* (1), 24−29.
(12) Pfeffermann, J.; Eicher, B.; Boytsov, D.; Hannesschlaeger, C.; Galimzyanov, T. R.; Glasnov, T. N.; Pabst, G.; Akimov, S. A.; Pohl, P. Photoswitching of Model Ion Channels in Lipid Bilayers. *J. Photochem. Photobiol. B* **2021**, *224*, No. 112320.
(13) Georgiev, V. N.; Grafmüller, A.; Bléger, D.; Hecht, S.; Kunstmann, S.; Barbirz, S.; Lipowsky, R.; Dimova, R.; Georgiev, V. N.; Grafmüller, A.; Kunstmann, S.; Lipowsky, R.; Dimova, R.; Bléger, D.; Hecht, S.; Barbirz, S. Area Increase and Budding in Giant Vesicles Triggered by Light: Behind the Scene. *Adv. Sci.* **2018**, *5* (8), No. 1800432.
(14) Pernpeintner, C.; Frank, J. A.; Urban, P.; Roeske, C. R.; Pritzl, S. D.; Trauner, D.; Lohmüller, T. Light-Controlled Membrane Mechanics and Shape Transitions of Photoswitchable Lipid Vesicles. *Langmuir* **2017**, *33* (16), 4083−4089.
(15) Albanese, P.; Cataldini, S.; Ren, C. Z. J.; Valletti, N.; Brunetti, J.; Chen, J. L. Y.; Rossi, F. Light-Switchable Membrane Permeability in Giant Unilamellar Vesicles. *Pharmaceutics* **2022**, *14* (12), 2777.
(16) Urban, P.; Pritzl, S. D.; Konrad, D. B.; Frank, J. A.; Pernpeintner, C.; Roeske, C. R.; Trauner, D.; Lohmüller, T. Light-Controlled Lipid Interaction and Membrane Organization in Photolipid Bilayer Vesicles. *Langmuir* **2018**, *34* (44), 13368−13374.
(17) Pritzl, S. D.; Urban, P.; Prasselsperger, A.; Konrad, D. B.; Frank, J. A.; Trauner, D.; Lohmüller, T. Photolipid Bilayer Permeability Is Controlled by Transient Pore Formation. *Langmuir* **2020**, *36* (45), 13509−13515.
(18) Socrier, L.; Ahadi, S.; Bosse, M.; Montag, C.; Werz, D. B.; Steinem, C. Optical Manipulation of Gb3 Enriched Lipid Domains: Impact of Isomerization on Gb3-Shiga Toxin B Interaction. *Chem.—Eur. J.* **2023**, *29* (4), No. e202202766.
(19) Hartrampf, N.; Leitao, S. M.; Winter, N.; Toombs-Ruane, H.; Frank, J. A.; Schwille, P.; Trauner, D.; Franquelim, H. G. Structural Diversity of Photoswitchable Sphingolipids for Optodynamic Control of Lipid Microdomains. *Biophys. J.* **2023**, *122* (11), 2325−2341.
(20) Pooler, D. R. S.; Lubbe, A. S.; Crespi, S.; Feringa, B. L. Designing Light-Driven Rotary Molecular Motors. *Chem. Sci.* **2021**, *12* (45), 14964−14986.
(21) Koumura, N.; Zijistra, R. W. J.; Van Delden, R. A.; Harada, N.; Feringa, B. L. Light-Driven Monodirectional Molecular Rotor. *Nature* **1999**, *401* (6749), 152−155.
(22) Dean Astumian, R.; Kay, E. R.; Leigh, D. A.; Zerbetto, F. Design Principles for Brownian Molecular Machines: How to Swim in Molasses and Walk in a Hurricane. *Phys. Chem. Chem. Phys.* **2007**, *9* (37), 5067−5083.
(23) Pfeifer, L.; Scherübl, M.; Fellert, M.; Danowski, W.; Cheng, J.; Pol, J.; Feringa, B. L. Photoefficient 2nd Generation Molecular Motors Responsive to Visible Light. *Chem. Sci.* **2019**, *10* (38), 8768−8773.
(24) Pfeifer, L.; Hoang, N. V.; Scherübl, M.; Pshenichnikov, M. S.; Feringa, B. L. Powering Rotary Molecular Motors with Low-Intensity near-Infrared Light. *Sci. Adv.* **2020**, *6* (44), No. eabb6165.
(25) Pfeifer, L.; Hoang, N. V.; Crespi, S.; Pshenichnikov, M. S.; Feringa, B. L. Dual-Function Artificial Molecular Motors Performing Rotation and Photoluminescence. *Sci. Adv.* **2022**, *8* (44), 410.
(26) Dervichian, D. G. The Physical Chemistry of Phospholipids. *Prog. Biophys. Mol. Biol.* **1964**, *14* (C), 263.
(27) Koenig, J. F.; Martel, D. Applying UV−Vis Spectroscopy to Step-by-Step Molecular Self Assembly on Surface: Does It Bring Pertinent Information? *Thin Solid Films* **2008**, *516* (12), 3865−3872.
(28) Song, X.; Perlstein, J.; Whitten, D. G. Supramolecular Aggregates of Azobenzene Phospholipids and Related Compounds in Bilayer Assemblies and Other Microheterogeneous Media: Structure, Properties, and Photoreactivity. *J. Am. Chem. Soc.* **1997**, *119* (39), 9144−9159.
(29) Guinart, A.; Doellerer, D.; Pooler, D. R. S.; de Boer, J. Y.; Doria, S.; Bussotti, L.; Di Donato, M.; Feringa, B. L. Two-Photon Absorption of Oxindole-Based Push−Pull Molecular Motors. *J. Photochem. Photobiol. A Chem.* **2024**, *453*, No. 115649.
(30) Pooler, D. R. S.; Doellerer, D.; Crespi, S.; Feringa, B. L. Controlling Rotary Motion of Molecular Motors Based on Oxindole. *Org. Chem. Front* **2022**, *9* (8), 2084−2092.
(31) Stranius, K.; Börjesson, K. Determining the Photoisomerization Quantum Yield of Photoswitchable Molecules in Solution and in the Solid State. *Sci. Rep.* **2017**, *7* (1), 41145.
(32) Regen-Pregizer, B. L.; Ozcelik, A.; Mayer, P.; Hampel, F.; Dube, H. A Photochemical Method to Evidence Directional Molecular Motions. *Nat. Commun.* **2023**, *14* (1), 4595.
(33) Wang, J.; Durbeej, B. Molecular Motors with High Quantum Efficiency and Visible-Light Responsiveness: Meeting Two Challenges in One Design. *Comput. Theor Chem.* **2019**, *1148*, 27−32.
(34) Qutbuddin, Y.; Guinart, A.; Gavrilović, G.; Al Nahas, K.; Feringa, B. L.; Schwille, P.; Qutbuddin, Y.; Gavrilović, S. G.; Al Nahas, K.; Schwille, P.; Guinart, A.; Feringa, B. L. Light-Activated Synthetic Rotary Motors in Lipid Membranes Induce Shape Changes Through Membrane Expansion. *Adv. Mater.* **2024**, *36* (16), No. 2311176.
(35) Nekipelova, T. D.; Shishkov, V. S.; Kuzmin, V. A. Mechanism of Photoinduced Addition of Water and Methanol to the Double Bond of 1,2-Dihydroquinolines. *High Energy Chem.* **2002**, *36* (3), 183−189.
(36) Lubbe, A. S. *Molecular Motors in New Media*, 2017.
(37) Pritzl, S. D.; Morstein, J.; Kahler, S.; Konrad, D. B.; Trauner, D.; Lohmüller, T. Postsynthetic Photocontrol of Giant Liposomes via Fusion-Based Photolipid Doping. *Langmuir* **2022**, *38* (39), 11941−11949.
(38) Chevalier, A.; Renard, P. Y.; Romieu, A. Azo-Based Fluorogenic Probes for Biosensing and Bioimaging: Recent Advances and Upcoming Challenges. *Chem. Asian J.* **2017**, *12* (16), 2008−2028.
(39) Harbron, E. J.; Vicente, D. A.; Hoyt, M. T. Fluorescence Modulation via Isomer-Dependent Energy Transfer in an Azobenzene-Functionalized Poly(Phenylenevinylene) Derivative. *J. Phys. Chem. B* **2004**, *108* (49), 18789−18792.
(40) Harbron, E. J. Fluorescence Intensity Modulation in Photochromic Conjugated Polymer Systems. *Isr J. Chem.* **2013**, *53* (5), 256−266.
(41) Peyret, A.; Ibarboure, E.; Tron, A.; Beauté, L.; Rust, R.; Sandre, O.; McClenaghan, N. D.; Lecommandoux, S. Polymersome Popping by Light-Induced Osmotic Shock under Temporal, Spatial, and Spectral Control. *Angew. Chem. Int. Ed* **2017**, *56* (6), 1566−1570.
(42) Malik, V. K.; Shin, S.; Feng, J. Light-Triggered Explosion of Lipid Vesicles. *Soft Matter* **2020**, *16* (38), 8904−8911.
(43) Peshev, D.; Vergauwen, R.; Moglia, A.; Hideg, É.; Van Den Ende, W. Towards Understanding Vacuolar Antioxidant Mechanisms: A Role for Fructans? *J. Exp Bot* **2013**, *64* (4), 1025−1038.
(44) Caetano, W.; Haddad, P. S.; Itri, R.; Severino, D.; Vieira, V. C.; Baptista, M. S.; Schröder, A. P.; Marques, C. M. Photo-Induced Destruction of Giant Vesicles in Methylene Blue Solutions. *Langmuir* **2007**, *23* (3), 1307−1314.
(45) Mertins, O.; Bacellar, I. O. L.; Thalmann, F.; Marques, C. M.; Baptista, M. S.; Itri, R. Physical Damage on Giant Vesicles Membrane

https://doi.org/10.1021/acs.langmuir.4c04173
Langmuir XXXX, XXX, XXX−XXX

as a Result of Methylene Blue Photoirradiation. *Biophys. J.* **2014**, *106* (1), 162−171.
(46) Bour, A.; Kruglik, S. G.; Chabanon, M.; Rangamani, P.; Puff, N.; Bonneau, S. Lipid Unsaturation Properties Govern the Sensitivity of Membranes to Photoinduced Oxidative Stress. *Biophys. J.* **2019**, *116* (5), 910−920.
(47) Heuvingh, J.; Bonneau, S. Asymmetric Oxidation of Giant Vesicles Triggers Curvature-Associated Shape Transition and Permeabilization. *Biophys. J.* **2009**, *97* (11), 2904−2912.
(48) Schiel, P.; Maaloum, M.; Moulin, E.; Nyrkova, I.; Semenov, A.; Dattler, D.; Accou, L.-A.; Christoulaki, A.; Buhler, E.; Lehn, J.-M.; Giuseppone, N. Supramolecular Polymerization Induced by the Rotation of Light-Driven Molecular Motors. *BioRxiv* **2024**.

https://doi.org/10.1021/acs.langmuir.4c04173
Langmuir XXXX, XXX, XXX−XXX

7
Assembling DNA origami on lipid membranes

In the past, DNA origami was used as cargo molecules with controllable membrane footprint, to decipher how a self-organizing protein system positions cargo molecules. [227] The high functionalizability and the equally high ease of designing, formulating and purifying DNA origami have made them an attractive tool for studying complex biochemical processes. This naturally instigates development of techniques and designs catered towards the use of DNA origami in specific applications. Inspired from various biochemical systems that use lipid membranes as a platform fo self-assembly, and as a result contributing to the dynamics of the lipid bilayer; we ventured to develop design features which would accelerate the formation of higher-order assemblies of DNA origami on supported membranes. Combined with the use of DNA-PAINT (points accumulation for imaging in nanoscale topography), we showed that our proposed design could not only form large assemblies in a small amount of time but also could be a platform for super-resolution readout of processes associated with these assemblies. In this chapter I will present the initial study and discuss the implications and further applications of these developments.

7.1 P4. Design Features to Accelerate the Higher-Order Assembly of DNA Origami on Membranes

This study compares different design features to optimize the assembly kinetics of higher-order DNA origami structures. We find that using low sequence complexity connector strands to cross-link DNA origami indirectly, rather than direct binding of high-complexity sequences to loops in the scaffold DNA, significantly accelerates the assembly process. They attribute this acceleration to two effects: the presence of multiple binding reading frames, which increases the effective local concentration of binding sites and thus the effective association rate, and the use of low-complexity sequences, which prevents the formation of hairpins. We also demonstrate the accessibility of DNA-PAINT super-resolution imaging to visualize the origami orientations at the nanoscopic scale. Shown in this study as a proof of concept, the DNA origami could be functionalized with spefici binders of interest and used with their complementary linkers, while simultaneously using DNA-PAINT to probe the orientation of the individual monomers to understand the process of assembly formation.

An implication of using such higher-order assemblies was observed with phase separated membranes, where the self-assembly of DNA origami induced domain formation. [228] We observed that the higher-order assembly of DNA origami induces an indirect decrease in lipid diffusion, and the clustering effect of the origami induces microscopic domain formation in cellular mimicking membrane compositions, which primarily have nanodomains. Moreover, DNA origami can be used to induce the micro-domains to acquire the same lat-

tice structure as that of the DNA origami assembly. Furthermore, the research contribution in the next section has also initiated a comprehensive study towards assembling synthetic nano-materials on membranes with the help of self-organizing protein machinery. [95]

Design Features to Accelerate the Higher-Order Assembly of DNA Origami on Membranes

Yusuf Qutbuddin†, Jan-Hagen Krohn†, Gereon A. Brüggenthies, Johannes Stein, Svetozar Gavrilović, Florian Stehr, Petra Schwille*

Author contributions:

P.S., J.S., and **Y.Q.**, conceived the project. **Y.Q.**, and J.H.K performed all experiments. J.S., and F.S. contributed to the DNA PAINT and SPT methodology. **Y.Q.**, J.H.K and G.B. designed the DNA origami. J.H.K performed the SPT and image correlation analysis and simulations. S.G., and **Y.Q.** performed the AFM experiments. S.G. performed AFM image analysis. P.S. acquired funding. **Y.Q.**, and J.H.K prepared the manuscript. All authors commented on the manuscript.

Yusuf Qutbuddin, Jan-Hagen Krohn, Gereon A. Brüggenthies, Johannes Stein, Svetozar Gavrilovic, Florian Stehr, and Petra Schwille The Journal of Physical Chemistry B 2021 125 (48), 13181-13191.
https://doi.org/10.1021/acs.jpcb.1c07694

published in

The Journal of Physical Chemistry B (2021)

THE JOURNAL OF PHYSICAL CHEMISTRY B
A JOURNAL OF THE AMERICAN CHEMICAL SOCIETY

pubs.acs.org/JPCB

Article

Design Features to Accelerate the Higher-Order Assembly of DNA Origami on Membranes

Published as part of The Journal of Physical Chemistry virtual special issue "W. E. Moerner Festschrift".

Yusuf Qutbuddin,[§] Jan-Hagen Krohn,[§] Gereon A. Brüggenthies, Johannes Stein, Svetozar Gavrilovic, Florian Stehr, and Petra Schwille*

Cite This: *J. Phys. Chem. B* 2021, 125, 13181−13191

Read Online

ACCESS | Metrics & More | Article Recommendations | Supporting Information

ABSTRACT: Nanotechnology often exploits DNA origami nanostructures assembled into even larger superstructures up to micrometer sizes with nanometer shape precision. However, large-scale assembly of such structures is very time-consuming. Here, we investigated the efficiency of superstructure assembly on surfaces using indirect cross-linking through low-complexity connector strands binding staple strand extensions, instead of connector strands binding to scaffold loops. Using single-molecule imaging techniques, including fluorescence microscopy and atomic force microscopy, we show that low sequence complexity connector strands allow formation of DNA origami superstructures on lipid membranes, with an order-of-magnitude enhancement in the assembly speed of superstructures. A number of effects, including suppression of DNA hairpin formation, high local effective binding site concentration, and multivalency are proposed to contribute to the acceleration. Thus, the use of low-complexity sequences for DNA origami higher-order assembly offers a very simple but efficient way of improving throughput in DNA origami design.

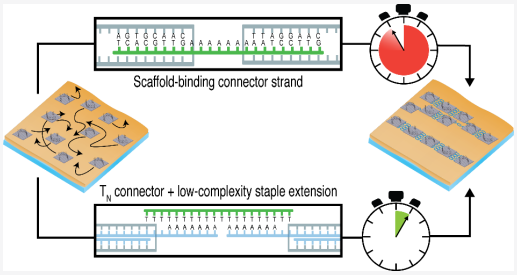

INTRODUCTION

Over the past 15 years, the development of DNA origami technology led to huge advances in the field of structural DNA nanotechnology, as it allows straightforward construction of large and complex nanostructures.[1] This is obtained by forcing long single-stranded DNA (ssDNA) "scaffold" strands into programmed conformations using many short "staple" strands. Diverse structures are possible, and multiple site-specific functionalizations can be introduced into a single structure with few-nanometer resolution.[2,3] Applications include single-molecule observation of chemical reactions,[4] positioning of nanoparticles for nanophotonics,[5] design of sensitive and specific biosensors,[6] and many others. Recent examples of DNA origami nanostructures designed in our lab include benchmark targets for single-molecule method development,[7] curved nanostructures to deform membranes,[8] or nanostructures serving as passive cargo to study transport processes in reaction−diffusion systems.[9]

The structural complexity allowed by the DNA origami technology is essentially limited by the length of the scaffold strand, typically 7−8 kb bacteriophage genomes. Even with cutting-edge strategies to increase the scaffold length up to 10 kb and modify it for different applications,[10,11] it is still challenging to produce DNA origami in sizes above 100 nm with high yield. To arrive at larger structures, the very first publication of the DNA origami technology already introduced the idea of cross-linking origami "monomer" particles into higher-order structures.[1] Nowadays, quite large and complex higher-order DNA origami structures ("superstructures") are being used for nanometer-precise positioning of structures over micrometer scales,[12,13] molecular "tubing" systems for linear transport of cargo,[14] or the encapsulation of cargo that itself is tens of nanometers in diameter.[15]

There are multiple strategies for assembling DNA origami superstructures. The most common ones exploit direct DNA−DNA binding, either sticky-end hybridization[16] or blunt-end stacking.[17] We focus on sticky-end hybridization strategies in the present manuscript: First, as sticky-end hybridization exploits Watson−Crick base pairing, the association is specific and programmable.[12] Second, sticky-end hybridization can be induced in a time-controlled manner by first preparing samples from DNA origami monomers and then cross-linking them by adding "connector strands".[18] Notably, programmability and

Received: August 31, 2021
Revised: November 13, 2021
Published: November 24, 2021

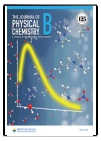

https://doi.org/10.1021/acs.jpcb.1c07694
J. Phys. Chem. B 2021, 125, 13181−13191

The Journal of Physical Chemistry B pubs.acs.org/JPCB Article

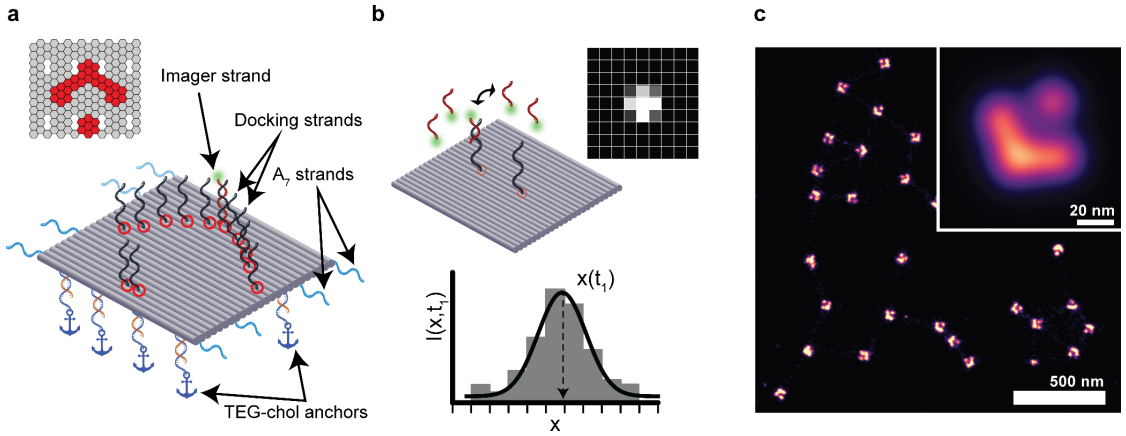

Figure 1. Design of DNA origami nanostructure used in this study. (a) Design schematic (elements not to scale). A 24-helix bundle is functionalized with a 36 docking sites for imager strands. Only a subset of these is shown for clarity, the Picasso Design[26] schematic in the corner shows the true arrangement. Additionally, the particle is functionalized for membrane binding (orange extensions binding dark-blue "anchor" sequences) and lateral extensions for linear cross-linking (light-blue). (b) DNA-PAINT super-resolution imaging. Imager strands reversibly bind to the docking sites on the particle, successively highlighting them and allowing their super-resolved position determination. (c) Experimental DNA-PAINT data from surface-immobilized DNA origami particles, with arrows shapes clearly resolved on many particles. Inset shows an average image from 32 901 particles.

time control are in principle also possible with blunt-end stacking but are more restricted.[17,19] Sticky-end hybridization is typically performed by two alternative approaches: One option is to directly prepare one origami species with staple strands that are extended with sticky ends binding to sequences in another origami, either directly in the scaffold, or in staple extensions.[12,20] Alternatively, to control the timing of association, one can prepare ssDNA stretches on the origami nanostructures and later add separate connector strands to bind and cross-link those ssDNA stretches *in situ*.[16,18] Here we will address the latter strategy (Figure 2), as DNA superstructure assembly with time-controlled onset is valuable for synthetic biology applications, such as mimicking cytoskeleton assembly in order to probe the response of *in vitro* reconstituted proteins to changes in their environment. Time control is also accessible through photoactivation schemes,[21] but this requires additional functionalization of oligomers. We aimed for a radically simple design for time-controlled DNA origami superstructure assembly, avoiding multistep assemblies,[12,14] special buffer requirements,[19] or non-DNA functionalizations.[21]

To allow time-controlled formation of DNA origami superstructures, the effective association rates after reaction initiation should be as high as possible. Past studies of DNA origami superstructures were often quite unsatisfactory in this regard, usually requiring incubation times in the order of 1 h or more,[22] up to overnight incubation.[16,23] Several ways to accelerate association have been identified. One option is multivalent binding between origami monomers to facilitate nucleation.[20,24] Specifically, for origami in 2D systems, increasing DNA origami monomer diffusion coefficients by adding monovalent cations and/or depositing particles on a fluid lipid bilayer rather than on a solid support accelerates assembly.[18,19,23] Additional acceleration comes from precisely matched and rigid geometries of the associating staple extensions to accelerate transition from monovalent binding nucleation to multivalent full binding.[20] Importantly, at least in solution, association rates for DNA origami dimerization reach values comparable to typical association rates for free DNA oligonucleotides.[20] This indicates that increasing effective association rates of the hybridization reaction itself may yield an additional gain in DNA origami superstructure assembly speed. With this idea in mind, we reasoned that recent developments toward increasing hybridization on-rates in DNA point accumulation for imaging in nanoscale topography (DNA-PAINT) microscopy could be transferred to accelerate DNA origami superstructure assembly.[25]

DNA-PAINT (Figure 1b) super-resolution microscopy is an implementation of single-molecule localization microscopy (SMLM) in which fluorophore-conjugated "imager strand" oligonucleotides reversibly bind to "docking sites" on the structure of interest. With low concentrations of imager strands, only a sparse random subset of docking sites is labeled at each time point, allowing their imaging in the single-molecule regime. Acquisition of thousands of frames and subsequent emitter point spread function fitting allows reconstruction of a super-resolved map of docking site coordinates.[26−28] Recent improvements in DNA-PAINT acquisition speed focus on improved docking site design. Specifically, docking sites with low-complexity sequences, i.e., repeats of a short sequence motif such as $[CTC]_N$, were found to be superior: These offer a large number of overlapping imager strand binding sites and thus increase the effective association rates for imager strand binding.[25] The same strategy can also be used in single-particle tracking (SPT) of sparse sets of DNA origami particles.[28] In this case, a long docking strand and a high concentration of imager strands yield unusually long tracks due to continuous replacement of bleached imager strands, circumventing photobleaching limitations to track duration.[29]

We thus set out to characterize two different sticky-end-based DNA origami superstructure assembly approaches in a lipid membrane-anchored 2D system. We use fluorescence techniques including single-particle tracking (SPT), DNA-PAINT, and image correlation analysis, complemented by atomic force microscopy (AFM), to characterize the assembly kinetics and the resulting structures. To this end, we employ a simple, stochastically assembling DNA origami superstructure based on

https://doi.org/10.1021/acs.jpcb.1c07694
J. Phys. Chem. B 2021, 125, 13181−13191

rectangular monomers.[1,26] We functionalized this DNA origami with staple extensions for cross-linking using low-complexity sequence connector strands to assemble superstructures *in situ* rather than preforming them in solution. We demonstrate assembly kinetics that are 1 order of magnitude faster than more traditional approaches by using low-complexity sequence connector strands. We discuss effects contributing to the acceleration, in particular the influence of length of the used sticky end. Our results provide useful insights for future experiments that require rapid cross-linking of DNA origami superstructures.

■ MATERIALS AND METHODS

Unless specified otherwise, chemicals were purchased from Sigma-Aldrich/Merck. DNA oligonucleotide sequences can be found in the Supporting Information.

Buffer Compositions. DNA origami folding buffer: 12.5 mM $MgCl_2$, 10 mM tris, 1 mM EDTA, pH 8.0. Buffer A: 100 mM NaCl, 10 mM tris, pH 8.0. Buffer B: 10 mM $MgCl_2$, 5 mM tris, 1 mM EDTA, pH 8.0. Buffer D: 140 mM NaCl, 7.5 mM $MgCl_2$, 20 mM tris, 0.75 mM EGTA, pH 7.6. SLB formation buffer: 150 mM KCl, 5 mM $MgCl_2$, 25 mM tris, pH 7.5. SLB washing buffer: 150 mM KCl, 25 mM tris, pH 7.5. AFM imaging buffer: 40 mM $MgCl_2$, 5 mM tris, pH 7.5.

Origami Folding and Purification. DNA origami were designed using Picasso Design software,[26] and modified using caDNAno.[30] Scaffold DNA (p7249, tilibit nanosystems, 10 nM in folding buffer) was mixed with a 10-fold molar excess of unmodified staple strands or staple strands with extensions for tetraethyleneglycol−cholesterol (TEG-chol)-anchoring to membranes. Staple strands with DNA-PAINT docking site extensions, the adapter sequence for the "tracking handle", or A_7 cross-linking extensions were added in a 100-fold molar excess. The folding reaction was performed via melting for 5 min at 80 °C and temperature ramping from 60 to 4 °C over 3 h. The folded origami were PEG-purified by two cycles of dilution (1:1 in folding buffer containing additional 15% *w*/*v* PEG-8000 (89510) and 250 mM NaCl), centrifugation (30 min, 17 900 rcf, 4 °C), and resuspension (in folding buffer, 30 min, shaking at 30 °C). DNA origami solutions were stored at −20 °C until use. Before use, DNA origami solutions were diluted with dilution factors adjusted differently for different sample types, typically on the order of 1:20 relative to the concentration obtained after PEG purification.

Surface-Immobilization of DNA Origami. Liquid chambers were assembled from coverslips (22 × 22 mm^2, no. 1.5, Marienfeld) and microscopy slides (Menzel-Gläser) using double-sided sticky tape (Scotch Transparent 665, Conrad) as a spacer. Chambers (ca. 20 μL volume) were passivated with biotinylated BSA (A8549; 1 mg/mL in buffer A, 3 min), washed with 40 μL of buffer A, and functionalized with streptavidin (S888, Thermo Fisher, 0.5 mg/mL in buffer A, 3 min). After washing with 40 μL buffer A and 40 μL buffer B, DNA origami were washed in (20 μL, in buffer B, 6 min). After incubation, unbound origami were washed out with 80 μL of buffer B. Finally, samples were washed with 40 μL of imaging solution (buffer D with imager strands and POCT oxygen scavenger) and sealed in an air-tight container with two-component epoxy glue (Toolcraft Epoxy Transparent, Conrad). The POCT oxygen scavenger consisted of 20 μg/μL catalase (P4234), 0.26 μg/μL pyranose oxidase (C40), 1 μg/μL trolox (238813), and 0.8% *w*/*w* glucose.

Supported Lipid Bilayer (SLB) Preparation and Membrane-Tethering of DNA Origami. SLBs were formed via vesicle fusion. Lipids dissolved in chloroform were mixed in glass vials, and after solvent evaporation under N_2 flow, the lipids were resuspended in SLB formation buffer to 4 μg/μL. The obtained large multilamellar vesicle suspensions were then sonicated (Bransonic 1510, Branson) until the solutions were clear. These small unilamellar vesicle (SUV) solutions were either used immediately or stored at −20 °C and re-sonicated before use. For fluorescence imaging of SLBs, sample chambers were assembled from cut 0.5 mL reaction tubes glued (NOA 68, Norland) onto ethanol- and water-rinsed coverslips and cured under 365 nm UV light exposure for 20 min. Immediately before use, chambers were surface-etched with oxygen plasma (30 s, 0.3 mbar, Zepto, Diener Electronics). Next, 75 μL of diluted SUV suspension (ca. 0.5 μg/μL in SLB formation buffer) were added into prewarmed (37 °C) chambers and incubated for 5 min, during which SLBs formed. After formation, SLBs were washed with 2 mL of SLB washing buffer, followed by 600 μL of buffer B. After the sample cooled to room temperature, the supernatant was replaced with 100 μL of 10 nM TEG-chol anchor oligonucleotide solution (buffer B, 3 min), followed by washing with 200 μL buffer B. Next, 100 μL of DNA origami solution was added (buffer B, 6 min), and the sample was washed with 200 μL of buffer B, followed by 200 μL of buffer D, and finally flushed twice with 200 μL of each imaging solution in buffer D with POCT. SLBs used in fluorescence experiments consisted of DOPC with 1 mol % biotinyl-cap-DOPE (both Avanti Polar Lipids) and 0.01 mol % Atto655-DOPE (ATTO-TEC). The biotin functionalization was not exploited in generating the data shown in this manuscript. SLBs for AFM imaging consisted of DOPC with 0.1 mol % Atto655-DOPE and were prepared on coverslips (22 mm diameter, no. 1, Marienfeld) in dedicated sample chambers for liquid-phase AFM (JPK). Atto655-DOPE was used to locate and quality-check membranes but not for generation of the data shown here. For preparation of SLBs for AFM, the same protocol was followed with the reagent volumes scaled up 2- to 3-fold compared to the chambers used for fluorescence imaging.

Total Internal Reflection Fluorescence Microscopy. Fluorescence microscopy was performed at a custom inverted microscope described in detail in a previous publication.[31] Light from a solid-state laser (561 nm, DPSS-System, MPB) was intensity-adjusted using a half-wave plate and a polarizing beam splitter (WPH05M-561 and PBS101, THORLABS). The beam passed through a refractive beam-shaping device (piShaper 6_6_VIS, AdlOptica) to create a flat illumination profile. To achieve evanescent-field illumination, the beam excentrically entered the oil immersion objective lens (100× NA 1.49 UAPON, Olympus). Fluorescence emission was collected by the same objective and filtered through suitable band-pass filters (605/64, AHF Analsentechnik) before detection on a CMOS camera (Zyla 4.2, Andor). During acquisitions, the temperature was stabilized at 23 °C (H101-CRYO-BL, Okolab), and *z*-positioning of the sample was stabilized via a piezo stage (Z-INSERT100, Piezoconcept and CRISP, ASI). The camera was operated with the open source acquisition software μManager[32] and images were acquired with 2 × 2 $pixel^2$ binning and field of view cropping to the central 700 × 700 (prebinned) pixels to achieve an effective pixel width of 130 nm and a field of view matching the circular flat illumination profile ca. 130 μm in diameter.

https://doi.org/10.1021/acs.jpcb.1c07694
J. Phys. Chem. B 2021, 125, 13181−13191

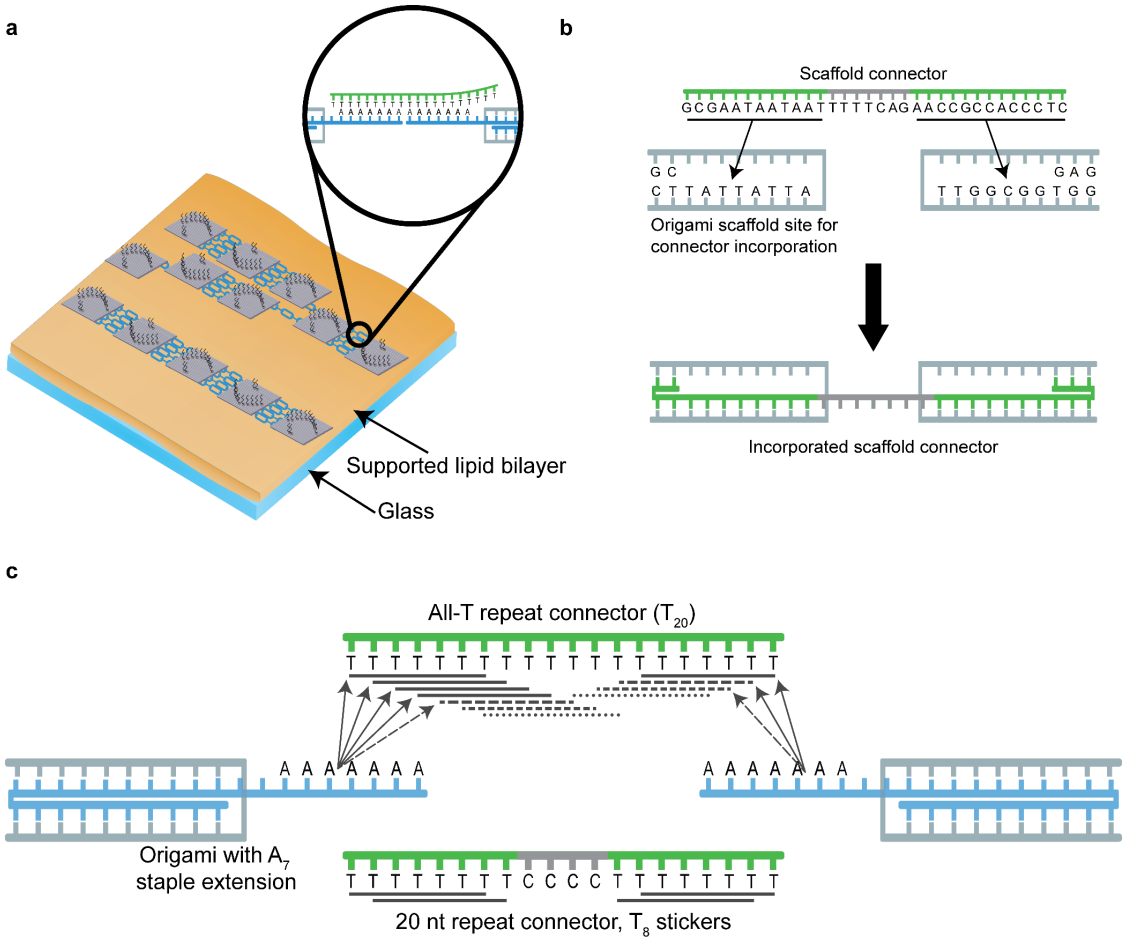

Figure 2. Schematic of DNA origami cross-linking kinetics on membranes. (a) Cross-linking geometry. Cross-linking sites are distributed on the DNA origami such that linear assemblies are expected, but with repeat connectors branching is also possible. (b) Scaffold connectors directly bind scaffold loops of two DNA origami particle, yielding highly site-specific assembly. (c) Repeat connectors bind the DNA origami indirectly via A_7 staple extensions. Depending on the design of the connector strand, many binding reading frames are available for the A_7.

Details for Different Acquisition Strategies. DNA-PAINT Microscopy. DNA origami nanostructures were functionalized with 5xR1 docking sites.[25] The imaging solution contained 1.25 nM $R1_{6nt}$-Cy3B imager strands. Illumination intensity was set to ca. 30 $\mu W\ \mu m^{-2}$. A total of 10 000 images per data set were acquired at a frame rate of 20 Hz.

Single Particle Tracking. DNA origami with a 20 nucleotide (nt) adapter sequence were deposited on membranes. A $[TCT]_{38}$ "tracking handle" docking site analogous to that described by Stehr et al.[29] was quasi-irreversibly recruited to the origami via the adapter complement: During DNA origami deposition, 10 nM tracking-handle−adapter conjugate were additionally present. To ensure a sparse subset of labeled DNA origami nanostructures suitable for SPT, a low density of tracking-handle-coupled particles was diluted in a 20-fold excess of unlabeled DNA origami particles, i.e., the same DNA origami, except without the adapter sequence. The imaging solution contained 10 nM $R5\_S2_{8nt}$-Cy3B imager strands. Illumination intensity was set to ca. 20 $\mu W\ \mu m^{-2}$. A total of 10 000 images per data set were acquired at a frame rate of 20 Hz.

Imaging for Correlation Analysis. DNA origami nanostructures were functionalized with 5xR1 docking sites,[25] which were quasi-irreversibly labeled through 4 min incubation with 10 nM $R1_{18nt}$-Cy3B. The imaging solution did not contain imager strands. Connector strands were added at 250 nM immediately before start of acquisition (ca. 10 s delay, limited by speed of pipetting and closing of microscope stage incubation chamber). A total of 300 images were acquired at a frame rate of 30 Hz at each time point along the cross-linking observation. The laser was shuttered between observation time points. Illumination intensity was set to ca. 2 $\mu W\ \mu m^{-2}$.

Fluorescence Image Analysis. Processing parameters for all fluorescence experiments are listed in Table S1.

DNA-PAINT Microscopy. Image stacks were processed using Picasso software.[26] Picasso Addon[7] was used for automation. The Python software can be found on Github (https://github.com/schwille-paint). The general pipeline started with Picasso

https://doi.org/10.1021/acs.jpcb.1c07694
J. Phys. Chem. B 2021, 125, 13181−13191

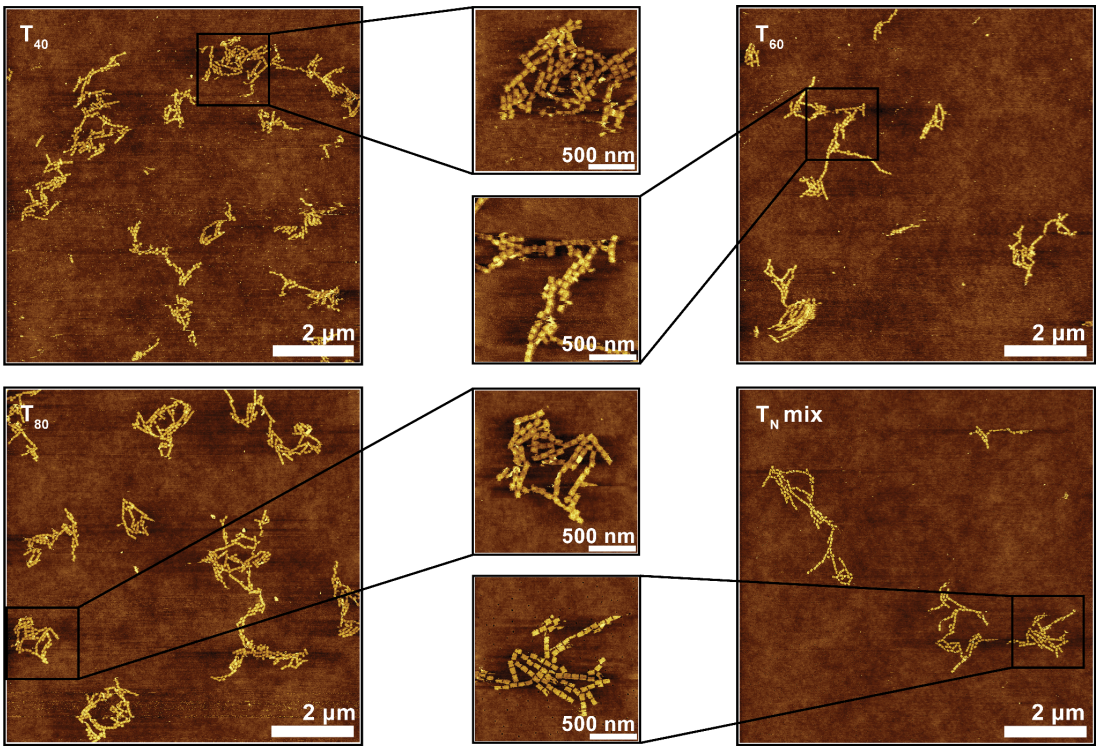

Figure 3. AFM characterization of DNA origami superstructures, showing conditions which yielded high-quality images. Additional conditions are shown in Figure S3. All images were acquired after 2 h incubation with 250 nM of the specified connector strand. The T_N mix is 50 nM each T_{14}, T_{20}, T_{40}, T_{60}, and T_{80}. The color-coded height scale in all panels is 6 nm.

Localize to pick and localize emitters, followed by Picasso Render for drift correction (RCC). In the case of biotin/streptavidin-immobilized origami, particles were manually picked in Picasso Render, followed by automated picking of similar particles and drift correction from picked particles. The average image from many immobilized DNA origami nanostructures was created using Picasso's Average3 module.

Single-Particle Tracking. The analysis pipeline started with localization in Picasso Localize as in the case of SMLM. Subsequent steps used the "SPT" package, which is also available via the above-mentioned GitHub page, for linking of localizations into tracks and mean-squared displacement analysis.

Correlation Analysis of Cross-Linking Kinetics. Image stacks were analyzed using a custom Python script, which is included in the Supporting Information. A detailed explanation of the analysis can be found in the Supporting Information, including a description of the simulations performed to test the accuracy of the analysis.

Atomic Force Microscopy. Measurements were performed on a JPK Nanowizard 3. The AFM images were taken in QI (quantitative imaging) mode using BioLever Mini BL-AC40TS-C2 cantilevers (Olympus). The set point force was 0.25−0.35 nN, acquisition speed 66.2 μm s^{-1}, Z-range 106 nm; 10 × 10 μm^2 fields of view were acquired with a 15 nm pixel size. Images were first processed in JPKSPM Data Processing (JPK, v6.1.142) performing a line-wise second-degree polynomial leveling followed by another second-degree polynomial leveling with limited data range (0% lower limit, 70% upper limit). Subsequent plane leveling, third-degree polynomial row alignment and scar correction were performed in Gwyddion (v2.58, http://gwyddion.net/).

RESULTS AND DISCUSSION

Simple DNA Origami Design for Cross-Linking Studies. To study DNA origami cross-linking, we first designed a suitable monomer structure. We reasoned that the use of a well-characterized modular structure would be most convenient and thus opted for a flat rectangular grid origami used in a number of previous single-molecule fluorescence studies.[7,25,29,33,34] On this monomer structure, we arranged 36 DNA-PAINT docking sites in the shape of an arrow. This design challenges the resolution in DNA-PAINT imaging and allows reading out the orientation of the origami on the surface (Figure 1). DNA-PAINT imaging of individual DNA origami particles immobilized on a glass surface via biotin−streptavidin anchoring indeed revealed the expected arrow pattern with high yield (Figure 1c).

We then functionalized the "bottom" side of the origami structure with staple extensions to bind it to supported lipid bilayer membranes (SLBs) via complementary TEG-chol-coupled oligonucleotides. Only two opposing lateral edges of the DNA origami were further functionalized for cross-linking into higher-order assemblies, aiming for linear chains rather than tilings, as the latter might be more difficult to distinuish from unspecific clustering (Figure 2a). In all cross-linking experiments described in this manuscript, each DNA origami edge

https://doi.org/10.1021/acs.jpcb.1c07694
J. Phys. Chem. B 2021, 125, 13181−13191

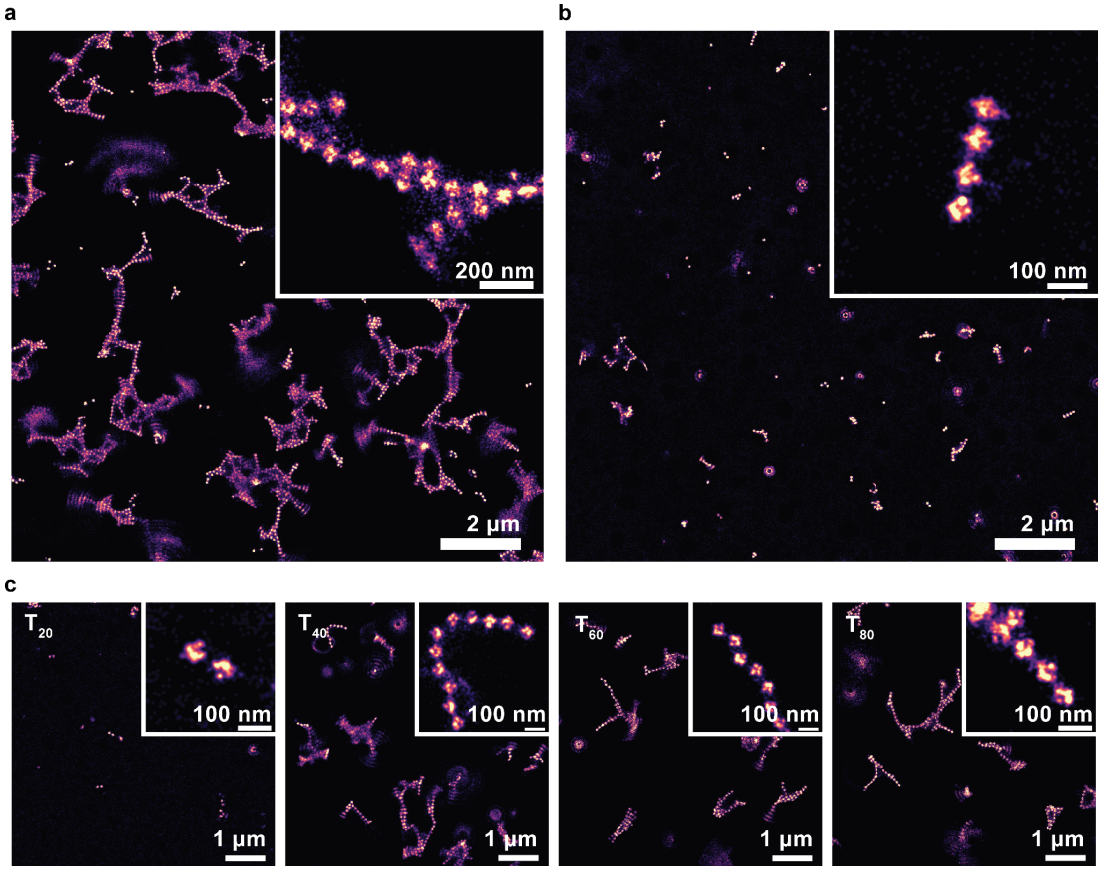

Figure 4. DNA-PAINT characterization of DNA origami superstructures cross-linked with different connector strands. (a) T_N repeat connector mix containing T_{14}, T_{20}, T_{40}, T_{60}, and T_{80} at 50 nM each (30 min incubation). (b) Scaffold connectors (250 nM total concentration, 20 h). (c) Individual repeat connectors (250 nM, 30 min).

participating in the association was designed to bind four connector strands. The DNA origami design exposes no blunt ends of DNA duplexes to avoid uncontrolled association via base stacking. Figure 2 gives a schematic summary of the DNA origami cross-linking strategies. One strategy that we employed has been frequently reported before.[16,18,23] Here, DNA origami nanostructures are cross-linked via connector strands that are essentially staple strands which incorporate into both monomers simultaneously (Figure 2b). For concision, we will call these "scaffold connectors". The other strategy is to incorporate modified staples into the DNA origami that carry extensions for indirect binding of connector strands to the DNA origami. We reasoned that DNA origami superstructure assembly could be accelerated through a connector strand design analogous to the above-mentioned high-on-rate docking site design[25,29,33] used for example in DNA-PAINT, i.e., the use of low-complexity sequences to increase the effective association rate (Figure 2c). We opted for short stretches of a single nucleotide species, specifically A_7 as an extreme case of such a low-complexity sequence. The connector strands were simply oligo-T sequences. These connector strands will be referred to as "repeat connectors". We note that we did not optimize our structure for highly specific assembly geometries. Instead, we aimed for a simple system that would serve as a model system for characterizing the assembly process itself. Thus, a stochastically assembling design was chosen in which also the shape of the formed structures would reveal the action of the connector strands in super-resolution imaging. With the basic origami design and cross-linking strategies at hand, we proceeded to create higher-order DNA origami assemblies on fluid membranes.

Repeat Connectors Are a Viable Option for Superstructure Assembly. We first characterized the structures of our cross-linked DNA origami structures using AFM to confirm the possibility of forming superstructures with desired geometry using repeat connectors. For AFM imaging, we prepared DNA origami samples on fluid SLBs and cross-linked them for 2 h using all-T repeat connectors of different lengths (T_{14}, T_{20}, T_{40}, T_{60}, T_{80}, or a mixture of all of these referred to as T_N mix). Before imaging, we exchanged the buffer, increasing the Mg^{2+} concentration from 7.5 to 40 mM to decrease mobility of the preformed structures for better AFM image quality. When using repeat connectors, ≥40 nt in length, high-quality images showing the expected formation of extended filaments were obtained which agree with the linear assembly geometry dictated by design (compare Figures 3 and 2). However, we saw hardly

https://doi.org/10.1021/acs.jpcb.1c07694
J. Phys. Chem. B 2021, 125, 13181−13191

any differences between different lengths ≥ 40 nt. Small oligomers formed by shorter repeat connector strands yielded lower quality images, suggesting that these led to hardly any superstructure formation within 2 h. In fact, the structures that we obtained with repeat connectors rather looked like unspecific association due to the high Mg^{2+} concentration (Figure S3). We did see some lateral assembly as well: As all cross-linking staple extensions have the same A_7 sequence and only differ by orientation of 3′- or 5′-ends, there is no strict specificity regarding the orientation of neighboring DNA origami monomers within the superstructure. This allows branching of linear assemblies, which leads to the formation of the observed 2-dimensional superstructures. We observed this branching somewhat less frequently when using scaffold connectors, which are site-specific in their binding to DNA origami and thus suppress branching (Figure S3). The presence of some branching even in this setting suggests Mg^{2+} unspecific association. Overall, the AFM data suggests that using long repeat connectors allows to cross-link DNA origami superstructures efficiently, albeit with trade-offs in specificity. However, there was no obvious difference between the different repeat connectors that efficiently cross-linked the DNA origami structures. In our AFM experiments, pushing of DNA origami structures by the AFM tip forced us to strongly increase the Mg^{2+} concentration, which led to unspecific association. Thus, at least with lengths ≥40 nt, repeat connectors do facilitate formation of DNA origami superstructures. To characterize the structures in more detail under origami-typical buffer conditions, we employed single-molecule fluorescence imaging.

Repeat Connectors Form Stable Superstructures Faster than Scaffold Connectors. Before acquiring super-resolution images of our samples, we used SPT to characterize particle mobility prior to cross-linking in the imaging buffer used for all following fluorescence microscopy experiments, containing 7.5 mM Mg^{2+} and 140 mM Na^{+}. SPT showed that our TEG-chol-anchored DNA origami particles diffused freely on the SLBs with a diffusion coefficient of ca. 0.2 $\mu m^2\ s^{-1}$ (Figure S4). However, upon addition of connector strands, we observed a strong decrease in mobility, indicating superstructure formation. A large fraction of particles was practically immobilized 30 min after addition of a mixture of oligo-T connector strands to A_7-functionalized origami (Figure S5). We reasoned that these may in fact be sufficiently immobilized for DNA-PAINT-based structural characterization using an accelerated acquisition protocol following Strauss and Jungmann,[25] which reduces the acquisition time to ca. 8 min. SMLM has been successfully applied to samples with slow but non-negligible motion such as live cells before, albeit with trade-offs between acquisition time and resolution.[35,36]

Even with that accelerated acquisition, we were unable to resolve any structures in DNA-PAINT imaging without cross-linking (Figure S6a). However, we were able to resolve large DNA origami superstructures on the membrane after cross-linking for only 30 min with the T_N repeat connector mixture (Figure 4a). Notably, in all our AFM and DNA-PAINT experiments, the connector strand solution had been replaced with connector strand-free imaging buffer before acquisition. This means that the observed assemblies were rather stable and did not undergo rapid dissociation/reassociation dynamics and, in particular, that the assemblies were not dependent on stabilization by the high Mg^{2+} concentration in the AFM imaging buffer. This confirms that the use of short A_7 sticker sequences combined with multivalent cooperative binding is sufficient for association of stable superstructures. In fact, the branching of oligomers seen in AFM and confirmed by SMLM suggests that our A_7 cross-linking extensions are too long for efficient "self-healing" of association sites into "ideal" association geometries.[12,37] We saw similar results when using scaffold connectors, but much longer incubation times were needed before high-quality imaging was possible: Compare Figure 4b acquired after 20 h to Figure S7 acquired after 2 h. This is in line with previous publications using scaffold connectors to cross-link DNA origami into 2D systems.[18,23] Each scaffold connector first needs to bind to its unique binding site on a DNA origami nanoparticle and then to the appropriate binding site on a second particle, requiring the DNA origami monomers to collide in the correct mutual orientation. Even after 20 h, only rather small assemblies were found. Thus, repeat connectors allowed assembly within less than 1 h, while scaffold connectors seemed quite unsatisfying regarding throughput of the experiment.

Although the image resolution in DNA-PAINT on membranes was lower than that in the image of origami directly immobilized on glass, we achieved resolution down to the 10 nm scale even on membranes. The resolution was limited by residual motion on the time scale of the acquisition, as demonstrated by the blurred clouds of localizations in various positions of the image. The orientation of some DNA origami monomers within the context of the superstructures was visible in the SMLM images, giving access to some information about the geometry in association. When repeat connectors are used, both parallel and antiparallel arrow orientations in neighboring particles are seen, which is obviously another consequence of the lack of site specificity in repeat connector binding. This is in stark contrast to the images obtained using scaffold connectors, which yield assemblies specifically with parallel orientation (Figure 4b). Notably, DNA-PAINT imaging of DNA origami deposited in a 3-fold higher density, but not exposed to connector strands, yielded low-resolution images of very different structures (Figure S6b). This confirms that despite the compromises in association geometry specificity when using repeat connectors, the retrieved superstructures are products of hybridization-based, connector strand-dependent association.

Finally, we compared superstructures formed by different lengths of all-T connector strands using DNA-PAINT imaging (Figure 4c). T_{14} (not shown) or T_{20} repeat connectors showed almost no cross-linking within 30 min, supporting the idea that assembly seen with AFM was mostly unspecific due to the high Mg^{2+} concentration. As in AFM, we saw little difference between the different all-T connectors of lengths ≥ 40 nt. From our DNA-PAINT experiments, we could thus confirm the connector strand-driven association of our DNA origami superstructures, and that long repeat connectors yield faster assembly than scaffold connectors. Motivated by these findings, we decided to characterize more quantitatively the differences between assembly kinetics of scaffold and repeat connectors, in order to obtain a mechanistic understanding of these differences.

Quantification and Mechanisms of Assembly Acceleration. In the next experiments, we set out to determine characteristic time scales for DNA origami higher-order assembly under different conditions. We opted for an image correlation analysis-based read-out of oligomerization (see Supplementary Note and Figure S1). The calculated correlation parameter, reporting the amplitude of temporal fluorescence fluctuations, increases as the particles associate into higher-order assemblies: Fluorescence fluctuations are larger when few bright particles diffuse through a pixel than many dim ones do. Later,

https://doi.org/10.1021/acs.jpcb.1c07694
J. Phys. Chem. B 2021, 125, 13181−13191

The Journal of Physical Chemistry B pubs.acs.org/JPCB Article

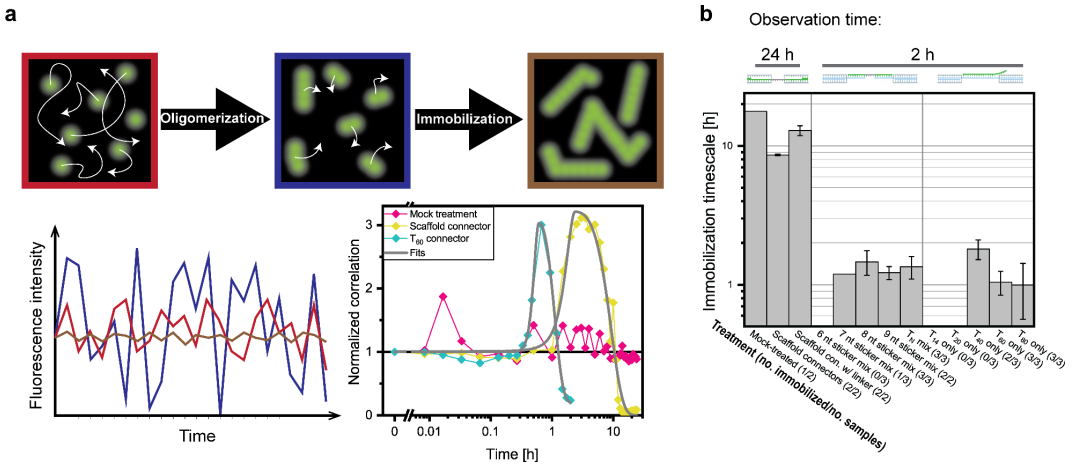

Figure 5. Correlation analysis of cross-linking kinetics. (a) Illustration and example data of correlation analysis. At the beginning of the experiments, monomers diffuse rapidly, creating moderate fluorescence fluctuations (red image and fluorescence intensity trace). As oligomerization begins, effectively fewer brighter particles are observed, increasing fluctuation amplitudes at unchanged average intensity (blue). As oligomerization progresses, yielding large, immobile particles, fluctuations become negligible (brown). The time traces of correlation parameter change show two examples of traces quite clearly undergoing these phases within observation time, and a buffer-treated negative control. (b) Kinetics of DNA origami higher-order assembly measured through image correlation analysis (mean ± s.d.). See the main text for details about the different conditions. Numbers in parentheses refer to the number of data sets for which an assembly time scale could be fitted compared to the number of data sets acquired for this condition. One of the mock-treated samples did show clear immobilization, which we attribute to unspecific sample degradation.

the correlation parameter falls to zero or a low baseline value, as the assemblies become so large that they are essentially immobile during the 10 s observation: Immobile particles yield an approximately constant signal over time (Figure 5a). The correlation analysis was found to be sensitive to oligomerization and immobilization in simulations of different ratios of mono- and oligomers (Figure S2). Additional advantages for long-term observation of the overall evolution of the sample are lower illumination intensities and the fact that in contrast to SMLM and AFM, this analysis captures the entire ensemble of particles rather than selectively showing immobile assemblies. Thus, image correlation analysis provided a convenient aggregate readout for higher-order assembly kinetics, from which we derived characteristic time scales of immobilization as a surrogate for assembly of DNA origami superstructures (Figure 5b). For these experiments, the spatial arrangement of docking sites previously used for DNA-PAINT plays no role (ca. 50 nm pattern width vs ca. 200 nm spatial resolution). Instead, we created bright particles through quasi-irreversible binding of multiple long $R1_{18nt}$-Cy3B imager strands to the full length of the docking site.[38] We systematically compared cross-linking by a variety of connector strands under otherwise constant conditions. These included the previously used scaffold connectors with and without short flexible linkers between the binding sites and all-T repeat connectors of lengths 14, 20, 40, 60, and 80 nt. In addition, we included mixtures of repeat connectors of all lengths, but with inserted oligo-C spacers that do not bind the oligo-A extensions, thus tuning the "sticker" length (i.e., number of binding reading frames) without changing the overall length of the connector strands (Figure 2c). The results are compiled in Figure 5b for comparison, but they will now be discussed sequentially.

Assembly kinetics were observed following addition of connector strands for either 24 h (scaffold connectors and negative controls) or 2 h (repeat connectors). Confirming the findings from DNA-PAINT imaging, very long incubation times in the order of 10 h were needed to create fully assembled structures using scaffold connectors. Adding a short flexible linker sequence to the scaffold connectors did not strongly affect the association kinetics. If anything, it slowed down association, which may be explained by the findings of Zenk et al.[20] that larger flexibility of connector binding sites can be detrimental to association.

We then characterized the repeat connectors with total lengths of 14, 20, 40, 60, and 80 nt. First, we looked at cross-linking kinetics for mixtures of repeat connectors with internal oligo-C stretches and terminal oligo-T stickers. Oligo-T sticker lengths varied from 6 nt (shorter than the A_7 docking site) to 9 nt (three binding reading frames). Using repeat connector mixtures for cross-linking, we saw a strong acceleration in association kinetics for sticker lengths of ≥7 nt. Within the 2 h acquisition time, we did not see any notable changes in the fluctuation data for 6 nt stickers, and for 7 nt stickers, only one out of three samples showed immobilization. Increasing the oligo-T sticker length at the end of the repeat connectors to 8 or 9 nt yielded robust assembly within <2 h, demonstrating the desired acceleration. These sticker lengths offer 2 or 3 reading frames for the A_7 binding partner, respectively, meaning that the data is entirely consistent with our idea of multiple reading frames accelerating binding. Another cause for acceleration is the same effect that is the cause for the reduced orientation specificity observed by nanoscale imaging: Repeat connectors can bind various positions on DNA origami nanoparticles, reproducing the effect of multivalent binding previously reported.[20,24] Time-resolved analysis of cross-linking kinetics thus confirms an order-of-magnitude acceleration in assembly dynamics by using our repeat connector strategy, as compared to our scaffold connector strategy.

Interestingly, no further acceleration of superstructure assembly was seen by using a mixture of all-T connector strands

https://doi.org/10.1021/acs.jpcb.1c07694
J. Phys. Chem. B 2021, 125, 13181−13191

of different lenths ("T_N mix" in Figure 5b) compared to those with 8 or 9 nt stickers. We hoped to find an explanation for this effect by comparing different lengths of all-T connector strands. The longer all-T repeat connectors accelerated assembly compared to shorter ones. While Zenk et al.[20] argued that increasing connector strand flexibility (i.e., length) can be detrimental to binding, here the increased length comes with an increase in the number of binding sites. We did not see immobilization within 2 h using T_{14} or T_{20} connectors. This suggests an explanation for the fact that using a mix of different all-T connectors did not further accelerate assembly relative to connectors with 9 nt stickers: The inefficient $T_{14,20}$ connectors likely competed with the more efficient $T_{40,60,80}$ connectors. The low efficiency of $T_{14,20}$ connectors may be explained by the fact that their short sequences cause A_7 docking sites to compete for overlapping binding sites on the same connector strand, which is clearly detrimental for cross-linking. This competition is suppressed in repeat connectors with internal oligo-C stretches and less relevant in long all-T ones.

Obviously, by comparing scaffold connectors to repeat connectors only consisting of oligo-T stretches, we looked at two extremes in a broad spectrum of thinkable cross-linker designs: one entirely optimized for assembly speed and the other entirely for specificity. Intermediate strategies would allow different trade-offs between these parameters. For example, one could combine oligo-A staple strand extensions with oligo-G staple extensions, creating two orthogonal cross-linking systems. These could also be combined through connectors concatenating oligo-T stretches and oligo-C stretches to link an oligo-A functionalized DNA origami face to an oligo-G functionalized one. This would increase specificity in assembly geometry, unlikely to result in antiparallel association of our DNA origami monomers. Repeats of 2 or 3 nt sequence motifs further increase the number of orthogonal motifs available for cross-linking,[25] but the number of binding reading frames will decrease rapidly with increasing motif length. Notably, such 2 nt motifs, albeit without repeats, were used previously to create very large DNA origami superstructures[12] with high specificity in assembly geometry. However, this specific formation of large structures required a multistep assembly that is slow and is not easily transferred to the *in situ* assembly in which we were interested.

Finally, an additional mechanism that likely contributes to the acceleration of binding using low-complexity sequences is the absence of internal hairpins from oligo-T or A_7 sequences. Hairpin formation can strongly reduce effective on-rates.[33,34] Due to sequence constraints from direct binding to the scaffold strand, hairpin formation could not be abolished completely in the design of the scaffold connectors used in this study according to the prediction by NUPACK.[39] One might thus consider high-complexity, yet hairpin-free, docking site extensions. While sequence design will become very challenging with increasing numbers of desired orthogonal sequences and the speed gain will likely remain modest compared to what our work demonstrates, such an approach remains highly attractive regarding specificity. In any case, our recommendation for designing rapidly cross-linking sequences for DNA origami superstructures is to avoid direct binding of connector strands to the scaffold and instead use staple extensions, designed with the lowest possible sequence complexity sufficient to ensure the required specificity.

CONCLUSIONS

In this work, we compared different design features to optimize assembly kinetics of higher-order DNA origami structures. A significant acceleration was achieved by cross-linking DNA origami indirectly via low sequence complexity connector strands binding to staple strand extensions, instead of direct binding of high-complexity sequences to loops in the scaffold DNA. We postulate two effects to contribute to the increased speed: The presence of multiple binding reading frames increases the effective local concentration of binding sites, and thus the effective association rate, and the used low-complexity sequences prevent the formation of hairpins. Using modifications of the strategy will allow multiple orthogonal sequences, increasing association specificity, with some trade-off in experimental throughput. This quite simple and generic approach to accelerate DNA origami superstructure assembly should prove useful to increase throughput of experiments in the field and to benefit experiments that require time-controlled assembly.

ASSOCIATED CONTENT

Supporting Information

The Supporting Information is available free of charge at https://pubs.acs.org/doi/10.1021/acs.jpcb.1c07694.

Methods, image correlation analysis workflow, simulations to assess sensitivity of image correlation analysis to oligomerization and immobilization, AFM results, example of single particle tracking results for monomeric DNA origami particles on DOPC SLBs, DNA-PAINT imaging of non-cross-linked and incompletely cross-linked DNA origami nanostructures, image analysis parameters, oligonucleotide sequences for DNA origami design, additional references (PDF)

MATLAB and Python scripts used for simulation and analysis of cross-linking kinetics (ZIP)

AUTHOR INFORMATION

Corresponding Author

Petra Schwille − *Department of Cellular and Molecular Biophysics, Max Planck Institute of Biochemistry, D-82152 Martinsried, Germany;* orcid.org/0000-0002-6106-4847; Email: schwille@biochem.mpg.de

Authors

Yusuf Qutbuddin − *Department of Cellular and Molecular Biophysics, Max Planck Institute of Biochemistry, D-82152 Martinsried, Germany;* orcid.org/0000-0003-0054-0608

Jan-Hagen Krohn − *Department of Cellular and Molecular Biophysics, Max Planck Institute of Biochemistry, D-82152 Martinsried, Germany; Exzellenzcluster ORIGINS, D-85748 Garching, Germany;* orcid.org/0000-0002-7383-3535

Gereon A. Brüggenthies − *Department of Cellular and Molecular Biophysics, Max Planck Institute of Biochemistry, D-82152 Martinsried, Germany*

Johannes Stein − *Department of Cellular and Molecular Biophysics, Max Planck Institute of Biochemistry, D-82152 Martinsried, Germany;* orcid.org/0000-0002-1335-1120

Svetozar Gavrilovic − *Department of Cellular and Molecular Biophysics, Max Planck Institute of Biochemistry, D-82152 Martinsried, Germany*

https://doi.org/10.1021/acs.jpcb.1c07694
J. Phys. Chem. B 2021, 125, 13181−13191

Florian Stehr − *Department of Cellular and Molecular Biophysics, Max Planck Institute of Biochemistry, D-82152 Martinsried, Germany*

Complete contact information is available at: https://pubs.acs.org/10.1021/acs.jpcb.1c07694

Author Contributions

[§]Y.Q. and J.-H.K. contributed equally to this work.

Funding

Open access funded by Max Planck Society.

Notes

The authors declare no competing financial interest.

■ ACKNOWLEDGMENTS

We thank H. G. Franquelim and L. Babl for useful discussions and H. G. Franquelim for help with AFM acquisitions. Y.Q., J.-H.K., and S.G. acknowledge support from the International Max Planck Research School for Molecular and Cellular Life Sciences (IMPRS-LS). J.S. and F.S. acknowledge support from Graduate School of Quantitative Bioscience Munich (QBM). All authors acknowledge support from the Center for Nano Science (CeNS). J.-H.K. received funding from the Deutsche Forschungsgemeinschaft (DFG, German Research Foundation) under Germany's Excellence Strategy, EXC-2094−390783311. Y.Q. received funding from the European Union's Horizon 2020 research and innovation programme under the Marie Skłodowska-Curie grant agreement no. 859416.

■ ABBREVIATIONS

AFM: Atomic force microscopy
DNA-PAINT: DNA point accumulation for imaging in nanoscale topography
FCS: Fluorescence correlation spectroscopy
SLB: Supported lipid bilayer
SMLM: Single-molecule localization microscopy
SPT: Single-particle tracking
ssDNA: Single-stranded DNA
SUV: Small unilamellar vesicle
TEG-chol: Tetraethyleneglycol−cholesterol

■ REFERENCES

(1) Rothemund, P. W. K. Folding DNA to create nanoscale shapes and patterns. *Nature* **2006**, *440*, 297−302.
(2) Wang, P.; Meyer, T. A.; Pan, V.; Dutta, P. K.; Ke, Y. The beauty and utility of DNA origami. *Chem.* **2017**, *2*, 359−382.
(3) Dey, S.; Fan, C.; Gothelf, K. V.; Li, J.; Lin, C.; Liu, L.; Liu, N.; Nijenhuis, M. A. D.; Saccà, B.; Simmel, F. C.; et al. DNA origami. *Nat. Rev. Methods Primers* **2021**, *1*, 13.
(4) Voigt, N. V.; Tørring, T.; Rotaru, A.; Jacobsen, M. F.; Ravnsbæk, J. B.; Subramani, R.; Mamdouh, W.; Kjems, J.; Mokhir, A.; Besenbacher, F.; et al. Single-molecule chemical reactions on DNA origami. *Nat. Nanotechnol.* **2010**, *5*, 200−203.
(5) Kuzyk, A.; Schreiber, R.; Fan, Z.; Pardatscher, G.; Roller, E.-M.; Högele, A.; Simmel, F. C.; Govorov, A. O.; Liedl, T. DNA-based self-assembly of chiral plasmonic nanostructures with tailored optical response. *Nature* **2012**, *483*, 311−314.
(6) Selnihhin, D.; Sparvath, S. M.; Preus, S.; Birkedal, V.; Andersen, E. S. Multifluorophore DNA origami beacon as a biosensing platform. *ACS Nano* **2018**, *12*, 5699−5708.
(7) Stein, J.; Stehr, F.; Schueler, P.; Blumhardt, P.; Schueder, F.; Mücksch, J.; Jungmann, R.; Schwille, P. Toward absolute molecular numbers in DNA-PAINT. *Nano Lett.* **2019**, *19*, 8182−8190.
(8) Franquelim, H. G.; Khmelinskaia, A.; Sobczak, J.-P.; Dietz, H.; Schwille, P. Membrane sculpting by curved DNA origami scaffolds. *Nat. Commun.* **2018**, *9*, 811.
(9) Ramm, B.; Goychuk, A.; Khmelinskaia, A.; Blumhardt, P.; Eto, H.; Ganzinger, K. A.; Frey, E.; Schwille, P. A diffusiophoretic mechanism for ATP-driven transport without motor proteins. *Nat. Phys.* **2021**, *17*, 850−858.
(10) Bush, J.; Singh, S.; Vargas, M.; Oktay, E.; Hu, C.-H.; Veneziano, R. Synthesis of DNA origami scaffolds: current and emerging strategies. *Molecules* **2020**, *25*, 3386.
(11) Engelhardt, F. A. S.; Praetorius, F.; Wachauf, C. H.; Brüggenthies, G.; Kohler, F.; Kick, B.; Kadletz, K. L.; Pham, P. N.; Behler, K. L.; Gerling, T.; et al. Custom-size, functional, and durable DNA origami with design-specific scaffolds. *ACS Nano* **2019**, *13*, 5015−5027.
(12) Tikhomirov, G.; Petersen, P.; Qian, L. Fractal assembly of micrometre-scale DNA origami arrays with arbitrary patterns. *Nature* **2017**, *552*, 67−71.
(13) Aghebat Rafat, A.; Pirzer, T.; Scheible, M. B.; Kostina, A.; Simmel, F. C. Surface-Assisted Large-Scale Ordering of DNA Origami Tiles. *Angew. Chem., Int. Ed.* **2014**, *53*, 7665−7668.
(14) Stömmer, P.; Kiefer, H.; Kopperger, E.; Honemann, M. N.; Kube, M.; Simmel, F. C.; Netz, R. R.; Dietz, H. A synthetic tubular molecular transport system. *Nat. Commun.* **2021**, *12*, 4393.
(15) Sigl, C.; Willner, E. M.; Engelen, W.; Kretzmann, J. A.; Sachenbacher, K.; Liedl, A.; Kolbe, F.; Wilsch, F.; Aghvami, S. A.; Protzer, U.; et al. Programmable icosahedral shell system for virus trapping. *Nat. Mater.* **2021**, *20*, 1281−1289.
(16) Jungmann, R.; Scheible, M.; Kuzyk, A.; Pardatscher, G.; Castro, C. E.; Simmel, F. C. DNA origami-based nanoribbons: assembly, length distribution, and twist. *Nanotechnology* **2011**, *22*, 275301.
(17) Woo, S.; Rothemund, P. W. K. Programmable molecular recognition based on the geometry of DNA nanostructures. *Nat. Chem.* **2011**, *3*, 620−627.
(18) Kocabey, S.; Kempter, S.; List, J.; Xing, Y.; Bae, W.; Schiffels, D.; Shih, W. M.; Simmel, F. C.; Liedl, T. Membrane-assisted growth of DNA origami nanostructure arrays. *ACS Nano* **2015**, *9*, 3530−3539.
(19) Woo, S.; Rothemund, P. W. K. Self-assembly of two-dimensional DNA origami lattices using cation-controlled surface diffusion. *Nat. Commun.* **2014**, *5*, 4889.
(20) Zenk, J.; Tuntivate, C.; Schulman, R. Kinetics and thermodynamics of Watson−Crick base pairing driven DNA origami dimerization. *J. Am. Chem. Soc.* **2016**, *138*, 3346−3354.
(21) Suzuki, Y.; Endo, M.; Yang, Y.; Sugiyama, H. Dynamic Assembly/Disassembly Processes of Photoresponsive DNA Origami Nanostructures Directly Visualized on a Lipid Membrane Surface. *J. Am. Chem. Soc.* **2014**, *136*, 1714−1717.
(22) Suzuki, Y.; Endo, M.; Sugiyama, H. Lipid-bilayer-assisted two-dimensional self-assembly of DNA origami nanostructures. *Nat. Commun.* **2015**, *6*, 8052.
(23) Kempter, S.; Khmelinskaia, A.; Strauss, M. T.; Schwille, P.; Jungmann, R.; Liedl, T.; Bae, W. Single particle tracking and super-resolution imaging of membrane-assisted stop-and-go diffusion and lattice assembly of DNA origami. *ACS Nano* **2019**, *13*, 996−1002.
(24) Jiang, S.; Yan, H.; Liu, Y. Kinetics of DNA tile dimerization. *ACS Nano* **2014**, *8*, 5826−5832.
(25) Strauss, S.; Jungmann, R. Up to 100-fold speed-up and multiplexing in optimized DNA-PAINT. *Nat. Methods* **2020**, *17*, 789−791.
(26) Schnitzbauer, J.; Strauss, M. T.; Schlichthaerle, T.; Schueder, F.; Jungmann, R. Super-resolution microscopy with DNA-PAINT. *Nat. Protoc.* **2017**, *12*, 1198−1228.
(27) Jungmann, R.; Steinhauer, C.; Scheible, M.; Kuzyk, A.; Tinnefeld, P.; Simmel, F. C. Single-molecule kinetics and super-resolution microscopy by fluorescence imaging of transient binding on DNA origami. *Nano Lett.* **2010**, *10*, 4756−4761.
(28) von Diezmann, L.; Shechtman, Y.; Moerner, W. E. Three-dimensional localization of single molecules for super-resolution imaging and single-particle tracking. *Chem. Rev.* **2017**, *117*, 7244−7275.

https://doi.org/10.1021/acs.jpcb.1c07694
J. Phys. Chem. B 2021, 125, 13181−13191

(29) Stehr, F.; Stein, J.; Bauer, J.; Niederauer, C.; Jungmann, R.; Ganzinger, K.; Schwille, P. Tracking single particles for hours via continuous DNA-mediated fluorophore exchange. *Nat. Commun.* **2021**, *12*, 4432.
(30) Douglas, S. M.; Dietz, H.; Liedl, T.; Högberg, B.; Graf, F.; Shih, W. M. Self-assembly of DNA into nanoscale three-dimensional shapes. *Nature* **2009**, *459*, 414−418.
(31) Stehr, F.; Stein, J.; Schueder, F.; Schwille, P.; Jungmann, R. Flat-top TIRF illumination boosts DNA-PAINT imaging and quantification. *Nat. Commun.* **2019**, *10*, 1268.
(32) Edelstein, A. D.; Tsuchida, M. A.; Amodaj, N.; Pinkard, H.; Vale, R. D.; Stuurman, N. Advanced methods of microscope control using μManager software. *Journal of Biological Methods* **2014**, *1*, No. e10.
(33) Schickinger, M.; Zacharias, M.; Dietz, H. Tethered multi-fluorophore motion reveals equilibrium transition kinetics of single DNA double helices. *Proc. Natl. Acad. Sci. U. S. A.* **2018**, *115*, No. E7512.
(34) Schueder, F.; Stein, J.; Stehr, F.; Auer, A.; Sperl, B.; Strauss, M. T.; Schwille, P.; Jungmann, R. An order of magnitude faster DNA-PAINT imaging by optimized sequence design and buffer conditions. *Nat. Methods* **2019**, *16*, 1101−1104.
(35) Biteen, J. S.; Thompson, M. A.; Tselentis, N. K.; Bowman, G. R.; Shapiro, L.; Moerner, W. E. Super-resolution imaging in live Caulobacter crescentus cells using photoswitchable EYFP. *Nat. Methods* **2008**, *5*, 947−949.
(36) Shroff, H.; Galbraith, C. G.; Galbraith, J. A.; Betzig, E. Live-cell photoactivated localization microscopy of nanoscale adhesion dynamics. *Nat. Methods* **2008**, *5*, 417−423.
(37) Tikhomirov, G.; Petersen, P.; Qian, L. Programmable disorder in random DNA tilings. *Nat. Nanotechnol.* **2017**, *12*, 251−259.
(38) Woehrstein, J. B.; Strauss, M. T.; Ong, L. L.; Wei, B.; Zhang, D. Y.; Jungmann, R.; Yin, P. Sub−100-nm metafluorophores with digitally tunable optical properties self-assembled from DNA. *Science Advances* **2017**, *3*, No. e1602128.
(39) Zadeh, J. N.; Steenberg, C. D.; Bois, J. S.; Wolfe, B. R.; Pierce, M. B.; Khan, A. R.; Dirks, R. M.; Pierce, N. A. NUPACK: Analysis and design of nucleic acid systems. *J. Comput. Chem.* **2011**, *32*, 170−173.

https://doi.org/10.1021/acs.jpcb.1c07694
J. Phys. Chem. B 2021, 125, 13181−13191

8
Membrane dynamics with Macromolecules

Many cellular processes involve macromolecule-membrane interactions, including signalling pathways, division, endocytosis, and many more. Most of these processes are understood from a biological perspective, and a holistic understanding of their mechanisms remain wanting. Synthetic macromolecules are an attractive tool for fundamental scientists to simplify the problem and take a bottom-up approach to answer "how something happens". Consequently, these synthetic macromolecules like carbohydrate polymers, polysaccharides or polypeptides can work as tools for pharmaceutical or chemical applications. A fundamental understanding of how macromolecules interact with lipid bilayers serves as a feedback loop for synthetic chemists to design more specific macromolecules for the desired effects.

To this end, this thesis contributes to the study of two systems of macromolecules with contrasting end goals. Firstly, I will describe our work with synthetic glycopolymers designed to mimic various components of the glycocalyx to gain insights on the molecular interactions with simplified model systems. Then, I will describe our work with understanding cardiolipin interactions with polypeptides specifically designed for targetting the mitochondria for drug delivery. In both the studies, exploring how these molecules interact and eventually affect the mechanical properties of the membrane, helped us gain insight into how these macromolecules could be utilized for biological applications.

8.1 P5. Mimicking glycolipids and glycoproteins to create fuzzy membranes

This study presents a simple synthetic glycopolymer system end-functionalized with cholesterol and varying number of mannose subunits. These synthetic glycopolymers are soluble in aqueos solutions, and thus can be used for engineering membrane surfaces post production. We characterized the shape and spatial organization of the glycopolymers in solution and measured their incorporation into model membranes. The cholesterol works as a membrane anchor resulting in spontaneous insertion into the membrane. We observed that increasing the carbohydrate chain length results in a higher degree of incorporation into the membrane, which was corroborated by the measurement of surface densities using fluorescence correlation spectroscopy. Furthermore, we observed an overall reduction in fluidity of the membrane possibly due to the increase of cholesterol content of the bilayer. We also demonstrate that these glycopolymers can mimic glycolipids and mucin-like glycoproteins, depending on their carbohydrate chain length. The glycopolymers modulate L_d/L_o lipid domains upon interaction, and higher chain length or higher surface densities reduce the line tension at the domain boundaries of giant unilamellar vesicles. We present that the glycopolymers can be used to engineer membrane surfaces, either as mimics of natural glycolipids and glycoproteins, showcasing their consequential similarities to the same. We contribute to the comprehensive understanding of the interactions between synthetic glycopolymers

and model membranes, shedding light on the behavior of the glycocalyx. Overall, this study demonstrates the potential of synthetic glycopolymers as a tool for understanding the complex interactions between the glycocalyx and cellular membranes, and for developing new applications in biomedicine and biotechnology.

Mimicking glycolipids and glycoproteins to create "fuzzy" membranes

Yusuf Qutbuddin†, Roberto Terracciano†, Giacomo Bassi, Mina Aleksanyan, Steven Huband, Svetozar Gavrilović, Gokhan Yilmaz, Rumiana Dimova, Petra Schwille*, and C Remzi. Becer*

Author contributions:

Y.Q., R.T., R.B., and P.S. conceived the project. R.T. synthesized and purified the polymers. R.T. and **Y.Q.** performed the confocal imaging and fluorescence intensity analyses of SLBs and GUVs. **Y.Q.** performed and analyzed FCS experiments with SLBs, GUVs, and polymers in solution. M.A. performed fluctuation spectroscopy experiments and imaging for symmetrically coated GUVs. S.H. performed SAXS experiments and analysis. **Y.Q.** and G.B. performed electrodeformation experiments. **Y.Q.** analyzed electrodeformation images of GUVs. **Y.Q.** and R.T. wrote the manuscript. All authors commented on the manuscript. R.B. and P.S. acquired funding.

to be submitted in

Biomacromolecules (2024)

Mimicking glycolipids and glycoproteins to create "fuzzy" membranes

Yusuf Qutbuddin,[†,‖] Roberto Terracciano,[‡,‖] Giacomo Bassi,[†] Mina Aleksanyan,[¶] Steven Huband,[§] Svetozar Gavrilović,[†] Gokhan Yilmaz,[‡] Rumiana Dimova,[¶] Petra Schwille,[*,†] and C Remzi. Becer[*,‡]

†*Department of Cellular and Molecular Biophysics, Max Planck Institute of Biochemistry, Martinsried, Germany*

‡*Department of Chemistry, University of Warwick, Coventry, UK*

¶*Sustainable and Bio-inspired Materials, Max Planck Institute of Colloids and Interfaces, Potsdam, Germany*

§*Department of Physics, University of Warwick, Coventry, UK*

‖*Contributed equally to this work*

E-mail: schwille@biochem.mpg.de; Remzi.Becer@warwick.ac.uk

Abstract

The glycocalyx, a densely glycosylated extramembrane coating, plays a crucial role in orchestrating cellular communication and contact with the extracellular environment. To understand its function, we synthesized glycopolymers of varying lengths with a cholesterol unit using reversible addition-fragmentation chain transfer (RAFT) polymerization. These synthetic glycopolymers effectively mimic various components of the glycocalyx, depending on the carbohydrate chain length. We investigated the mechanism of adsorption and incorporation of these glycopolymers onto model membranes and explored their implications on the mechanical properties of the lipid bi-

layer. Additionally, we compared our experimental results with the theoretical models of polymer-membrane interactions. Our results provide insights into the interactions between synthetic glycopolymers and model membranes, shedding light on the behavior of the glycocalyx. This study serves as a benchmark for understanding the function of the glycocalyx and has implications for glycocalyx engineering, including the development of efficient drug delivery systems and synthetic cells with sugar-coated extracellular matrices.

Introduction

The intricate and heterogeneous cell membrane, comprising lipids, saccharides, and proteins, plays a pivotal role in orchestrating and modulating essential cellular processes and interactions.[1–4] This complexity affords opportunities for in-depth exploration of cellular behaviors, adhesive properties, recognition mechanisms, and signal transduction pathways. The implications of these investigations extend to diverse scientific domains, including drug delivery, cell-based therapeutic approaches, and tissue engineering.

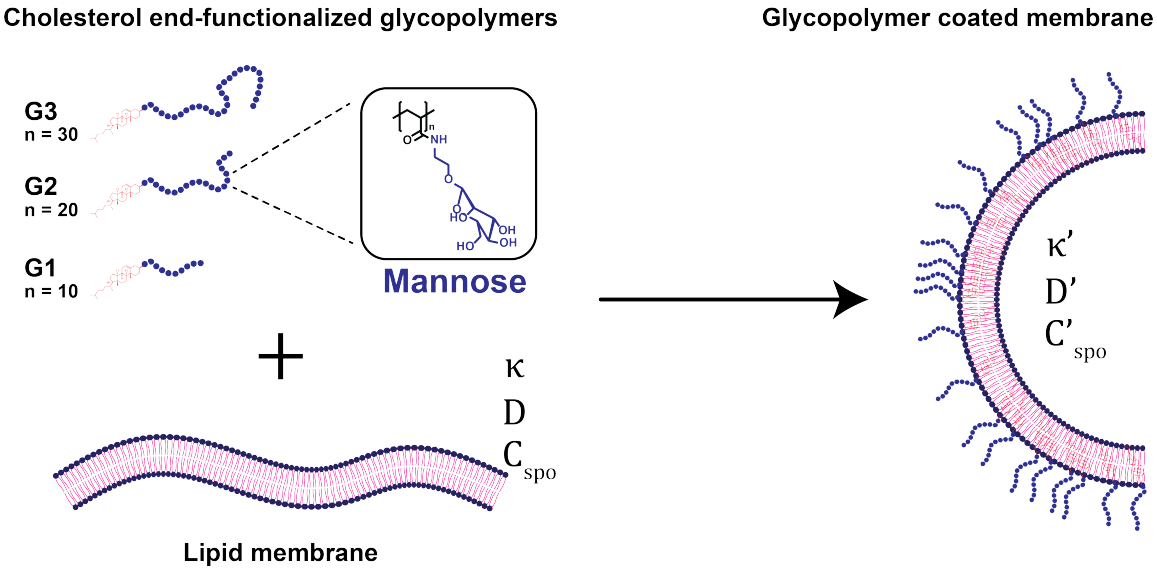

Figure 1: Schematic representation of cholesterol end-functionalized glycopolymers interacting with lipid bilayers changing the mechanical properties of the membrane

A paramount objective within this scientific realm involves the development of a universally applicable and user-friendly methodology for the presentation of bio-active macromolecules on cell membranes. Notably, polysaccharides, distinguished by their involvement in multifaceted biological functions such as molecular recognition, immunological responses, and inflammatory processes, have emerged as subjects of substantial interest for their exogenous attachment to cell membranes.[5–7] However, traditional methods attaching natural saccharides to lipids suffer from extraction and purification processes, which are further complicated by the structural diversity inherent in native glycans.[8,9] Synthetic glycopolymers, surpassing oligosaccharides in utility, enable the incorporation of multiple saccharides along a polymer chain, facilitating cell interactions through the cluster-glycoside effect.[4] Various polymerization techniques, such as reversible deactivation radical polymerizations, ring-opening metathesis polymerization, and ring-opening polymerizations, have been harnessed to synthesize glycopolymers.[10–12] On the other hand, one of the most straightforward methods to manage cell-surface glycan display is through the passive insertion of lipid-anchored glycopolymers into the plasma membrane.[13–15] One prevalent scientific approach centres on the utilization of cholesterol derivatives as anchoring molecules due to strong affinity for integration into cellular membranes.[16,17] Experiments conducted with various synthetic lipid-terminated glycopolymers also highlighted the superior performance of cholesterol-substituted ones in glycocalyx engineering within living cells over an extended period.[18] Furthermore, the integration of glycopeptides with single- and double-cholesterol substitutions was explored in giant unilamellar vesicles (GUVs).[19,20]

Giant unilamellar vesicles (GUVs) are large, unilamellar vesicles with diameters ranging from a few micrometres to hundred micrometres, allowing for the observation of membrane processes at the single-vesicle level. One of the key advantages of GUVs is their ability to be composed of well-defined, tuneable lipid mixtures, which can be tailored to mimic specific biological membranes. This control over composition enables researchers to investigate the effects of individual lipid components on membrane properties, such as curvature, fluidity,

bending rigidity, and phase behavior. Polymer-membrane interactions have been a hot topic for membrane biophysicists in the last several decades. Extensive theoretical models were developed to understand the average modifications of the membrane bending and stretching parameters upon presence of polymers in the vicinity. Theoretical models for reversible and irreversible adsorption of polymers were developed, and eventually membrane systems with end-grafted polymers were extensively studied.[21,22]

Glyco-engineering has become an increasingly important subject in the field of nanoscale drug delivery systems. Lipid nanoparticles (LNPs) are drug delivery systems that are formed with lipids and has seen tremendous development in the last decade. Compared to conventional LNPs, LNPs exposed to cholesterol-amine conjugated mannose had an enhanced potency and uptake by antigen presenting cells.[23] Mannosylated LNPs, with the use of mannose-conjugated lipids, have further exhibited increase in uptake from dendritic cells of mRNA *in vitro* and *in vivo*.[24,25]

The promise of enhancing delivery efficiencies and a growing interest in synthetically mimicking the glycocalyx has triggered synthetic chemists to synthesize various well-controlled glycopolymers. Natural glycans are immensely complex in their structure, and each complexity contributes heavily to the outcome of their interactions with membrane surfaces. Synthetic glycopolymers thus offer an ability to factor-in controlled number of parameters to build a bottom-up understanding of the implications of their structure. In this study, reversible addition–fragmentation chain transfer polymerization (RAFT) was exploited to provide cholesterol end-functionalized glycopolymers. We present a mannose based glycopolymer with three different carbohydrate chain length (see Figure 1) and study their insertion onto GUVs and SLBs using confocal microscopy. Fluorescence correlation spectroscopy (FCS) was employed to study membrane fluidity and the diffusivity of glycopolymers after their incorporation. By measuring the surface density of the glycopolymers, we correlated their adsorption behavior with the induced mechanical properties of the system. . Other mechanical properties such as curvature and bending rigidity were also obtained

to develop a profound understanding in the mechanism of polymer-membrane interactions. These developments in glyco-engineering offer a simple system that can be used, on the one hand, for improving drug delivery candidates and, on the other hand, to build a deeper foundational understanding of the glycocalyx that covers our cells.

Results and discussion

Synthesis, labeling and characterization of cholesterol end-functionalized glycopolymers

A small library of three polymers (**P1-P3**, and **PH3**) were synthesized using RAFT polymerization (see Figure 2A). Polymerization was performed with the Cholesterol CTA at 70 °C using thermal initiation with AIBN and the general conditions were selected as $[CTA]/[initiator]$ = [10]/[1]. They were prepared by varying the content of Acetylated Mannose Acrylamide (10, 20 and 30 units, see Table 1). Next, the RAFT end-groups of each polymer were cleaved by aminolysis to convert into thiol functionalities, and the reaction mixture directly precipitated in diethyl ether. The disappearance of RAFT end-groups can be observed with the decrease in the absorbance at 309 nm for trithiocarbonate (see Supplementary section). No obvious change in the GPC traces was observed and the molar mass was similar to that of before treatment according to RI detector of GPC (Figure S8). However, Variable Wavelength Detector (VWD) of GPC at 309 nm did not show any significant peak after treatment suggesting that the polymer-SH chains were successfully obtained. Conversely, an intense UV signal corresponding to polymer RAFT terminal elution was observed. Additionally, the color of the polymers, attributed to the RAFT terminal group, changed from yellow to white following the successful cleavage of the RAFT end group.

The isolated product was dried under vacuum and subsequently de-protected to obtain the final polymers (G1-G3) used in this study. The peaks observed at δ 1.75 to 2.25 for acetyl protons in the NMR spectra of protected polymers were completely absent in the case of de-

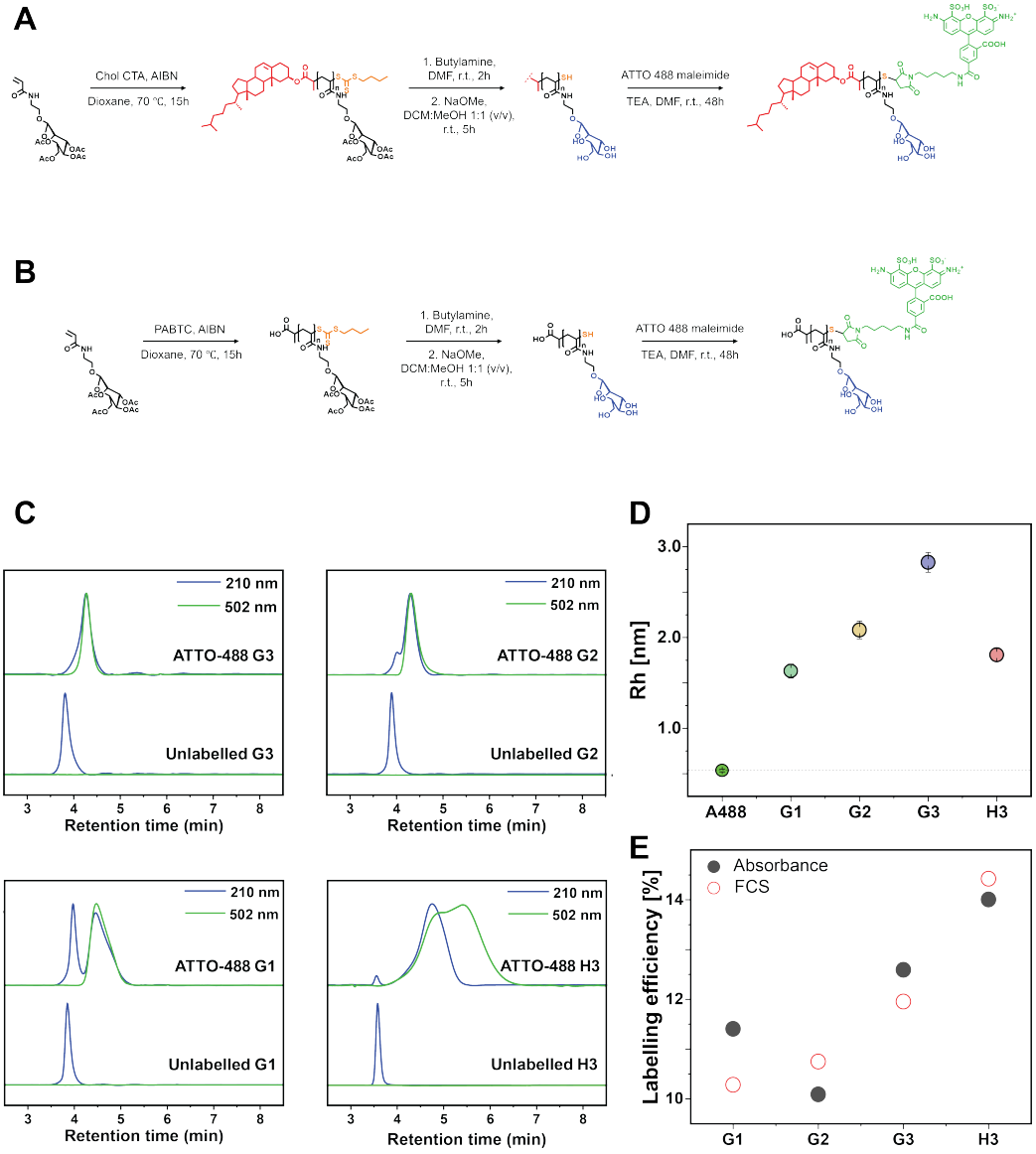

Figure 2: A) Reaction scheme of cholesterol end-functionalized poly-mannose glycopolymers labelled with Atto488. B) without cholesterol. C) HPLC curves for labelled and unlabelled glycopolymers with mannose chain length 10 (**G1**), 20 (**G2**), 30 (**G3**), and without cholesterol glycopolymer of chain length 30 (**H3**). D) Hydrodynamic radius of the different glycopolymers **G1**, **G2**, **G3**, and **H3** labelled with Atto488 as compared to the free dye Atto488 maleimide. E) Measurement of labeling efficiencies determined by FCS and absorbance peaks for **G1**, **G2**, **G3**, and **H3**.

protected polymers (see Figure S5-S7). Corresponding GPC chromatograph of the polymers are shown in the Supporting Information (see Figure S9). Monomodal chromatograms and negligible increase of polydispersity index after deacetylation indicate the absence of any side-reactions during de-protection. The de-protected glycopolymers were readily soluble in water compared to their precursor protected ones, which were insoluble in water.

Full conditions and ^{1}H-NMR of **P1-P3**, and **G1-G3** are provided in the Supporting Information (see Table S1 and Figure S5-S7). ^{1}H-NMR spectroscopy revealed the successful polymer deacetylation with retention of the sugar moieties as well as the cholesterol end-group.

Table 1: Mass characterization of the glycopolymers synthesized in this study

Polymer	Composition	$M_{n,th}(g.mol^{-1})$[a]	$M_{n,GPC}(g.mol^{-1})$[b]	Đ[b]
P1	Chol-$AcMan_{10}$	4900	5300	1.14
P2	Chol-$AcMan_{20}$	9500	9400	1.17
P3	Chol-$AcMan_{30}$	14000	12400	1.20
PH3	$AcMan_{30}$	13600	12900	1.21
G1	Chol-Man_{10}	3400	4600	1.18
G2	Chol-Man_{20}	6200	6200	1.25
G3	Chol-Man_{30}	8900	8100	1.31
H3	Man_{30}	8800	8200	1.27

[a] Calculated using eq 1.
[b] Determined using DMF-GPC

The polymers were analyzed by high-performance liquid chromatography (HPLC) on a reversed phase column to determine their conjugation with ATTO488 maleimide and to verify the absence of free dye. The UV absorption of the unlabelled polymers, which exhibited a peak at 210 nm but not at 502 nm, was compared to that of the labelled ones using the 502 nm signal (see Figure 2B). The signal at 210 nm was selected as it gave the clearest peak in the chromatogram, whereas the signal at 502 nm did not provide any peak for the unlabelled polymers. In a gradient eluent of water and acetonitrile, ATTO488 maleimide eluted at a retention time of 5.8 min. All the glycopolymers had shorter retention times of 3.8 min to 4.5 min, and no peak from the free dye was detected, indicating that the conjugation and the

further purification were efficient. Additionally, we performed fluorescence correlation spectroscopy with the labelled polymers. The autocorrelation curves displayed single component decay characteristics which corroborate the absence of free dye in solution. Furthermore, the hydrodynamic radius of the respective polymers were calculated from the measured diffusion coefficients and compared with the size of free dye (see Figure 2C). In polymer physics, the ρ-ratio, simply defined by $\rho = R_g/R_h$, indicates the topology of the scattering particle for comparatively small particles. We employed Guinier analysis of small angle X-ray scattering (SAXS) data to determine the radius of gyration for our cholesterol end-functionalized polymers (see Table 2, see Supplementary Figure S14), and observed that the ρ-ratio deviates from the theoretical value of a random polymer coil, 1.505.[26] Evidently, this could be due to the cholesterol functionalization, which is why the deviation decreases uniformly as the carbohydrate chain length increases. This is also in line with the assumption of **G1** as a glycolipid with a smaller headgroup as compared to a mucin like **G3**. Additionally, the Porod law describes that the slope of the plot $ln(I(q))$ vs $ln(q)$ for wide angles allows for direct determination of the fractal dimension of the scattering particle.[26] The fractal dimension d_f for our cholesterol functionalized glycopolymers (approx. 2) was consistent with the value expected for Gaussian coils (see Supplementary Table S2). With the preceding experiments and analysis, we were able to accurately determine important structural properties of the compounds in this study which are crucial to model their behavior with lipid bilayer. In the next sections, we will discuss how these cholesterol end-functionalized glycopolymers interact, and influence the mechanical properties of lipid membranes.

Asymmetric Coating and Interaction of Glycopolymers with Fluid Lipid Membranes

Glycopolymers used in this study are classified as end-grafted polymers, with cholesterol serving as the membrane insertion moiety. Extensive theoretical modelling exists for end-grafted polymers interacting with lipid membranes, including some experimental studies

Table 2: Size and structure factor of the glycopolymers synthesized in this study

Polymer	R_h [nm][a]	R_g [nm][b]	ρ
G1	1.63 ± 0.08	3.77	2.31
G2	2.08 ± 0.10	4.23	2.03
G3	2.83 ± 0.11	5.42	1.92
H3	1.81 ± 0.07	2.36	1.30

[a] Measured using FCS
[b] Determined using SAXS

with sterol functionalized polymers.[27–29] Theoretically, such uncharged end-grafted polymers induce the membrane to bend away from the polymer, and a symmetric coating on lipid bilayer would result in an increase in the rigidity of the membrane.[30,31] In this study, we endeavored to estimate how the carbohydrate chain length affects these seemingly simple behaviours. In the following sections, we present how a simple synthetic glycopolymer system can be tuned to behave as a glycolipid or a mucin-mimic by simply tuning the carbohydrate chain length.

Asymmetric coating of fluid supported membranes by glycopolymers

Synthetic model membranes offer the possibility of observing specific interactions of different particles with lipids.[32,33] Supported lipid bilayers (SLBs) offer a controllable and versatile platform for understanding the dynamics of membrane binding agents. SLBs are flat lipid bilayers supported on solid substrate typically glass or mica. Although, the close proximity with the substrate make SLBs less fluid, their attachment to the surface allows for a complete change of solution facing the membrane.

To assess how the different chain length affects membrane properties when added asymmetrically, we incubated the glycopolymers with both SLBs and GUVs composed of fluid phase lipids. To achieve this, we formed SLBs composed of pure **POPC** (or **DOPC**) with 0.05 mol% of lipid conjugated dye Atto655-DOPE and then incubated them with different concentrations of **G1**, **G2**, and **G3** (see Supplementary Figure S10). Before imaging the

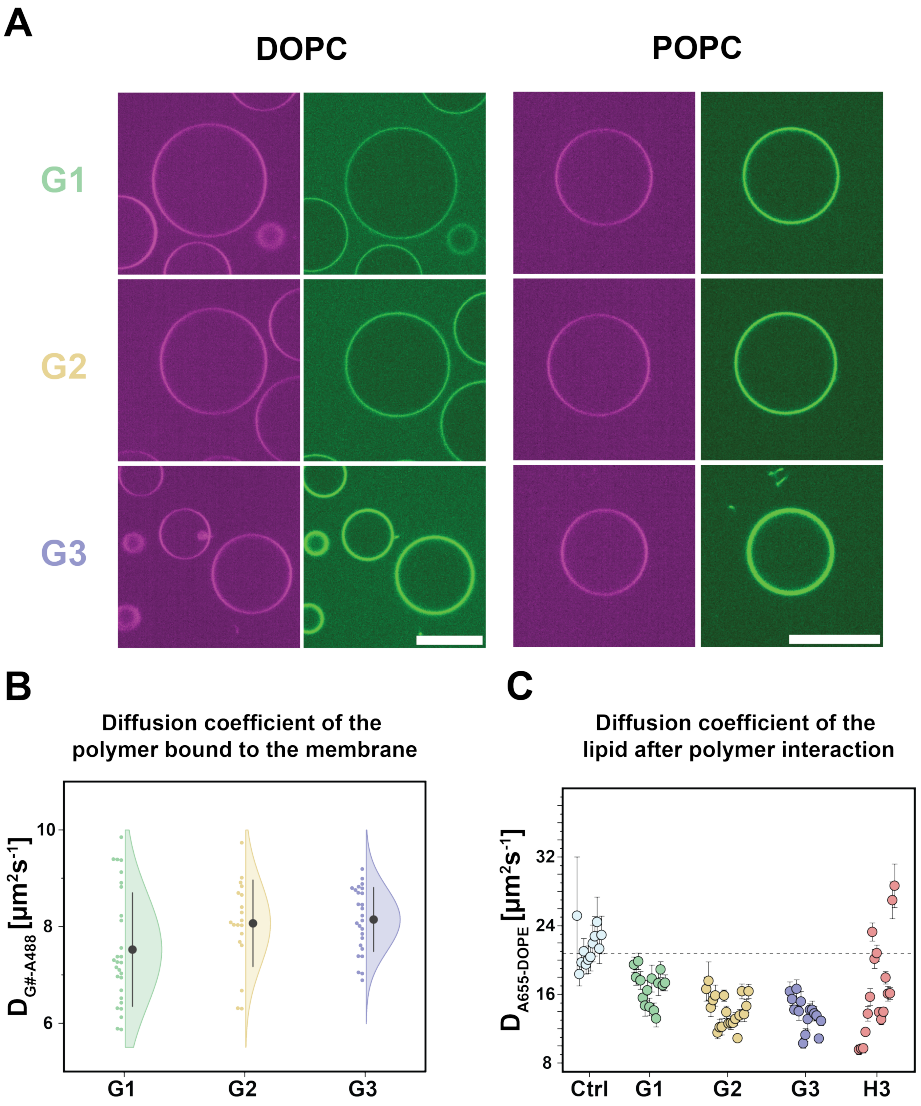

Figure 3: Interaction of cholesterol end-functionalized glycopolymers with fluid lipid membranes. A) TIRF images of co-existing liquid-liquid phases in SLBs composing of **DOPC**, **DSPC**,and cholesterol (molar ratio 35:35:30) at 25 °C (magenta) and insertion of glycopolymers **G1**, **G2**, and **G3** (green). Average rescaled intensities for L_d and L_o domains in the green channel show preferential incorporation of the glycopolymers. Composite images have been individually contrast-enhanced. B) Diffusion coefficient of the inserted glycopolymer as a function of their carbohydrate chain length on GUVs composing of **POPC** at 28 °C. C) Diffusion coefficient of A655-**DOPE** after incubation with the different glycopolymers on GUVs composing of **POPC** at 28 °C. **Scale bar:** 10 µm.

SLBs at 30 °C, we washed the membrane with 10x volume to get rid of all the unbound glycopolymers. As expected, increasing the incubation concentrations of the glycopolymers

resulted in a greater incorporation into the SLB, which was confirmed by the higher fluorescence intensity in the labelled glycopolymer channel (see Supplementary section S5). Interestingly, at the same incubation concentration, we observed that incorporation increased with longer polymer chains. Fluorescence intensities were corrected for the labelling efficiencies of the respective glycopolymers to avoid misrepresentation (see Figure 2D). We observed a uniform incorporation of the glycopolymers as evident from their fluorescence signal, similar to how other glycopolymers have been decorated on cell surfaces.[13]

For a more profound understanding of how the engineering of the lipid bilayer affects the mechanical aspects of the membrane and that of the polymers themselves, we chose **POPC** as our model lipid and chose an incubation concentration of 5 µM as the standard for different chain lengths of the glycopolymers. We performed Z-scan fluorescence correlation spectroscopy (Z-scan FCS) to measure the mobility of the respective glycopolymers once incorporated in the lipid membrane (see Supplementary Figure S15, and Supplementary Table S3 for the diffusion coefficients). Additionally, we obtained number surface densities σ of the respective glycopolymers on the supported membrane (see Figure 4D). The increase in surface density with higher chain length corroborates to our qualitative assessment using fluorescence intensities. In contrast to previously reported mucin mimics which use lipid-like hydrophobic tails as membrane anchors,[13,15,18,34] the presence of cholesterol as an anchor for our polymers offer a much higher incorporation in the membrane for long chain length glycopolymers. Interestingly, **G1** displays a lower incorporation in the membrane, which lead to some intriguing effects on membrane properties as discussed later. We can offer various speculations; i) the low amount of glycans result in a weaker adsorption on the membrane which might precede cholesterol insertion, or ii) the entropic gain for the polymer from the membrane bending away is not balanced by the bending energy. More detailed characterizations would be required to further understand the energy landscape behind this intriguing phenomenon.

Asymmetric coating of fluid free-standing membranes

Giant unilamellar vesicles (GUVs) are free-standing structures that closely resemble cellular membranes in shape, size and composition.[35] GUVs function as an accessible platform for studying membrane dynamics owing to its size compatibility with microscopy techniques. To decorate GUVs with the cholesterol end-functionalized glycopolymers used in this study, we formulated the vesicles composed of pure **POPC** (or **DOPC**) with 0.05 mol% lipid conjugated dye Atto655-DOPE using the electroformation technique such that the vesicles swell in 300 mM sucrose solution under AC electric field. Glycopolymers were then incubated at varying concentrations of 1 µM, 5 µM, and 15 µM and their incorporation in the vesicle membrane was assessed using the fluorescence signal of the conjugated dye ATTO488 (see Figure 3A). Since the lipid membrane is not permeable to the glycopolymers, we expect them to asymmetrically coat the membrane from the outside. The analysis of the fluorescence intensity of the glycopolymer fluorescence was conducted as a function of the carbohydrate chain length, and different incubation concentrations (see Supplementary Section S6). As expected, our observations with the GUVs align with the findings from the previous section, showing that longer carbohydrate chain lengths lead to greater, and uniformly distributed, glycopolymer incorporation with no patch formation observed across the membrane. Saffman-Delbrück model suggests that the diffusion of an intercalated particle within the membrane is only weakly dependent on the size of the embedded particle.[36,37] For all quantitative characterizations, we formed GUVs composed of pure POPC (with 0.002 mol% Atto655-**DOPE**) and incubated with a total concentration of 5 µM of the respective glycopolymer (such that the labelled glycopolymer is in the FCS regime, see Methods section). We performed Z-scan FCS measurements on the labelled glycopolymers and found that the diffusion coefficient of **G1** is lower than **G2** and **G3**, which show similar diffusivity in the membrane (see Figure 3B). Since all the three glycopolymers have the same membrane anchor, this suggests that **G1** has a larger embedded size which leads to slower diffusion upon insertion. This further verifies that **G1** behaves more as a glycolipid when compared to glycopolymers with chain length

greater than n=10. Furthermore, the diffusivity of the membrane reduces with increasing the amount of carbohydrate units (see Table 3, Figure 2C). We associate this reduction in diffusivity to the addition of cholesterol and weak adsorption of the mannose moieties on the membrane due to hydrogen bonding. The addition of the non-end-functionalized glycopolymer **H3** similarly reduces membrane diffusivity, supporting our hypothesis that these polymers exhibit weak adsorption to the membrane. No noticeable increase in polymer signal was detected at the membrane for **H3**. Furthermore, FCS measurements revealed only a fast 3D diffusion component for **H3** when incubated with **POPC** GUVs. Overall, we were able to show that a customizable glycopolymer system can function as a glycolipid like **GM1** or a mucin mimic based on the size of the carbohydrate chain.[38–42]

Effect of glycopolymers on phase separated lipid membranes

GM1 ganglioside has been a recurring subject of interest in the field of biophysics due to its ceramide-like hydrophobic structure.[43,44] This feature has led researchers to explore its role in modulating liquid-disordered (L_d) and liquid-ordered (L_o) phases in membranes.[45] Moreover, at low concentrations, **GM1** partitions from L_d to L_o phase upon binding to **CTxB** and, above 4 mol% doping, it has been shown to spontaneously phase separate into micron-sized L_o domains.[38,46] For this study, we used lipid membranes with **DOPC**, **DSPC** and cholesterol (molar ratio of 35:35:30) containing 0.05 mol% Atto655-**DOPE**. This lipid mixture phase separates into L_d/L_o domains at room temperature.[47] To understand how the glycopolymers in this study would distribute into phases, we incubated them with at desired concentrations for 30 min, before washing off the unbound compounds. All incubation concentrations of the glycopolymers **G1**, **G2**, and **G3** demonstrated a higher incorporation in the L_d domain compared to the L_o domain. The presence of cholesterol as a hydrophobic anchor promotes the incorporation of the polymers in both liquid domains. For **G1**, higher incubation concentrations only increased the degree of polymer incorporation in the L_o domain, while the amount in the L_d domain remained constant (see Figure 4A (right)).

In contrast, for **G3**, the amount of incorporated glycopolymer in either domain did not change significantly with varying incubation concentrations. **G2** exhibited an intermediate behavior, where increasing incubation concentrations from 1 µM to 5 µM led to increased glycopolymer incorporation in the L_d domain, but further increases beyond 5 µM showed no additional effect. Figure 3A (left) shows **TIRF** images of phase-separated SLBs (magenta) after incubation with 5 µM of the specified glycopolymer (green). For a more detailed discussion on the observations, the authors refer to Supplementary section S5.

To gain a holistic understanding of how the preferential incorporation of these glycopolymers impacts membrane phases, we employed phase-separated giant vesicles with the aforementioned lipid composition. Primarily, we observed similar trends upon increasing incubation concentrations as we had observed for phase-separated SLBs (see Figure 4B). Bare vesicles were imaged in the red channel (A655-**DOPE**) to observe the L_d phase (see Supplementary Figure S16). At the same incubation concentrations, we clearly observed that the curvature differences between the L_d and L_o phases decrease as the carbohydrate chain length of the glycopolymer increases (see Figure 4B). This implies a reduction in the line tension at the domain boundary, and similar reduction has been previously reported upon protein binding.[48] Additionally, we observed a reduction in line tension with increasing glycopolymer concentrations (see Supplementary Figure S17). Cholesterol has been shown to reduce the line tension at the domain boundary and lead to the microscopic to nanoscopic domain transitions.[49]

At the domain boundary, cholesterol can "buffer" the interfacial energy, and the glycopolymers could effectively shield the exposed hydrophobic regions induced due to the height mismatch between phases. Therefore, we propose that the overall effect is a result of both the increase in cholesterol content and the glycan shielding at the domain boundary. **GM1** ganglioside displays a similar decrease in line tension when incorporated at molar concentrations below 1 mol%.[50] The authors refer the reader to Supplementary section S9 for a short discussion on the expected molar concentrations of the glycopolymers in this study

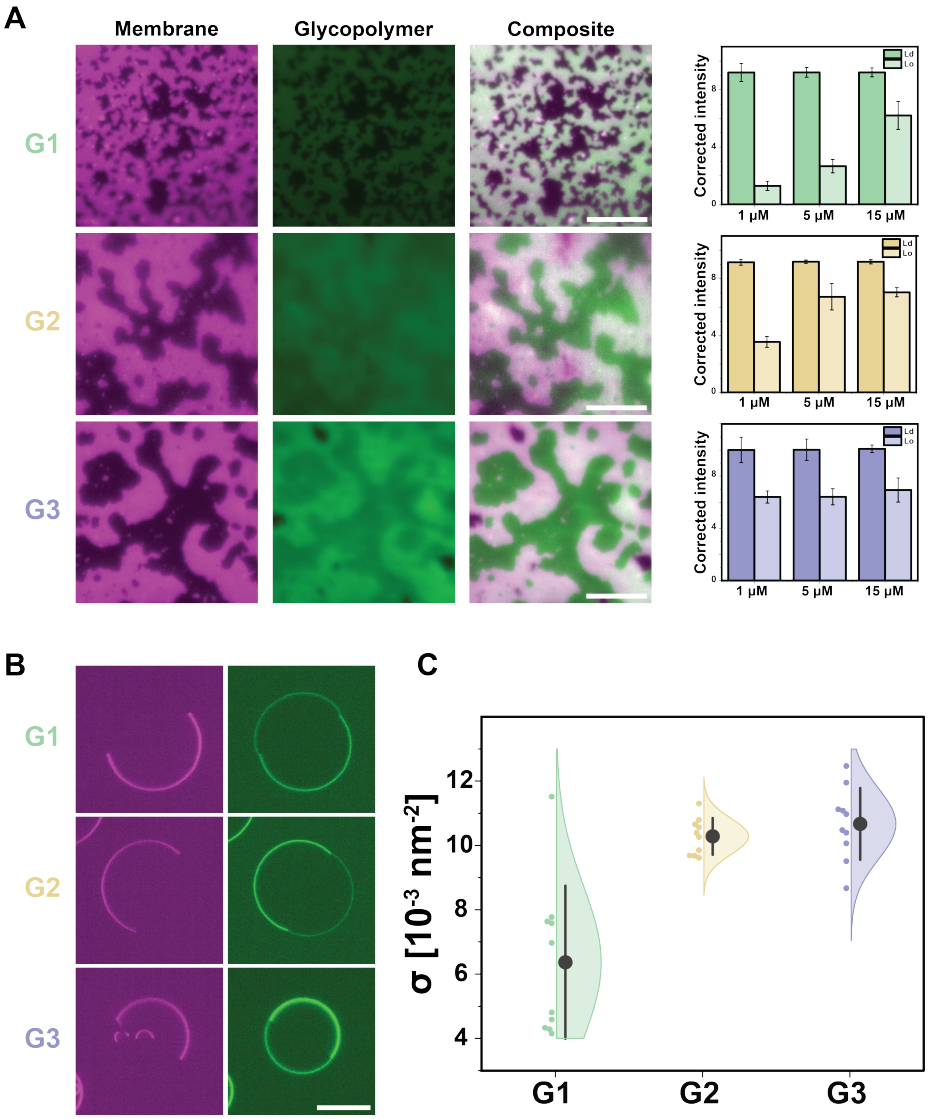

Figure 4: Interaction of cholesterol end-functionalized glycopolymers with phase separated lipid membranes. A) (left) TIRF images of phase separated SLBs (magenta) with incorporated glycopolymers (green) added at 5 µM. concentration. Composite image has been adjusted for contrast. (right) Labelling corrected fluorescence intensity for different incubation concentrations of the glycopolymer in L_d/L_o domains. B) Confocal images of GUVs composed of **DOPC**, **DSPC**, and cholesterol (molar ratio 35:35:30) with glycopolymers added at 5 µM displaying reduction in line tension at the domain boundary. C) Glycopolymer surface number density σ measured using FCS on SLBs composing of **POPC** at 28 °C. **Scale bar:** 10 µm.

after incorporation in the membrane. Supplementary section S10 discusses the outward tubulation at the L_d domain observed with high concentrations of glycopolymers. Thus, a glycopolymer system can be tuned to modulate the phase behavior of lipid bilayers by changing simple parameters such as concentration and carbohydrate chain length.

Membrane curvature and rigidity with symmetric incorporation of glycopolymers across both leaflets

In the preceding sections, we demonstrated how the glycopolymers in this study effectively mimic glycolipids and mucin-like glycoproteins, depending on their carbohydrate chain length. Previously, researchers have shown the effects of polymer adsorption on the bending and elastic modulus of lipid membranes.[21,30,31] Using both mean-field and scaling functional approach, Brooks et al. showed that for both strong and weak adsorption the membrane bends towards the polymer and $\Delta C_{spo} < 0$ and $\Delta\kappa < 0$.[21] On the other hand, for end-grafted polymers, Hiergeist and Lipowsky calculated that the membrane would bend away from the bound polymers with $\Delta C_{spo} > 0$ and $\Delta\kappa > 0$.[28] Additionally, Skau and Blokhuis extended this model for an irreversible adsorption where the desorption kinetics are slow, i.e. irreversible attachment of the polymer to the membrane. They propose that for a model where the amount of irreversibly adsorbed polymer is fixed to a value larger than equilibrium (i.e., the polymers are forced onto the surface), the reduction in rigidity would become less, and ultimately lead to an increased bending rigidity.[22]

With the glycopolymers in this study having the same monomer units (mannose), we assessed how their respective degrees of incorporation change the membrane bending rigidity. To decorate the GUVs symmetrically on both the leaflets, we employed a modified electroformation technique (see Methods section). The vesicles were then diluted in equimolar glucose solutions to measure the bending rigidity using fluctuation spectroscopy. Confocal images of these vesicles show that for **G1**, the vesicles display the formation of microdomains, whereas for **G2** and **G3** no microscopic domains were observed. This is not surprising,

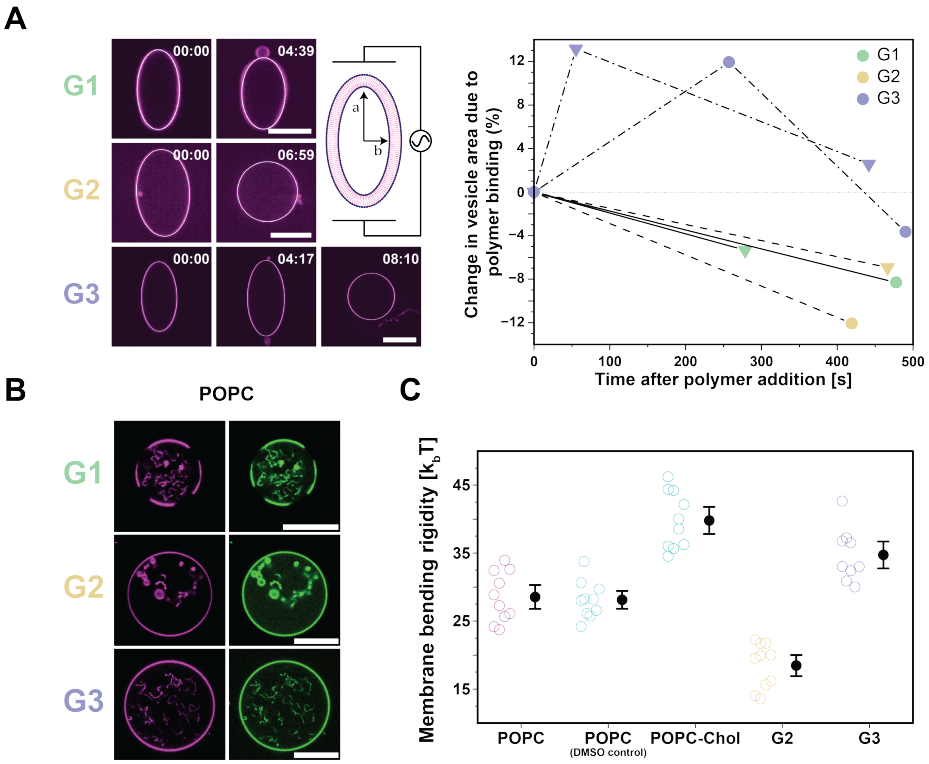

Figure 5: A) (left) Representative images of vesicles deformed under the electric field, the vesicles throw outward tubes or buds when coated with the glycopolymers. The glycopolymers are added to a final concentration of 5 µM. (right) Change in vesicle surface area over time after glycopolymer addition. B) Confocal images of GUVs composing of **POPC** mixed with the respective glycopolymer during formation. Upon dilution in equimolar glucose solution **G1** displays formation of microdomains. C) Membrane bending rigidity for **POPC** vesicles symmetrically coated with the glycopolymers **G2** and **G3** measured using fluctuation spectroscopy. Vesicles with **G1** could not be measured due to microdomain formation and budding. **Scale bar:** 10 µm.

considering that **GM1** has been shown to phase separate above 4 mol% concentration in fluid membranes.[38] Additionally, glucose can act as a crosslinker between mannose units of neighbouring polymers, promoting a "clustering" effect similar to **GM1**.[51] Surprisingly, the labelled glycopolymers partitioned into the L_d phase (see Figure 5B), which can be attributed to the presence of the partially charged fluorophore Atto488. The absence of microdomains for **G2** and **G3** could be linked to the reduced line tension promoting nanodomains. Similar phase-separating effects have also been discussed for high concentrations of diacyl lipid functionalized PEG (**PEGL**) polymers in the past.[29] **G1** also induced budding and shape

transitions upon dilution in glucose, which prevented the measurement of bending rigidity for this case (see Supplementary video S1). Vesicles consisting of **POPC** and **G2** showed a decreased bending rigidity as compared to pure **POPC** vesicles (see Figure 5C). Contrarily, vesicles composed of **POPC** and **G3** showed an increase in bending rigidity. Considering the spontaneous shape transitions, we propose that vesicles containing **G1** would qualitatively be the least rigid among them. Additionally, as the carbohydrate chain length increases, the polymers are increasingly forced onto the membrane, aligning with the predictions of Skau and Blokhuis for irreversible adsorption. Thus, we observe that the implications of intercalation in the membrane, driven by variations in polymer length, significantly impacts the membrane mechanical properties. Moreover, varying the chain length of the polymer offers a precise control over this effect. Future studies will focus on decoupling the contribution of the membrane anchor on the bending elasticity of the membranes.

It was observed that for higher concentrations of polymer addition, some vesicles spontaneously excluded membrane tubes visible in both the membrane and polymer channels. This is in agreement with the proposed theory for end-grafted polymers inducing a positive spontaneous curvature change upon asymmetric incorporation in the membrane.[28] Since the polymers are added from the outside, and these large carbohydrates do not permeate through the bilayer, they are expected to produce a compositional asymmetry across the bilayer. Such membrane curvatures are omnipresent in nature, leading to the formation of a plethora of membrane morphology.[52] Tubulation in GUVs has been previously reported as a result of adsorption of polymers and the molecular mechanism behind the generation of these spontaneous curvatures has been elucidated. Budding and tubulation were also shown when anchoring amphiphilic polymers as well as sugar co-polymers.[53–55]

To observe induced spontaneous curvatures, glycopolymers were incorporated at a final concentration of 5 µM on giant vesicles composed purely of POPC under hyper-osmotic conditions. We observe the change in the surface area of the vesicle to qualitatively measure the fraction of membrane expelled as tubes. We employed electrodeformation of vesicles

under AC electric fields to pull out the thermal fluctuations of the membrane, and restrict the vesicles in a prolate shape (see Figure 5A).[56] We calculated the membrane surface area before addition of the polymers, and then recorded the change in membrane surface area as glycopolymers adsorb on the vesicle and outward tubes are expelled (see Supplementary video S2). Addition of **G1** and **G2** did not show a significant difference between them, and the membrane relaxed through expelling tubes or buds. On the other hand, upon addition of **G3**, a clear increase in surface area was observed before the membrane relaxed by expelling tubes (see Figure 5A). Clearly, the asymmetric addition of the glycopolymers result in a positive C_{spo}. The fraction of surface area expelled as lipid tubes offers a qualitative insight into the change in spontaneous curvatures as higher ΔC_{spo} would result in higher tubulation of the membrane. Accordingly, controlling the chain length of these polymers also allows us to vary the degrees of shape transitions for synthetic cells.

Conclusions

In summary, we present a simple synthetic glycopolymer system with an n-mer of mannose subunits end-functionalized with a cholesterol. These glycopolymers are soluble in aqueous solutions and thus offer the ability to be added to cellular membranes. We measured the hydrodynamic radius and radius of gyration of the glycopolymers to accurately characterize their overall shape and spatial organization in solution. Using FCS, we determined the surface number density σ of the glycopolymers after incorporation at 5 µM incubation concentration on SLBs. We observed that increasing the polymer chain length resulted in a higher degree of incorporation into the membrane. Moreover, upon coating giant vesicles asymmetrically, glycopolymers induced an overall reduction in the membrane fluidity.

Furthermore, the glycopolymers in this study with carbohydrate chain length, n = 10, 20, and 30, respectively, exhibit functionality ranging from glycolipid to mucin mimics. Similar to glycolipids, these glycopolymers modulate L_d/L_o lipid domains upon interaction. We

observed that they initially saturate the L_d phase, before incorporating into the L_o phase. Additionally, higher chain length reduced the line tension at the domain boundaries of giant unilamellar vesicles. We demonstrated that **G1** effectively mimics glycolipids, like **GM1**, and results in softening of the **POPC** vesicles. Upon dilution in glucose, **POPC** vesicles symmetrically coated with **G1** also displayed phase-separation into microdomains. On the other hand, **G3** was shown to mimic glycoproteins like mucins and result in the rigidification of **POPC** vesicles. Interestingly, we also demonstrate that the length can be fine-tuned to produce intermittent effects as with **G2** where the degree of incorporation is much higher than **G1**, and it induces a reduction in the membrane bending rigidity.

Understanding how the glycocalyx influences the cellular membrane, as well as advancements in glycocalyx engineering, are crucial for disease prevention and treatment. Glycocalyx is involved in a variety of processes and remains to be a recurrent topic in glycobiology. Theoretical models for polymer-membrane interactions have been extensively developed over multiple decades; however experimental evidence has been lacking. We applied these models to predict the expected behavior of polymer size and, in turn, generated experimental data points to further refine the theory.

Use of lipid nanoparticles for vaccination and drug delivery has seen an immense interest in this decade, subsequently requiring effective ways of engineering lipid surfaces. Using naturally occurring glycans pose significant challenges in extraction and purification, and subsequently scalability. On the other hand, synthetic glycopolymers remain poorly understood in the context of lipid membranes. We have provided a class of synthetic glycopolymers that can be used for engineering of membrane surfaces, on the one hand as mimics of natural glycolipids and glycoproteins to study complex processes triggered by lectins. On the other hand, these polymers can be used for coating lipid encapsulations used for drug delivery.

Materials and methods

General procedure of glycopolymers syntheses via RAFT polymerization

The syntheses of Acetylated D-Mannose Acrylamide and Cholesterol CTA are described in the Supplementary Section SXX. The polymer was synthesized using the following procedure, utilizing the conditions described in Table S1. To a nitrogen-purged microwave vial, a solution of Cholesterol CTA, AcManEAA, and AIBN in 1,4-dioxane was added and degassed with N_2 for 30 min. The resulting mixture was heated at 70 °C in an oil bath until the polymerization reached 99% monomer conversion as determined by ^{1}H-NMR spectroscopy. Once complete, the polymerization solution was removed from the oil bath, cooled to room temperature, and exposed to oxygen to quench the polymerization.

Reduction of RAFT agent end group

The RAFT agent terminal group of the obtained glycopolymers was reduced to a thiol-terminal in the presence of triethylamine to react it in a thiol-ene reaction with ATTO488 maleimide. ^{1}H-NMR and SEC were used to analyze the polymers before and after reduction. The RAFT end group of the obtained polymers was reduced by the addition of butylamine as the reducing agent in THF. The polymers were added into a microwave vial with THF (130 mg ml^{-1}) and the solution was bubbled for 30 min with nitrogen. Next, butylamine was added to start the reaction (molar ratio of butylamine:RAFT agent end group was 3:1). After that, the mixture was allowed to react for 2 h. Following reduction, the reaction solution was precipitated in a large excess of diethyl ether and isolated by centrifugation. The isolated product was dried under vacuum and characterized by ^{1}H-NMR and DMF SEC analysis.

Deprotection of Glycopolymers

Following the RAFT agent reduction, deacetylation of the mannose moieties was performed. The isolated product was diluted with a methanol/DCM 1:1 mixture to a final polymer concentration of $10\,\mathrm{mg\,ml^{-1}}$. A solution of sodium methoxide in methanol (2 wt%) was added drop-wise under vigorous stirring. After 6 h, the deprotected polymer precipitated out and, after concentrated the solution *in vacuo*, was further purified by extensive dialysis against milliQ water (3 d, with frequent exchanges of the dialysis medium). The resulting clear solution was lyophilized and yielded a fluffy white powder that could readily be re-dispersed in aqueous solutions.

Synthesis of labelled glycopolymers

The obtained de-protected polymers were labelled according to previous literature[57] with slight modifications. Glycopolymers (20 mg) and ATTO488 maleimide (0.12 equ.) were dissolved in DMF (200 µl). The solution was purged with nitrogen for 30 min. A solution of TEA in DMF was prepared, purged with nitrogen, and added slowly to the reaction mixture (2 equ.). The solution was left to react at rt for 48 h. The polymer was dialyzed (MWCO = 2000 Da) against a DMF/water mixture (90/10 V%) for 3 d (the DMF solution was changed twice a day), followed by dialysis against pure water for 3 d to remove DMF. The polymers were freeze dried and analyzed by HPLC, UV-Vis spectrometry and FCS (Fluorescence correlation spectroscopy) to assess their degree of functionalization.

High-performance liquid chromatography (HPLC)

HPLC chromatograms were measured using an Agilent 1260 Infinity II LC system equipped with an InfinityLab Poroshell 120 EC-C18 column ($4.6 \times 100\,\mathrm{mm^2}$) with 2.7 µm packing. Water and acetonitrile were used as mobile phases A and B, respectively, and both contained 0.04vol % TFA. Samples were prepared in water (with 0.04vol% TFA), and the injection

volume was 10 µl. A gradient elution was used where B was increased from 5% to 95% in 20 min and held at that ratio for 5 min and the UV absorbances at 210 nm and 502 nm were measured.

Supported Lipid Bilayer (SLB) Preparation

SLBs were formed via vesicle fusion. Lipids dissolved in chloroform were mixed in glass vials, and after solvent evaporation under N_2 flow, the lipids were resuspended in SLB formation buffer (25 mM tris, 150 mM KCl, 5 mM $MgCl_2$, pH 7.5) to 4 µg µl^{-1}. The obtained large multilamellar vesicle suspensions were then sonicated (Bransonic 1510, Branson) until the solutions were clear. These small unilamellar vesicle (SUV) solutions were either used immediately or stored at −20 °C and re-sonicated before use. For fluorescence imaging of SLBs, sample chambers were assembled from cut 0.5 ml reaction tubes glued (NOA 68, Norland) onto ethanol- and water-rinsed coverslips and cured under 365 nm UV light exposure for 20 min. Immediately before use, chambers were surface-etched with O_2 plasma (30 s, 0.3 mbar, Zepto, Diener Electronics). Next, 75 µl of diluted SUV suspension (ca. 0.5 µg µl^{-1} in SLB formation buffer) were added into prewarmed (37 °C) chambers and incubated for 5 min, during which SLBs formed. After formation, SLBs were washed with 5 ml to 10 ml of SLB washing buffer (25 mM tris, 150 mM KCl, 1 mM EDTA, pH 7.5). Next, each glycopolymer was added at a concentration of 1 µM, 5 µM, and 15 µM and incubated for 30 min at 37 °C. Finally, the samples were washed with 1 ml of SLB washing buffer. SLBs used in fluorescence experiments consisted of **POPC** or **DOPC** with 0.05 mol% Atto655-**DOPE** (ATTO-TEC). For preparation of phase separated SLBs, a slightly different procedure was applied. A freshly cleaved piece of mica was glued onto ethanol- and water-rinsed coverslips and cured under 365 nm UV light exposure for 20 min. Immediately after curing, 75 µl of diluted SUV suspension (ca. 0.5 µg µl^{-1} in SLB formation buffer) were added into prewarmed (65 °C) chambers and incubated for 5 min, during which SLBs formed. After formation, SLBs were washed with 5 ml to 10 ml of SLB washing buffer (25 mM tris, 150 mM KCl,

1 mM EDTA, pH 7.5). Following, the SLBs were left to slowly cool down to 37 °C. Next, each glycopolymer was added at a concentration of 1 µM, 5 µM, and 15 µM, and incubated for 30 min at 37 °C. Finally, the samples were washed with 1 ml of SLB washing buffer. SLBs used in fluorescence experiments consisted of 35 mol % **DSPC**, 35 mol % **DOPC**, 30 mol % Cholesterol, and 0.05 mol % Atto655-**DOPE** (ATTO-TEC).

Electroformation (homogenous GUVs)

Giant Unilamellar Vesicles (GUVs) utilized throughout this work were prepared by electroformation in PTFE chambers with Pt electrodes, as previously described elsewhere with minor modifications.[58] The lipid composition chosen was either **POPC** or **DOPC** doped with 0.05 mol% Atto655-**DOPE**. Briefly, 6 µl of the lipid mixture (2 mg ml^{-1} in chloroform) was spread onto two Pt wires to make a thin film and dried in a desiccator for 30 min. The PTFE chamber was filled with 350 µl of an aqueous solution of sucrose with approximate 300 mOsm kg^{-1} osmolarity (iso-osmolar compared to the imaging buffer). While keeping the PTFE chambers at 37 °C, an AC electric field of 2 V (rms) was applied at a frequency of 10 Hz for 0.75 h, followed by 2 Hz for 0.5 h. The chambers were allowed to cool down to room temperature before performing any experiments. For electrodeformation experiments, GUVs were formed with 100 mM sucrose and 0.5 mM NaCl, and formed with an AC electric field of 3 V (peak to peak) for 1 h.

Electroformation (phase-separated GUVs)

Phase separated Giant Unilamellar Vesicles (GUVs) utilized throughout this work were prepared by electroformation in PTFE chambers with Pt electrodes, as previously mentioned. The lipid composition chosen was **DOPC**: **DSPC**: Cholesterol (35:35:30) doped with 0.05 mol% Atto655-**DOPE** to introduce phase separation. Briefly, 6 µl of the lipid mixture (2 mg ml^{-1} in chloroform) was spread onto two Pt wires to make a thin film and dried in a desiccator for 30 min. The PTFE chamber was filled with 350 µl of an aqueous solution

of sucrose with approximate 300 mOsm kg^{-1} osmolarity (iso-osmolar compared to the imaging buffer). While keeping the PTFE chambers at 65 °C, aan AC electric field of 2 V (rms) was applied at a frequency of 10 Hz for 0.75 h, followed by 2 Hz for 0.5 h. The chambers were allowed to cool down to room temperature before performing any experiments.

GUV preparation with symmetric doping of glycopolymers and confocal imaging

GUVs were prepared by the electroformation method as described elsewhere.[59–61] 1-palmitoyl-2-oleoyl-sn-glycero-3-phosphatidylcholine (**POPC**) (Avanti Polar Lipids, Germany) dissolved in Chloroform (Merck, Germany) were mixed with either 25 mol % cholesterol (Merck, Germany) or each glycopolymer dissolved in dimethyl sulfoxide (DMSO, purchased from Sigma Aldrich, USA) to obtain a solution of final lipid/glycopolymer at a concentration of 4 mM. Then, 20 µl of this lipid solution were spread as a film on a pair of electrically conductive, indium-tin oxide (ITO)-coated glass plates (PGO GmbH, Germany) at room temperature. Afterwards, they were exposed to a stream of N_2 to dry and then placed in a desiccator for 2 h for complete evaporation of the organic solvent. A rectangular Teflon spacer with 2 mm thickness was sandwiched between two ITO glasses with their conductive sides facing each other, to form a chamber of 1.8 ml in volume. The chamber was filled with 20 mM sucrose solution (Sigma Aldrich, USA) and connected to a function generator (Agilent Technologies, USA). To facilitate the electroswelling process, a sinusoidal alternating current (AC) electric field at 10 Hz frequency with a 1.6 V (peak to peak) amplitude was applied for 1 h at room temperature. The obtained vesicles were then harvested and used within 24 h after preparation. Control groups were prepared with pure **POPC** GUVs (in which lipid stocks were dissolved in just chloroform or chloroform and an equivalent volume of DMSO) and 25 mol% cholesterol containing GUVs (while the rest of the lipid solution was **POPC**). Harvested GUVs containing 25 mol % of glycopolymer (without any dye) were 5-fold diluted in 22 mM Glucose solution (Sigma Aldrich, USA) and analyzed via fluctuation spectroscopy

to obtain membrane bending rigidity. GUVs containing dye-conjugated glycopolymers and POPC in 25:75 molar ratio and 0.1 mol% of 1,2-dioleoyl-sn-glycero-3-phosphoethanolamine labeled with Atto647N (Atto647N-**DOPE**, obtained from ATTO-TEC GmbH, Germany) were monitored under confocal microscopy to compare the morphological changes. The osmolarities of the solutions were adjusted with an osmometer (Osmomat 3000, Gonotec GmbH, Germany). The effect of the dilution of GUVs on the morphology was monitored through a Leica TCS SP8 scanning confocal microscope (Wetzlar, Germany) using a 63x (1.2 NA) water immersion objective. The pinhole size during the experiment was set to 1 AU (Airy unit) and the scanning speed was 600 Hz in unidirectional mode. Dye conjugated glycopolymers were excited with a 488 nm laser and the emission signal was collected with HyD (hybrid) detector in the 498 nm to 551 nm range. Atto647N-**DOPE** was excited with a HeNe 633 nm laser and the emission signal was collected with a HyD detector in the range 645 nm to 709 nm.

SAXS data and analysis

Small angle X-ray Scattering (SAXS) measurements were made on a Xenocs Xeuss 2.0 equipped with a Cu kα source collimated by two sets of Scatterless slits. A Pilatus 300k detector mounted on a translation stage was used to record the scattered signal. Measurements were made with a sample to detector distance of 1.196(3) m and the sample chamber filled with air. Giving a q range for the detector between 0.006 Å^{-1} and 0.325 Å^{-1}. The magnitude of the scattering vector (q) is given by $q = (4\pi.sin(\theta))/\lambda$, where 2θ is the angle between the incident and scattered X-rays and λ is the wavelength of the incident X-rays. Azimuthal integrations of the 2D scattering data and background subtractions were performed using Xenocs XSACT software. Samples were mounted in 1 mm thick borosilicate glass capillaries. Samples were measured in 1 h increments and collected data summed for a total counting time of 2 h to 3 h depending on the stability of the sample. The measured scattering signal has been fitted using a unified fit approach which combines a Guinier fit and a Porod fit.[62]

The Guinier region is dependent on the radius of gyration (R_g) of the particles. The Porod gradient provides information on the mass fractal dimension of the particle. All fitting was done using the Irena SAXS macros running in Igor Pro.[63]

Electrodeformation of asymmetrically decorated GUVs

Custom sample chambers were built for performing electrodeformation of vesicles. Briefly, two platinum wires spaced 1 mm were installed on a PTFE chamber which was fixed on top of a #1.5 glass coverslip with the help of magnets. 5 µl to 10 µl of GUV solution was added to 120 µl of outside aqueous solution (50 mM sucrose and 55 mM glucose) to create a hypertonic condition. 20 V (peak to peak) at 0.5 MHz to 1 MHz was applied to attain prolate shape of the vesicles, before adding glycopolymers to the sample chamber to attain a final concentration of 5 µM glycopolymer concentration.

Confocal Fluorescence Microscopy

The same osmolarity was reached in the inner and outer compartments of the vesicle, and the presence of sucrose inside made the vesicle slightly denser than the outer phase, which enables their sedimentation onto the bottom of the wellplate for easier observation. A droplet (16 µl) of diluted sample in glucose solution (300 mM) was deposited on a bovine serum albumin (BSA)-passivated glass plate (the plates were incubated in a water solution of 50 g l^{-1} BSA for 10 min and rinsed with water). To mix vesicles with polymer, an aliquot of polymer stock solution (in the same dilution buffer as the vesicles) was added at the desired concentration and homogenized with gentle agitation with the tip of the pipette. The fluorescence of giant vesicles' membrane was excited at 655 nm, while the fluorescence of the polymers was excited at 488 nm. The fluorescence was recorded on a Nikon/Yokogawa CSU-W1 spinning disk confocal microscope, employing the 488 nm and 641 nm laser lines. The 50 µm pinhole spinning disk was used at 4000 rpm. Nikon Apo TIRF 60x Oil DIC N2 immersion oil objective was used for sample illumination and the images were recorded on pco.edge sCMOS cameras

(pco.edge 4.2 LT USB) at 100 ms exposure time.

Fluorescence Correlation Spectroscopy

Fluorescence correlation spectroscopy (FCS) was performed on the Zeiss LSM980 (Carl Zeiss, Germany) with 488 nm and 639 nm laser lines depending on the experiment, all the data were acquired using Zen 3.5 software (Carl Zeiss, Germany). Z-scan FCS was acquired using a custom macro for adding z-steps which are 200 nm. All data were analyzed using custom MATLAB and Python scripts for generating the auto-correlation curves and for fitting.

Bending Rigidity Analysis

For fluctuation spectroscopy, the harvested vesicle solution was 5-fold diluted in 22 mM Glucose as indicated in the section on GUV preparation. The vesicles were also deflated before imaging by letting water from the vesicle suspension to evaporate at room temperature for 3 min. Membrane fluctuations were observed under phase contrast using an Axio Observer D1 microscope (Zeiss, Germany) equipped with a PH2 40x (0.6 NA) objective. High-speed video recordings were obtained with a Pco.Edge camera (PCO AG, Germany). The image acquisition rate was set to 25 frames per second (fps) and exposure time was 200 µs. Low crossover modes were selected as 3-5 for eliminating effects of vesicle tension. Only defect-free quasi-spherical vesicles with low tension values in the range $1 \times 10^{-7}\,\mathrm{N\,m^{-1}}$ to $1 \times 10^{-9}\,\mathrm{N\,m^{-1}}$ and 5 µm to 20 µm in radius were analyzed. 3000 images were obtained for each set of experiments. All experiments were performed at 25 °C. Vesicle contour was detected through the lab owned software as described previously[64,65] and decomposed in Fourier modes. The bending rigidity was obtained from the mean square amplitude of the Fourier modes. The amplitudes were fit with the Levenberg-Marquardt algorithm for statistical analysis and characterization of the bending rigidity. A χ^2 test was applied to determine the range of modes included, with values in the range of 0.8 to 1.2. At least 10 vesicles were examined per composition.

Acknowledgement

The authors thank Sophia Burick for her help with the electroformation setup. The authors thank Dr. Nishu Kanwa for help with phase-separating membranes. Y.Q. and S.G. acknowledged support from the International Max Planck Research School for Molecules of Life (IMPRS-ML). S.G. was part of the ONE MUNICH Project supported by the Federal Ministry of Education and Research (BMBF), as well as the Free State of Bavaria under the Excellence Strategy of the Federal Government and the Länder. P.S. acknowledged support from Center for NanoScience (CeNS). Y.Q. and A.G. received funding from the European Union's Horizon 2020 research and innovation programme under the Marie Skłodowska-Curie grant agreement no. 859416.

Supporting Information Available

The following files are available free of charge.

- Supplementary information: Supplementary information and figures
- Supplementary Video S1: ...

References

(1) Zhao, T.; Terracciano, R.; Becker, J.; Monaco, A.; Yilmaz, G.; Becer, C. R. Hierarchy of Complex Glycomacromolecules: From Controlled Topologies to Biomedical Applications. *Biomacromolecules* **2022**, *23*, 543–575.

(2) Reily, C.; Stewart, T. J.; Renfrow, M. B.; Novak, J. Glycosylation in health and disease. *Nature Reviews Nephrology* **2019**, *15*, 346–366.

(3) Bogdanov, M.; Mileykovskaya, E.; Dowhan, W. *Lipids in Health and Disease*; Springer Netherlands, 2008; p 197–239.

(4) Lundquist, J. J.; Toone, E. J. The Cluster Glycoside Effect. *Chemical Reviews* **2002**, *102*, 555–578.

(5) Yilmaz, G.; Becer, C. R. Glycopolymer Code: Programming Synthetic Macromolecules for Biological Targeting. *Macromolecular Chemistry and Physics* **2020**, *221*.

(6) Hudak, J.; Bertozzi, C. Glycotherapy: New Advances Inspire a Reemergence of Glycans in Medicine. *Chemistry & Biology* **2014**, *21*, 16–37.

(7) Smith, B. A. H.; Bertozzi, C. R. The clinical impact of glycobiology: targeting selectins, Siglecs and mammalian glycans. *Nature Reviews Drug Discovery* **2021**, *20*, 217–243.

(8) Nguyen, T. H.; Kim, S.-H.; Decker, C. G.; Wong, D. Y.; Loo, J. A.; Maynard, H. D. A heparin-mimicking polymer conjugate stabilizes basic fibroblast growth factor. *Nature Chemistry* **2013**, *5*, 221–227.

(9) Sangaj, N.; Kyriakakis, P.; Yang, D.; Chang, C.-W.; Arya, G.; Varghese, S. Heparin Mimicking Polymer Promotes Myogenic Differentiation of Muscle Progenitor Cells. *Biomacromolecules* **2010**, *11*, 3294–3300.

(10) Vázquez-Dorbatt, V.; Lee, J.; Lin, E.; Maynard, H. D. Synthesis of Glycopolymers by Controlled Radical Polymerization Techniques and Their Applications. *ChemBioChem* **2012**, *13*, 2478–2487.

(11) Pramudya, I.; Chung, H. Recent progress of glycopolymer synthesis for biomedical applications. *Biomaterials Science* **2019**, *7*, 4848–4872.

(12) Miura, Y.; Hoshino, Y.; Seto, H. Glycopolymer Nanobiotechnology. *Chemical Reviews* **2015**, *116*, 1673–1692.

(13) Rabuka, D.; Forstner, M. B.; Groves, J. T.; Bertozzi, C. R. Noncovalent Cell Surface Engineering: Incorporation of Bioactive Synthetic Glycopolymers into Cellular Membranes. *Journal of the American Chemical Society* **2008**, *130*, 5947–5953.

(14) Belardi, B.; O'Donoghue, G. P.; Smith, A. W.; Groves, J. T.; Bertozzi, C. R. Investigating Cell Surface Galectin-Mediated Cross-Linking on Glycoengineered Cells. *Journal of the American Chemical Society* **2012**, *134*, 9549–9552.

(15) Hudak, J. E.; Canham, S. M.; Bertozzi, C. R. Glycocalyx engineering reveals a Siglec-based mechanism for NK cell immunoevasion. *Nature Chemical Biology* **2013**, *10*, 69–75.

(16) Peterson, B. R. Synthetic mimics of mammalian cell surface receptors: prosthetic molecules that augment living cells. *Organic & Biomolecular Chemistry* **2005**, *3*, 3607.

(17) Kanwa, N.; Gavrilovic, S.; Brüggenthies, G. A.; Qutbuddin, Y.; Schwille, P. Inducing Lipid Domains in Membranes by Self-Assembly of DNA Origami. *Advanced Materials Interfaces* **2023**, *10*.

(18) Woods, E. C.; Yee, N. A.; Shen, J.; Bertozzi, C. R. Glycocalyx Engineering with a Recycling Glycopolymer that Increases Cell Survival In Vivo. *Angewandte Chemie International Edition* **2015**, *54*, 15782–15788.

(19) Stuhr-Hansen, N.; Vagianou, C.; Blixt, O. Synthesis of BODIPY-Labeled Cholesterylated Glycopeptides by Tandem Click Chemistry for Glycocalyxification of Giant Unilamellar Vesicles (GUVs). *Chemistry – A European Journal* **2017**, *23*, 9472–9476.

(20) Stuhr-Hansen, N.; Madl, J.; Villringer, S.; Aili, U.; Römer, W.; Blixt, O. Synthesis of Cholesterol-Substituted Glycopeptides for Tailor-Made Glycocalyxification of Artificial Membrane Systems. *ChemBioChem* **2016**, *17*, 1403–1406.

(21) Brooks, J. T.; Marques, C. M.; Cates, M. E. Role of Adsorbed Polymer in Bilayer Elasticity. *Europhysics Letters (EPL)* **1991**, *14*, 713–718.

(22) Skau, K.; Blokhuis, E. Mean-field theory for polymer adsorption on curved surfaces. *The European Physical Journal E* **2002**, *7*, 13–22.

(23) Goswami, R.; O'Hagan, D. T.; Adamo, R.; Baudner, B. C. Conjugation of Mannans to Enhance the Potency of Liposome Nanoparticles for the Delivery of RNA Vaccines. *Pharmaceutics* **2021**, *13*, 240.

(24) Lei, J.; Qi, S.; Yu, X.; Gao, X.; Yang, K.; Zhang, X.; Cheng, M.; Bai, B.; Feng, Y.; Lu, M.; Wang, Y.; Li, H.; Yu, G. Development of Mannosylated Lipid Nanoparticles for mRNA Cancer Vaccine with High Antigen Presentation Efficiency and Immunomodulatory Capability. *Angewandte Chemie International Edition* **2024**, *63*.

(25) Das, R.; Ge, X.; Fei, F.; Parvanian, S.; Weissleder, R.; Garris, C. S. Lipid Nanoparticle-mRNA Engineered Dendritic Cell Based Adoptive Cell Therapy Enhances Cancer Immune Response. *Small Methods* **2024**,

(26) *Light Scattering from Polymer Solutions and Nanoparticle Dispersions*; Springer Berlin Heidelberg, 2007.

(27) Lipowsky, R.; Döbereiner, H.-G.; Hiergeist, C.; Indrani, V. Flexible membranes with anchored polymers. *MRS Proceedings* **1996**, *463*.

(28) Hiergeist, C.; Lipowsky, R. Elastic Properties of Polymer-Decorated Membranes. *Journal de Physique II* **1996**, *6*, 1465–1481.

(29) Evans, E.; Rawicz, W. Elasticity of "Fuzzy" Biomembranes. *Physical Review Letters* **1997**, *79*, 2379–2382.

(30) De Gennes, P. G. Interactions between polymers and surfactants. *The Journal of Physical Chemistry* **1990**, *94*, 8407–8413.

(31) Brooks, J. T.; Marques, C. M.; Cates, M. E. The effect of adsorbed polymer on the elastic moduli of surfactant bilayers. *Journal de Physique II* **1991**, *1*, 673–690.

(32) Schubert, T.; Römer, W. How synthetic membrane systems contribute to the understanding of lipid-driven endocytosis. *Biochimica et Biophysica Acta (BBA) - Molecular Cell Research* **2015**, *1853*, 2992–3005.

(33) Sharma, B.; Moghimianavval, H.; Hwang, S.-W.; Liu, A. P. Synthetic Cell as a Platform for Understanding Membrane-Membrane Interactions. *Membranes* **2021**, *11*, 912.

(34) Rabuka, D.; Parthasarathy, R.; Lee, G. S.; Chen, X.; Groves, J. T.; Bertozzi, C. R. Hierarchical Assembly of Model Cell Surfaces: Synthesis of Mucin Mimetic Polymers and Their Display on Supported Bilayers. *Journal of the American Chemical Society* **2007**, *129*, 5462–5471.

(35) Nair, K. S.; Bajaj, H. Advances in giant unilamellar vesicle preparation techniques and applications. *Advances in Colloid and Interface Science* **2023**, *318*, 102935.

(36) Venable, R. M.; Ingólfsson, H. I.; Lerner, M. G.; Perrin, B. S.; Camley, B. A.; Marrink, S. J.; Brown, F. L. H.; Pastor, R. W. Lipid and Peptide Diffusion in Bilayers: The Saffman–Delbrück Model and Periodic Boundary Conditions. *The Journal of Physical Chemistry B* **2017**, *121*, 3443–3457.

(37) Saffman, P. G.; Delbrück, M. Brownian motion in biological membranes. *Proceedings of the National Academy of Sciences* **1975**, *72*, 3111–3113.

(38) Fricke, N.; Dimova, R. GM1 Softens POPC Membranes and Induces the Formation of Micron-Sized Domains. *Biophysical Journal* **2016**, *111*, 1935–1945.

(39) Patel, D.; Park, S.; Wu, E.; Yeom, M.; Widmalm, G.; Klauda, J.; Im, W. Influence of Ganglioside GM1 Concentration on Lipid Clustering and Membrane Properties and Curvature. *Biophysical Journal* **2016**, *111*, 1987–1999.

(40) Dasgupta, R.; Miettinen, M. S.; Fricke, N.; Lipowsky, R.; Dimova, R. The glycolipid

GM1 reshapes asymmetric biomembranes and giant vesicles by curvature generation. *Proceedings of the National Academy of Sciences* **2018**, *115*, 5756–5761.

(41) Blawitzki, L.-C.; Bartels, N.; Bonda, L.; Schmidt, S.; Monzel, C.; Hartmann, L. Glycomacromolecules to Tailor Crowded and Heteromultivalent Glycocalyx Mimetics. *Biomacromolecules* **2024**, *25*, 5979–5994.

(42) Delaveris, C. S.; Webster, E. R.; Banik, S. M.; Boxer, S. G.; Bertozzi, C. R. Membrane-tethered mucin-like polypeptides sterically inhibit binding and slow fusion kinetics of influenza A virus. *Proceedings of the National Academy of Sciences* **2020**, *117*, 12643–12650.

(43) Brunetti-Pierri, N.; Scaglia, F. GM1 gangliosidosis: Review of clinical, molecular, and therapeutic aspects. *Molecular Genetics and Metabolism* **2008**, *94*, 391–396.

(44) Nicoli, E.-R.; Annunziata, I.; d'Azzo, A.; Platt, F. M.; Tifft, C. J.; Stepien, K. M. GM1 Gangliosidosis—A Mini-Review. *Frontiers in Genetics* **2021**, *12*.

(45) Puff, N.; Watanabe, C.; Seigneuret, M.; Angelova, M. I.; Staneva, G. Lo/Ld phase coexistence modulation induced by GM1. *Biochimica et Biophysica Acta (BBA) - Biomembranes* **2014**, *1838*, 2105–2114.

(46) Bacia, K.; Schwille, P.; Kurzchalia, T. Sterol structure determines the separation of phases and the curvature of the liquid-ordered phase in model membranes. *Proceedings of the National Academy of Sciences* **2005**, *102*, 3272–3277.

(47) Zhao, J.; Wu, J.; Heberle, F. A.; Mills, T. T.; Klawitter, P.; Huang, G.; Costanza, G.; Feigenson, G. W. Phase studies of model biomembranes: Complex behavior of DSPC/DOPC/Cholesterol. *Biochimica et Biophysica Acta (BBA) - Biomembranes* **2007**, *1768*, 2764–2776.

(48) Hutchison, J. B.; Weis, R. M.; Dinsmore, A. D. Change of Line Tension in Phase-Separated Vesicles upon Protein Binding. *Langmuir* **2012**, *28*, 5176–5181.

(49) Tsai, W.-C.; Feigenson, G. W. Lowering line tension with high cholesterol content induces a transition from macroscopic to nanoscopic phase domains in model biomembranes. *Biochimica et Biophysica Acta (BBA) - Biomembranes* **2019**, *1861*, 478–485.

(50) Galimzyanov, T. R.; Lyushnyak, A. S.; Aleksandrova, V. V.; Shilova, L. A.; Mikhalyov, I. I.; Molotkovskaya, I. M.; Akimov, S. A.; Batishchev, O. V. Line Activity of Ganglioside GM1 Regulates the Raft Size Distribution in a Cholesterol-Dependent Manner. *Langmuir* **2017**, *33*, 3517–3524.

(51) Kabbani, A. M.; Raghunathan, K.; Lencer, W. I.; Kenworthy, A. K.; Kelly, C. V. Structured clustering of the glycosphingolipid GM1 is required for membrane curvature induced by cholera toxin. *Proceedings of the National Academy of Sciences* **2020**, *117*, 14978–14986.

(52) Lipowsky, R. Multispherical shapes of vesicles highlight the curvature elasticity of biomembranes. *Advances in Colloid and Interface Science* **2022**, *301*, 102613.

(53) Liu, Y.; Agudo-Canalejo, J.; Grafmüller, A.; Dimova, R.; Lipowsky, R. Patterns of Flexible Nanotubes Formed by Liquid-Ordered and Liquid-Disordered Membranes. *ACS Nano* **2015**, *10*, 463–474.

(54) Tsafrir, I.; Caspi, Y.; Guedeau-Boudeville, M.-A.; Arzi, T.; Stavans, J. Budding and Tubulation in Highly Oblate Vesicles by Anchored Amphiphilic Molecules. *Physical Review Letters* **2003**, *91*.

(55) Shurer, C. R. et al. Physical Principles of Membrane Shape Regulation by the Glycocalyx. *Cell* **2019**, *177*, 1757–1770.e21.

(56) Dimova, R.; Riske, K. A. *Handbook of Electroporation*; Springer International Publishing, 2016; p 1–18.

(57) Boyer, C.; Davis, T. P. One- pot synthesis and biofunctionalization of glycopolymers via RAFT polymerization and thiol–ene reactions. *Chemical Communications* **2009**, 6029.

(58) García-Sáez, A. J.; Carrer, D. C.; Schwille, P. *Liposomes*; Humana Press, 2009; p 493–508.

(59) Angelova, M. I.; Dimitrov, D. S. Liposome electroformation. *Faraday Discussions of the Chemical Society* **1986**, *81*, 303.

(60) Dimova, R. Giant Vesicles and Their Use in Assays for Assessing Membrane Phase State, Curvature, Mechanics, and Electrical Properties. *Annual Review of Biophysics* **2019**, *48*, 93–119.

(61) Dimova, R.; Stano, P.; Marques, C. M.; Walde, P. *The Giant Vesicle Book*; CRC Press: Boca Raton, FL : CRC Press, Taylor & Francis Group, [2020], 2019; pp 3–15.

(62) Beaucage, G. Approximations Leading to a Unified Exponential/Power-Law Approach to Small-Angle Scattering. *Journal of Applied Crystallography* **1995**, *28*, 717–728.

(63) Ilavsky, J.; Jemian, P. R. Irena: tool suite for modeling and analysis of small-angle scattering. *Journal of Applied Crystallography* **2009**, *42*, 347–353.

(64) Gracià, R. S.; Bezlyepkina, N.; Knorr, R. L.; Lipowsky, R.; Dimova, R. Effect of cholesterol on the rigidity of saturated and unsaturated membranes: fluctuation and electrodeformation analysis of giant vesicles. *Soft Matter* **2010**, *6*, 1472.

(65) Faizi, H. A.; Reeves, C. J.; Georgiev, V. N.; Vlahovska, P. M.; Dimova, R. Fluctuation spectroscopy of giant unilamellar vesicles using confocal and phase contrast microscopy. *Soft Matter* **2020**, *16*, 8996–9001.

8.2 P6. Polyproline-polyornithine diblock copolymers with inherent mitochondria tropism

This study reports the design, synthesis, and characterization of novel polyproline-based diblock copolymers as mitochondrially-targeted cell-penetrating oligomers (mt-CPOs). The authors evaluated the potential of these diblock copolymers as efficient mt-CPOs, assessing their cell viability, cellular uptake, and subcellular localization. They found that diblock copolymers with a 1:3 n:m ratio of poly-L-ornithine (PLO) to polyproline (PLP) exhibited enhanced cell viability, uptake, and mitochondrial colocalization in triple-negative breast cancer (TNBC) cells. This study also investigates the interactions of polyproline-based diblock copolymers with model membranes containing cardiolipin (CL), a unique double-negative charged phospholipid present in mitochondrial membranes. Using a combination of biophysical techniques, including atomic force microscopy (AFM), fluorescence correlation spectroscopy (FCS), and fluorescence lifetime imaging microscopy (FLIM), we probed the interactions of the diblock copolymers with CL-rich membranes. Our results show that the diblock copolymers induce physical changes in the membrane properties, including membrane remodeling and buckling, which contribute to their mitochondrial targeting ability. Our study provides valuable insights into the interactions of diblock copolymers with CL-rich membranes, which can be used to design better mitochondrially-targeted drugs. By understanding how diblock copolymers interact with membranes, we can develop drugs that can selectively target mitochondria and avoid non-specific interactions with other cellular membranes. This can lead to improved therapeutic efficacy and reduced side effects. Overall, this study demonstrates the potential of polyproline-based diblock copolymers as efficient mt-CPOs and provides a novel mitochondrially-targeted therapeutically relevant platform for the treatment of various diseases.

Polyproline-polyornithine diblock copolymers with inherent mitochondria tropism

Camilla Pegoraro, Ekaterina Karpova, **Yusuf Qutbuddin**, Esther Masiá Sanchis, Pavels Dimitrijevs, Cristián Huck-Iriart, Svetozar Gavrilović, Pavel Arsenyan, Petra Schwille, Carles Felip-León, Aroa Duro-Castaño, Inmaculada Conejos-Sánchez*, and María J. Vicent*

Author contributions:

C.P. led the synthesis of the conjugate, conformational studies, data curation, formal analysis, investigation, methodology, and writing of the original draft. Cell viability assays and biological studies were carried out by C.P. with support from E.M.S. E.K., CF-L and A D-C led the synthesis of the diblocks and the scale-up demonstration including DoE. **Y.Q.** and P.S. led the synthetic membrane studies and FCS analysis. P.D. and P.A. led the cardiolipin interaction studies and the Oroboros, C.H-I led the SAXS analysis, I.C-S and M.J.V. cosupervise the whole study and contributing to the data curation and formal analysis, as well as in the writing process. Conceptualization, funding acquisition and project administration were led by M.J.V with support from I.C.S. The manuscript was revised by C.P., I.C.-S. and M.J.V., with reviewing and editing contributions from all authors. All authors have read and approved the final version of the manuscript.

C. Pegoraro, E. Karpova, Y. Qutbuddin, E. M. Sanchis, P. Dimitrijevs, C. Huck-Iriart, S. Gavrilović, P. Arsenyan, P. Schwille, C. Felip-León, A. Duro-Castano, I. Conejos-Sanchez, M. J. Vicent, Polyproline-Polyornithine Diblock Copolymers with Inherent Mitochondria Tropism. Adv. Mater. 2025, 2411595.
https://doi.org/10.1002/adma.202411595

RESEARCH ARTICLE

ADVANCED MATERIALS
www.advmat.de

Polyproline-Polyornithine Diblock Copolymers with Inherent Mitochondria Tropism

Camilla Pegoraro, Ekaterina Karpova, Yusuf Qutbuddin, Esther Masiá Sanchis, Pavels Dimitrijevs, Cristián Huck-Iriart, Svetozar Gavrilović, Pavel Arsenyan, Petra Schwille, Carles Felip-León, Aroa Duro-Castano, Inmaculada Conejos-Sanchez, and María J. Vicent**

Mitochondria play critical roles in regulating cell fate, with dysfunction correlating with the development of multiple diseases, emphasizing the need for engineered nanomedicines that cross biological barriers. Said nanomedicines often target fluctuating mitochondrial properties and/or present inefficient/insufficient cytosolic delivery (resulting in poor overall activity), while many require complex synthetic procedures involving targeting residues (hindering clinical translation). The synthesis/characterization of polypeptide-based cell penetrating diblock copolymers of poly-L-ornithine (PLO) and polyproline (PLP) (PLO_n-PLP_m, n:m ratio 1:3) are described as mitochondria-targeting nanocarriers. Synthesis involves a simple two-step methodology based on N-carboxyanhydride ring-opening polymerization, with the scale-up optimization using a "design of experiments" approach. The molecular mechanisms behind targetability and therapeutic activity are investigated through physical/biological processes for diblock copolymers themselves or as targeting moieties in a poly-L-glutamic (PGA)-based conjugate. Diblock copolymers prompt rapid cell entry via energy-independent mechanisms and recognize mitochondria through the mitochondria-specific phospholipid cardiolipin (CL). Stimuli-driven conditions and mitochondria polarization dynamics, which decrease efficacy depending on disease type/stage, do not compromise diblock copolymer uptake/targetability. Diblock copolymers exhibit inherent concentration-dependent anti-tumorigenic activity at the mitochondrial level. The diblock copolymer conjugate possesses improved safety, significant cell penetration, and mitochondrial accumulation via cardiolipin recognition. These findings may support the development of efficient and safe mitochondrial-targeting nanomedicines.

1. Introduction

Subcellular targeting has emerged as a promising strategy in precision medicine, offering advantages such as enhanced specificity and efficacy, minimized resistance issues, and reduced off-target toxicities. Reports of multivalent approaches and studies tracking specific subcellular biomarkers or metabolites have paved the way forward;[1] however, only a few drug delivery platforms have successfully crossed biological barriers and arrived at a target subcellular location. Mitochondria represent the principal target of subcellular targeting efforts due to their critical role in energy generation and cell survival.[2] Multiple studies have reported the design of mitochondrially-targeted nanomedicines that navigate the complex routes required to influence function; nonetheless, significant hurdles remain before they become suitable for clinical use.[3]

Drawbacks associated with mitochondrially-targeted nanomedicines have hampered their clinical progress. For example, mitochondria-targeting moieties such as triphenylphosphonium (TPP) require molecular functionalization,[4] and mitochondrial targeting relies exclusively

C. Pegoraro, E. M. Sanchis, I. Conejos-Sanchez, M. J. Vicent
Príncipe Felipe Research Center
Polymer Therapeutics Lab.
Valencia 46012, Spain
E-mail: iconejos@cipf.es; mjvicent@cipf.es

The ORCID identification number(s) for the author(s) of this article can be found under https://doi.org/10.1002/adma.202411595

DOI: 10.1002/adma.202411595

E. Karpova, C. Felip-León, A. Duro-Castano
Curapath
Av. Benjamín Franklin, 19, Paterna, Valencia 46980, Spain

Y. Qutbuddin, S. Gavrilović, P. Schwille
Max Planck Institute of Biochemistry
Am Klopferspitz 18, 82152 Martinsried, Germany

E. M. Sanchis, I. Conejos-Sanchez, M. J. Vicent
Centro de Investigación Biomédica en Red en Cáncer (CIBERONC)
Instituto de Salud Carlos III
Madrid 28029, Spain

E. M. Sanchis, M. J. Vicent
Príncipe Felipe Research Center
Screening Platform, Valencia 46012, Spain

ADVANCED SCIENCE NEWS
www.advancedsciencenews.com

ADVANCED MATERIALS
www.advmat.de

on mitochondrial membrane potential (promoting charge-based accumulation) that fluctuates as a mode of, e.g., cell cycle status after pharmacological intervention or disease stage.[5] Furthermore, mitochondrially-targeted nanomedicine internalization via endocytic uptake requires endosomal escape (often limiting efficiency,[6]) while the complex synthetic procedures for mitochondrially-targeted nanomedicines remain untranslatable to industrial processes. Overall, we require the definition of alternative designs that solve these issues and must consider rational design approaches to support precise subcellular therapeutic targeting/delivery.

We here report the design of novel diblock copolymers based on the PLO and PLP polypeptides that target mitochondria without functionalization and that can be easily manufactured to support clinical translation. We based the selection of PLP on the results of Chmielewski et al., which highlighted N-functionalized PLP with hydrophobic and/or cationic residues as a concentration- and potential-dependent cell-penetrating mitochondria-targeting peptide.[7–10] We selected PLO given its polycationic nature, which we leveraged to enhance cell uptake and favor cell internalization (by impairing amphiphilicity).[11,12] As opposed to previous related studies, we developed a universal, rapid (two-step), and scalable N-carboxyanhydride ring-opening polymerization (NCA-ROP) methodology for the synthesis of novel biodegradable diblock copolymers that target mitochondria – **PLO$_n$-PLP$_m$**. Selected diblocks (at a 1:3 n:m ratio) targeted mitochondria through a CL-specific potential-independent mechanism following direct cell membrane permeation. Notably, these diblock copolymers exhibited inherent concentration-dependent anti-tumorigenic activity at the mitochondrial level, highlighting their potential as standalone anti-cancer agents or as components of larger drug delivery systems that could provide adequate safety and pharmacokinetic profiles toward clinical translation. To achieve proof of concept in this latter concept, we designed and synthesized a non-toxic polypeptide-based conjugate derivative of **PLO$_6$-PLP$_{22}$** that displayed an improved safety profile, significant direct cell penetration, and subsequent mitochondria tropism. Overall, our results emphasize the versatility of these novel diblock copolymers, establishing a mitochondrial targeting platform that can be translated to an industrial-scale clinical translation.

2. Results and Discussion

2.1. Synthesis and Characterization of Novel Polyproline-based Diblock Polymers

PLO and PLP possess characteristics that aid cellular internalization via direct membrane penetration;[7–12] therefore, we evaluated the suitability of diblock copolymers of PLO and PLP (PLO$_n$-PLP$_m$) as mitochondrially-targeted cell-penetrating oligomers (**mt-CPOs**). To screen candidate mt-CPOs, we first synthesized a family of well-defined PLO$_n$-PLP$_m$ diblock copolymers with different block (n:m) ratios and lengths (**Table 1**, diblock copolymers **6a–i**). We also explored replacing the PLO block with polylysine (PLL), polyhistidine (PHis), or polyarginine (PArg) to evaluate the impact of different polycationic blocks on mitochondrial targeting (Table 1; diblock copolymers 7, 11, and 14). These diblock copolymers were synthesized with the same block ratios and lengths as **6b**, providing analogs to **6b** for comparison. We next performed extensive physicochemical characterization of the above-described diblock copolymers. Table 1 summarizes the critical features, including molecular weight (Mw), polydispersity index (PDI), identity confirmation via gel permeation chromatography (GPC) and nuclear magnetic resonance (NMR), secondary structure analysis using circular dichroism (CD), Zeta potential through dynamic light scattering (DLS), particle size distribution, and aggregation profile determined by small angle x-ray scattering (SAXS). For the sake of brevity, **Figure 1** presents the physicochemical profiles of diblock copolymers **6b**, **h**, and **i** (n:m ratio 1:3), identified as effective mt-CPOs among all evaluated diblock copolymers (detailed in the following sections). The Supporting Information contains comprehensive characterization data for all remaining diblock copolymers. Due to its safer biological profile compared to **6 h** and **i** (detailed in the following sections), we selected diblock copolymer **6b** as our primary mt-CPO candidate.

Scheme 1 (and Schemes S1 and S2, Supporting Information) illustrates the synthesis of diblock copolymers (summarized in Table 1). In brief, we performed the ROP of the protected NCA corresponding to the polycationic component as a first block, adjusting the theoretical degree of polymerization (DP) using n-butylamine (nBuNH$_2$) as the initiator and anhydrous dimethylformamide (DMF) as the solvent. After converting ornithine (Orn) benzyloxycarbonyl (Z), lysine (Lys) benzyloxycarbonyl (Z), and histidine (His) dinitrophenyl (DNP) monomers (in the form of N-carboxyanhydride (NCA) derivatives, Orn(Z)-NCA, Lys(Z)-NCA, and His(DNP)-NCA) into their corresponding polycationic polypeptides PLO(Z), PLL(Z), or PHis(DNP), we added them to a suspension of proline (Pro)-NCA in acetonitrile. The reactions reached completion within 1 h, resulting in good yields (>80%) of the protected diblock copolymers PLO(Z)$_n$-PLP$_m$, PLL(Z)$_n$-PLP$_m$, PHis(DNP)$_n$-PLP$_m$ (described in the Supporting Information as intermediate diblock copolymers **4a-i**, **5** and **10** respectively), with corresponding DP values closely correlating with theoretical values. Given that PLP displays low solubility in the organic solvents typically employed for GPC, we exclusively analyzed the intermediate-protected diblock copolymers via NMR (Figures S1–S4, Supporting Information).

Next, protected diblock copolymers **4a-i** and **5** underwent deprotection with HBr in acetic acid, yielding fully water-soluble diblock copolymers PLO$_n$-PLP$_m$ (diblock copolymers **6a-i**; Figure 1A) (Figures 1B and S5 (Supporting Information) depict examples of NMR spectra for diblock copolymer **6b**) and PLL$_n$-PLP$_m$ (diblock copolymer **7**; NMR spectra in Figure S6, Supporting Information), which displayed a monomodal distribution (Figures 1C and S7 and S8, Supporting Information) and low PDI values (Table 1). In the case of the diblock copolymer **10**, we conducted deprotection using 2-mercaptoethanol in DMF, followed by the acidification of the histidine group to obtain PHis$_n$-PLP$_m$ (diblock copolymer **11**, NMR spectra in Figure S9, Supporting

P. Dimitrijevs, P. Arsenyan
Latvian Institute of Organic Synthesis
Aizkraukles Street 21, Riga LV-1006, Latvia
C. Huck-Iriart
Experiments Division
ALBA Synchrotron Light Source
Cerdanyola del Vallès 08209, Spain

ADVANCED SCIENCE NEWS
www.advancedsciencenews.com

ADVANCED MATERIALS
www.advmat.de

Table 1. Physicochemical properties of polyproline-based diblock copolymers synthesized.

Code	Structure	DP[a] (n) for Polycation	DP[a] (m) for PLP	n:m Ratio	MW by SEC -RALS (kDa)[b]	PDI	Mean Rg_{corr} (nm)[c]	q^{-s}	Zeta Potential (mV)[d]	Secondary Structure[e]
6b	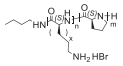	6	22	1:3	3.8	1.090	4.3 ± 0.4	0.2	2.9 ± 0.5	PPII
6h		18	54	1:3	9.5	1.180	3.5 ± ± 0.4	1.66	2.0 ± 0.2	PPII
6i	**PLO_n-PLP_m**	22	64	1:3	11.5	1.190	3.9 ± 0.5	0.36	1.6 ± 0.4	PPII
6a		14	5	3:1	3.0	1.095	1.55 ± 0.1	0.29	6.3 ± 0.2	Random coil
6c		16	30	1:2	13.1	1.289	–	–	7.5 ± 0.2	PPII
6d		35	6	6:1	10.4	1.102	3.8 ± 0.5	1.74	–	Random coil
6e		35	15	2:1	10.2	1.129	1.7 ± 0.2	0.72	13.3 ± 0.6	Random coil
6f		6	12	1:2	3.1	1.052	1.8 ± 0.3	1.31	8.2 ± 0.6	PPII
6g		6	7	1.1	2.5	1.089	1.3 ± 0.5	1.2	10.7 ± 0.3	Random coil
7	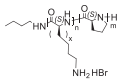	6	19	1:3	3.3	1.090	4.1 ± 0.5	0.0	3.3 ± 0.5	PPII
	PLL_n-PLP_m									
11	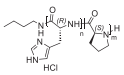	6	25	1:3	–	–	4.7 ± 0.3	0.2	4.4 ± 0.8	PPII
	$PHis_n$-PLP_m									
14	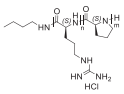	7	23	1:3	4.7	1.039	4.5 ± 0.5	0.0	2.0 ± 1	PPII
	$PArg_n$-PLP_m									

[a] Estimated by nuclear magnetic resonance (NMR); DP – Degree of Polymerization; PLP – Polyproline; [b] Determined by gel permeation chromatography (GPC) wherein the cited numbers are subject to a reasonable uncertainty within the range ±20%; Mw -Molecular Weight; SEC-RALS – Size Exclusion Chromatography-Right Angle Light Scattering; PDI – Polydispersity index; [c] Determined by small angle x-ray scattering (SAXS); q-s represents the power law dependence at low angles in the Guinier region, which correlates with particle aggregation; Rg_{corr} – Correlative Radius of Gyration; [d] Determined by dynamic light scattering (DLS). mV – millivolt; [e] Determined by circular dichroism (CD); PPII corresponds to type II helical conformation.

Information). Finally, we synthesized $PArg_n$-PLP_m (diblock copolymer **14**) by functionalizing the amine groups of diblock copolymer **6b** with 1-guanyl-1,2,4-triazole (Scheme S2, Supporting Information). As the reaction did not introduce new hydrogens discernible in proton NMR, we validated conversion indirectly via NMR by observing proton shifts in adjacent groups (Figure S10, Supporting Information) and through GPC (Figure S11, Supporting Information). We also synthesized homopolymers of PLP (**15a** and **b**) to validate the influence of the polycationic block in further biological studies (SchemeS3 and Table S1, Supporting Information).

We evaluated the secondary structure of all resultant diblock copolymers by CD in water to elucidate structure-activity correlations. PLP homopolymers adopt a type II helical conformation (PPII) in polar solvents, with a pronounced negative band at 206 nm and a weak positive band at 228 nm in CD[13] (example of **15a** and **b** in Figure S12, Supporting Information). Diblock copolymers **6b**, **h**, and **i** exhibited a PPII spectrum (Figure 1D), demonstrating that an n:m ratio 1:3 of PLO and PLP blocks did not alter the typical CD spectra of PLP; however, the intensity of the typical PPII bands increased with PLP block length. Diblock copolymers **6c** and **f** (n:m ratio 1:2) also maintained their PPII features (Figure S13, Supporting Information). Despite the reported increase in stability of the PPII structure due to cationic residues at the C-terminus of the proline block,[14] the higher relative content of PLO (which possesses a random coil structure)[12] masked the contribution of PLP in diblock copolymers **6a**, **d**, **e**, and **g** (Figure S13, Supporting Information). These results highlight the relevance of the PLO: PLP ratio in diblock copolymer conformation. Furthermore, the polycationic block nature did not affect the PPII of diblock copolymers **6b** or analog diblock copolymers **7**, **11**, and **14**, with Lys, His, and Arg as positively charged residues (Figure S14, Supporting Information). We also assessed the stability of the conformation of diblock copolymer **6b**, finding a stable PPII even after multiple freezing and thawing cycles

ADVANCED SCIENCE NEWS
www.advancedsciencenews.com

ADVANCED MATERIALS
www.advmat.de

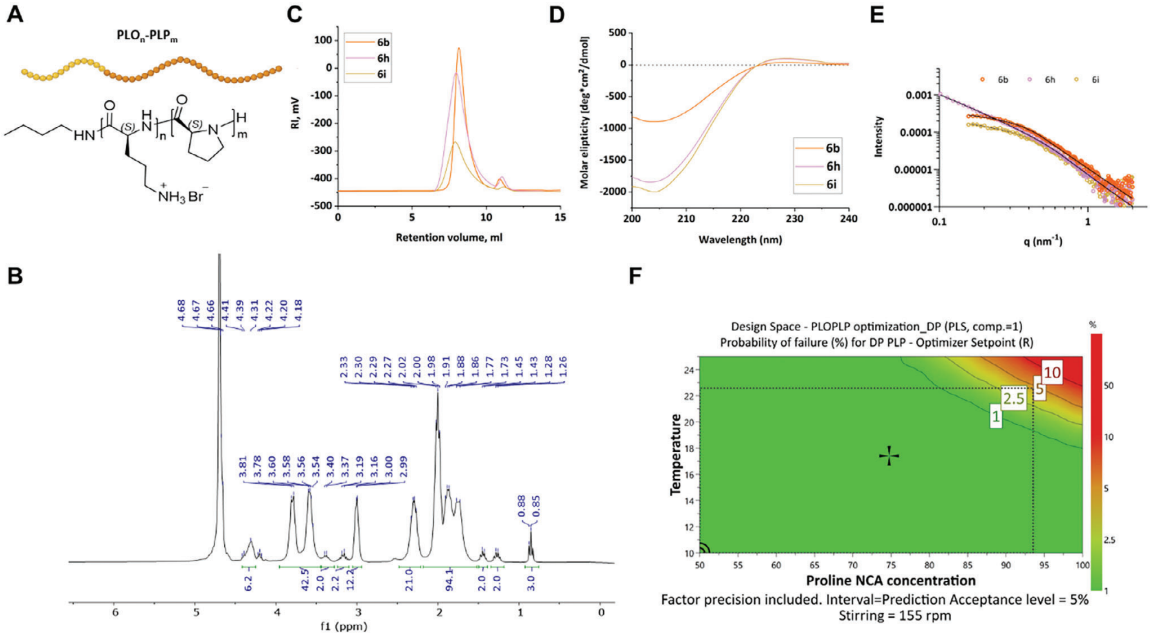

Figure 1. Physicochemical characterization of novel polyproline-based diblock copolymers. A) Schematic representation of the PLO$_n$-PLP$_m$ family of diblock copolymers. B) Nuclear magnetic resonance (NMR) spectra of diblock copolymers **6b** in deuterated water with the characteristic peaks of PLO$_n$-PLP$_m$ diblock copolymers highlighted. C) Gel permeation chromatography (GPC) elugrams of diblock copolymers **6b**, **h**, and **i** in $NaNO_3$ containing 0.005% NaN_3. D) Circular dichroism (CD) spectra of diblock copolymers **6b**, **h,** and **i** in Milli-Q water. E) Small-angle X-ray Scattering (SAXS) data for diblock copolymers **6b**, **h** and **i**. Intensity expressed as a function of the scattering momentum transfer, q ($q = 4\pi\sin(\theta)/\lambda$. F) Proven acceptable range (PAR) defined by the design space for the scale-up optimization of diblock copolymer **6b**.

(Figure S15, Supporting Information) and at physiological temperatures that mimic diblock copolymer storage and biological conditions (Figure S16, Supporting Information). We also discovered that Cy5 labeling (Scheme S4, Supporting Information) did not affect the CD spectra of all diblock copolymers (Figures S17–S19, Supporting Information), indicating that conjugation of a dye (Figure S20, Supporting Information) used for tracking diblock copolymers in vitro and in vivo did not alter diblock copolymer conformation or, potentially, any biological effects.

Diblock copolymers families **6**, **7**, **11**, and **14** exhibited similar radius of gyration (Rg) values, and their Porod exponent "d" of ca. 3 corresponded to the branched polymers of a dense core,[15] as determined by SAXS (Table 1, Figures 1E and S21 and S22, Supporting Information). We applied the Guinier-Porod semiempirical model to identify differences due to variations in DP and monomer composition;[16] the results revealed concentration-independent behavior in PBS – a power law dependence at low angles (q^{-s}) indicated the tendency to form aggregated structures (estimated aggregated particle of Rg maximum < 2.5 nm) for diblock copolymers such as **6 h**, **d**, and **f** (s > 0). Interestingly, diblock copolymer **6b** and analogs **7**, **11**, and **14** did not form aggregates in solution. While diblock copolymers **6b**, **h**, and **i** presented different power "s" values (Table 1), the variation in emission polarity index and the inability to determine a critical aggregation concentration (CAC) by pyrene experiment (Figure S23, Supporting Information) revealed the dynamic nature of compact domain aggregation, which had no impact on their biological effect as demonstrated in section 2.2. The evaluation of Rg values considers a correlative radius of gyration ($R_{g,corr}$) to mitigate the high correlation effects (possibly due to aggregation) in the fitting process.[17] Considering the influence of polymer branching, we considered an expected d-value of 3 for this computation (see the Supporting Information for detailed information).

Even though SAXS experiments revealed similar sizes for all evaluated diblock copolymers, the increased zeta potential for PLO$_n$-PLP$_m$ with differing n:m ratio compared to diblock copolymers **6b**, **h**, and **i** or alternative diblock copolymers (**7**, **11** and **14**) with the same n:m ratio might indicate differences in their solution conformation, which could influence uptake and mitochondrial targeting.

To prepare our synthetic approach for robust scaled-up manufacturing, we employed (for the first time to the best of our knowledge) a design of experiments (DoE)-based approach to optimize the scaled-up synthesis of diblock copolymer precursor of **6b** via one-pot cascade ROP. Given the interdependence of the polymerization processes in steps 1 and 2 (Scheme 1), we proposed sequential process development, starting with improving PLO(Z) screening by focusing on a limited number of factors. We applied critical parameters identified from this optimization to then synthesize the PLO(Z)$_n$-PLP$_m$ diblock copolymer. An initial DoE study on PLO(Z) synthesis evaluated Orn(Z)-NCA and $nBuNH_2$ concentrations and reaction temperature (T) (Table S2, Figures S24 and S25, Supporting Information). We used NMR and GPC to monitor diblock copolymer DP, confirming the attainment of

ADVANCED SCIENCE NEWS
www.advancedsciencenews.com

ADVANCED MATERIALS
www.advmat.de

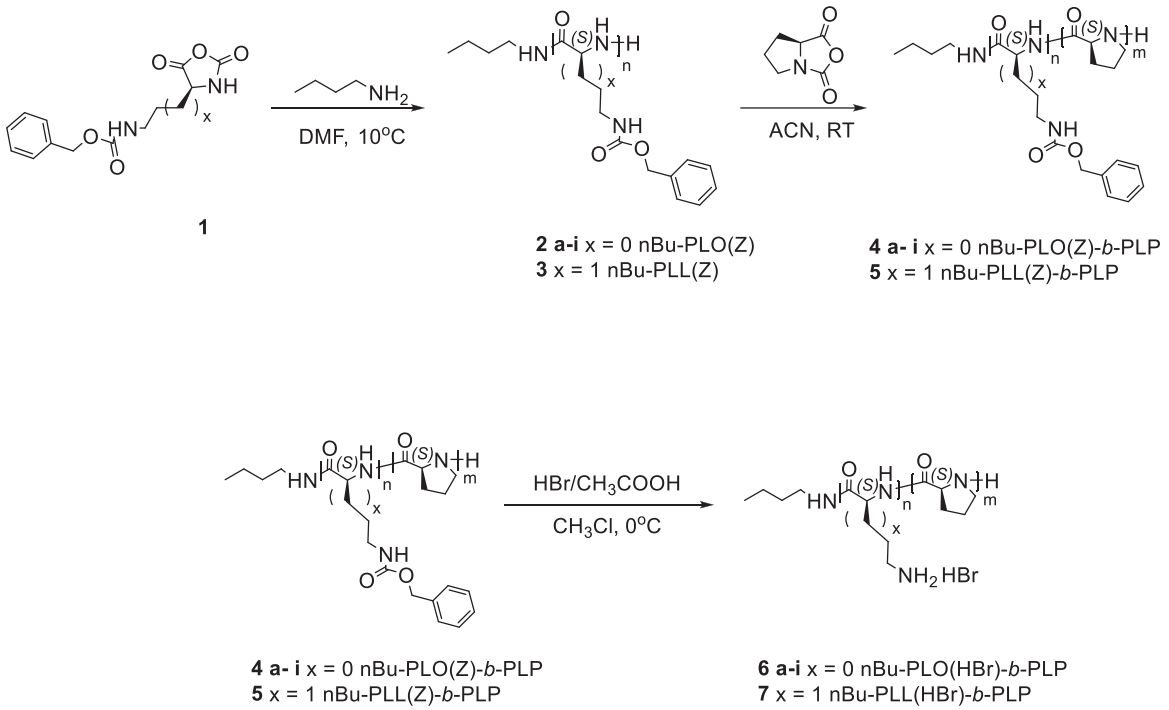

1

2 a-i x = 0 nBu-PLO(Z)
3 x = 1 nBu-PLL(Z)

4 a- i x = 0 nBu-PLO(Z)-*b*-PLP
5 x = 1 nBu-PLL(Z)-*b*-PLP

4 a- i x = 0 nBu-PLO(Z)-*b*-PLP
5 x = 1 nBu-PLL(Z)-*b*-PLP

6 a-i x = 0 nBu-PLO(HBr)-*b*-PLP
7 x = 1 nBu-PLL(HBr)-*b*-PLP

Scheme 1. General synthesis of PLO-*b*-PLP and PLL-*b*-PLP diblock copolymers.

desired Mw values at 4 °C. MODDE simulations predicted optimal concentrations of Orn(Z)-NCA (200-2-36 mg mL^{-1}) and $nBuNH_2$ (23–29 mg mL^{-1}), which combined to give an overall Orn(Z)-NCA concentration range of 140–170 mg mL^{-1}. We applied these values in $PLO(Z)_n$-PLP_m screening, which also considered Pro-NCA and PLO(Z) concentrations, temperature, and stirring rate (Table S3, Supporting Information). We fixed the initiator temperature at room temperature for simplicity despite PLO(Z) synthesis occurring at 4 °C. Monte Carlo simulations identified the optimal Mw and DP (Figure S26, Supporting Information). We employed NMR due to PLP's low solubility in standard GPC mobile phases (DMF and hexafluoroisopropanol); the coefficient plot (Figure S27, Supporting Information) indicated that Pro-NCA concentration, stirring, and temperature affected DP. We set Orn(Z)-NCA at 155 mg mL^{-1} and reduced stirring to 200–350 rpm for future reactor-based scale-up. The new ranges were 50–100 mg mL^{-1} for Pro-NCA, 10–20 °C, and stirring at 270–350 rpm (Figure S28, Supporting Information). Using the circumscribed central composite (CCC) design model, we optimized diblock copolymer precursor **6b** synthesis, focusing on temperature, stirring, and Pro-NCA concentration. The proven acceptable ranges (PAR) were 50–93.5 mg mL^{-1} for Pro-NCA and 10–22.6 °C, ensuring less than 1% failure risk and suitability for reactor transfer with a fixed stirring rate of 155 rpm (Figure 1F). Table S4 and Figure S29 (Supporting Information) detail the experimental matrix and model terms.

The scaled-up synthesis of the candidate diblock copolymer precursor of **6b** (7-fold scale-up concentration) using the estimated parameters obtained in the sequential DoE yielded the corresponding protected polymer with an 80% overall yield and a $PLO(Z)_6$-PLP_{20} ratio (n:m ratio 1:3). Figure S30 (Supporting Information) reports the NMR spectra of this batch. We deprotected the diblock copolymer in dry chloroform using standard conditions with HBr/CH_3COOH yielding **6b**. Figures S31–S33 (Supporting Information) present the NMR spectra, GPC, and MALDI mass spectra of **6b**.

In summary, we successfully synthesized novel PLP-based diblock copolymers using a two-step NCA-ROP method optimized for industrial scalability. The synthesized diblock copolymers exhibited small sizes (<5 nm) and a PPII secondary structure dependent on the n:m ratio and independent of the polycationic block nature. Additionally, variations in zeta potential and dynamic aggregation behavior demonstrated by SAXS suggest that different diblock copolymers may adopt distinct solution conformations. These features may help to define structure-properties relationships that define the cell uptake and mitochondrial-targeting capabilities of diblock copolymers (Table 1).

2.2. PLP-based Diblock Copolymer 6b Exhibits Enhanced Cell Viability, Uptake, and Mitochondrial Colocalization in TNBC Cells

To comprehensively evaluate the potential of PLP-based diblock copolymers as efficient **mt-CPOs**, we extensively screened the

ADVANCED SCIENCE NEWS
www.advancedsciencenews.com

ADVANCED MATERIALS
www.advmat.de

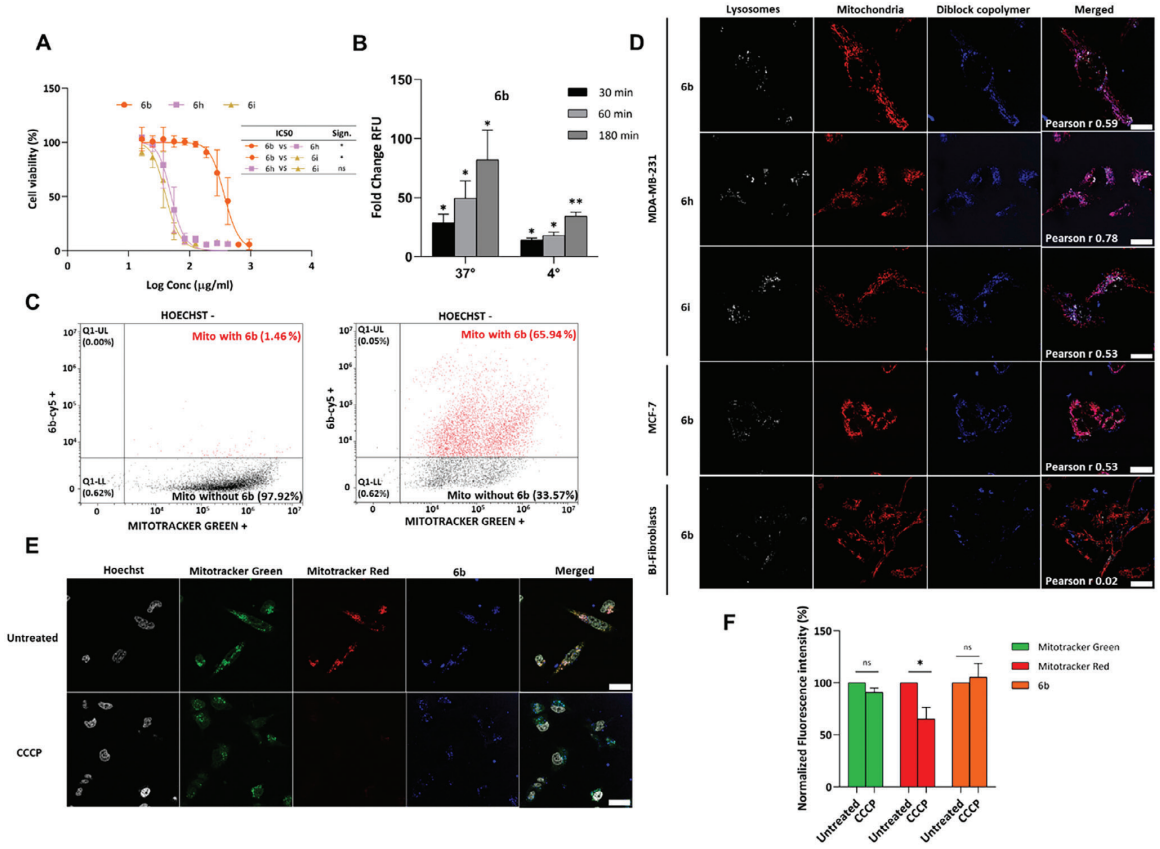

Figure 2. Uptake mechanism and mitochondrial targeting of polyproline-based Diblock Polymers. A) MDA-MB-231 cell viability by MTS assay in response to exposure to diblock copolymers **6b** (IC_{50} = 0.40 mg mL^{-1}), **6 h** (IC_{50} = 0.05 mg mL^{-1}), **6i** (IC_{50} = 0.04 mg mL^{-1}) (72 h, n = 3, mean ± SEM). Sign – Significance **B)** Internalization of diblock copolymer **6b** at 30, 60, and 180 min at 37° (endocytic-dependent pathway) and 4° (endocytic-independent pathway) by flow cytometry (n = 3, mean ± SEM). Data expressed as fold change in relative fluorescence units (RFU) to t = 0; t-test comparing to the control set as 100% (n = 3, mean ± SEM). Significance reported as $*p \leq 0.05$, $**p \leq 0.01$. **C)** Quantification of diblock copolymer **6b** in isolated mitochondria; Cy5 for **6b** and MitoTracker Green FM for isolated mitochondria (black dots: isolated mitochondria positive to MitoTracker Green FM; red dots: isolated mitochondria positive to MitoTracker Green FM and **6b**-Cy5). Upper X-axis: Hoechst-negative population (isolated mitochondria); Y-axis: **6b-Cy5** positive events; Lower X-axis: MitoTracker Green FM positive events. **D)** Confocal images of diblock copolymers **6b**, **h**, and **i** uptake at 2 h post-treatment in MDA-MB 231 cells and **6b** uptake at 2 h post-treatment in MCF-7 cells and BJ fibroblasts following a pulse-chase experiment (see Table S5, Supporting Information) (White – LysoTracker Blue for lysosomes; Red – MitoTracker Red CM-H2Xros for mitochondria; Blue – Cy5-labeled diblock copolymers **6b**, **h**, and **i**. Colocalization with Mitotracker Red was observed (purple) for MDA-MB-231 and MCF-7 cells, and the Pearson r (2 h) value was calculated using the ImageJ JACoP plugin. Scale bar: 10 µm. **E)** Confocal images of diblock copolymer **6b** at 3 h post-treatment in MDA-MB-231 cells in polarized (untreated) and depolarized mitochondria. CCCP-induced depolarization was qualitatively observed by the reduced accumulation of the potential-dependent MitoTracker Red CM-H2Xros, while the potential-independent MitoTracker Green FM maintained its mitochondrial colocalization upon CCCP treatment. Hoechst-stained nuclei in live cells. Scale bar: 10 µm. **F)** Fluorescence intensity quantification of Cy5-labeled diblock copolymer **6b** in polarized and depolarized mitochondria by InCell Analyzer 2200. Cells with polarized mitochondria set as control (100%) (n = 3, mean ± SEM). Significance reported as $*p \leq 0.05$ (ns – not significant).

compounds listed in Table 1, assessing their cell viability, cellular uptake, and subcellular localization.

Cell viability assays using the triple-negative breast cancer (TNBC) human MDA-MB-231 cells as a model revealed the safer profile of the diblock copolymer **6b** compared to **6 h** and **6i** after 72 h of exposure (**Figures** 2A and S34 (Supporting Information) depicts cell viability at 24 h) and other PLO_n-PLP_m diblocks with differing n:m ratios (Figure S35, Supporting Information). The longer length of the cationic block results in higher zeta potential (Table 1), translating into higher toxicity. In contrast, diblock copolymers with Lys, Arg, and His as positively charged residues (**7**, **14**, and **11**) exhibited a safer cytotoxicity profile than the **6b** PLO analog (Figure S36, Supporting Information) despite sharing the same block length and comparable zeta potential. Differences in toxicity profiles may suggest distinct interactions with cell membranes; for instance, PArg interacts more strongly and cooperatively with phospholipid bilayers than PLL, leading to a higher degree of membrane disruption and cytotoxicity.[18–22]

ADVANCED SCIENCE NEWS
www.advancedsciencenews.com

ADVANCED MATERIALS
www.advmat.de

Flow cytometry-based studies of Cy5-labeled diblock copolymer **6b** revealed significant internalization at 4 °C that increased steadily over time, suggesting that energy-independent mechanisms contribute to its significant cellular internalization at 37 °C, with the coexistence of different uptake pathways (Figure 2B). Further quantitation of Cy5-labeled diblock copolymer **6b** accumulation in isolated mitochondria by flow cytometry resulted in a 66% accumulation after 3-hour incubation prior to mitochondria isolation (Figure 2C). The analog diblock copolymer **7** entered MDA-MB-231 cells via energy-dependent pathways at 37 °C, with no significant uptake observed 4 °C at the different time points analyzed (Figure S37, Supporting Information). These results suggest differential uptake mechanisms between **6b** and **7**, which could impact their mitochondrial targeting abilities.

After establishing a range of non-toxic concentrations for diblock copolymer families **6** and **7**, we studied cell internalization and sub-organelle localization using Cy5-labeled derivatives for live-cell confocal fluorescence microscopy monitoring in MDA-MB-231 cells performed at different times (pulse-chase study – 1, 2, 4, 6, 24 h). We could not functionalize diblock copolymer families **11** and **14** with Cy5 (or other biologically relevant molecules such as drugs or biomacromolecules) due to the absence of secondary amines; therefore, we discarded them from further investigation. Image processing using Pearson's correlation coefficient (Pearson r) revealed significant (Pearson $r > 0.5$) mitochondrial colocalization for PLO_n-PLP_m with a 1:3 n:m ratio (Figure 2D). Interestingly, no other PLO_n-PLP_m diblock copolymer colocalized with the mitochondria (Table S5, Supporting Information), with very low Pearson r values observed at all incubation times evaluated. We observed diblock copolymer **6b** in the mitochondria after 2 h of incubation but decreased at 6 h, as observed in the pulse-chase study (Table S5, Supporting Information). The behavior of diblock copolymer **6i** remained similar to **6b**, although mitochondrial colocalization occurred earlier, while we observed the mitochondrial colocalization of **6 h** at 1 h, which remained stable even after 24 h. The lack of mitochondrial targeting observed in diblock copolymers with different n:m ratios and block lengths, compared to **6b**, **h**, and **i**, suggests that Cy5 functionalization does not affect their subcellular localization. Unlike previous studies, where anionic polymers were functionalized with high Cy5 concentration (above μ1 M, > 1 eq.) to favor passive cellular diffusion and mitochondrial targeting,[23–25] in our study, we used a lower concentration (0.015 eq. Cy5 per polymeric chain) and copolymers with a polycationic block. To evaluate the selectivity of **6b**'s mitochondrial targeting activity, we included non-cancer cell lines (BJ fibroblasts and BV-2 microglial cells), an additional cancer line (estrogen-responsive MCF-7 breast cancer cells), and HepG2 cells, a liver-derived cell line employed in toxicology. After establishing non-toxic concentration ranges in 24- and 72-h cell viability studies (Figure S38, Supporting Information), we performed a pulse-chase study for 6b-Cy5 as previously described for MDA-MB-231 cells to assess differential cell internalization and sub-organelle localization. We observed mitochondrial colocalization in MCF-7 cells at 2 h (Figure 2D), which remained stable after 24 h (Table S6, Supporting Information). In contrast, we failed to detect mitochondrial colocalization in BJ fibroblast (Figure 2D), BV-2, or HepG2 cells (Table S6, Supporting Information). These results indicate the differential targeting behavior of 6b in cancer and non-cancer cell lines, suggesting tumor mitochondria specificity. For subsequent investigations, we focused on MDA-MB-231 cells due to their metabolic profile and metastatic potential, providing an ideal model for evaluating the efficacy of our mitochondria-targeted approach in aggressive breast cancer subtypes.

We synthesized and evaluated diblock copolymer **7** as a potential alternative to **6b** given the relevance of PLL as cell-penetrating peptides and their feasible chemical functionalization; however, colocalization analysis revealed lower levels of mitochondria colocalization over time, reaching a maximum Pearson r value of 0.4 at 2 h (Table S5, Supporting Information). Interestingly, we failed to find any diblock copolymer in lysosomes before mitochondrial colocalization, suggesting their significant direct translocation through the cell membrane, as demonstrated by the uptake studies and, thereby, their suitability as efficient mt-CPOs. Moreover, the lack of lysosomal colocalization implies that, in addition to direct cell membrane permeation, the uptake of compound **6b** could be clathrin-independent. These findings would align with previous observations by Kabanov and collaborators, where amphiphilic block copolymers (Pluronics) entered the cell through a concentration-dependent caveolae-mediated endocytosis pathway and subsequently targeted mitochondria.[26–28] To address potential safety concerns related to non-specific membrane disruption that may occur through a direct translocation mechanism, we evaluated the lytic properties of diblock copolymers **6b**, **6 h**, and **6i** using erythrocytes as a model system. Our findings revealed that diblock copolymers **6b**, **6 h**, and **6i** exhibited a robust non-hemolytic profile, with less than 10% hemolysis observed under physiological extracellular conditions (pH 7.4) across all tested concentrations, even displaying lower hemolytic activity than the negative control dextran (Figure S39, Supporting Information). Additionally, the lack of hemolytic activity at a more acidic pH (pH 5.5) (Figure S39, Supporting Information), representative of the lysosomal environment, indicated that diblock copolymers **6b**, **6 h**, and **6i** did not compromise the integrity of intracellular vesicle membranes and supported clathrin-independent uptake mechanisms.

Although colocalization analysis indicated that diblock copolymers **6b**, **h**, and **i** exhibited stronger mitochondrial tropism than diblock copolymer **7**, the Pearson r values suggest that the interaction between diblock copolymer **7** and mitochondria remains non-efficient and non-specific, implying weak and non-specific binding rather than an absence of any interaction. Overall, we found significantly lower direct cellular internalization efficiency of diblock copolymer **7** compared to our candidate mt-CPO **6b**, resulting in lower levels of mitochondrial targeting.

We next explored potential conformational variances between diblock copolymers **7** and **6b** to further decipher the physicochemical reasons behind differential cell uptake patterns. CD analysis of the secondary structure revealed the prevalence of the PLP chain in both diblock copolymers in a similar PPII structure (Figure S14, Supporting Information). Given this lack of insight into the conformational distinctions, we turned to diffusion-ordered NMR spectroscopy (NMR-DOSY), which leverages variations in diffusion coefficients to differentiate between species based on their hydrodynamic radii.[29] While diblock copolymer **6b** displayed a monomodal distribution in agreement with CD, providing evidence of a PPII conformation, diblock

ADVANCED SCIENCE NEWS
www.advancedsciencenews.com

ADVANCED MATERIALS
www.advmat.de

copolymer **7** displayed a temperature-independent bimodal profile, indicating the coexistence of different conformations in solution attributed to the presence of PLL (PPII from PLP contribution and most probably alpha-helix conformation from PLL block) (Figure S40, Supporting Information). These findings agree with the study of Huesmann et al., which demonstrated a similar bimodal distribution in short-protected homopolylysines using GPC, CD, and NMR-DOSY.[30] While they observed the disappearance of the bimodal profile after deprotection, we attributed the persistent bimodal profile in our deprotected diblock copolymer **7** to the charge density λ, defined as the ratio between the net charge on amino acid residues and the total number of amino acids. Notably, at a medium charge density λ (≈0.3, as calculated for diblock copolymer **7**), diblock polypeptides composed of Lys and Leu exhibit a transition region where helical and random coil conformations may coexist rather than solely falling within the random coil region.[31] This transition is characterized by a gradual decrease in helicity, leading to varying solvation environments and water shell interactions that result in distinct hydration radii, as evidenced by our NMR-DOSY results. Due to the presence of PLL, the bimodal conformation in solution of diblock copolymer **7** compared to **6b** (as shown by NMR-DOSY) may justify differential interactions with biological membranes, which could result in less pronounced cellular internalization by direct penetration and reduced mitochondrial targeting of diblock copolymer **7** compared to **6b**, as demonstrated by the biological studies.

Among all evaluated PLO_n-PLP_m diblock copolymers, we identified **6b**, **h**, and **i** as mt-CPOs. Our data indicate that a 1:3 n:m ratio, which ensures PPII formation and low zeta potential (<3 mV), as potentially crucial for mitochondrial targeting. Of note, the nature of the polycationic block also plays a significant role in mitochondrial targeting.

2.3. Understanding the Mitochondrial Targeting of Polyproline-based Diblock Polymers: Binding to Cardiolipin

To investigate the mechanism driving mitochondrial targeting and rationalize the preferential accumulation of PLO_n-PLP_m diblock copolymers with an n:m ratio 1:3, we performed studies involving mitochondria depolarization, interaction with CL, and membrane transformation properties (physical changes, fluidity, and tension).

Mimicking reported mitochondria depolarization studies using flow cytometry,[32] we first explored whether mitochondrial targeting of diblock copolymer **6b** relies on charge affinity due to the highly negative mitochondrial membrane potential. We qualitatively assessed mitochondrial depolarization in MDA-MB-231 cells following a 4-h incubation with 30 µM carbonyl cyanide chlorophenyl hydrazine (CCCP), a mitochondrial uncoupler. We observed a decrease in the fluorescence intensity of the potential-dependent MitoTracker Red CM-H2Xros compared to the potential-independent MitoTracker Green FM in control cells, indicating mitochondrial depolarization (Figure 2E). We then exposed the CCCP-treated MDA-MB-231 cells to Cy5-labeled diblock copolymer **6b** for 3 h (1 h after CCCP incubation) and confirmed the mitochondrial accumulation of diblock copolymer **6b** even under depolarization conditions, as evident from the confocal fluorescence microscopy images (Figure 2E).

We further quantified the fluorescence intensity of Cy5-labeled diblock copolymer **6b** in polarized and depolarized mitochondria, labeled both by MitoTracker Red CM-H2Xros (potential-dependent) and MitoTracker Green FM (potential-independent). In depolarized mitochondria (CCCP versus untreated), we detected a significant reduction in the labeling by the potential-dependent MitoTracker Red CM-H2Xros compared to the polarized mitochondria (red bars; Figure 2F), while labeling by the potential-independent MitoTracker Green FM remained consistent (green bars; Figure 2F). Moreover, we observed no statistically significant variation in Cy5-labeled diblock copolymer **6b** fluorescence between polarized and depolarized mitochondria (orange bars; Figure 2F). These findings suggest that diblock copolymer **6b** targets mitochondria in a potential-independent manner. In contrast to conventional cationic targeting ligands like TPP, which rely solely on the mitochondria potential for their binding affinity, our candidate mt-CPO may be applied when potentials fluctuate, such as during specific cell cycles, after pharmacological interventions, or in distinct disease states.

The mitochondrial membrane differs from all other membranes due to the presence of the unique double-negative charged phospholipid CL, which plays a vital role in mitochondrial bioenergetics, dynamics, mitophagy, and apoptosis and may influence cancer progression and aggressiveness.[33] We studied multiple CL-rich membrane model systems using various approaches to investigate diblock copolymer interactions with CL. We employed a competitive binding assay to study the affinities of our diblock copolymers for CL employing a CL-specific fluorescent probe (MitoCLue)[34] and an artificial membrane model (small unilamellar vesicles (SUVs) composed of 1,2-dioleoyl-sn-glycero-3-phosphocholine (DOPC) and CL (3:1 molar ratio)) or a more complex and biologically relevant model (mitoplasts isolated from rat heart and liver) (Figures S41 and S42, Supporting Information). The results revealed the essential nature of the polycationic component of all tested diblock copolymers for interactions with CL (Table S7, Supporting Information). Diblock copolymers containing PLO (**6b**, **f**, and **g**), PLL (**7**), and PArg (**14**) blocks exhibited comparably high (EC_{50} ≈ 1–1.7 µM) affinity for CL in SUVs (very close to the affinity of the natural CL ligand – cytochrome c; EC_{50} = 0.323 ± 0.017 µM) while PHis: PLP diblock copolymer **11** and homopolymers of PLP (**15a and b**) did not bind to CL-rich SUVs even at a 1 mM (Table S7, Supporting Information). We observed the same trend using the mitoplast membrane model (Figures S41 and S42, Table S7, Supporting Information), although diblock copolymer **6b** had slightly higher affinity compared to other diblock copolymers regardless of mitoplast source (heart or liver tissue, EC_{50} = 3.456 ± 0.065 µM and 3.845 ± 0.314 µM, respectively).

We next confirmed the intercalation of diblock copolymers in the bilayer of CL-containing SUVs using an alternative fluorescent probe – 1,6-diphenyl-1,3,5-hexatriene (DPH) (Figure S43, Supporting Information). DPH fluorescence quenches when displaced from the bilayer hydrophobic region. We again found the superior nature of diblock copolymer **6b** compared to **f** and **g**, which quenched the fluorescence of DPH more effectively at a lower concentration when incubated with CL-containing SUVs (Figure S43, Supporting Information). In contrast, we observed

ADVANCED SCIENCE NEWS
www.advancedsciencenews.com

ADVANCED MATERIALS
www.advmat.de

no interaction between the hydrophobic region of DOPC SUVs (CL-free SUVs) and diblock copolymers **6b**, **f**, and **g**, highlighting the crucial role of CL in facilitating the interaction with the polycationic block of the tested diblock copolymers (Figure S43, Supporting Information). These studies emphasize the significance of polycationic blocks to the mitochondria-targeting properties of our diblock copolymers; however, the high affinity for CL of diblock copolymers **6f** and **g** does not fully account for the lack of their mitochondria targeting in live cells, as seen in Table S5 (Supporting Information). Moreover, our in vitro results revealed mitochondria potential-independent accumulation of diblock copolymers (Figure 2E,F), suggesting that although the electrostatic interaction between the polycationic component and the negatively charged CL strengthens mutual binding, we hypothesized that this interaction does not represent the sole binding force.

To explore our hypothesis, we employed additional model-membrane systems. Supported lipid bilayers (SLBs) serve as valuable model membranes to investigate interactions between polymeric carriers, including diblock copolymers and lipid membranes. SLBs offer numerous advantages, including their ability to replicate the fluidity and composition of biological membranes, thereby creating a physiologically relevant environment for studying membrane interactions.[35] We assembled SLBs with a lipid composition of 2:1 POPC (1-palmitoyl-2-oleoyl-sn-glycero-3-phosphocholine) to CL and a lipid-conjugated dye Atto655-DOPE. We employed Atto488-labeled diblock copolymers to qualitatively image their presence on the membrane. We examined the interaction of diblock copolymers with the membrane after adding 5 µM diblock copolymers to SLBs in buffer B (150 mM KCl, 25 mM Tris, pH 7.2). Simpler model membranes based on SUVs for CL-competitive binding assays and Z-potential measurements (Figure S44, Supporting Information) revealed that diblock copolymers interacted with lipid membranes primarily through ionic interactions, owing to the high negative charge of CL. To discern interactions specific to CL from overall charged interactions, we employed a control membrane composed of equimolar POPC and POPG (1-palmitoyl-2-oleoyl-sn-glycero-3-phosphoglycerol). Notably, diblock copolymers **6b** and **h** formed membrane patches atop CL-rich SLBs that persisted after subsequent washing steps (**Figures 3**A and S45 (Supporting Information) for **6b** titration in CL-rich SLBs). Previous studies employing coarse-grained molecular dynamics (MD) simulations revealed intriguing physicochemical properties of CL-rich membranes; the presence of CL is associated with a reduction in the required lateral pressure for bilayer buckling, rendering membranes more responsive to curvature-inducing agents.[36,37] Additionally, CL tends to accumulate in regions of negative curvature, resulting in localized negative charges. Our observations revealed that diblock copolymers **6b** and **h** form membrane patches, indicating their involvement in curvature-inducing interactions with CL-containing membranes (Figure 3A). Moreover, cationic polymers can bridge these patches, as negatively curved regions display enrichment in negatively charged CL. Overall, our data suggest that polycationic diblock copolymers induce membrane remodeling by facilitating buckling and patch formation, particularly in CL-rich environments, as opposed to the membrane with the same charge distribution as POPG (Figure S46, Supporting Information).

We next employed atomic force microscopy (AFM) to determine the height of the diblock copolymer patches, revealing a doubling in height (≈6 nm) compared to a single lipid bilayer (Figure 3B), consistent with the previous reports on Langmuir monolayers that suggest CL-rich bilayers undergo folding upon increasing lateral pressure.[38] We propose that such CL-rich membranes can generate patches of membrane facilitated by ionic bridging through polycationic diblock copolymers (model shown in Figure 3C). These observations underscore the preference of diblock copolymers **6b** and **6h** to bind CL-rich membranes and induce physical changes in membrane behavior. The alternative diblock copolymer **7** did not reproduce this patch-formation effect in CL-rich membranes (Figure S47, Supporting Information), which may be attributed to its distinct conformation in solution (as previously described). Moreover, for diblock copolymer ratios such as **6a** (n:m ratio 3:1) and **6c** (n:m ratio 1:2), the initial patch formations observed in CL-rich SLBs disappeared rapidly after washing for **6a** and dramatically reduced for **6c** (Figure S48, Supporting Information). As previously discussed, membrane patch formation requires preceding membrane remodeling processes induced by the interaction of diblock copolymers such as **6b** with the CL-rich lipid bilayer. The orientation of the diblock copolymer within the membrane may vary depending on the relative mismatch between PLP length and bilayer thickness;[39] the distinction in proline unit content may prompt a weaker binding affinity to the membrane for diblock copolymer **6a** compared to **6b**, **h**, and **c**, thus resulting in the cessation of induced buckling upon washing. Overall, our data suggest that PLP content and n:m ratio may represent crucial factors controlling CL interactions. Of note, we also established a correlation between patch formation and mitochondrial colocalization in vitro for mt-CPO candidates **6b** and **h** (n:m 1:3 ratio).

Next, we explored membrane transformation upon interaction with diblock copolymers more deeply and investigated membrane fluidity responses. Membrane fluidity – reflecting the interaction of membrane-active agents – of a lipid bilayer is influenced by temperature, lipid composition, substrate (in the case of SLBs), and cholesterol content. CL presence in model membranes significantly impacts bilayer fluidity; consequently, the changing fluidity of model CL membranes after exposure to polymers indicates the degree of membrane interactions. We employed z-scan fluorescence correlation spectroscopy (z-scan FCS) to measure the diffusion of the lipid-conjugated dye Atto655-DOPE and Atto488-labeled diblock copolymers in the lipid bilayer.[40] After adding 5 µM of diblock copolymers and subsequent washing, diblock copolymers **6b** and **h** significantly decreased membrane fluidity (Figure 3D, $D_{6b} = 4.13 \pm 0.25\ \mu m^2 s^{-1}$ and $D_{6\ h} = 5.12 \pm 0.94\ \mu m^2 s^{-1}$) compared to the blank (PBS). We observed consistent membrane fluidity across different membrane regions, with no significant difference between the diffusion coefficients in membrane patches (**6b**$_{patch}$ and **6h**$_{patch}$ in Figure 3D) and regions without patches (**6b** and **6 h** in Figure 3D). These findings suggest that incorporating diblock copolymers **6b** and **6 h** into the membrane uniformly decreased membrane fluidity without localized effects, suggesting that these diblock copolymers induced membrane ordering to initiate buckling. Furthermore, the correlation amplitude from FCS measurements provided insight into the average number of particles in the focal area. A comparison of the average number of

ADVANCED SCIENCE NEWS
www.advancedsciencenews.com

ADVANCED MATERIALS
www.advmat.de

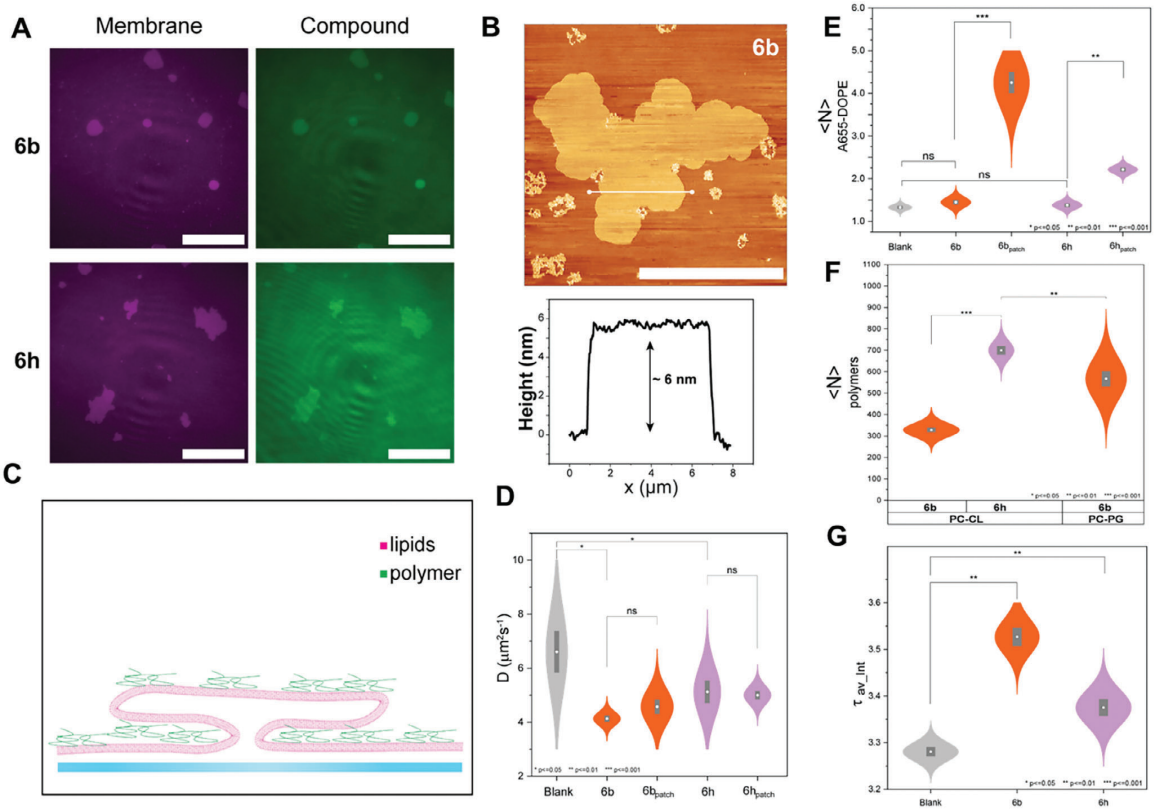

Figure 3. Physical studies of polyproline-based diblock copolymers in cardiolipin-rich membrane models. A) Total internal reflection microscopy images of POPC:CL 2:1 membrane model labeled with Atto655-DOPE (magenta) and diblock copolymers labeled with Atto488 (green). Images depict the formation of patches for diblock copolymers **6b** and **h**. Scale bar: 20 μm. B) Atomic force spectroscopy (AFM) image of a membrane patch. The top Image depicts a POPC:CL 2:1 membrane incubated with 5 μM diblock copolymer **6b** after washing. Scale bar: 10 μm. The bottom graph indicates the membrane patch height (nm) along the selected region (denoted by the white line) in the AFM top figure (x-axis – width in μm). C) Schematic of the proposed membrane buckling and folding procedure that forms patches. D) Diffusion coefficient (D, $\mu m^2 s^{-1}$) of the membrane at 28 °C for Atto655-DOPE for cardiolipin-rich membranes incubated with diblock copolymers at patch-containing (**6b**$_{patch}$ and **6h**$_{patch}$) and patch-lacking (**6b** and **6 h**) regions. E) Average number of A655-DOPE particles (<N> A655-DOPE, number of membrane particles) for cardiolipin-rich membranes incubated with diblock copolymers at patch-containing (**6b** and **6 h**) and patch-lacking (**6b**$_{patch}$ and **6h**$_{patch}$) regions acquired through fluorescence correlation spectroscopy. F) Average number of diblock copolymer particles (<N> polymer) bound to cardiolipin-rich membranes acquired through fluorescence correlation spectroscopy of labeled diblock copolymers **6b** and **6h**. G) Intensity-averaged fluorescence lifetime of Flipper-TR-stained small unilamellar vesicles (τ_{av_Int}) incubated with diblock copolymers **6b** and **6h**. Figure C, D, E, and G data were analyzed using two-way ANOVA. Significance reported as $*p \leq 0.05$, $**p \leq 0.01$, $***p \leq 0.001$ (ns = not significant).

Atto655-DOPE membrane particles revealed an $\frac{\langle N_{patch} \rangle}{\langle N_{no\ patch} \rangle}$ value for diblock copolymer **6b** of 2.94 and **6 h** of 1.60 (Figure 3E), indicating a 2-fold higher concentration of lipid particles in the focal area for **6b** compared to **6h**. We performed similar measurements for Atto488-labeled diblock copolymers, wherein diffusion in the lipid membrane reflects interaction strength (Figure S49, Supporting Information); overall, diblock copolymer **6 h** demonstrated a significantly lower diffusion coefficient than **6b**, suggesting stronger membrane interactions. Overall, diblock copolymer **6 h** displayed a significantly higher binding affinity to the CL membrane than **6b** (from the correlation amplitude), while we observed no significant differences upon incubation of **6b** with equimolar POPC-POPG control membranes (Figure 3F).

Agents inducing membrane curvature also modulate local membrane tension.[41] The fluorescent membrane tension probe, Flipper-TR (termed Flipper hereafter), displays alterations in fluorescence lifetime in response to changing membrane tension/order[42] and can probe the response of different polymers incubated with CL-containing SUVs.[43] After adding 1 μM Flipper, we incubated SUVs with 5 μM diblock copolymers; subsequently, we diluted the SUVs 10-fold before measuring Flipper fluorescence lifetime at 25 °C (Figure S50, Supporting Information). The intensity-averaged fluorescence lifetime of Flipper increased for diblock copolymers **6b** and **6 h** compared to a blank sample with CL-containing SUVs ($\tau^{blank} = 3.28 \pm 0.02$ ns), while diblock copolymer **6b** exhibited a significantly higher response compared to **6 h** ($\Delta\tau^{6b} = 0.18$ ns and $\Delta\tau^{6h} = 0.09$ ns) (Figure 3G).

ADVANCED SCIENCE NEWS
www.advancedsciencenews.com

ADVANCED MATERIALS
www.advmat.de

An increase in fluorescence lifetime indicates elevated CL membrane tension, corroborating the previously observed reduced fluidity and demonstrating the ability of diblock copolymers **6b** and **6 h** with a n:m ratio 1:3 to alter CL-containing membrane order.

Overall, the CL-specific interaction of diblock copolymers suggests their unique affinity for mitochondria, which holds relevance for developing mt-CPOs and their potential use as antitumorigenic therapeutics.

2.4. Unveiling the Inherent Biological Activity of Novel Mitochondrial Targeting Polyproline-Based Diblock Polymers at the Mitochondrial Level

Common mitochondrial abnormalities in cancer cells, such as hyperpolarized mitochondrial membrane potential (−220 vs −140 mV in normal cells), elevated pH, and increased reactive oxygen species (ROS) production, highlight the significance of targeting mitochondria in cancer therapy.[4,44] One example is the Warburg effect – using glycolysis for energy production even in the presence of oxygen – representing the primary type of metabolic reprogramming in cancer cells (including MDA-MB-231). However, flexible mitochondrial metabolism also supports cells' ability to adapt to metabolic stress and maintain their metastatic potential, which plays a crucial role in cancer cell survival.[45] For these reasons, we next performed activity studies to explore the impact of our diblock copolymers (evaluated at sub-IC_{50} concentrations (>IC_{15})) on mitochondrial metabolism and cell morphology in MDA-MB-231 cells.

Given the pivotal role of mitochondrial membrane potential in regulating membrane permeability, cell apoptosis, and the selection of non-functional mitochondria, a treatment strategy that induces mitochondrial depolarization may hold promise as an antitumorigenic therapy. First, we sought to demonstrate that diblock copolymers **6b**, **h**, and **i** induced rapid mitochondrial depolarization in cells using the fluorescent probe 5,5′,6,6′-tetrachloro-1,1′,3,3′-tetraethylbenzimidazolcarbocyanine iodide (JC-1). After accumulating in polarized mitochondria, JC-1 emits red fluorescence due to the formation of aggregates; meanwhile, JC-1 emits green fluorescence from J-monomers released into the cytosol when in depolarized mitochondria.[46] We quantified changes in membrane potential by measuring the red/green fluorescence intensity ratio; overall, we observed a significant loss of mitochondrial membrane potential after a 6-h incubation with diblock copolymers **6b** and **6 h** compared to non-treated control cells (set at 100%) that displayed partial restoration by 24 h (**Figure** 4A). Diblock copolymer **6i** initially induced significant mitochondrial depolarization, which recovered after 6 h but became re-established after 24 h (Figure 4A). Despite cell adaptation to membrane potential perturbation, induced mitochondrial depolarization may represent a crucial initial mechanism that alters the mitochondria, particularly in cancer cells. Indeed, mitochondrial depolarization may serve as a critical early event that triggers various downstream effects, including increased ROS production, disrupted ATP synthesis, and activation of apoptotic pathways.[47,48]

We next demonstrated that diblock copolymers **6b**, **h**, and **i** induced significant increases in ROS production (**6b<6h<6i**) after 24 h of treatment compared to non-treated control cells (set as 100%) (Figure 4B). Although cancer cells exhibit higher ROS levels due to increased hypoxia and levels of electrons leaking from the electron transport chain (ETC), the upregulation of antioxidant enzymes (e.g., superoxide dismutase) maintains redox homeostasis.[49,50] However, additional ROS production in cancer cells beyond basal levels can disrupt redox homeostasis and trigger oxidative stress, which leads to cell death.

Given the pivotal role of mitochondria in cellular energy production via oxidative phosphorylation (OXPHOS), we analyzed metabolic alterations following diblock copolymer **6b**, **h**, and **i** treatment at sub-IC_{50} final concentrations (>IC_{40} (C1)) and a diluted concentration (>IC_{15} (C2, dilution factor C1/C2 = 1.5)) to study concentration-dependent effects. Seahorse XF Analyzer studies revealed a compromised oxygen consumption rate (OCR; related to different mitochondrial functions) after a 24-h exposure to certain diblock copolymers (Figure 4C). Diblock copolymers **6 h** and **i** induced a significant concentration-independent reduction of OCR related to the spare respiration capacity (SRC) (Figure 4C, left), a functional parameter that measures how cells respond to increased energy demands by enhancing mitochondrial activity. Even though cancer cells compensate for ATP demand through aerobic glycolysis (the Warburg effect), which positively correlates with the aggressive nature of tumor cell lines such as MDA-MB-231,[51] the decreased SRC induced by diblock copolymers **6 h** and **i** holds relevance considering that conventional chemotherapy increases SRC as a drug resistance mechanism.[52] Diblock copolymers **6b**, **6 h** (both concentration-independent), and **6i** (concentration-dependent) significantly reduced the OCR related to ATP production, indicating decreased basal respiration to produce ATP coupled to the ETC during OXPHOS in mitochondria (Figure 4C, right), particularly by diblock copolymer **6b**.

To confirm Seahorse results and investigate the mechanisms of action of diblock copolymer with the most significant therapeutic potential, we analyzed OCR after acute treatment with diblock copolymer **6b** using a substrate-uncoupler-inhibitor titration (SUIT) protocol in the Oroboros Oxygraph O2k system (Figure 4D). We treated MDA-MB-231 cells at sub-IC_{50} final concentrations (>IC40 (C1)) and diluted concentrations (>IC_{15} (C2 and C3, dilution factor C1/C2 = 2; C2/C3 = 5)) to study potential concentration-dependent effects. Diblock copolymer **6b** induced a significant concentration-dependent reduction in OCR in LEAK and OXPHOS states in the presence of complex I (CI) substrates pyruvate and malate (Figure S51, Supporting Information). The LEAK state, characterized by a non-phosphorylating resting state, is a reference point for measuring ATP production efficiency in the OXPHOS state. Adding glutamate as another NADH-dependent CI substrate did not compensate for the **6b**-induced decreased OCR observed in the presence of pyruvate and malate (Figure 4D). These results suggest either direct CI inhibition of or CI-CL complex disruption that significantly reduces CI activity.[53] The strong dependence of CI function on CL may be compromised by **6b**-induced membrane structural rearrangements (patch formation), leading to decreased enzymatic activity. The addition of the complex II (CII) substrate succinate induced maximal electron transfer capacity (Figure 4D), as evidenced by the absence of any effect after standard uncoupler CCCP treatment (Figure S51, Supporting Information). This data indicates that diblock copolymer **6b** significantly reduces the ETC coupling

ADVANCED SCIENCE NEWS
www.advancedsciencenews.com

ADVANCED MATERIALS
www.advmat.de

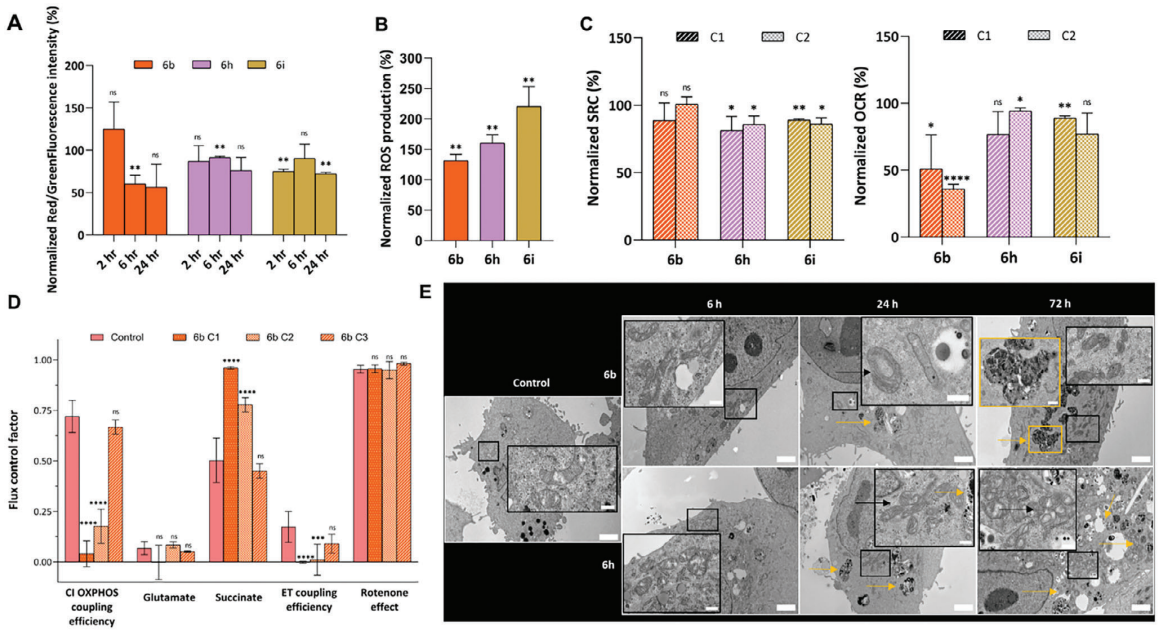

Figure 4. Mitochondria-dependent biological activity of polyproline-based diblock copolymers. **A)** Mitochondrial membrane potential measured after treatment with diblock copolymers **6b**, **h,** and **i** over time (Concentration (C): C < IC_{50}; t-test comparing to control set as 100%; $n = 3$, mean ± SEM). **B)** Reactive oxygen species (ROS) production analysis after a 24-h treatment with diblock copolymers **6b**, **h,** and **i** (Concentration (C): C < IC_{50}; t-test comparing to control set as 100%; $n = 3$, mean ± SEM) **C)** Spare respiration capacity (SRC, left) and oxygen consumption rate (OCR) (right) analysis by Seahorse XF after a 24-h treatment with diblock copolymers **6b**, **h,** and **i** (Concentration (C): C1 < IC_{50}, diluted concentration C2 (C1/C2 = 1.5); OCR measured in pmol/min/2 × 10^4 cells; t-test comparing to the control set as 100%; $n = 3$, mean ± SEM. **D)** Flux control factor analysis (see **SI** for details) after treatment with diblock copolymers **6b** (Concentration (C): C1 < IC_{50}, diluted concentration C2 and C3, dilution factor C1/C2 = 2; C2/C3 = 2); OCR measured in pmol/(s*1 × 10^6 cells), two-way-ANOVA test comparing to control, $n = 3$, mean ± SEM). **E)** Mitochondria morphological analysis by transmission electron microscopy after treatment with diblock copolymers **6b** and **h** (Concentration (C): C < IC_{50}) over time. Lysosomal degradation is highlighted by the yellow arrows. Scale bar main images: 20 µm; scale bar inset images: 500 nm. Significance reported as *$p \leq 0.05$, **$p \leq 0.01$, ***$p \leq 0.001$, ****$p \leq 0.0001$ (ns = not significant).

efficiency to OXPHOS, enabling the ETC to operate maximally independent of ATP synthesis via OXPHOS. These findings, supported by reduced CI OXPHOS and ETC coupling efficiency, provide evidence that diblock copolymer **6b** affects mitochondrial metabolism.

We morphologically analyzed MDA-MB-231 cells after treatment with diblock copolymers **6b** and **h** at various time points to investigate the relationship between metabolic alterations and mitochondrial morphology. Transmission electron microscopy (TEM) analysis revealed several changes in mitochondrial morphology in treated cells compared to control cells (Figure 4E). The qualitative analysis by TEM revealed a time-dependent increase in the number of lysosomes engulfing mitochondrial material (yellow arrows in Figure 4E), suggesting lysosomal-dependent mitophagy, a selective degradation process for damaged/dysfunctional mitochondria. Mitophagy impairments (usually preceded by lost mitochondrial homeostasis[54]) that include mitochondrial depolarization and increased ROS production have been linked to cancer progression and drug resistance;[55] however, studies have reported the efficacy of therapies targeting mitochondrial dysfunction in TNBC models via apoptotic and mitophagy-dependent mechanisms.[54] The increased presence of rounded mitochondria may indicate swelling of the mitochondrial matrix in treated cells, suggesting mitochondrial damage or stress (black arrows and squares in Figure 4E); of note, diblock copolymer **6 h** treatment induced particularly evident effects (Figure 4E). Exposure to diblock copolymer **7** did not affect mitochondrial function/morphology in MDA-MB-231 cells, as demonstrated by the unaltered OCR profile (Figure S52, Supporting Information) and morphology (FigureS53, Supporting Information). Overall, these findings underline the mitochondria-dependent biological activity of diblock copolymers **6b**, **h,** and **i**.

In summary, candidate mtCPOs **6b**, **6**, and **i** exhibited antitumorigenic properties via a concentration-dependent mitochondrial pathway. These diblock copolymers induced mitochondrial depolarization, increased ROS production, and reduced CI OXPHOS and ETC coupling efficiency, leading to altered mitochondrial metabolism. Our findings suggest that diblock copolymers may trigger lysosomal-dependent mitophagy, highlighting their potential as novel therapeutic agents for cancer treatment.

ADVANCED SCIENCE NEWS
www.advancedsciencenews.com

ADVANCED MATERIALS
www.advmat.de

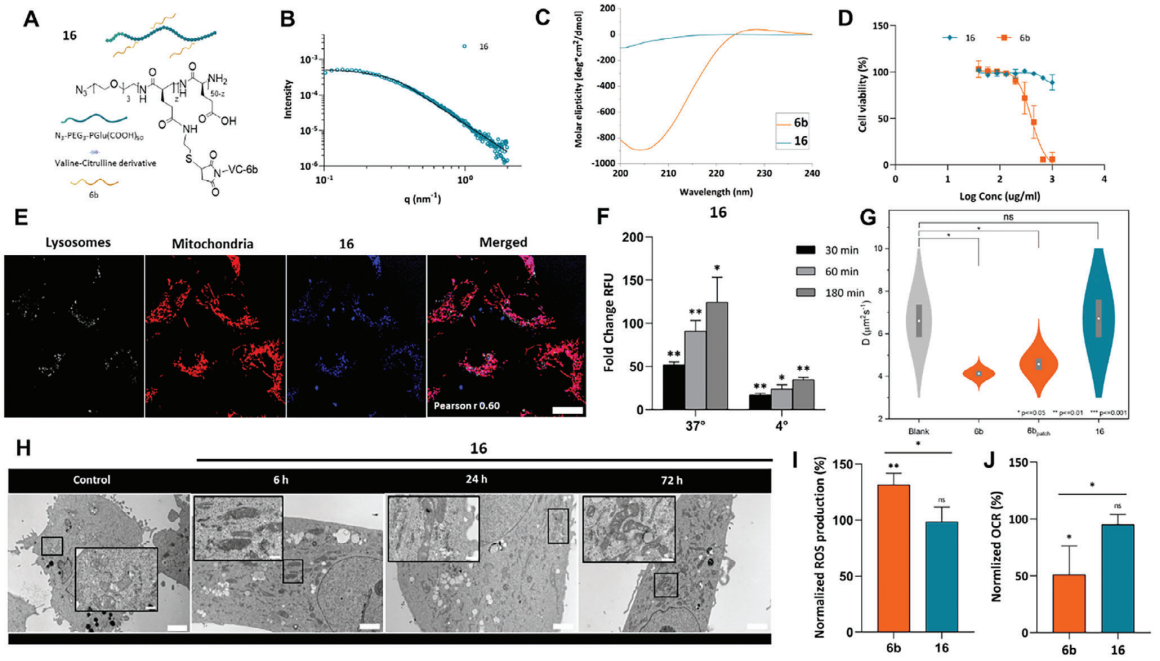

Figure 5. PGA- diblock copolymer 6b conjugate functions as a non-toxic mitochondrially-targeted cell penetrating platform. **A)** Schematic representation of nanoconjugate **16** (See **SI** for complete synthesis and characterization). **B)** Small-angle x-ray scattering (SAXS) data for nanoconjugate **16** where intensity is expressed as a function of the scattering momentum transfer, q ($q = 4\pi\sin(\theta)/\lambda$). **C)** Circular dichroism (CD) spectra of nanoconjugate **16** compared to diblock copolymer **6b**. **D)** MDA-MB 231 cell viability by MTS assay after treatment with nanoconjugate **16** or diblock copolymer **6b** (IC_{50} > 1 mg/ml) (72 h, $n = 3$, mean ± SEM). **E)** Confocal images of **16** uptake at 2 h post-treatment in MDA-MB-231 cells following a pulse-chase experiment (Table S8, Supporting Information) (White – LysoTracker Blue for lysosomes; Red – MitoTracker Red CM-H2Xros for mitochondria; Blue – Cy5 for **16**). The colocalization of nanoconjugate **16** with Mitotracker Red is shown in the merged image (in purple). The Pearson r (2 h) value was calculated using the ImageJ – JACoP plugin. Scale bar: 10 µm. **F)** Internalization of **16** measured over time at 37° (endocytic-dependent pathway) and 4° (endocytic-independent pathway) by flow cytometry ($n = 3$, mean ± SEM). Data expressed as fold change in relative fluorescence units (RFU) to $t = 0$; t-test comparing to the control set as 100% ($n = 3$, mean ± SEM). **G)** Diffusion coefficient (D, $\mu m^2 s^{-1}$) of the membrane at 28 °C for Atto655-DOPE for CL-rich membranes incubated with diblock copolymers at patch-containing (**6b**$_{patch}$) and patch-lacking (**6b** and **16**) regions. **H)** Mitochondria morphological studies by TEM after treatment with **16** (at an equivalent concentration of diblock copolymer **6b**) at 6, 24, and 48 h. Scale bar main images: 20 µm; scale bar insert images: 500 nm **I)** ROS production analysis after a 24-h treatment with nanoconjugate **16** (at an equivalent concentration of diblock copolymer **6b**) (t-test comparing to control set as 100% and treatments **6b** and **16**; $n = 3$, mean ± SEM). **J)** Oxygen consumption rate (OCR) related to ATP-production coupled respiration analysis by Seahorse XF after a 24-h treatment with **16** (at an equivalent concentration of diblock copolymer **6b**) (OCR measured in pmol/min/2^10^4 cells, t-test comparing to control set as 100% and diblock copolymer **6b** as 16%; $n = 3$, mean ± SEM). Significance reported as $*p \leq 0.05$, $**p \leq 0.01$ (ns = not significant).

2.5. Envisioning the Translatability of a Selected Mitochondrial Targeting Candidate: Targeting Mitochondria for Future Applications

Our findings have reported the biological activity of diblock copolymers **6b**, **h**, and **i**, thereby demonstrating the potential of these mtCPOs as a mitochondria-dependent anti-tumorigenic approach at sub-IC_{50} concentrations (>IC_{15}). To leverage the potential use of the selected candidate diblock copolymer **6b** as a mitochondria-targeting ligand, we selected a linear PGA modified with a short PEG chain (PEG_3-PGA_{50}, diblock copolymer **17**) as a non-toxic nanocarrier for functionalization with **6b** through a valine-citrulline (VC) linker (**Figure** 5A). The VC linker self-immolates in cathepsin B-rich lysosomal environments,[56] thus ensuring complete intracellular nanocarrier degradation and efficient diblock copolymer release. We obtained the final functionalized nanocarrier N_3-PEG_3-PGA_{50}-VC-6b (diblock copolymer conjugate **16**) through a convergent synthetic scheme (Scheme S5 (Supporting Information), detailed synthesis described in the SI) involving a VC-functionalized diblock copolymer **6b** (**6b-VC**, Scheme S6, Figures S54 and S55, Supporting Information) and N_3-PEG_3-PGA_{50} functionalized with S-(2-pyridylthio)cysteamine hydrochloride (**17-PD**, Scheme S7, Figures S56 and S58, Supporting Information). We achieved a 3.3% wt. Functionalization of **17-PD** with **6b-VC** (Figures S59 and S60, Supporting Information), ensuring that the concentration of diblock copolymer **6b** incorporated into the final nanocarrier remained below the IC_{15} threshold, the lowest concentration that we observed mitochondrial anti-tumorigenic activity.

Physicochemical characterization of nanoconjugate **16** revealed a comparable branched structure, compact core (with no aggregated structures in solution (q–s = 0)), and a Rg_{corr}

ADVANCED SCIENCE NEWS
www.advancedsciencenews.com

ADVANCED MATERIALS
www.advmat.de

close to that of parental **6b** (Figure 5B). Zeta potential assessment confirmed the expected negatively-charged nature of PGA (-15.7 ± 0.2 mV), while CD analysis indicated a random coil conformation due to PGA content (Figure 5C). As expected, final functionalized nanoconjugate **16** presented a safer biological profile, demonstrating over 80% cell viability at all concentrations evaluated in MDA-MB-231 cells (Figure 5D) and BJ fibroblasts (Figure S61, Supporting Information) after 24 and 72 h. A Cy5-labeled derivative of final functionalized nanoconjugate 16 (Scheme S8, Figure S62, Supporting Information) revealed the maintenance of the mitochondria colocalization capability observed for diblock copolymer **6b,** but this time, a high Pearson r value (>0.6) was obtained after only 30 min after incubation in MDA-MB-231 cells (Figure 5E; Table S8, Supporting Information). Interestingly, we failed to find nanoconjugate **16** in lysosomes before mitochondrial colocalization, as we observed for parental **6b**, suggesting its direct translocation through the cell membrane; however, additional studies (outside the scope of the current manuscript) would be required to fully understand the whole cell internalization mechanism. These results indicate that nanocarrier charge and secondary structure play a role in mitochondrial targeting, but they do not represent the primary driving force. Furthermore, although zeta potential analysis in SUVs demonstrated no significant increase after incubation compared to the blank (SUVs treated with PBS) (Figure S63, Supporting Information), nanoconjugate **16** formed selective membrane patches in CL-rich SLBs that remained even after washing (Figure S64, Supporting Information). Reduced ionic interaction, possibly due to the small %wt of **6b** conjugated in **16**, may explain the decreased number and size of patches compared to the parent **6b**; however, we demonstrated that the nanoconjugate **16** binds to CL-rich membranes to induce folding and, as such, reproduces the behavior observed of the original diblock copolymer **6b** (Figure S64, Supporting Information).

Our flow cytometry findings revealed that the PGA nanoconjugate **16** supported significant cell internalization at 4 °C via an unconventional energy-independent uptake that increased steadily over time (as previously observed for **6b**) (Figure 5F). Indeed, although previously reported cell-penetrating peptides boost the internalization efficiency of anionic nanoparticles via an energy-dependent mechanism,[57–59] we observed significant direct cell membrane penetration for nanoconjugate **16** (Figure 5F). The small size (Rg 5.0 ± 0.3 nm by SAXS), and the suggested flexibility/deformability of **16** attributed to the VC spacer and the linear architecture of PGA, might represent primary factors contributing to preferential uptake through direct penetration. Indeed, small particle sizes (<10 nm) and surface functionalization with CPOs represent valuable strategies to tune material to use direct cell membrane permeation as an uptake mechanism.[60] Van Lehn et al. reported that the ligand flexibility, such as for diblock copolymer **6b** in our case, favors the non-disruptive interaction of anionic nanoparticles within the cell membrane.[61,62] Analysis of CL-rich SLBs, where **16** revealed a lack of significant differences in membrane fluidity ($D_{16} = 6.71 \pm 1.98\ \mu m^2 s^{-1}$) (Figure 5G) or the number of Atto655-DOPE particles (Figure S65, Supporting Information) compared to the blank (treated with PBS), suggesting a non-significant buckling phenomenon. The lower number of nanoconjugate **16** particles in the confocal volume (Figure S66, Supporting Information), which indicates lower binding strength than **6b**, may support the maintenance of the membrane's physical properties. However, we confirmed the interaction of **16** with CL-rich membranes by the intensity-averaged fluorescence lifetime of Flipper, which increased ($\Delta\ \tau^{16} = 0.1\ ns$) compared to the lifetime for a blank sample (treated with PBS) (Figure S67, Supporting Information), indicating an altered membrane order when interacting with **16** (Figure S68, Supporting Information). The comparable diffusion coefficient of Atto488-labeled **16** to **6b** through CL-rich membranes supports the affinity of the polymer derivative for the CL membrane (Figure S69, Supporting Information).

Activity studies at the mitochondria level confirmed the safer biological profile of nanoconjugate **16** compared to **6b**; specifically, we failed to observe altered mitochondrial morphology at all incubation times (Figure 5H), increased ROS production (Figure 5I) or significantly altered OCR related to ATP production (Figure 5J) compared to **6b** and control cells (set as 100%) in agreement with greater cell viability due to the absence of membrane disruption.

In conclusion, we successfully designed a nanoconjugate derivative of diblock copolymer **6b**, which retained its mitochondrial targeting ability and CL-specific interaction while exhibiting a safer biological profile and minimal activity at the mitochondrial level. Furthermore, our findings confirm the concentration-dependent behavior of diblock copolymer **6b**, functioning as a mitochondrial targeting anti-tumorigenic polymer at sub-IC_{50} concentrations (>IC_{15}) or as an efficient mitochondrial targeting moiety to functionalize different materials at low concentrations (<IC_{15}). Our proof-of-concept with diblock copolymer conjugate **16** exemplifies this concept, demonstrating the versatility and potential of diblock copolymer **6b** as a mitochondrial targeting agent for various applications.

3. Conclusion

Targeting drug delivery to subcellular compartments represents an expanding area in drug development/precision therapy due to the advantages of promoting therapeutic agent accumulation in organelles, such as reducing threshold dosages and minimizing drug-related side effects. Mitochondria represent prime targets given their role in cell metabolism $^{-1}$survival; as such, targeting these organelles may prevent/ameliorate conditions such as cancer, neurodegeneration, or diabetes, reverse multidrug resistance mechanisms, and leverage synergistic effects by applying more than one anti-cancer drug/therapeutic strategy via nanomedicine strategies. As mitochondrially-targeted nanomedicines have not achieved clinical translation, we require a deeper understanding of mitochondrial targeting and the development of novel approaches/simple synthetic procedures to facilitate industrial translation.

Our mtCPO platform – PLO_n-PLP_m – can be easily scaled up and translated to industrial development via a simple two-step methodology based on robust NCA-ROP, a rapid, cost-effective, and well-described methodology. DoE revealed the critical influence of initiator and monomer concentrations and reaction temperature, which permitted the scale-up of an optimal diblock copolymer candidate (**6b**) (7.3 g; 80% overall yield).

We introduced variations in the PLO_n-PLP_m platform by altering polycationic blocks (PLL, PHis, or PArg instead of PLO) and

ADVANCED SCIENCE NEWS
www.advancedsciencenews.com

ADVANCED MATERIALS
www.advmat.de

diblock lengths (n:m ratio) to decipher each component's contribution to mitochondrial targeting. Diblock copolymers **6b**, **h**, and **i** (n:m ratio of 1:3) and nanoconjugate **16** promoted rapid energy-independent cell entry and efficient mitochondrial targeting (as such, serving as mt-CPOs), thereby overcoming problems associated with entrapment in endo/lysosomal compartments after cell entry by endocytosis, which rely on inefficient endo/lysosomal disrupting mechanisms for cytosolic delivery. PLO – the most efficient polycationic block – prompted more rapid cell internalization and significant mitochondrial accumulation than PLL, a well-known cell-penetrating peptide. Diblock copolymers **6b** and **7** – same n:m ratio and lengths but different polycationic blocks (PLO and PLL) – presented comparable size, charge, and type II helix structure. The PLO-PLP diblock displayed a monomodal distribution in solution, while the PLL-PLP diblock displayed a bimodal profile due to its favored random coil-to-helix conformational transition, which reduces helicity (affecting solvation environments and water shell interactions) and results in distinct hydration radii and lower cellular internalization by direct penetration of diblock copolymer **7**.

When evaluating targeting mechanisms, we discovered that mitochondrial depolarization did not influence diblock copolymer accumulation, suggesting that charge affinity between positively charged nanocarriers and negatively charged mitochondrial membranes does not account for targeting. This concept enhances the applicability of our diblock copolymers due to their mitochondrial targeting ability in distinct stages of disease, regardless of depolarization processes.

We studied diblock copolymer interactions with CL using artificial and biological CL-rich membrane models. Our results revealed the essential presence of the polycationic component to CL affinity (PLP homopolymers did not bind); however, this electronic interaction does not represent the only binding force involved, as n:m ratios of 1:1 and 1:2 demonstrated CL affinity but did not result in efficient mitochondrial accumulation. Instead, PLP content proved crucial to patch formation (observed here for the first time); only an n:m ratio of 1:3 supported membrane patch formation in CL-rich regions with negative curvature. These findings suggest the induction of physical changes, such as membrane remodeling, by facilitating buckling and patch formation in CL-rich environments but not in membranes with an equivalent charge distribution lacking CL. Thus, lower proline content may prompt weaker membrane-binding affinities, thereby inhibiting buckling; moreover, the lack of patch formation for diblock copolymer **7** suggests the essential nature of the polycationic block for efficient binding to CL-rich membranes. Overall, our data suggest that PLP content, n:m ratio, and polycationic block nature represent crucial factors controlling CL interactions. Further studies of membrane transforming properties corroborated the ability of PLO_n-PLP_m diblock copolymer with an n:m ratio of 1:3 to decrease membrane fluidity and increase membrane tension in CL-rich membrane regions, which can induce membrane ordering and initiate buckling phenomena.

In addition to their mitochondria-targeting capacity, diblock copolymers **6b**, **h**, and **i** displayed inherent biological activity, functioning as concentration-dependent anti-tumorigenic agents that prompted altered mitochondria metabolism, morphology, and respiration. These diblock copolymers induced mitochondrial depolarization and increased ROS production, contributing to downstream effects that induce cell death; furthermore, morphological alterations and an increased proportion of lysosomes engulfing affected mitochondria indicated impairment. We observed metabolic alterations after treatment with diblock copolymers **6b**, **h**, and **I** – OCR, which became compromised in a concentration-dependent manner, with reduced CI OXPHOS and ETC coupling efficiency.

To leverage the mitochondrial-targeting effect of our diblock copolymers, we also designed a polypeptide-based diblock copolymer nanoconjugate. Our strategy incorporated PGA to maintain biodegradability/biocompatibility and a cathepsin B-sensitive self-immolation linker to ensure stability in circulation while supporting biodegradation. PGA conjugation of diblock copolymer **6b** to yield nanoconjugate **16** enhanced cell viability and mitochondrial targeting without damaging mitochondria but maintained original physicochemical characteristics (comparable size and compact core structure compared to diblock copolymer **6b**). Despite differing from the parent diblock copolymer regarding secondary structure (random coil) and charge (negative), nanoconjugate **16** displayed enhanced energy-independent cell uptake and mitochondrial targeting via CL-affinity mechanisms. These findings suggest that the nanocarrier's small size, polyanionic nature, and the "availability" of diblock copolymer **6b**, facilitated by ligand flexibility provided by the linker, contributed to therapeutically relevant outcomes. Activity studies at the mitochondria level confirmed the safer profile of nanoconjugate **16**, which failed to alter mitochondrial morphology, increase ROS production, or significantly alter OCR, in agreement with greater cell viability due to the absence of membrane disruption.

In summary, PLO_n-PLP_m diblock copolymers with an n:m ratio of 1:3 function as efficient cell-penetrating oligomers and support cardiolipin-specific mitochondrial targeting (mt-CPOs). Mt-CPOs demonstrated inherent anti-tumorigenic properties via a mitochondrial-dependent pathway in a human TNBC cell model at sub-IC_{50} concentrations. These findings pave the way for the construction of novel mitochondrially-targeted treatments for various diseases. Our efforts focused on physicochemical characterization and providing proof-of-concept for a novel mitochondrially-targeted therapeutically relevant platform. Our materials also fulfill biodegradable and biocompatible standards, contributing to safety. Our results suggest the potential of PLO_n-PLP_m diblock copolymers as safe, mitochondria-specific nanocarriers; this supported the development of a mitochondrially-targeted polypeptide-based nanoconjugate that could provide a paradigm shift in addressing precise treatments through subcellular organelle-targeting strategies.

4. Experimental Section

Materials, selected methods, and the synthesis of compounds listed in Table 1 and nanoconjugate **16** are documented in detail in the Supporting Information. Here, a summarized selection of the materials and methods used as representative of the variety of techniques implemented in this work was presented.

Materials: All chemicals used were of analytical grade. N-carboxyanhydride (NCA) monomers, including L-Pro-NCA and L-Orn(Z)-NCA, were obtained from PMC-ISOCHEM. Solvents such as DMF, trifluoroacetic acid (TFA), and chloroform were sourced from Sigma-Aldrich and Fisher Scientific. Lipids for vesicle studies, such as

ADVANCED SCIENCE NEWS
www.advancedsciencenews.com

ADVANCED MATERIALS
www.advmat.de

DOPC and CL, were purchased from Avanti Polar Lipids. Fluorescent dyes, including JC-1 and 2,7-dichlorodihydrofluorescein (DCFH), were obtained from MedChemExpress. Cell culture reagents, including DMEM/F-12 media, fetal bovine serum (FBS), and antibiotics, were purchased from Gibco Life Technologies. Ultrapure Milli-Q water (18 MΩ cm^{-1} resistivity) was used for all aqueous solutions.

Ethical Statements: Animal experiments for erythrocyte isolation were conducted in accordance with European Communities Council Directive 86/609/ECC and Spanish Royal Decree 1201/2005, with approval from the Institutional Animal Care and Use Committee. Eight-week-old female Balb/c mice were housed under specific-pathogen-free conditions with controlled temperature, humidity, a 12-hour light-dark cycle, and ad libitum food and water access. Mice were euthanized using CO_2 inhalation following ethical protocols.

Organs for mitoplast isolation were collected post-mortem from healthy animals assigned to control groups in unrelated experiments, adhering to the 3R principles (Replace, Reduce, Refine). All experimental procedures complied with EU Directive 2010/63/EU and relevant local regulations. Ethical approval for experiments involving animals used for organelle isolation was obtained from the Latvian Animal Protection Ethical Committee of the Food and Veterinary Service in Riga, Latvia (Nr.132/2022).

Physicochemical Methods: *Gel Permeation Chromatography (GPC)*: GPC measurements were conducted using a Malvern Instruments system with a TSKGel PWXL G5000 column. The mobile phase comprised 0.1 M sodium nitrate with 0.005% sodium azide, and the flow rate was set to 0.7 mL $mi^{-1}n$. The system was calibrated with polyethylene oxide (PEO) (molecular weight (Mw) = 24 kDa; PDI = 1.01). For Mw determination, an integrated triple detection system was used (refractive index, light scattering (2 angles: 7 and 90°), and ultraviolet-visible detectors).

Nuclear Magnetic Resonance (NMR): NMR spectra were recorded at 500 MHz on a Bruker spectrometer. Samples were dissolved in d-TFA or D_2O at a concentration of 10 mg m^{-1}. Diffusion-ordered spectroscopy (DOSY) was performed using bipolar pulse pair stimulated echo sequences with 64 gradient increments ranging from 5% to 95% of the maximum field strength. MestReNova software was used for data processing.

Circular Dichroism (CD): CD spectroscopy was conducted using a J-815 CD Spectrometer equipped with a Peltier thermostated cell holder and a recirculating cooler. A nitrogen flow of 1.5 L $mi^{-1}n$, regulated by a nitrogen flow monitor, was maintained throughout the experiments. Samples (0.03–0.25 mg mL^{-1}) were prepared in Milli-Q water or PBS and analyzed in a 1 mm quartz cuvette. Measurements were performed at varying temperatures, with each sample analyzed in triplicate ($n = 3$).

Small-Angle X-Ray Scattering (SAXS): SAXS experiments were conducted at the ALBA Synchrotron on the NCD-SWEET beamline. Samples were prepared in quartz capillaries (1 mm diameter) and exposed to monochromatic X-rays at 12.4 keV. Scattering intensities were collected using a Pilatus 1 M detector. Background subtraction and data reduction were performed using pyFAI, and radius of gyration (Rg) values were calculated using a Guinier-Porod model.

Fluorescence Correlation Spectroscopy (FCS): Z-scan fluorescence correlation spectroscopy (FCS) was performed on a Zeiss LSM980 confocal microscope. Measurements were collected over a 2 µm z-range in 0.2 µm steps, and autocorrelation curves were analyzed to determine diffusion times (τ_D) and particle numbers (N_0) using positional fitting and custom scripts. The temperature was maintained at 28 °C.

Atomic Force Microscopy (AFM): AFM was performed on a JPK Nanowizard 3 microscope combined with a Zeiss LSM800 confocal microscope using a C-Apochromat 20xA objective. Diblock copolymers (Atto488) and membranes (Atto655-DOPE) were excited with 488 nm and 633 nm lasers, respectively. Confocal microscopy localized areas of interest, followed by AFM imaging in quantitative mode using BioLever Mini cantilevers. Imaging parameters included a nominal force of 0.3 nN, an acquisition speed of 61.1 µm $^{-1}$s, and a Z-range of 110 nm. Images were processed in Gwyddion (v2.58) with leveling, alignment, scar correction, outlier removal, and denoising.

Membrane Model Systems: *Small Unilamellar Vesicles (SUVs)*: CL-containing SUVs were prepared using the thin-film method. Stock solutions of DOPC and CL were mixed and evaporated under reduced pressure to form a lipid film. The film was resuspended in 20 mM HEPES buffer (pH 6.8). The vesicles were sonicated at room temperature for 30 min and extruded through a 100 nm polycarbonate filter. SUV quality was confirmed by dynamic light scattering (DLS), and samples were freshly prepared for each experiment.

Mitoplasts: Mitoplasts were isolated via differential centrifugation. Heart and liver tissues from a healthy Sprague Dawley rat were homogenized in ice-cold buffer (180 mM KCl, 10 mM Tris/HCl, 1 mM EGTA, pH 7.7). The homogenate was centrifuged at 750 g to remove debris, and the supernatant was centrifuged at 6800 g to pellet mitochondria. The mitochondrial pellet was washed, resuspended in a hypotonic solution (5 mM sucrose, 5 mM HEPES, 1 mM EGTA, pH 7.2), and incubated on ice for 20 min to remove the outer membrane. To eliminate cytochrome *c*, the sample was treated with 300 mM KCl and centrifuged at 14 500 g. The pellet was washed, centrifuged, and resuspended in 20 mM HEPES buffer (pH 6.8). Mitoplasts were stored at −20 °C until use.

Biological Studies: Biological experiments were performed on MDA-MB-231, MCF-7, Hep G2, BJ fibroblasts, and BV-2 cells.

Cell Viability Assay: Cells were seeded in 96-well plates and incubated for 24 h at 37 °C with 5% CO_2. Diblock copolymer stock solutions were prepared in PBS, diluted in DMEM/F-12 medium with 10% FBS and 1% P/S, sterilized through a 0.2 µm filter, and added to wells at final concentrations of 0–1 mg mL^{-1}. After 24 or 72 h of treatment, MTS/PMS reagent was added, and cells were incubated for 4 h. Absorbance at 490 nm was measured using a plate reader, and cell viability was calculated as a percentage relative to untreated controls. Data were expressed as Mean ± SD ($n = 3$).

Cellular Uptake Studies: The uptake of Cy5-labeled diblock copolymers was analyzed using confocal microscopy and flow cytometry. For live-cell imaging, pulse-chase and time-lapse studies were performed on a Leica TCS SP8 confocal microscope equipped with a 63× oil immersion objective. MitoTracker Red and LysoTracker Blue were used to track mitochondrial and lysosomal localization. For pulse-chase studies, cells were treated with polymers for 1, 2, 4, 6, and 24 h, while the fluorescent markers were added 1 h before imaging. Time-lapse imaging captured uptake dynamics over a 20-second interval. Images were analyzed using LAS X and ImageJ for colocalization and Pearson correlation calculations. For flow cytometry, cells were incubated with polymers at 37 or 4 °C for 0, 30, 60, and 180 min. After incubation, cells were washed, harvested, and stained with propidium iodide (PI) to assess viability. Cell-associated fluorescence was measured using a CytoFLEX S flow cytometer, collecting 10 000 events per sample. Background fluorescence was subtracted, and data were expressed as fold changes relative to t = 0 using CytExpert software.

Hemocompatibility Assay: Polymer solutions were prepared in PBS (pH 7.4) and citrate buffer (pH 5.5) and added to wells in triplicate at sub-IC50 concentrations (C1 and C2, with C1/C2 = 1.5). Controls included buffer for background, Triton X-100 (1%) for positive control, and dextran (2 mg mL^{-1}) for negative control. After 1 h of incubation at 37 °C, plates were centrifuged at 3000 rpm for 10 min, and supernatants were collected for hemoglobin release assessment. Absorbance at 570 nm was measured, and hemolysis percentages were calculated relative to the 100% hemolysis control (Triton X-100).

Mitochondrial Membrane Potential: Cells were seeded in 96-well plates, treated with sub-IC50 diblock copolymer solutions (>IC40) for 2, 6, and 24 h, and stained with 2 µM JC-1 for 30 min. CCCP (50 µM) was used as a positive control. Fluorescence was measured at 550/605 nm (red) and 484/528 nm (green), and the red/green ratio was normalized to untreated controls (set as 100%). Data were presented as Mean ± SD ($n = 3$).

Oxygen Consumption Rate (OCR): OCR was measured using the Oroboros O2k and Seahorse XF systems. For Oroboros, permeabilized cells treated with diblock copolymers at sub-IC50 concentrations were sequentially exposed to pyruvate and malate for LEAK respiration, ADP for OXPHOS, and glutamate and succinate for CI-II-linked respiration. CCCP was titrated to determine maximal respiration, while rotenone and antimycin A were used to evaluate residual oxygen consumption. Flux control factors were calculated based on substrate-dependent respiration changes. For Seahorse XF analysis, intact cells treated with diblock

ADVANCED SCIENCE NEWS
www.advancedsciencenews.com

ADVANCED MATERIALS
www.advmat.de

copolymers were incubated in an XF medium with pyruvate, glutamine, and glucose. Inhibitors (1.5 µM oligomycin, 1 µM FCCP, and 0.5 µM rotenone/antimycin A) were sequentially injected to assess spare and ATP-linked respiration. Results were normalized using Hoechst staining for viability and expressed relative to untreated controls as Mean ± SD ($n = 3$).

Reactive Oxygen Species (ROS): Cells were seeded in 6-well plates and treated with sub-IC50 concentrations of sterilized diblock copolymer solutions (>IC40) for 24 h. After treatment, cells were washed, trypsinized, and resuspended in a fresh medium. Cells were then incubated with 5 µg mL^{-1} DCFH for 30 min, followed by propidium iodide (2 µg mL^{-1}) for viability assessment. Samples were analyzed using a CytoFLEX S flow cytometer, collecting 10 000 events per sample. Data were normalized to untreated controls (100%) and expressed as Mean ± SD ($n = 3$).

Mitochondrial Morphology Analysis: Cells were seeded in 8-well chambers and treated with sub-IC50 concentrations (>IC40) of selected compounds for 6, 24, and 48 h. After treatment, cells were pre-fixed with 3% glutaraldehyde, post-fixed with 2% OsO_4, and stained with 2% uranyl acetate. Samples were dehydrated in ethanol, embedded in Durcupan resin, and sectioned into 0.08 µm slices. Sections were stained with lead citrate and imaged using a transmission electron microscope. Twenty images per sample were captured at 1900× and 11 000× magnifications.

Supporting Information

Supporting Information is available from the Wiley Online Library or from the author.

Acknowledgements

This project was supported by Horizon Europe H2020-MSCA-ITN-2019 BIOMOLMACS (proposal no. 859416). The authors acknowledge the Asociación Española contra el Cáncer (ICS INVES211323CONE Junior AECC grant), Ministerio de Ciencia e innovacion (PID2019-108806RB-I00, PID2023-152459OB-I00), NextGeneration EU i+d+I funding through GVA Conselleria Innovació- Pol@Mets. Ref. MFA/2022/065 and European Regional Development Fund (PO FEDER Comunitat Valenciana 2014–2020) Generalitat Valenciana for financial support. SAXS measurements were acquired at the NCD-SWEET beamline at the ALBA Synchrotron Light source in Barcelona, Spain, through Project ID 2022097124. The mass spectrometry analysis was performed in the proteomics facility of SCSIE University of Valencia. Support from the project "BioMedPharm" (VPP-EM-BIOMEDICINA-2022/1-0001) and Horizon Europe EU-OPENSCREEN IMPULSE (Grant Agreement No. 101132028) is gratefully acknowledged. Y.Q. and S.G. acknowledged support from the International Max Planck Research School for Molecules of Life (IMPRS-ML). S.G. was part of the ONE MUNICH Project supported by the Federal Ministry of Education and Research (BMBF) and the Free State of Bavaria under the Excellence Strategy of the Federal Government and the Länder. The authors thank Dr. Stuart P. Atkinson for his help in manuscript development and English editing, Alberto Hernandez for confocal imaging support, Alicia Martinez Romero for flow cytometry analysis, and Mario Soriano for TEM support. The authors thank Agustín Lahoz Rodríguez from the Instituto de Investigación Sanitaria Hospital La Fe for providing access to and help with the Seahorse XF Analyzer. The authors would also thank Prof. Beatriu Escuder from UJI and Prof. Ignacio Alonso from IQAC who facilitated the MALDI analysis. The authors would like to acknowledge Isabel Montoya for the support with the BV2 cells study and Jan-Hagen Krohn for the help with the z-scan FCS setup.

Conflict of Interest

The authors declare a filed patent. – MJ Vicent; I Conejos-Sanchez; C Pegoraro; E Karpova; G Sogorb; C Felip; VJ Nebot; P Schwille; Y Qutbuddin. PCT/EP2024/06 8352 (Priority claimed: European Patent Application no. EP23382668.4). Polyproline-based Block-copolymers 28/06/2024. CIPF, PTS SL, and Max Planck Society.

Author Contributions

C.P. led the synthesis of the conjugate, conformational studies, data curation, formal analysis, investigation, methodology, and writing of the original draft. Cell viability assays and biological studies were carried out by C.P. with support from E.M.S. E.K., C.F.-L., and A.D.-C. led to the synthesis of the diblocks and the scale-up demonstration including DoE. Y.Q. and P.S. led the synthetic membrane studies and FCS analysis. P.D. and P.A. led the cardiolipin interaction studies and the Oroboros, C.H.-I. led the SAXS analysis, I.C-S and M.J.V. cosupervise the whole study and contributed to the data curation and formal analysis, as well as in the writing process. Conceptualization, funding acquisition, and project administration were led by M.J.V. with support from I.C.S. The manuscript was revised by C.P., I.C.-S., and M.J.V., with reviewing and editing contributions from all authors. All authors have read and approved the final version of the manuscript.

Data Availability Statement

The data supporting this study's findings are available from the corresponding author upon reasonable request.

Keywords

cardiolipin-specific mitochondrial targeting, design of experiments (doe), membrane remodeling, mitochondrial tropism, polypeptide-based nanoconjugates, polyproline, subcellular organelle targeting

Received: August 6, 2024
Revised: November 25, 2024
Published online:

[1] X. Fu, Y. Shi, T. Qi, S. Qiu, Y. Huang, X. Zhao, Q. Sun, G. Lin, *Signal Transduct. Target. Ther.* **2020**, *5*, 262.
[2] S. S. Liew, X. Qin, J. Zhou, L. Li, W. Huang, S. Q. Yao, *Angew. Chem., Int. Ed.* **2021**, *60*, 2232.
[3] C. Pegoraro, I. Domingo-Ortí, I. Conejos-Sánchez, M. J. Vicent, *Adv. Drug Delivery Rev.* **2024**, *207*, 115195.
[4] H. Cho, Y. Y. Cho, M. S. Shim, J. Y. Lee, H. S. Lee, H. C. Kang, *Biochim. Biophys. Acta – Mol. Basis Dis.* **2020**, *1866*, 165808.
[5] L. D. Zorova, V. A. Popkov, E. Y. Plotnikov, D. N. Silachev, I. B. Pevzner, S. S. Jankauskas, V. A. Babenko, S. D. Zorov, A. V. Balakireva, M. Juhaszova, S. J. Sollott, D. B. Zorov, *Anal. Biochem.* **2018**, *552*, 50.
[6] S. A. Smith, L. I. Selby, A. P. R. Johnston, G. K. Such, *Bioconjug. Chem.* **2019**, *30*, 263.
[7] D. Kalafut, T. N. Anderson, J. Chmielewski, *Bioorg. Med. Chem. Lett.* **2012**, *22*, 561.
[8] Y. A. Fillon, J. P. Anderson, J. Chmielewski, *J. Am. Chem. Soc.* **2005**, *127*, 11798.
[9] I. M. Geisler, J. Chmielewski, *Pharm. Res.* **2011**, *28*, 2797.
[10] L. Li, I. Geisler, J. Chmielewski, J.-X. Cheng, *J. Control. Rel.* **2010**, *142*, 259.
[11] A. Dirisala, S. Uchida, J. Li, J. F. R. Van Guyse, K. Hayashi, S. V. C. Vummaleti, S. Kaur, Y. Mochida, S. Fukushima, K. Kataoka, *Macromol. Rapid Commun.* **2022**, *43*, 1.
[12] I. Conejos-Sánchez, E. Gallon, A. Niño-Pariente, J. A. Smith, A. G. De la Fuente, L. Di Canio, S. Pluchino, R. J. M. Franklin, M. J. Vicent, *Nanoscale* **2020**, *12*, 6285.
[13] J. L. S. Lopes, A. J. Miles, L. Whitmore, B. A. Wallace, *Protein Sci.* **2014**, *23*, 1765.
[14] K.-Y. Huang, J.-C. Horng, *J. Phys. Chem. B* **2019**, *123*, 138.
[15] B. Hammouda, *Macromol. Theory Simulations* **2012**, *21*, 372.

ADVANCED SCIENCE NEWS
www.advancedsciencenews.com

ADVANCED MATERIALS
www.advmat.de

[16] B. Hammouda, *J. Appl. Crystallogr.* **2010**, *43*, 716.
[17] G. Quintero-Marquina, G. Segovia, V. Oestreicher, D. Lamas, C. Huck-Iriart, *ChemRxiv* **2024**. https://doi.org/10.26434/chemrxiv-2024-8jqp7.
[18] B. Ghaemi, S. Tanwar, A. Singh, D. R. Arifin, M. T. McMahon, I. Barman, J. W. M. Bulte, *ACS Appl. Mater. Interfaces* **2024**, *16*, 11159.
[19] M. T. H. Nguyen, D. Biriukov, C. Tempra, K. Baxova, H. Martinez-Seara, H. Evci, V. Singh, R. Šachl, M. Hof, P. Jungwirth, M. Javanainen, M. Vazdar, *Langmuir* **2022**, *38*, 11284.
[20] A. D. Robison, S. Sun, M. F. Poyton, G. A. Johnson, J.-P. Pellois, P. Jungwirth, M. Vazdar, P. S. Cremer, *J. Phys. Chem. B* **2016**, *120*, 9287.
[21] C. Tempra, Z. Brkljača, M. Vazdar, *Phys. Chem. Chem. Phys.* **2023**, *25*, 27204.
[22] B. D. Monnery, M. Wright, R. Cavill, R. Hoogenboom, S. Shaunak, J. H. G. Steinke, M. Thanou, *Int. J. Pharm.* **2017**, *521*, 249.
[23] Z. Jiang, H. Liu, H. He, N. Yadava, J. J. Chambers, S. Thayumanavan, *Bioconjug. Chem.* **2020**, *31*, 1344.
[24] A. M. Mahmoud, J. P. Morrow, D. Pizzi, A. M. Azizah, T. P. Davis, R. F. Tabor, K. Kempe, *Biomacromolecules* **2020**, *21*, 3007.
[25] A. M. Mahmoud, P. A. J. M. de Jongh, S. Briere, M. Chen, C. J. Nowell, A. P. R. Johnston, T. P. Davis, D. M. Haddleton, K. Kempe, *ACS Appl. Mater. Interfaces* **2019**, *11*, 31302.
[26] G. Sahay, E. V. Batrakova, A. V. Kabanov, *Bioconjug. Chem.* **2008**, *19*, 2023.
[27] D. Y. Alakhova, N. Y. Rapoport, E. V. Batrakova, A. A. Timoshin, S. Li, D. Nicholls, V. Y. Alakhov, A. V. Kabanov, *J. Control. Rel.* **2010**, *142*, 89.
[28] G. Sahay, V. Gautam, R. Luxenhofer, A. V. Kabanov, *Biomaterials* **2010**, *31*, 1757.
[29] G. A. Morris, Diffusion-Ordered Spectroscopy (DOSY), In: R.K. Harris, R.L. Wasylishen, eds. EMagRes **2009**.
[30] D. Huesmann, A. Birke, K. Klinker, S. Türk, H. J. Räder, M. Barz, *Macromolecules* **2014**, *47*, 928.
[31] N. K. Singh, M. Agarwal, M. Radhakrishna, *Proteins Struct. Funct. Bioinforma.* **2023**, *91*, 268.
[32] Y. Liu, J. Zhang, Y. Tu, L. Zhu, *ACS Nano* **2022**, *16*, 1409.
[33] S. T. Ahmadpour, K. Mahéo, S. Servais, L. Brisson, J.-F. Dumas, *Int. J. Mol. Sci.* **2020**, *21*.
[34] P. Dimitrijevs, P. Arsenyan, *Sensors Actuators B Chem* **2021**, *346*, 130537.
[35] J. Sarkis, V. Vié, *Front. Bioeng. Biotechnol.* **2020**, *8*.
[36] K. J. Boyd, N. N. Alder, E. R. May, *Biophys. J.* **2018**, *114*, 2116.
[37] K. J. Boyd, N. N. Alder, E. R. May, *Langmuir* **2017**, *33*, 6937.
[38] M. D. Phan, K. Shin, *Biophys. J.* **2015**, *108*, 1977.
[39] V. Kubyshkin, S. L. Grage, A. S. Ulrich, N. Budisa, *Phys. Chem. Chem. Phys.* **2019**, *21*, 22396.
[40] A. J. García-Sáez, D. C. Carrer, P. Schwille, Fluorescence Correlation Spectroscopy for the study of membrane dynamics and organization in giant unilamellar vesicles In: (Eds: V. Weissig), Lipid-Proteins Interactions, vol 2: Biological membrane models, Humana Press, Totowa, NJ **2010**, pp. 493–508.
[41] P. Rangamani, K. K. Mandadap, G. Oster, *Biophys. J.* **2014**, *107*, 751.
[42] A. Colom, E. Derivery, S. Soleimanpour, C. Tomba, M. D. Molin, N. Sakai, M. González-Gaitán, S. Matile, A. Roux, *Nat. Chem.* **2018**, *10*, 1118.
[43] F. Ragaller, E. Sjule, Y. B. Urem, J. Schlegel, R. El, D. Urbancic, I. Urbancic, H. Blom, E. Sezgin, *J. Phys. Chem. B* **2024**, *128*, 2154.
[44] N. Badrinath, S. Y. Yoo, *Carcinogenesis* **2018**, *39*, 1419.
[45] A. Reda, A. Refaat, A. A. Abd-Rabou, A. M. Mahmoud, M. Adel, S. Sabet, S. S. Ali, *Sci. Rep.* **2019**, *9*, 13748.
[46] F. Sivandzade, A. Bhalerao, L. Cucullo, *Bio-protocol* **2019**, *9*, 1.
[47] C. Nguyen, S. Pandey, *Cancers* **2019**, *11*.
[48] H. M. Begum, K. Shen, *WIREs Mech. Dis.* **2023**, *15*, e1595.
[49] L. B. Sullivan, N. S. Chandel, *Cancer Metab.* **2014**, *2*, 17.
[50] C.-L. Kuo, A. Ponneri Babuharisankar, Y.-C. Lin, H.-W. Lien, Y. K. Lo, H.-Y. Chou, V. Tangeda, L.-C. Cheng, A. N. Cheng, A. Y.-L. Lee, *J. Biomed. Sci.* **2022**, *29*, 74.
[51] M. E. Zare, A. N. Kansestani, S. Hemmati, K. Mansouri, A. Vaisi-Raygani, *J. Diabetes Metab. Disord.* **2021**, *20*, 523.
[52] P. Marchetti, Q. Fovez, N. Germain, R. Khamari, J. Kluza, *FASEB J.* **2020**, *34*, 13106.
[53] A. Jussupow, A. Di Luca, V. R. I. Kaila, *Sci. Adv.* **2024**, *5*, eaav1850.
[54] T. G. Biel, V. A. Rao, *Oncotarget* **2017**, *9*, 1.
[55] C. Song, S. Pan, J. Zhang, N. Li, Q. Geng, *Cell Prolif* **2022**, *55*, e13327.
[56] J. D. Bargh, A. Isidro-Llobet, J. S. Parker, D. R. Spring, *Chem. Soc. Rev.* **2019**, *48*, 4361.
[57] J. M. Steinbach, Y.-E. Seo, W. M. Saltzman, *Acta Biomater.* **2016**, *30*, 49.
[58] Y. Shamay, L. Shpirt, G. Ashkenasy, A. David, *Pharm. Res.* **2014**, *31*, 768.
[59] Z. Niu, E. Samaridou, E. Jaumain, J. Coëne, G. Ullio, N. Shrestha, J. Garcia, M. Durán-Lobato, S. Tovar, M. J. Santander-Ortega, M. V. Lozano, M. M. Arroyo-Jimenez, R. Ramos-Membrive, I. Peñuelas, A. Mabondzo, V. Préat, M. Teixidó, E. Giralt, M. J. Alonso, *J. Control. Rel.* **2018**, *276*, 125.
[60] J. Dolai, K. Mandal, N. R. Jana, *ACS Appl. Nano Mater.* **2021**, *4*, 6471.
[61] R. C. Van Lehn, P. U. Atukorale, R. P. Carney, Y.-S. Yang, F. Stellacci, D. J. Irvine, A. Alexander-Katz, *Nano Lett.* **2013**, *13*, 4060.
[62] R. C. Van Lehn, A. Alexander-Katz, *Soft Matter* **2014**, *10*, 648.

9
Discussions and Future Perspectives

Through the work in my thesis, we aimed to develop a more fundamental understanding of how lipid bilayers function as cellular membranes and how external agents interact with lipid membranes. Through gaining insight, the ulterior motive is to manipulate membranes of living and synthetic cells, extending arbitrary control over the mechanical properties of lipid bilayers. Through the use of various biophysical characterization techniques, we studied the effects of a diverse set of external agents including polypeptide based diblock-copolymers, glycopolymers, DNA-condensates, assembly of DNA origami, and light-activated rotary motors on membrane mechanical and physico-chemical properties. In the following sections I will discuss the aim and challenges that are expected in the future.

9.1 Light-triggered control

The results presented in Chapter 6 has extended the previous work on lipid membranes with light-activated molecules. Light-triggered oxidation of lipids had been used in the past in the context of synthetic cells, but because of its *permanent* change of the bilayer, it needs active metabolism for it to be sustainable for artificial life. Photoswitchable lipids on the other hand offer a tremendous reversibility on top of a great control over changing membrane properties. These photoswitches drive the system from one equilibrium to another, perfectly analogous to a "switch", the effect is either *ON* or *OFF*. Synthetic rotary motors by design are unidirectional, and thus are driven between meta-stable states, constantly out of equilibrium in the presence of light. A major achievement that life has is the state of constant non-equilibrium, something necessary for the prospect of synthetic biology. The Feringa-motors studied in Chapter 6 already show promising potential for being easily controllable and readily compatible with model membranes. There are a wide range of molecular motors present in living cells, that drive the cells out of equilibrium, and they have also been reconstituted in model membranes. Using protein machinery from nature has its drawbacks, primarily lack of absolute control over the desired outcome. Synthetic machines (like Feringa-motors) in theory can be modified chemically to achieve the objectives. We already took the first baby-steps in this direction by producing a database of interactions and their strength with already synthesized rotary motors, which will be useful for the design of novel rotary motors specifically designed for membrane manipulations. One must remember, that the inherent non-equilibrium of the molecular motors are a benefit but also a major challenge when it comes to control. As we already observed in our studies, since the trigger is light, acquiring data at real time point $t = 0$ is rather tricky. Another challenge with light-activated systems, in general, is the unwanted production of reactive oxygen species (ROS) that permanently affect the system. As discussed in Section 6.3, destabilization of these photo-active compounds can turn them into photosensitizers resulting in irreversible photo-damage. Especially, the precursors during synthesis of these compounds are highly prone to radical generation upon light-activation,

which means that it is crucial that the compounds used are highly pure. Moreover, it is important to make sure that the environmental factors do not destabilize or disintegrate these compounds, which again leads to irreversible photo-oxidation. Overall, we envision that we have only initiated part of what is to come with the use of synthetic rotary motors within lipid membranes. Additionally, photoactivatable compounds, especially photoswitches hold promising prospects of use in drug delivery applications. With the use of molecular motors and switches, scientists can potentially regulate the traffic and transport within and across cellular membranes. This can provide crucial insights into disease pathology and lead the way towards development of targeted therapeutic agents. The out-of-equilibrium fluctuations in the lipid membrane caused by the rotary motors are going to be interesting with respect to their fusogenecity. Their effect of modulating the surface area of the lipid bilayer in compartmentalized systems, like vesicles, make them useful candidates for use in synthetic cells. Fundamentally, an extensive theoretical framework of these rotary motors in lipid bilayers is desired, and a more through investigation into the various mechanical properties of the membrane affected by their action is still lacking. The future of motors and membranes (often mentioned as M&Ms by us and our collaborators) shines bright, lending justice to their photoactivity.

9.2 Membranes with macromolecules

The results presented in Chapter 7 has provided a simple method for self-assembling DNA origami on lipid membranes. We demonstrated how this polymerization results in immobilization, and the ability to acquire super-resolved DNA-PAINT images. As a consequence, we also saw that such self-assembling behaviors can be used to manipulated the phase-behaviors of lipid membranes, to drive nanoscopic domains to microscopic domains. In the last decade, DNA nanotechnology has seen an immense spurt in attention especially in their use with lipid membranes. Researchers use DNA tiles for producing cytoskeleton mimicking filaments, their hybridization kinetics have also been used to produce DNA-based condensates, and ingenious designs of DNA origami to produce membrane spanning pores and channels have become common with a lot of research groups. There is still a growing interest to produce nanoparticles capable of nutrient or drug delivery, and researchers have successfully reported their use in creating compartmentalization. Similarly, DNA nanotechnology is being used in biosensing applications with point of care (POC) devices and has seen a significant commercial value. There are of course still some challenges when it comes to use of DNA nanomachines in pharmaceutical settings as organisms are highly sensitive to foreign DNA.

The results presented in Chapter 8 show how synthetic mannose-based glycopolymers can mimic the interactions with lipid membranes of various components of the glycocalyx depending on the carbohydrate chain length. The glycocalyx plays a crucial role in many signalling pathways and understanding the intricacies of these processes is crucial as they are involved in many disease progressions. A lot of pathogenic cells use glycocalyx recognition as their first step of attack, for instance, viruses have glycan binding receptors that help them dock to the victim cells to initiate viral entry. Extracting and purifying naturally occurring glycans is extremely challenging and has accelerated the need for synthetic glycopolymers that are well-defined. As with any simplified system, these synthetic glycopolymers are not an absolute representation of the glycocalyx but they can be designed to mimic specific aspects. Such synthetic glycopolymers have been used in the past to develop targeted dendritic cell vaccines, coated surfaces, decorated model membranes for studying lectin binding process, and for studying adhesion among other applications. Researchers are simultaneously developing advanced synthesis techniques for formulating such glycopolymers with high precision in their chain lengths and functionalization. In synthetic cells, decoration with glycopolymers would be pivotal to target carbohydrate-involved mechanisms for therapeutic strategies. Such glyco-engineering can also provide synthetic cells with controlled molecular recognition capabilities, and moreover functionalize the synthetic cells to be able to carry

cell-like function such as adhesion, migration and signalling.

Part III

Appendix

A
Appendix to Section 6.2

Supporting Information

Elucidating the physicochemical processes of light activated rotary motors embedded in lipid membranes

Ainoa Guinart [‡,a], Yusuf Qutbuddin [‡,b], Alexander Ryabchun [a], Jan-Hagen Krohn[b], Petra Schwille[b,*], and Ben L. Feringa[a,*]

[a] Stratingh Institute for Chemistry, University of Groningen, 9747AG Groningen, The Netherlands.

[b] Cellular and Molecular Biophysics, Max Planck Institute of Biochemistry, 82152 Martinsried, Germany

[‡] Authors contributed equality to this work

* Corresponding author. E-mail: b.l.feringa@rug.nl

Table of contents

1. Chemical Characterization

a. General information

Chemicals were purchased from commercial sources, by name Sigma-Aldrich, Fluorochem, TCI, BLDpharm and used without further purification. Dried solvents were obtained from Acros Organics, Alfa Aesar or from a solvent purification system (MBraun SPS-800).

NMR spectra were recorded on a Varian Mercury-Plus 400, a Varian Unity Plus 500 or a Bruker 600 MHz NMR spectrometer at 298 K unless stated otherwise. Chemical shifts are reported in parts per million (ppm) and referenced to the residual solvent signal ($CDCl_3$: δ = 7.26 for ^1H and 77.2 for $^{13}C\{^1H\}$; $(CD_3)_2SO$: δ = 2.50 for ^1H and 39.5 for $^{13}C\{^1H\}$; CD_3OD: δ = 3.31 for ^1H and 49.0 for $^{13}C\{^1H\}$; CD_2Cl_2: δ = 5.32 for ^1H and 53.8 for $^{13}C\{^1H\}$) and thereby relatively stated to TMS. The resonance multiplicity is indicated as s = singlet, d = doublet, t = triplet, m = multiplet, dd (doublet of doublets), dt (doublet of triplets), td (triplet of doublets), tdd (triplet of doublets of doublets), br = broad and the coupling constant values (J) are given in hertz (Hz). High resolution mass spectra (HRMS) were recorded on a LTQ Orbitrap XL spectrometer. UV-Vis absorption spectra were recorded on an Agilent 8453 UV-Vis Diode Array System, equipped with a Quantum Northwest Peltier controller in 10 mm quartz cuvettes. Irradiation experiments were performed using LEDs from Thorlabs Incorporated (365, 405 a nm).

b. Compound characterization

All compounds used in this work have been previously synthesized and reported extensively in previous works (see each for references).

MM1 (9-(2-methyl-2,3-dihydro-1H-cyclopenta[a]naphthalen-1-ylidene)-9H-fluorene). Details on the synthesis can be found[1].

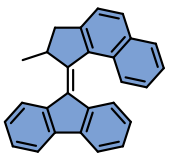

MM1
$C_{27}H_{20}$
344.457 g/mol

^1H NMR (600 MHz, $CDCl_3$): δ = 7.98 – 7.89 (m, 3H), 7.89 – 7.77 (m, 2H), 7.65 (d, J = 8.4 Hz, 1H), 7.59 (d, J = 8.2 Hz, 1H), 7.53 (d, J = 8.3 Hz, 1H), 7.48 (t, J = 7.7 Hz, 1H), 7.36 (t, J = 7.5 Hz, 1H), 6.94 (d, J = 8.5 Hz, 1H), 6.54 (d, J = 8.5 Hz, 1H), 4.27 (p, J = 6.6 Hz, 1H), 3.58 (dd, J = 15.1, 5.6 Hz, 1H), 2.79 (d, J = 15.0 Hz, 1H), 1.37 (d, J = 6.7 Hz, 3H). **^{13}C NMR** (151 MHz, $CDCl_3$): δ = 153.2, 148.2, 140.7, 140.2, 138.8, 136.1, 135.9, 132.9, 131.7, 130.4, 129.8, 129.4, 129.0, 128.7, 127.3, 127.2, 127.1, 125.7, 125.5, 124.2, 123.2, 122.5, 121.1, 121.1, 45.61, 42.1, 19.4. **HRMS-APCI:** calculated for $C_{27}H_{18}Br_2^+$ $[M]^+$ 499.9770, found 499.9749.

MM2 (9-(2-phenyl-2,3-dihydro-1H-cyclopenta[a]naphthalen-1-ylidene)-9H-fluorene). Details on the synthesis can be found[2].

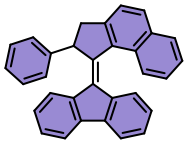

MM2
$C_{32}H_{22}$
406.528 g/mol

^{1}H NMR (600 MHz, $CDCl_3$): δ 8.01 (d, J = 8.4 Hz, 1H), 7.96 – 7.92 (m, 1H), 7.87 (d, J = 8.2 Hz, 1H), 7.80 (d, J = 7.5 Hz, 1H), 7.77 (d, J = 7.5 Hz, 1H), 7.53 – 7.47 (m, 2H), 7.45 (d, J = 8.2 Hz, 1H), 7.42 (ddd, J = 8.3, 6.8, 1.3 Hz, 1H), 7.31 (td, J = 7.5, 1.0 Hz, 1H), 7.28 – 7.25 (m, 3H), 7.22 – 7.17 (m, 2H), 7.16 – 7.10 (m, 2H), 6.85 (td, J = 7.6, 1.2 Hz, 1H), 6.80 (d, J = 7.9 Hz, 1H), 5.37 (d, J = 6.4 Hz, 1H), 3.99 (dd, J = 15.0, 6.5 Hz, 1H), 3.23 (d, J = 15.1 Hz, 1H). **^{13}C{1H} NMR** (125 MHz, $CDCl_3$): δ 146.43, 146.22, 143.99, 140.12, 139.91, 139.56, 137.66, 137.10, 133.09, 132.81, 131.19, 129.07, 128.92, 128.62, 128.03, 127.83, 127.29, 127.06, 126.84, 126.45, 126.18, 126.03, 125.87, 125.53, 124.46, 123.72, 119.91, 119.55, 119.11, 56.61, 44.13.

MM3 (2-((1-(9H-fluoren-9-ylidene)-2-methyl-2,3-dihydro-1H-cyclopenta[a]naphthalen-5-yl)oxy)ethan-1-ol). Details on the synthesis can be found[3].

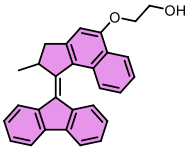

MM3
$C_{29}H_{24}O_2$
404.509 g/mol

^{1}H NMR (600 MHz, $CDCl_3$): δ 8.40 (dt, J = 8.5, 1.0 Hz, 1H), 8.03 – 7.98 (m, 1H), 7.91 – 7.86 (m, 1H), 7.80 (dt, J = 7.6, 0.9 Hz, 1H), 7.76 (d, J = 8.4 Hz, 1H), 7.50 (ddd, J = 8.2, 6.7, 1.2 Hz, 1H), 7.43 – 7.39 (m, 2H), 7.37 (ddd, J = 8.2, 6.7, 1.3 Hz, 1H), 7.23 (td, J = 7.4, 1.0 Hz, 1H), 7.01 (s, 1H), 6.84 (ddd, J = 8.2, 7.2, 1.2 Hz, 1H), 6.75 (d, J = 7.9 Hz, 1H), 4.46 – 4.38 (m, 2H), 4.35 (p, J = 6.6 Hz, 1H), 4.21 (s, 2H), 3.59 (dd, J = 15.0, 5.6 Hz, 1H), 2.75 (d, J = 15.0 Hz, 1H), 1.43 (d, J = 6.7 Hz, 3H). **^{13}C NMR** (151 MHz, $CDCl_3$): δ 156.9, 151.5, 149.1, 140.0, 139.9, 139.4, 137.4, 130.8, 129.3, 128.6, 127.6, 127.4, 126.9, 126.6, 126.5, 126.0, 125.8, 125.0, 124.7, 123.9, 122.6, 119.8, 119.0, 103.7, 70.0, 61.7, 45.3, 42.6, 19.7. **HRMS (ESI+, m/z):**: calculated for $C_{29}H_{25}O_2$ [M+H] 405.1849, found 405.1848

MM4 (5-((1-(9H-fluoren-9-ylidene)-2-methyl-2,3-dihydro-1H-cyclopenta[a]naphthalen-5-yl)oxy)pentanoic acid). Details on the synthesis can be found[4].

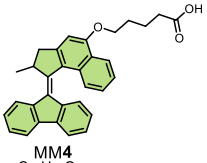

MM4
$C_{32}H_{28}O_3$
460.573 g/mol

^{1}H NMR (600 MHz, $CDCl_3$): δ 8.37 (d, J = 8.4 Hz, 1H), 8.01 – 7.95 (m, 1H), 7.90 – 7.84 (m, 1H), 7.77 (d, J = 7.5 Hz, 1H), 7.71 (d, J = 8.4 Hz, 1H), 7.46 (ddd, J = 8.2, 6.7, 1.2 Hz, 1H), 7.38 (td, J = 6.7, 4.1 Hz, 2H), 7.33 (ddd, J = 8.3, 6.8, 1.3 Hz, 1H), 7.20 (t, J = 7.4 Hz, 1H), 6.93 (s, 1H), 6.85 – 6.78 (m, 1H), 6.73 (d, J = 7.9 Hz, 1H), 4.36 – 4.23 (m, 3H), 3.73 (q, J = 7.0 Hz, 1H), 3.55 (dd, J = 15.0, 5.6 Hz, 1H), 2.71 (d, J = 15.0 Hz, 1H), 2.56 (t, J = 7.2 Hz, 2H), 2.07 (dt, J = 10.8, 6.0 Hz, 2H), 2.05 – 1.97 (m, 2H), 1.40 (d, J = 6.7 Hz, 3H). **^{13}C NMR** (151 MHz, $CDCl_3$): δ 178.6, 157.6, 152.1, 149.6, 140.4, 140.2, 139.6, 137.7, 131.1, 129.0, 128.6, 127.8, 127.6, 127.2, 126.8, 126.7, 126.3, 126.2, 125.2, 125.1, 124.2, 123.2, 120.1, 119.3, 103.6, 68.3, 45.6, 43.0, 34.0, 29.1, 22.1, 20.1.

MM5 (2,2'-((1-(9H-fluoren-9-ylidene)-2,7-dimethyl-2,3-dihydro-1H-indene-5,6-diyl)bis(oxy))bis(ethan-1-ol). Details on the synthesis can be found[5,6].

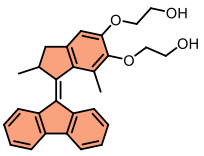

MM5
$C_{28}H_{28}O_4$
428.528 g/mol

^{1}H NMR (600 MHz, $CDCl_3$): δ 7.89 – 7.84 (m, 1H), 7.84 – 7.79 (m, 1H), 7.76 (dt, J = 7.6, 0.9 Hz, 1H), 7.38 – 7.35 (m, 2H), 7.33 (d, J = 7.8 Hz, 1H), 7.28 (td, J = 7.4, 1.0 Hz, 1H), 7.14 – 7.08 (m, 1H), 6.87 (s, 1H), 4.24 – 4.18 (m, 2H), 4.18 – 4.11 (m, 2H), 4.05 (ddd, J = 10.3, 5.4, 2.5 Hz, 1H), 4.01 (t, J = 4.3 Hz, 2H), 4.00 – 3.95 (m, 1H), 3.93 (ddd, J = 12.1, 5.5, 2.8 Hz, 1H), 3.32 (dd, J = 14.6, 5.8 Hz, 1H), 2.56 (d, J = 14.6 Hz, 1H), 2.21 (s, 3H), 1.34 (d, J = 6.7 Hz, 3H). **^{13}C NMR** (151 MHz, $CDCl_3$): δ 152.8, 152.0, 145.9, 144.4, 140.2, 140.1, 139.8, 138.3, 134.5, 132.5, 129.7, 127.4, 127.3, 127.2, 126.9, 124.2, 123.7, 120.1, 119.7, 108.5, 74.8, 71.1, 62.6, 61.5, 45.3, 42.1, 19.4, 16.4. **HRMS (ESI+, m/z):** calculated for $C_{28}H_{28}O_4$ 428.1987, found 428.1998.

MM6 **(9-(2-methyl-2,3-dihydro-1H-cyclopenta[a]naphthalen-1-ylidene)-9H-fluorene-2,7-dicarboxylic acid).** Details on the synthesis can be found (molecule 3.9, p 66)[7].

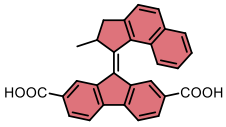

MM6
$C_{29}H_{20}O_4$
432.470 g/mol

^{1}H NMR (600 MHz, MeOD): δ 8.74 (d, J = 1.4 Hz, 1H), 8.08 (dd, J = 7.9, 1.3 Hz, 1H), 7.99 – 7.95 (m, 2H), 7.93 (d, J = 8.3 Hz, 1H), 7.91 – 7.85 (m, 2H), 7.61 (d, J = 8.2 Hz, 1H), 7.57 (d, J = 8.4 Hz, 1H), 7.41 (ddd, J = 8.1, 6.8, 1.2 Hz, 1H), 7.37 (d, J = 1.2 Hz, 1H), 7.24 (ddd, J = 8.3, 6.8, 1.3 Hz, 1H), 4.41 (p, J = 6.5 Hz, 1H), 3.61 (dd, J = 15.2, 5.6 Hz, 1H), 2.83 (d, J = 15.2 Hz, 1H), 1.42 (d, J = 6.7 Hz, 3H). **^{13}C NMR** (151 MHz, $CDCl_3$): δ 169.07, 168.53, 153.85, 147.93, 142.33, 141.92, 140.09, 137.45, 135.22, 132.53, 131.47, 129.73, 129.42, 128.43, 128.40, 128.23, 127.98, 127.33, 126.52, 126.43, 125.38, 125.03, 123.48, 119.76, 119.04, 45.10, 41.55, 18.78. **HRMS (ESI+, m/z):** calculated for C29H21O4 [M+H]+ 433.1434, found 433.1433.

MM7 **(((9-(2-methyl-2,3-dihydro-1H-cyclopenta[a]naphthalen-1-ylidene)-9H-fluorene-2,7-diyl)bis(oxy))bis(ethane-2,1-diyl) bis(dimethylcarbamate)).** Details on the synthesis can be found[8].

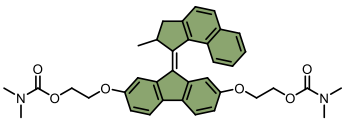

MM7
$C_{37}H_{38}N_2O_6$
606.720 g/mol

^{1}H NMR (600 MHz, $CDCl_3$): δ 7.97 – 7.89 (m, 2H), 7.76 (d, J = 8.4 Hz, 1H), 7.61 (d, J = 8.3 Hz, 1H), 7.58 (d, J = 8.2 Hz, 1H), 7.55 – 7.47 (m, 2H), 7.44 (ddd, J = 8.2, 6.7, 1.3 Hz, 1H), 7.36 (ddd, J = 8.2, 6.7, 1.3 Hz, 1H), 6.95 (dd, J = 8.3, 2.2 Hz, 1H), 6.78 (dd, J = 8.2, 2.3 Hz, 1H), 6.24 (d, J = 2.3 Hz, 1H), 4.49 (dd, J = 5.6, 3.9 Hz, 2H), 4.30 (dd, J = 5.6, 4.3 Hz, 3H), 3.99 (td, J = 4.3, 1.3 Hz, 2H), 3.57 (dd, J = 15.1, 5.6 Hz, 1H), 3.30 (ddd, J = 10.4, 5.8, 4.2 Hz, 1H), 3.11 – 3.02 (m, 1H), 2.94 (s, 6H), 2.88 (s, 3H), 2.82 – 2.74 (m, 4H), 1.40 (d, J = 6.8 Hz, 3H). **^{13}C NMR** (151 MHz, $CDCl_3$): δ 157.4, 156.4, 156.2, 151.5, 147.7, 140.9, 137.9, 135.8, 132.9, 132.3, 131.2, 130.0, 129.4, 128.9, 127.6, 126.7, 125.2, 124.2, 119.5, 119.0, 115.7, 112.8, 111.1, 110.4, 66.7, 65.4, 63.9, 63.6, 45.1, 41.8, 36.5, 36.4, 36.1, 35.9, 19.25

MM8 (6-((9-(6-((6-(acryloyloxy)hexyl)oxy)-2,4,7-trimethyl-2,3-dihydro-1H-inden-1-ylidene)-9H-fluoren-2-yl)oxy)hexyl acrylate). Details on the synthesis can be found[9].

MM8 was used as a 75:25 mixture of the E/Z isomers.

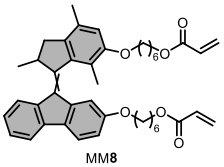

MM**8**
$C_{43}H_{50}O_6$
662.867 g/mol

^{1}**H NMR-*E*** (600 MHz, $CDCl_3$): δ 7.66 (dd, J = 12.36, 7.90 Hz, 2H), 7.45 (d, J = 2.21 Hz, 1H), 7.34 (d, J = 7.84 Hz, 1H), 7.25 (t, J = 7.40 Hz, 1H), 7.11 – 7.01 (m, 1H), 6.92 (dd, J = 8.37, 2.10 Hz, 1H), 6.73 (s, 1H), 6.41 (ddd, J = 17.30, 3.16, 1.53 Hz, 2H), 6.13 (ddd, J = 17.30, 10.36, 3.27 Hz, 2H), 5.82 (ddd, J = 10.36, 3.90, 1.58 Hz, 2H), 4.28 – 4.14 (m, 6H), 4.09 (q, J = 6.46 Hz, 4H), 3.96 (dd, J = 9.13, 6.52 Hz, 1H), 3.17 (dd, J = 14.47, 5.74 Hz, 1H), 2.54 (d, J = 14.42 Hz, 1H), 2.32 (s, 3H), 2.12 (s, 3H), 1.85 (m, J = 15.24, 8.67, 7.52 Hz, 5H), 1.74 (td, J = 6.73, 3.55 Hz, 5H), 1.63 – 1.41 (m, 11H), 1.35 (d, J = 6.64 Hz, 3H). ^{13}**C NMR-*E*** (151 MHz, $CDCl_3$): δ 166.4, 158.8, 156.7, 152.4, 141.3, 141.0, 139.5, 137.8, 136.7, 133.3, 131.8, 130.6, 130.6, 130.5, 128.6, 127.1, 125.5, 124.0, 123.9, 120.2, 118.3, 113.6, 113.3, 110.9, 68.6, 68.2, 64.6, 64.6, 44.2, 39.3, 29.5, 29.3, 28.7, 28.6, 26.0, 25.9, 25.8, 19.1, 18.8, 15.7.**HRMS (ESI) m/z calculated for [M+Na]+ C43H50O6**: 685.3500, found: 685.3529.

^{1}**H NMR-*Z*** (600 MHz, $CDCl_3$): δ 7.82 (d, J = 7.59 Hz, 1H), 7.67 (d, J = 7.08 Hz, 1H), 7.58 (d, J = 8.79 Hz, 1H), 7.27 (m, J = 21.55, 7.50 Hz, 2H), 7.00 (d, J = 2.20 Hz, 1H), 6.85 – 6.79 (m, 1H), 6.70 (s, 1H), 6.39 (d, J = 17.26 Hz, 2H), 6.11 (dd, J = 17.34, 10.39 Hz, 2H), 5.79 (d, J = 10.43 Hz, 2H), 4.14 (m, J = 15.76, 7.63, 6.93 Hz, 5H), 4.00 (dd, J = 21.79, 7.99, 7.04 Hz, 2H), 3.78 (m, J = 23.29, 8.36, 7.52 Hz, 2H), 3.14 (dd, J = 14.67, 5.68 Hz, 1H), 2.52 (d, J = 14.92 Hz, 1H), 2.30 (s, 3H), 2.15 (s, 2H), 1.83 (m, J = 7.08 Hz, 3H), 1.78 – 1.62 (m, 6H), 1.59 – 1.36 (m, 9H), 1.31 (d, J = 6.50 Hz, 3H). ^{13}**C NMR-*Z*** (151 MHz, $CDCl_3$): δ 166.3, 166.3, 158.6, 156.7, 152.4, 140.9, 140.1, 139.5, 139.4, 136.6, 132.7, 131.9, 130.6, 130.6, 130.5, 128.6, 128.6, 126.9, 125.7, 123.9, 123.6, 119.7, 118.8, 114.8, 113.5, 109.3, 68.5,67.7, 64.6, 64.6, 44.1, 39.3, 29.6, 29.2, 28.7, 28.6, 26.0, 25.9, 25.8, 25.7, 19.1, 18.8, 15.8. **HRMS (ESI) m/z calculated for [M+Na]+ C43H50O6**: 685.3500, found: 685.3495.

MM9 ((Z)-N-(9-(6-benzamido-2-methyl-2,3-dihydro-1H-inden-1-ylidene)-9H-fluoren-2-yl)benzamide). Details on the synthesis can be found[10].

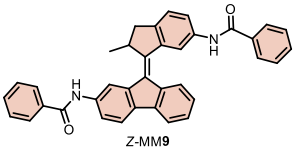

Z-MM**9**
$C_{37}H_{28}N_2O_2$
532.643 g/mol

^{1}**H NMR** (600 MHz, $CDCl_3$): δ 8.73 (s, 1H), 8.27 (s, 1H), 8.05 (s, 2H), 7.95 (s, 2H), 7.81 (d, J = 8.1 Hz, 2H), 7.75 (d, J = 8.5 Hz, 3H), 7.71 (d, J = 7.5 Hz, 2H), 7.63 (s, 2H), 7.58 (s, 4H), 7.37 (s, 2H), 7.22 (d, J = 7.4 Hz, 1H), 6.83 – 6.79 (m, 2H), 6.73 (d, J = 7.9 Hz, 2H), 3.60 (dd, J = 15.1, 5.5 Hz, 1H), 2.80 (d, J = 15.0 Hz, 1H), 1.48 (d, J = 6.7 Hz, 3H). ^{13}**C NMR** (151 MHz, $CDCl_3$): 167.0, 166.8, 144.5, 144.1, 143.9, 142.8, 140.1, 138.8, 138.5, 138.4, 137.2, 135.1, 134.9, 133.9, 131.9, 131.7, 129.6, 128.8, 128.6, 128.5, 128.4, 128.3, 128.2, 124.6, 124.3, 120.3, 119.9, 118.9, 117.2, 113.7, 113.4, 37.2, 36.6, 20.1.

2. Computations

Computational analysis was carried out using Orca 5.0.3 software package[11]. The ground state geometries of the molecules were optimized using density functional theory (DFT) at the r2scan-3c level. Vertical excitation spectra were calculated in the optimized geometry using TD-DFT within the Tamm-Dancoff approximation[12] with the WB97X-D3 functional and def2-TZVP basis set. The transition dipole moments for the S0→S1 transition were extracted from the calculation and used in the interpretation of the polarized light absorbance measurements.

	Energy	Dipole moment				Transition electric dipole moment				
		Mag [Debye]	x	y	z	Mag [eV]	T2 [au^2]	TX [au]	TY [au]	TZ [au]
MM1	-1040.3625	1.70939	-0.41452	0.51154	0.13701	3.619	8.07399	2.47644	-1.3308	-0.41257
MM2	-1232.0111	1.66533	-0.36355	0.3748	0.39574	3.576	8.21345	-1.50693	1.01837	2.21484
MM3	-1269.324	3.23636	-0.62665	0.80536	0.7615	3.548	9.67078	-2.69379	0.72986	1.3717
MM4	-1461.2074	2.45294	0.81081	0.50126	0.15043	3.553	9.91288	2.94496	-0.65696	-0.89917
MM5	-1383.9834	1.32141	0.44129	0.27481	0.00301	3.826	9.10572	-0.81392	2.90573	0.00019
MM6	-1417.4624	2.88955	0.17825	0.09237	1.11894	3.477	7.75843	0.06857	2.28776	1.58741
MM7	-1992.6842	4.39076	-0.05843	-0.20601	1.7141	3.473	0.70671	-0.25358	-0.72616	-0.33925
MM8-E	-2121.2072	4.34262	-1.55299	-0.4077	0.58389	3.775	1.54454	0.93912	0.74283	0.33287
MM9-Z	-1685.9673	5.14519	0.25135	-2.00353	-0.14214	3.741	7.13784	0.24056	-2.5986	0.57208

Table S1. Calculated optimized energies of the ground state geometry (MM1-9) with associated dipole moment and transition dipole moments using DFT and TD-DFT respectively.

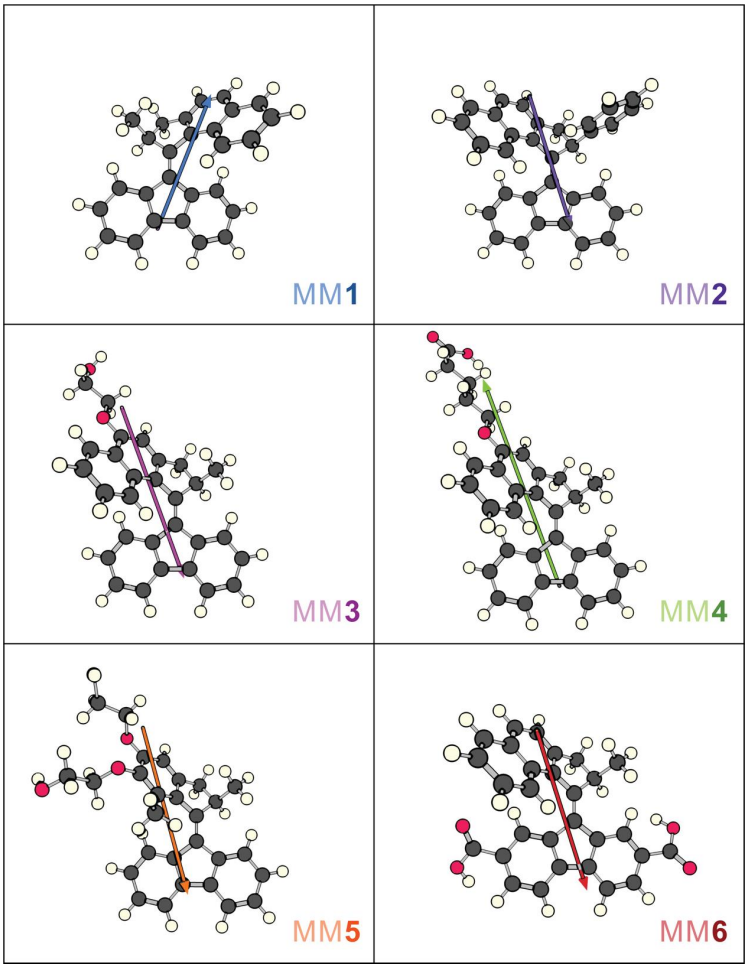
MM1
MM2
MM3
MM4
MM5
MM6

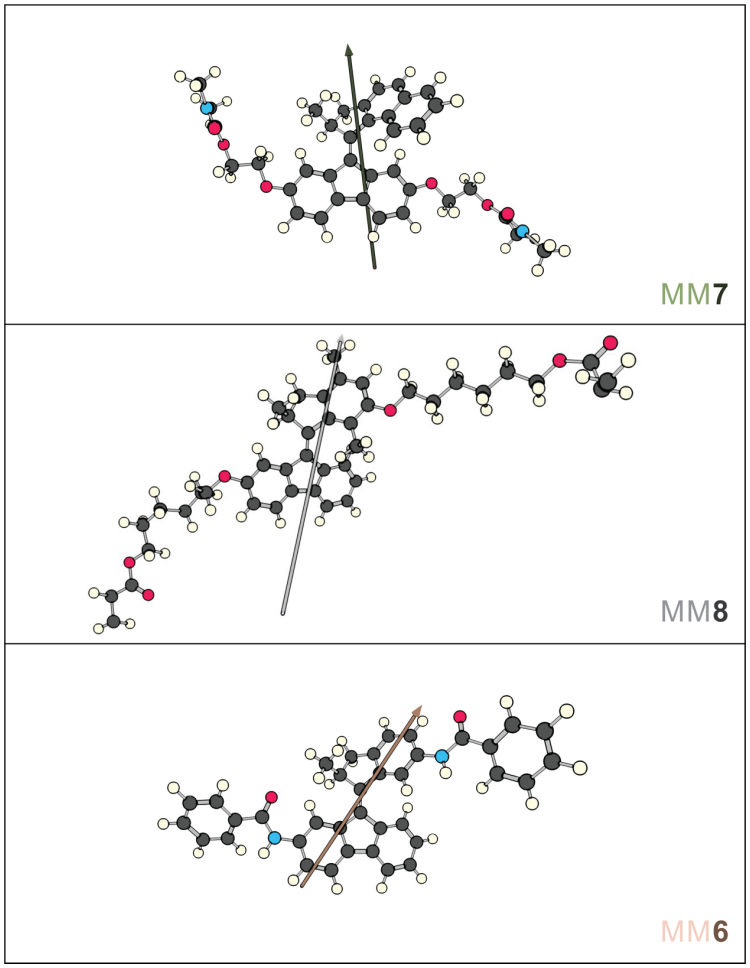

Figure S1. Transition dipole moment of MM1-9 optimized using TD-DFT using WB97X-D3 functional and def2-TZVP basis set.

3. Linear Dichroism

The absorption spectra were measured using a spectrometer HR2000+ (Ocean Optics). For the polarized light absorbance measurements, the spectrometer was equipped with a polarizer (Glan-Taylor prism) mounted on rotatable stage. The dichroism D was calculated according to the Equation:

$$Linear\ Dichroism\ (LD) = A_h - A_v$$

where A_h and A_v are the absorbance of polarized light, horizontal and vertical to the membrane alignment direction, respectively. The positive or negative sign of the LD value reflects the preferential absorption in either the vertical (positive) or horizontal (negative) direction. A zero value corresponds to no ordering. The absorption spectra (dotted lines) was measured using an Agilent 8453 UV–vis Diode Array System (see 7. UV-Vis spectroscopy for more details).

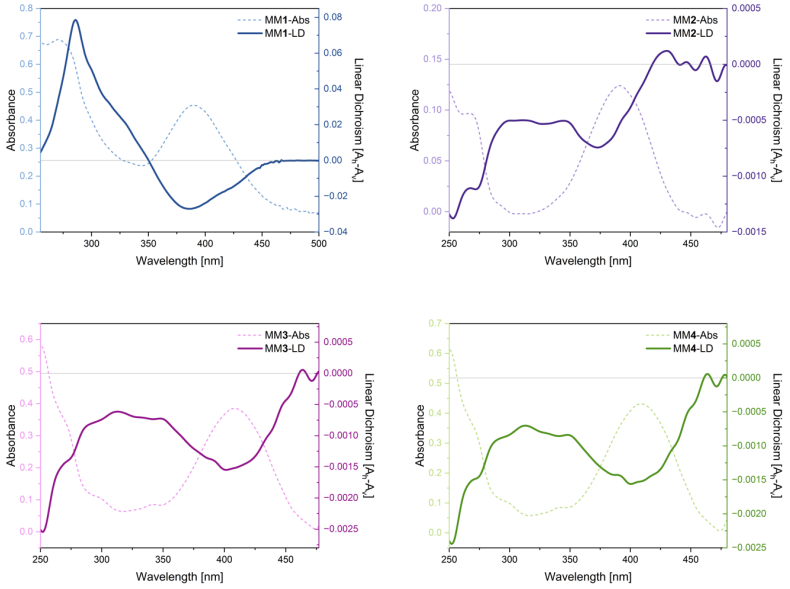

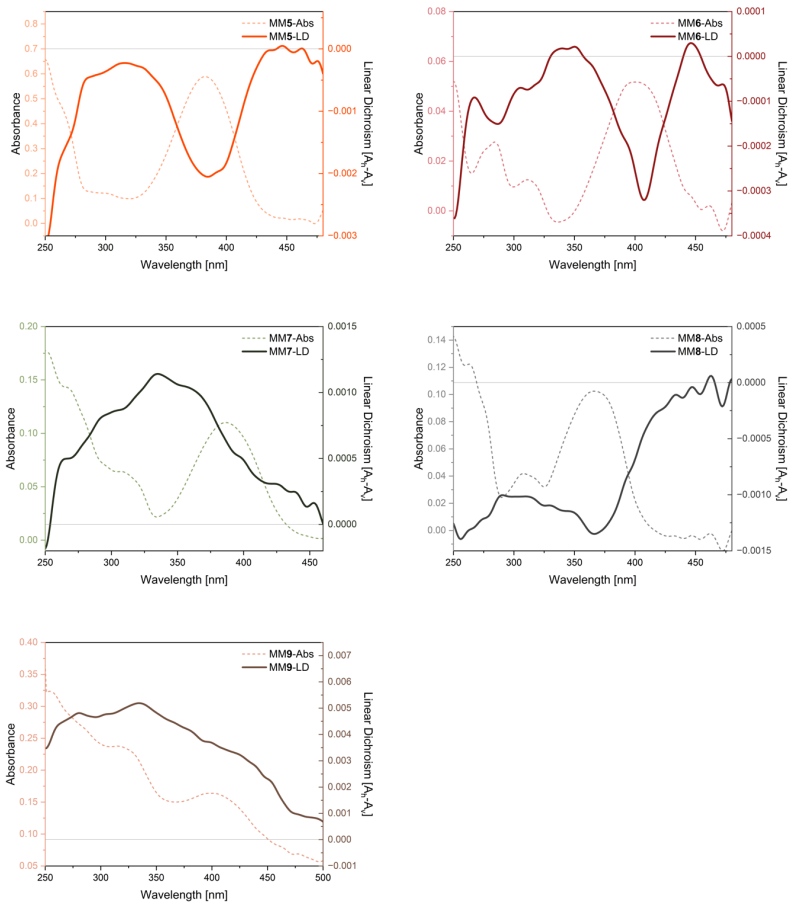

Figure S2. Linear dichroism (dark line, right) and absorbance (dotted line, left) measurements for MM**1-9**.

4. Fluorescence Correlation Spectroscopy

Fluorescence correlation spectroscopy was performed with Zeiss LSM980 laser scanning confocal microscope (Carl Zeiss, Germany). A custom macro was used to define z-locations above and below the desired focus and each z-position was measured for 30 sec acquisition time. All measurements were performed at 28°C. The individual autocorrelation curves were calculated and fitted with custom MATLAB and Python scripts, with 2D FCS diffusion fits.

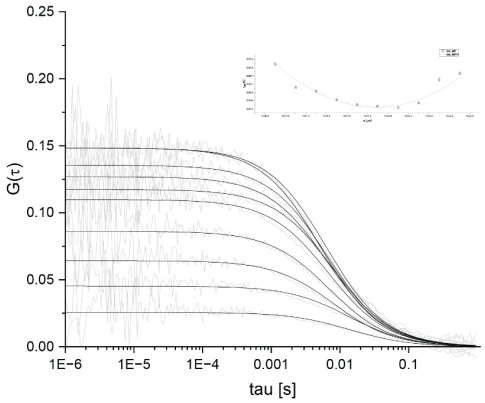

Figure S3. Representative autocorrelation curves and fits for a z-scan FCS measurement. Inset shows the fitted parabola for the measurement of corrected diffusion time from the z-scan FCS fits.

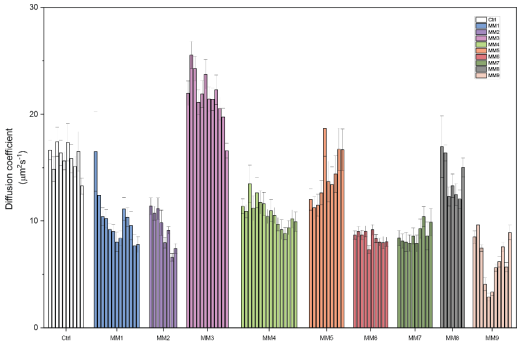

Figure S4. Diffusion coefficients and standard deviations calculated after the analysis of z-scan FCS

5. Fluorescence Lifetime of Flipper-TR

MicroTime200 (PicoQuant GmBH, Germany) equipped with a dual SPAD detection unit and a MultiHarp 150 TCSPC unit was used to measure fluorescence lifetime of Flipper-TR. SUVs of the desired composition incubated with 1 μM Flipper-TR was deposited on a passivated coverslip (#1.5) and the sample was measured with a pulsed 488 nm laser at 40 MHz, and the emitted fluorescence was collected through a 488LP long pass filter. SymphoTime64 was used to analyze and fit the TCSPC histograms, and the decays were fit with 2-component reconvolution fit to calculate the intensity averaged fluorescence lifetime.

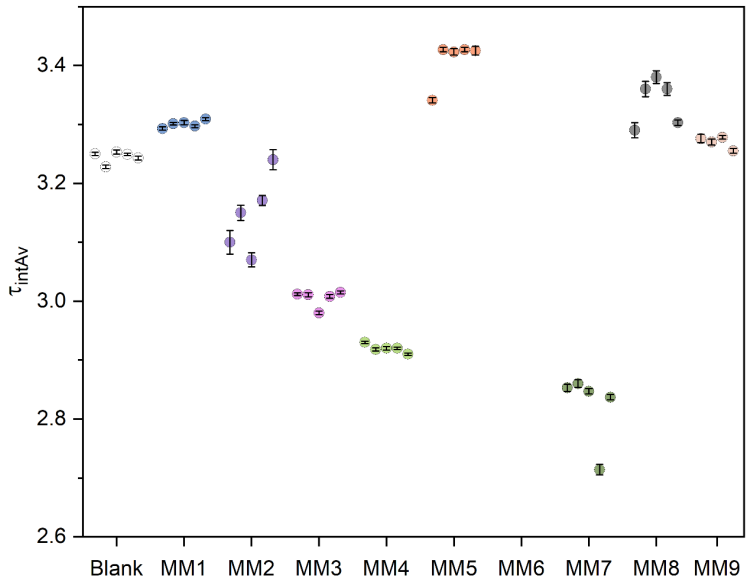

Figure S5. Measurement of intensity averaged fluorescence lifetime calculated of Flipper-TR with samples of POPC SUVs with 10 mol% MM**X** incubated with 1μM Flipper-TR.

6. NMR Irradiation Studies

A solution (1.5 mM) of molecular motors **1-9** was prepared in deuterated chloroform and transferred into an NMR tube which subsequently fitted with a glass optic fiber for in situ irradiation studies. The sample was place in a Varian Unity Plus 500 MHz NMR and cooled to -15 °C. ^{1}H NMR spectra were recorded before irradiation started, while irradiating with the appropriated wavelength LED (405, 395, 365 nm) until reaching PSS, and until the THI step was completed in the dark.
Three characteristic spectra (Start, PSS, THI) are displayed below for each molecular motor of study.
The evolution of two characteristic peaks corresponding to the stable and metastable states of motors **1-9** are shown in Figure S6 from the start of the irradiation until PSS is reached, the last point corresponds to the sample left in the dark after PSS until THI was completed.

NMR irradiation spectra – Dark/PSS/THI

MM**1** irradiation @405 nm

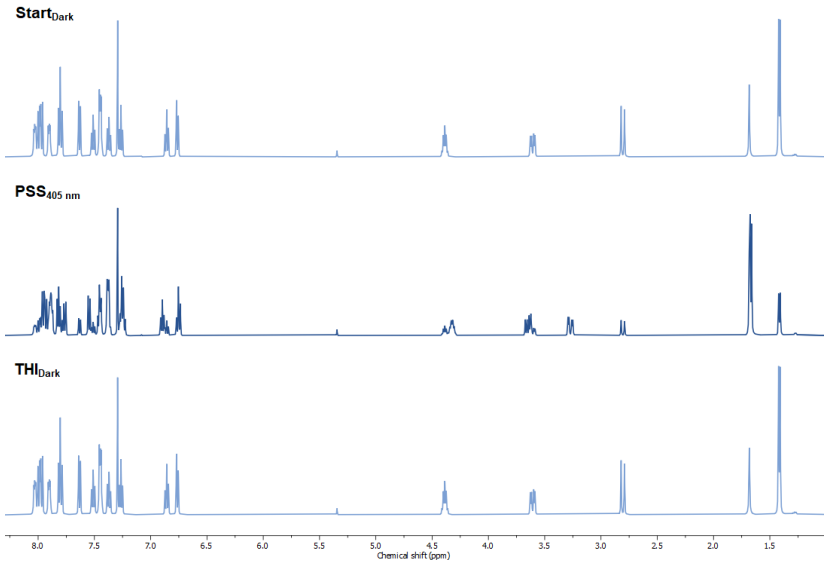

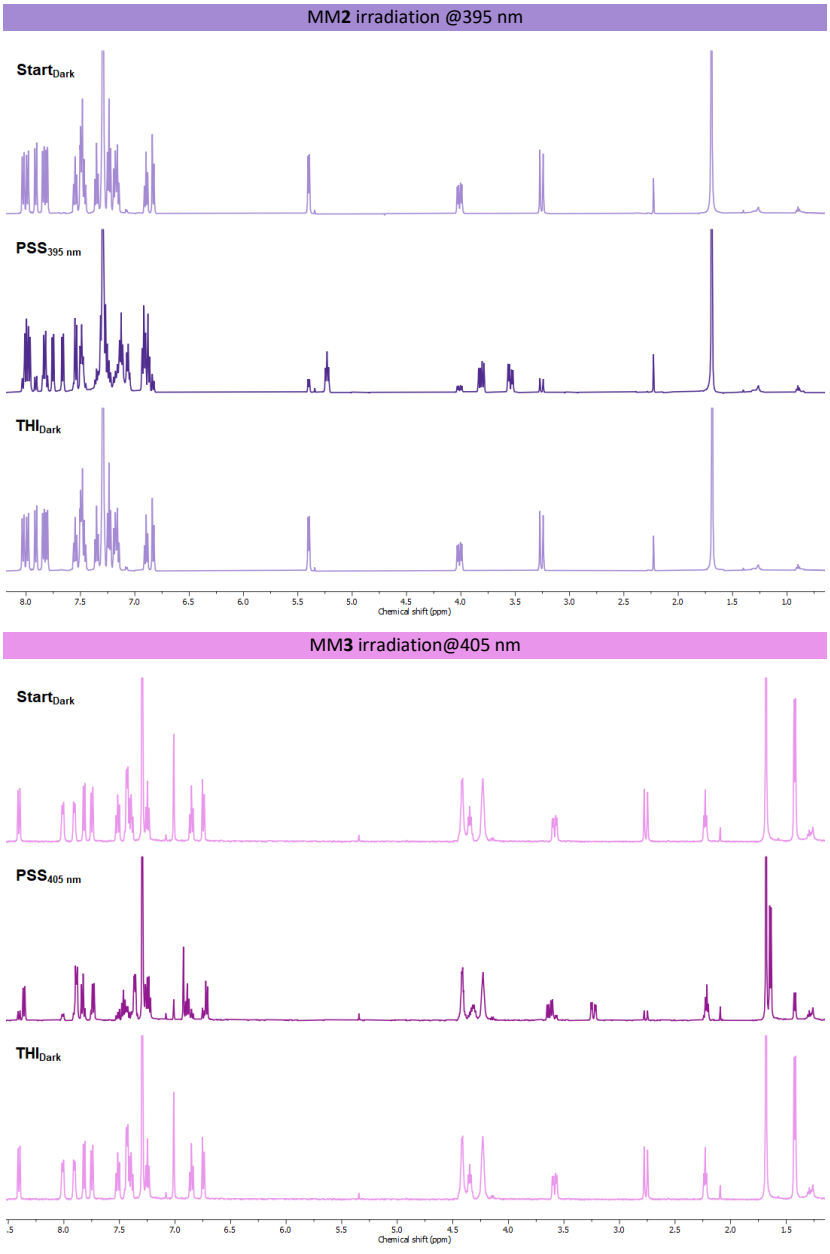
MM2 irradiation @395 nm
Start Dark
PSS 395 nm
THI Dark
8.0 7.5 7.0 6.5 6.0 5.5 5.0 4.5 4.0 3.5 3.0 2.5 2.0 1.5 1.0
Chemical shift (ppm)
MM3 irradiation@405 nm
Start Dark
PSS 405 nm
THI Dark
.5 8.0 7.5 7.0 6.5 6.0 5.5 5.0 4.5 4.0 3.5 3.0 2.5 2.0 1.5
Chemical shift (ppm)

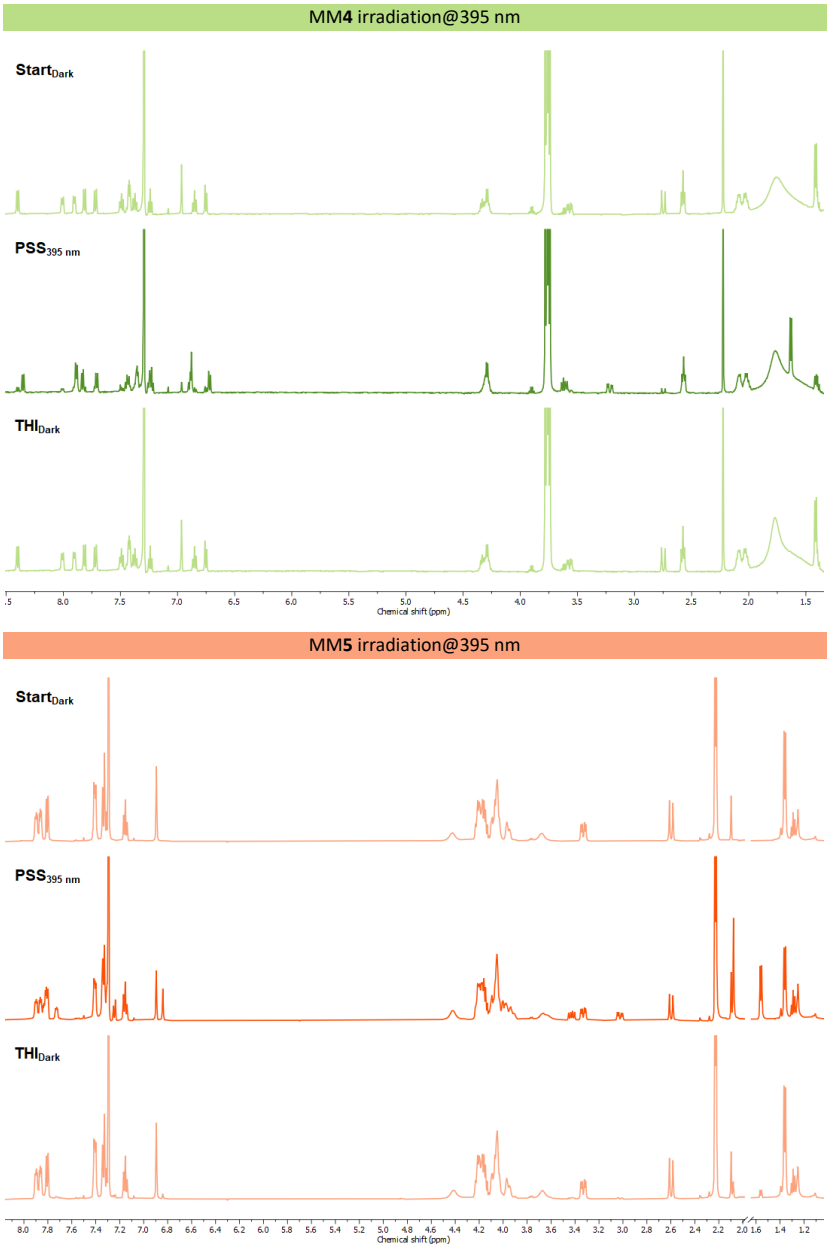
MM4 irradiation@395 nm
Start Dark
PSS 395 nm
THI Dark
Chemical shift (ppm)
MM5 irradiation@395 nm
Start Dark
PSS 395 nm
THI Dark
Chemical shift (ppm)

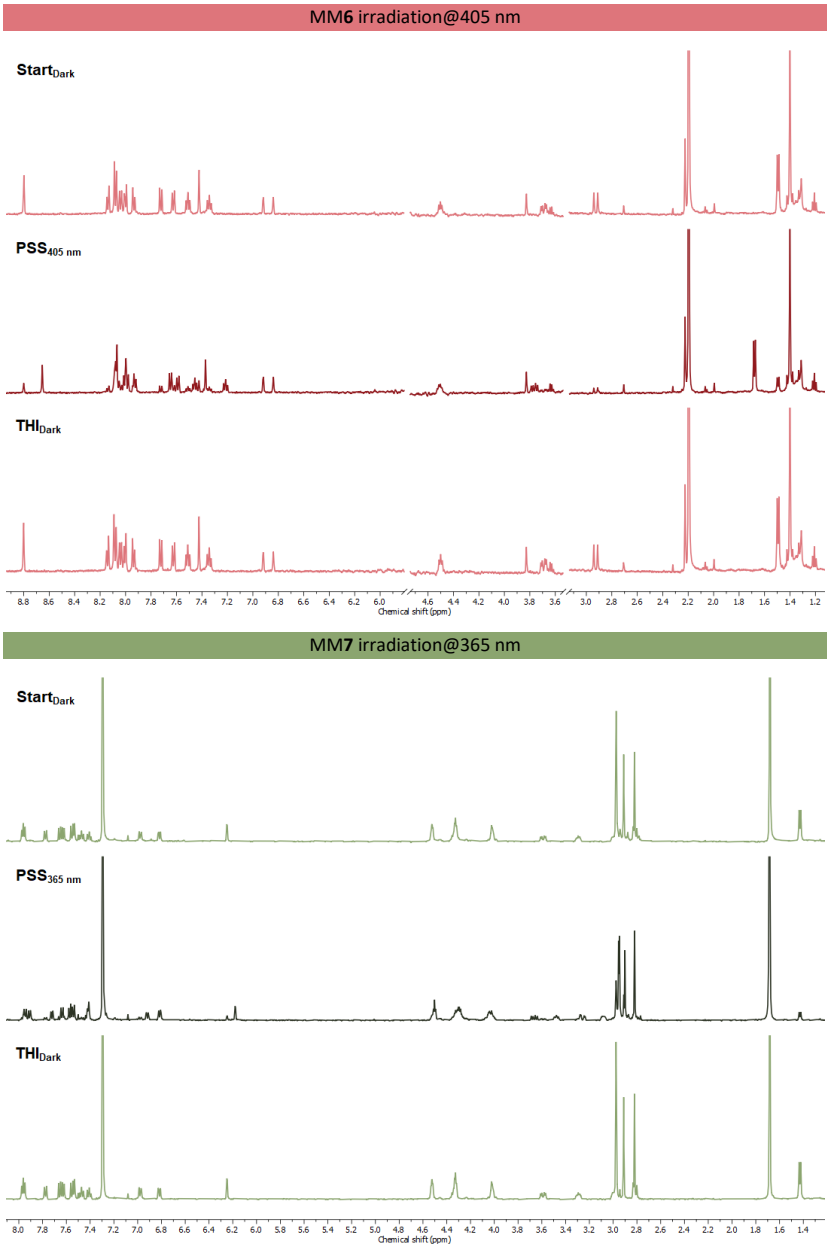
MM6 irradiation@405 nm
Start Dark
PSS 405 nm
THI Dark
Chemical shift (ppm)
MM7 irradiation@365 nm
Start Dark
PSS 365 nm
THI Dark
Chemical shift (ppm)

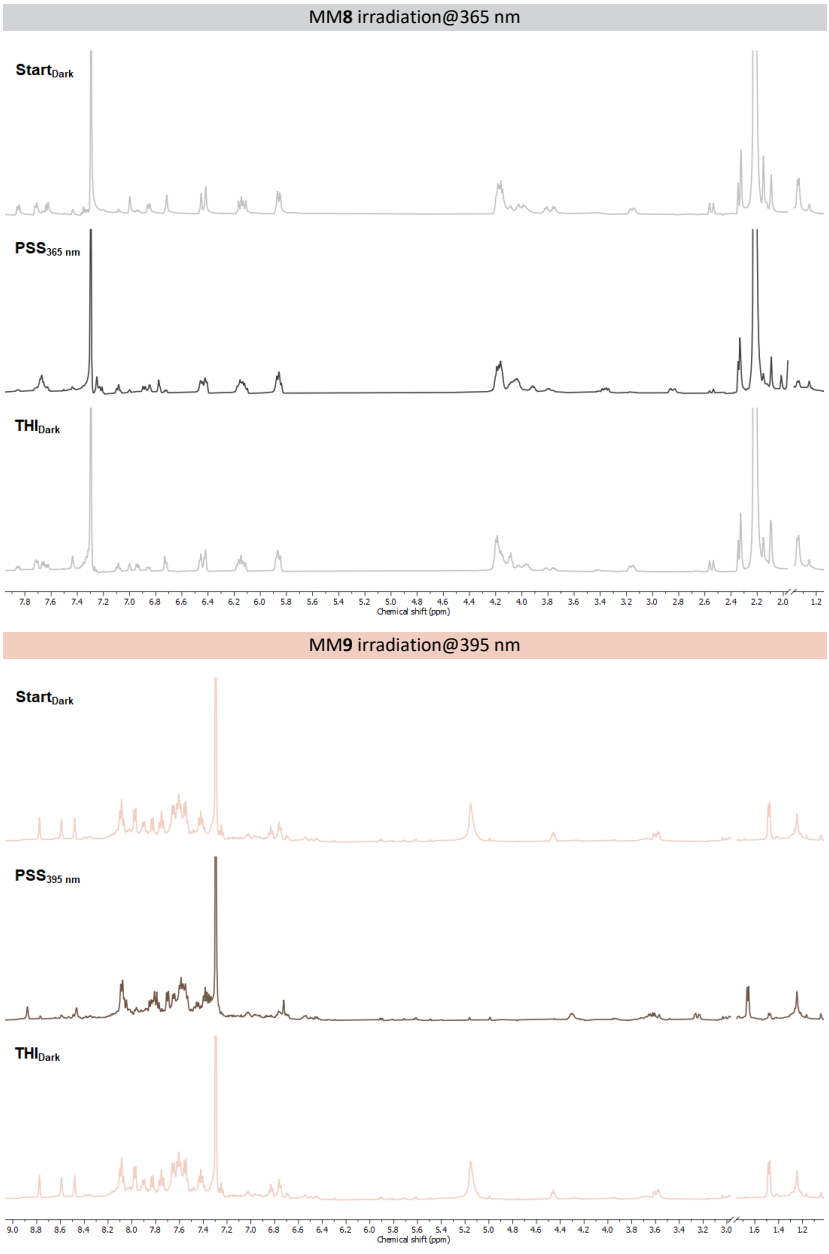
MM8 irradiation@365 nm
Start Dark
PSS 365 nm
THI Dark
7.8 7.6 7.4 7.2 7.0 6.8 6.6 6.4 6.2 6.0 5.8 5.6 5.4 5.2 5.0 4.8 4.6 4.4 4.2 4.0 3.8 3.6 3.4 3.2 3.0 2.8 2.6 2.4 2.2 2.0 1.2
Chemical shift (ppm)
MM9 irradiation@395 nm
Start Dark
PSS 395 nm
THI Dark
9.0 8.8 8.6 8.4 8.2 8.0 7.8 7.6 7.4 7.2 7.0 6.8 6.6 6.4 6.2 6.0 5.8 5.6 5.4 5.2 5.0 4.8 4.6 4.4 4.2 4.0 3.8 3.6 3.4 3.2 3.0 1.6 1.4 1.2
Chemical shift (ppm)

NMR peak integrals during irradiation/after THI – PSS ratio determination

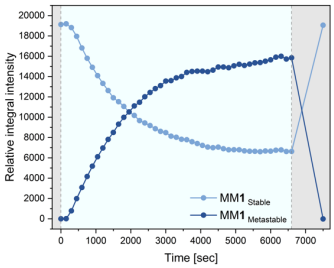

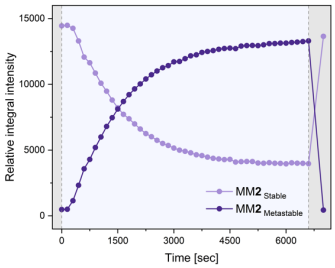

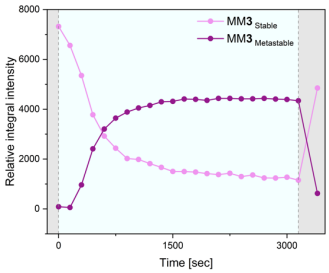

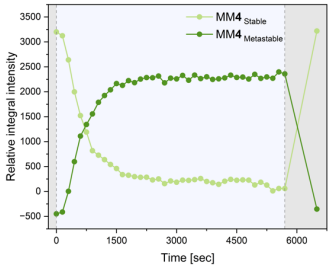

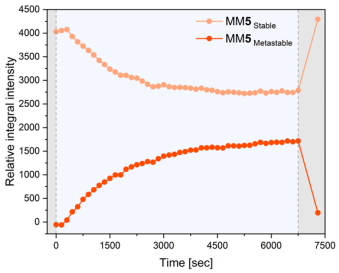

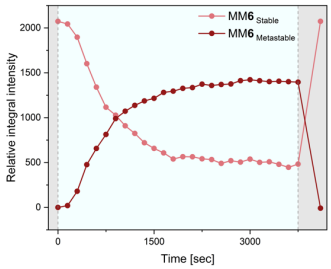

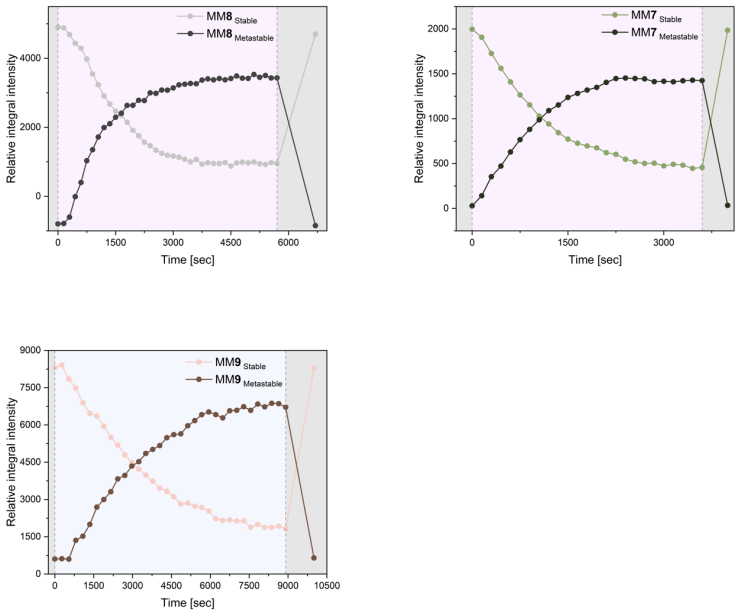

Figure S6. Following of a stable and metastable peak of interest under appropriate wavelength of Irradiation until PSS was reached for motors **1** to **9** (pink background). Stop irradiation and integral intensity after 16 h in the dark (grey background).

7. UV-Vis Spectroscopy

UV–vis spectroscopy was used for determination of molecular motor abruption peak maxima, uptake efficiency into lipid systems, partition coefficient, quantum yield of photoisomerization and thermodynamic studies. Briefly, samples containing free-standing lipid systems or molecular motor solutions were measured using an Agilent 8453 UV–vis Diode Array System, equipped with a Quantum Northwest Peltier controller. If specified, irradiations were done using a built-in setup coupled to an LED. Solutions were prepared and measured using a quartz cuvette.

a. Aggregation

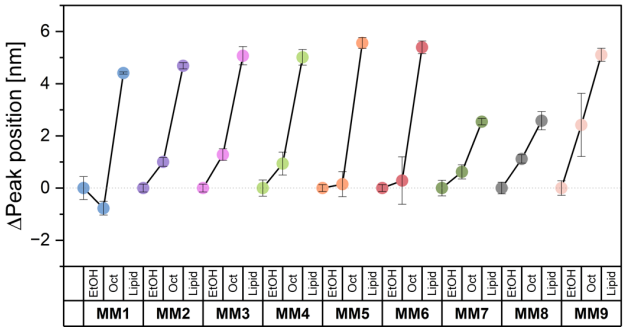

Figure S7. Difference in max absorbance peak position between different environments.

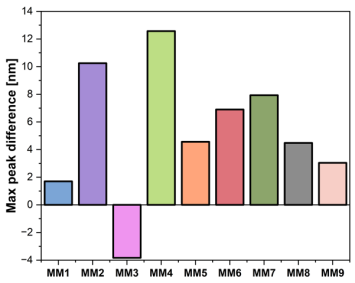

	Spectral shift in POPC SUVs [nm]	*Exponential fit t-value*		
MM1	**1.7**	**4.9**	±	1.0
MM2	**10.25**	**2.8**	±	1.0
MM3	**-3.83**	**-15.4**	±	3.4
MM4	**12.57**	**0.7**	±	0.1
MM5	**4.56**	**3.7**	±	0.6
MM6	**6.9**	**0.7**	±	0.1
MM7	**7.93**	**5.9**	±	1.9
MM8	**4.48**	**0.2**	±	0.0
MM9	**3.04**	**8.0**	±	2.5

Figure S8. Peak displacement of 1 mol% *vs* 25 mol% MM**1-9** mixtures in POPC (left graph).
Table S2. Peak displacement values and exponential fit values of H/J aggregates for MM**1-9** (right, table)

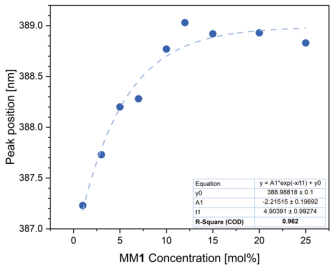
Peak position [nm]
MM1 Concentration [mol%]
Equation y = A1*exp(-x/t1) + y0
y0 388.98818 ± 0.1
A1 -2.21515 ± 0.19692
t1 4.90391 ± 0.99274
R-Square (COD) 0.962

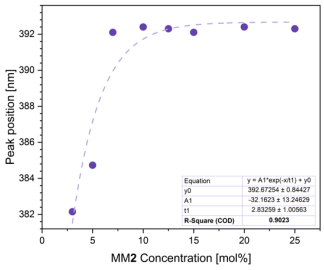
Peak position [nm]
MM2 Concentration [mol%]
Equation y = A1*exp(-x/t1) + y0
y0 392.87254 ± 0.84427
A1 -32.1623 ± 13.24629
t1 2.83259 ± 1.00563
R-Square (COD) 0.9023

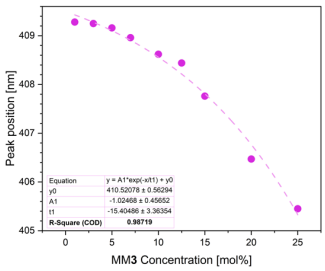
Peak position [nm]
MM3 Concentration [mol%]
Equation y = A1*exp(-x/t1) + y0
y0 410.52078 ± 0.56294
A1 -1.02468 ± 0.45652
t1 -15.40486 ± 3.36354
R-Square (COD) 0.98719

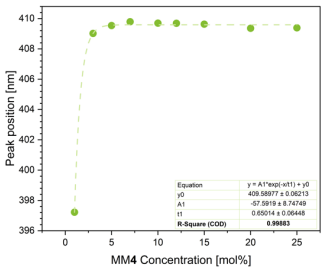
Peak position [nm]
MM4 Concentration [mol%]
Equation y = A1*exp(-x/t1) + y0
y0 409.58977 ± 0.06213
A1 -57.5919 ± 8.74749
t1 0.65014 ± 0.06448
R-Square (COD) 0.99883

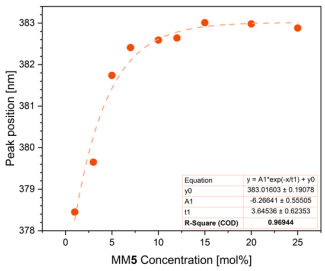
Peak position [nm]
MM5 Concentration [mol%]
Equation y = A1*exp(-x/t1) + y0
y0 383.01603 ± 0.19078
A1 -6.26641 ± 0.55505
t1 3.64536 ± 0.62353
R-Square (COD) 0.96944

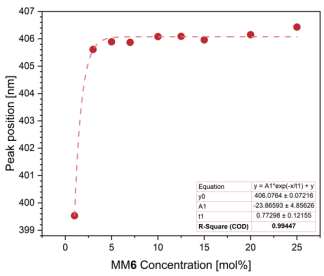
Peak position [nm]
MM6 Concentration [mol%]
Equation y = A1*exp(-x/t1) + y
y0 406.0764 ± 0.07216
A1 -23.86593 ± 4.85626
t1 0.77298 ± 0.12155
R-Square (COD) 0.99447

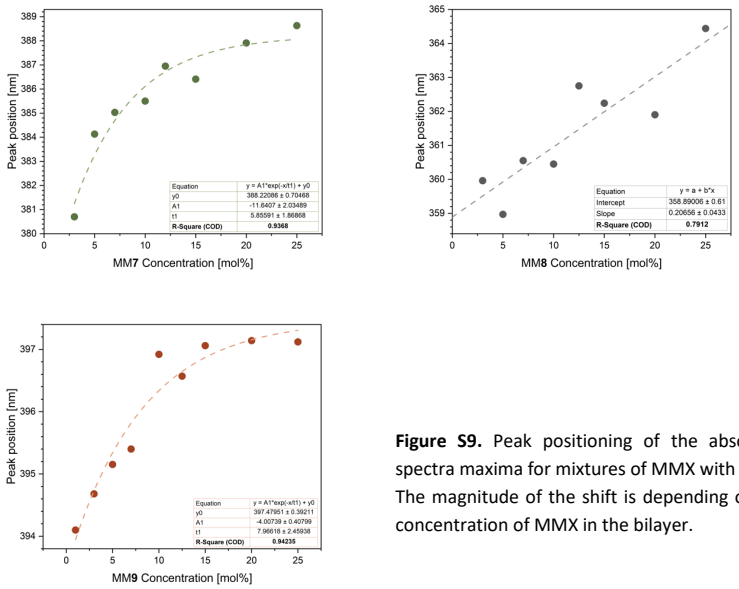

Figure S9. Peak positioning of the absoption spectra maxima for mixtures of MMX with POPC. The magnitude of the shift is depending on the concentration of MMX in the bilayer.

b. Standard curves

A solution of four known concentrations (13.5, 18, 27, and 54 µM) of molecular motors **1** to **9** in EtOH were measured and their absorbance at the peak maxima recorded and used to build a standard curve (linear analysis using Origin 2023 software package[13]. Following the Lambert-Beer law the resulting equations were used to determine the uptake efficiency of motor incorporation into free-standing lipid systems (see section 7c). The slope of the calculated curves was used as the absorption epsilon of the molecular motor stable state (see section 7e).

		Value	Std. Error	t-Value	Prob>|t|
MM1	Intercept	-0.00536	0.0037	-1.44922	0.2843
	Slope	62892.76	1147.200	54.8228	3.32553E-4
MM2	Intercept	-0.00583	0.00284	-2.05138	0.17669
	Slope	31660.39	882.9283	35.8584	7.76805E-4
MM3	Intercept	-0.00688	0.00183	-3.76299	0.06392
	Slope	20028.26	567.4962	35.29232	8.01894E-4
MM4	Intercept	-0.00693	0.00827	-0.83827	0.4901
	Slope	45423.58	2567.630	17.69086	0.00318
MM5	Intercept	0.00181	0.00221	0.81632	0.50008
	Slope	42258.34	686.710	61.53734	2.63968E-4
MM6	Intercept	-0.01161	0.00491	-2.36401	0.14184
	Slope	32243.19	1524.350	21.15208	0.00223
MM7	Intercept	0.00655	0.00228	2.87922	0.10243
	Slope	18473.50	706.248	26.15721	0.00146
MM8	Intercept	0.03736	7.59398E-4	49.19685	0.01294
	Slope	30791.53	212.611	144.82533	0.0044
MM9	Intercept	8E-5	0.01202	0.00666	0.99576
	Slope	26396.82	3365.127	7.84423	0.08072

Table S3. Standard curve equation values of linear analysis for motors **1** to **9**.

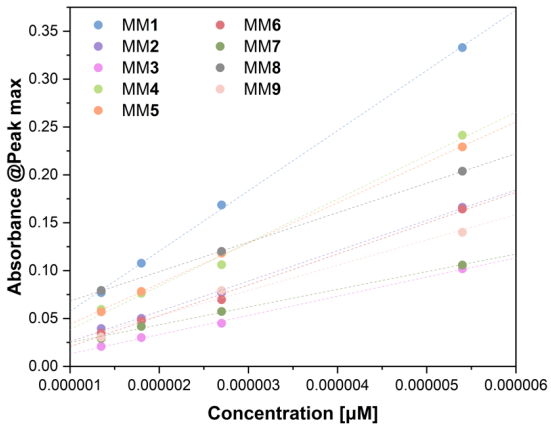

Figure S10. Standard curve plots for motors **1** to **9**.

c. Uptake efficiency

Free-standing lipid systems of POPC + 10 mol% molecular motors **1** to **9** were prepared using the thin film rehydration method and extruded through a polycarbonate membrane of 100 nm pore size 15 times. Absorbance measurements of the obtained peak maxima for each sample were recorded and compared to the theoretical value corresponding to the initial concentration (10 mol%) using the corresponding standard curve equation.
Uptake efficiency was calculated as:

$$\%\ uptake\ efficiency = 10\ mol\%\ \boldsymbol{MMX}\ \frac{Absorbance\ theoretical\ value}{Absorbance\ experimental\ value} * 100$$

d. Partition coefficient

In order to get better understanding of the behavior of MM1-9 in the presence of a phospholipid bilayer the partition coefficient (*n*-octanol/water) was determined via the shake flask method[14]. Briefly, a stock solution of known concentration of each MM**1**-**9** in *n*-octanol with water was prepared. Before the partition coefficient was determined, the two solvents were mutually saturated at the temperature of the experiment (20 °C) by shaking them for 24 hours on a mechanical shaker and letting them stand long enough to allow the phases to separate. To determine the partition coefficient the test vessels are placed in a mechanical shaker. For a first run, a volume of *n*-octanol to water and a quantity of motor are chosen. For a second run, the original volume ratio is divided by two and for a third run it is multiplied by two. The concentration of each test substance was determined in both phases by means of UV-Vis spectroscopy. The partition coefficient ($P_{O/W}$) and log $P_{O/W}$ were determine using:

$$P_{O/W} = \frac{C_{n-octanol}}{C_{water}}$$

	$P_{O/W}$	log ($P_{O/W}$)
MM**1**	7.23 ± 2.08	0.86 ± 0.029
MM**2**	27.62 ± 0.98	1.44 ± 0.035
MM**3**	8.96 ± 2.42	0.95 ± 0.271
MM**4**	10.16 ± 3.93	1.01 ± 0.387
MM**5**	6.64 ± 1.03	0.82 ± 0.156
MM**6**	12.66 ± 1.32	1.10 ± 0.105
MM**7**	3.01 ± 0.54	0.48 ± 0.180
MM**8**	11.10 ± 4.83	1.05 ± 0.435
MM**9**	3.87 ± 1.20	0.59 ± 0.310

Table S4. $P_{O/W}$ and log($P_{O/W}$) values for motors **1** to **9**.

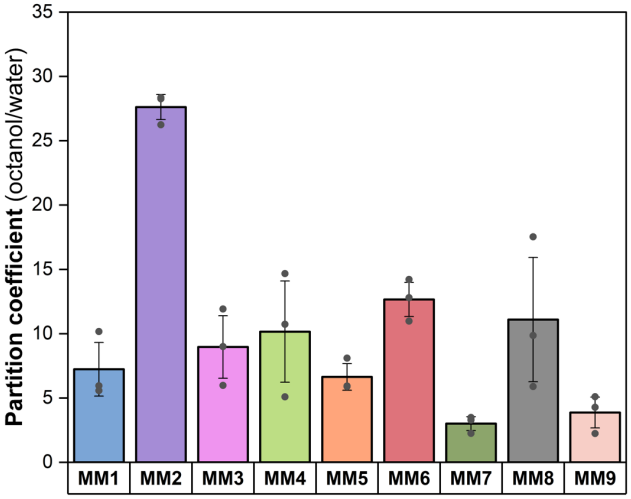

Figure S11. Individual POW values for three independent measurements for motors 1 to 9. Column high representing mean value with standard deviation marked with black bars.

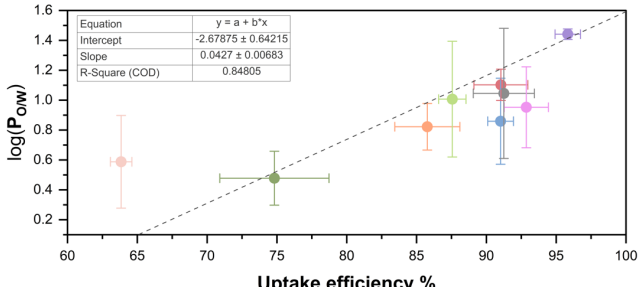

Figure S12. Graph representing mean log($P_{O/W}$) values of motors **1** to **9** *versus* their uptake efficiency (10 mol% MM**X** in POPC SUVs). Linear analysis (dotted line + box) of the relationship between lipophilicity and uptake values of the studied compounds.

e. Quantum yield determination

Quantum yield determinations of molecular motors **1** to **9** in ethanol solution, octanol solution and SUVs (POPC+10mol% MM**X**) in water were carried out at 5 °C, ensuring the stability of the metastable state over the duration of the study. For all the experiments, solutions of the stable state in the different environments at a concentration of 50 µM were prepared in a 10 mm quartz cuvette. UV-Vis measurements were taken every 1 s over the first 60 s of constant irradiation until PSS was reached using the appropriate wavelength for each system, following the evolution of the absorption maximum. Baseline corrections were carried out to account for baseline drifting, and the absorbance at 450 or 475 nm (depending on the compound of study) over the course of the measurement was extracted. The data was subsequently processed in Copasi, using a method outlined by Stranius & Börjesson[15], based on Equation 1:

$$\frac{d[A]}{dt} = -\frac{QY_{SM} * I * \beta_S(t)}{N_A * V} + \frac{QY_{MS} * I * \beta_M(t)}{N_A * V}$$

Where I is the molar photon flux of the appropiate LED (previously determined by chemical actinometry[16], V is the total volume of the irradiated solution (1.5 mL), and β is the fraction of photons absorbed by either the stable or metastable isomer, a number that is determined using the PSS ratio and the corresponding molar extinction coefficient of each isomer. Molar absorption coefficients of stable (ε_S $[M^{-1}c^{-1}]$) and metastable (ε_M $[M^{-1}c^{-1}]$) motor isomers were determined by measuring UV-Vis spectra at three different known concentrations and volumes following Lambert-Beer law[17]. Data shown in Table S5 corresponds to the averaged QY data over five separate runs for each system.

MM #	Solvent	PSS	Rep	Epsilon STABLE	Epsilon META		hv flux [mE/s]	QY_S		±	QY_M		±	C_S	C_M	%ERROR
MM1	EtOH	405 nm	1	20030	16955	16267	1.25E-04	8.40%	**8.84%**	1.59%	9.08%	**9.71%**	0.52%	2.09	5.01	0.99
			2		15300			7.14%			9.71%			2.29	5.28	0.98
			3		16546			10.97%			10.35%			2.26	5.54	1.00
	POPC	29:71	1		15080	15527		3.56%	**5.51%**	1.48%	8.40%	**9.09%**	0.65%	1.67	3.57	0.96
			2		15331			4.73%			8.74%			1.63	3.58	0.97
			3		15591			4.89%			8.71%			1.59	3.50	0.97
			4		15952			6.72%			9.38%			1.61	3.60	0.97
			5		15680			7.67%			10.23%			1.61	3.56	0.97
	Octanol		1		15910	16176		8.60%	**8.86%**	0.28%	8.30%	**8.80%**	0.36%	5.41	7.06	0.80
			2		16617			9.24%			9.11%			2.26	5.02	0.97
			3		16002			8.73%			9.00%			3.09	6.10	0.94
MM2	EtOH	395 nm	1	42260	29578	28895	9.67E-05	5.47%	**5.65%**	0.16%	1.91%	**2.13%**	0.16%	1.16	4.61	1.01
			2		28561			5.63%			2.18%			1.17	4.37	1.00
			3		28547			5.85%			2.29%			1.14	4.26	1.00
	POPC	21:79	1		25484	25901		2.23%	2.01%	0.22%	1.03%	0.92%	0.17%	0.47	1.66	0.99
			2		26155			2.03%			0.91%			0.64	2.26	0.99
			3		23986			2.15%			1.09%			0.57	1.94	0.98
			4		27979			1.64%			0.64%			0.80	2.86	0.99
	Octanol		1		28480	28079		7.03%	**6.67%**	0.45%	3.09%	**2.87%**	0.31%	1.03	3.49	0.98
			2		27764			6.95%			3.08%			1.00	3.45	0.98
			3		27992			6.03%			2.44%			0.34	1.26	1.00

		405 nm	1		54215			1.27%			0.20%			0.97	3.58	1.00
	EtOH		2		53377	53737		1.44%	**1.40%**	0.09%	0.29%	**0.27%**	0.05%	0.92	3.56	1.01
			3		53619			1.48%			0.33%			0.96	3.51	0.99
			1		45685			1.39%			0.61%			0.05	1.40	1.22
MM3	POPC	21:79	2	62890	45345	46135	1.25E-04	1.47%	**1.37%**	0.07%	0.62%	**0.58%**	0.05%	0.05	1.51	1.23
			3		44974			1.32%			0.59%			0.05	1.55	1.23
			4		48535			1.28%			0.49%			0.60	2.00	0.98
			1		32160			1.75%			0.91%			0.55	2.06	1.00
	Octanol		2		34429	33738		2.13%	**2.04%**	0.21%	1.02%	**1.03%**	0.11%	0.36	1.36	1.00
			3		34624			2.23%			1.18%			0.36	1.24	0.98
		395 nm	1		11575			3.08%			2.60%			2.49	7.69	0.99
	EtOH		2		11677	11628		3.19%	**3.23%**	0.14%	2.59%	**2.67%**	0.11%	2.48	7.90	1.00
			3		11633			3.42%			2.82%			2.29	7.26	1.00
			1		17670			0.43%			0.24%			0.57	1.63	0.98
MM4	POPC	25:75	2	30751	17229	17605	9.67E-05	0.40%	**0.42%**	0.02%	0.23%	**0.23%**	0.02%	0.53	1.52	0.97
			4		18046			0.39%			0.20%			0.47	1.42	0.99
			3		17475			0.44%			0.25%			0.50	1.47	0.98
			1		11264			4.26%			2.78%			0.54	2.24	1.06
	Octanol		2		11549	11672		3.74%	**4.19%**	0.34%	3.40%	**2.90%**	0.37%	0.72	2.09	0.98
			3		12204			4.57%			2.52%			0.55	2.10	1.04
		395 nm	1		32704			1.13%			2.26%			3.81	2.46	1.03
	EtOH		2		33585	32375		1.14%	**1.13%**	0.01%	2.28%	**2.37%**	0.14%	3.69	2.34	1.02
			3		30837			1.11%			2.57%			3.85	2.30	0.98
			1		33027			0.65%			0.94%			2.57	2.27	1.23
MM5	POPC	62:38	2	45420	32657	32891	9.67E-05	0.70%	**0.73%**	0.06%	1.15%	**1.20%**	0.19%	2.53	2.05	1.18
			3		32838			0.74%			1.25%			2.57	2.04	1.16
			4		33041			0.81%			1.47%			2.58	1.92	1.12
			1		23832			1.80%			5.39%			1.31	0.82	1.01
	octanol		2		30922	29415		1.91%	**1.78%**	0.12%	4.74%	**4.56%**	0.76%	7.14	4.22	0.98
			3		33490			1.62%			3.56%			6.45	2.44	0.72
		405 nm	1		22810			5.57%			1.70%			1.42	6.21	1.10
	EtOH		2		21855	22287		5.92%	**5.88%**	0.24%	2.04%	**1.94%**	0.17%	1.45	5.95	1.09
			3		22195			6.15%			2.08%			1.39	5.74	1.09
			1		14919			0.70%			0.51%			0.49	1.33	0.99
			2		13052			0.66%			0.52%			0.47	1.31	1.00
MM6	POPC	26:74	3	31660	20000	16589	1.25E-04	0.58%	**0.67%**	0.05%	0.23%	**0.43%**	0.11%	0.38	1.20	1.03
			4		18152			0.65%			0.37%			0.41	1.15	1.00
			5		16822			0.74%			0.51%			0.46	1.19	0.98
			1		18044			2.22%			1.25%			0.59	1.79	1.02
	Octanol		2		23876	21147		2.18%	**2.38%**	0.25%	0.77%	**0.80%**	0.36%	1.13	3.63	1.03
			3		21521			2.73%			0.37%			0.53	1.10	0.91
		365 nm	1		5869			0.95%			0.74%			1.41	4.30	0.99
	EtOH		2		5425	5966		1.09%	**1.07%**	0.09%	1.07%	**0.87%**	0.14%	1.43	4.26	0.99
			3		6605			1.18%			0.81%			1.44	4.40	0.99
			1		8272			0.41%			0.21%			1.06	3.07	0.98
MM7	POPC	24:76	2	18470	7606	8219	8.10E-05	0.41%	**0.47%**	0.08%	0.19%	**0.23%**	0.05%	0.59	1.89	1.00
			3		8778			0.59%			0.30%			0.98	2.66	0.96
			1		4686			0.45%			0.50%			1.24	3.91	1.00
	Octanol		2		6766	6095		0.63%	**0.56%**	0.08%	0.53%	**0.52%**	0.01%	6.86	0.21	0.04
			3		6832			0.60%			0.52%			1.13	3.43	0.99
		365 nm	1		18870			4.67%			1.11%			0.74	4.68	1.04
	EtOH		2		19261	19073		4.83%	**4.84%**	0.14%	1.14%	**1.18%**	0.08%	0.71	4.52	1.04
			3		19088			5.02%			1.29%			0.72	4.39	1.04
			1		16493			2.56%			1.00%			0.29	1.35	0.99
			2		15795			2.95%			1.25%			0.28	1.32	0.99
MM8	POPC	17:83	3	32240	15906	16672	8.10E-05	3.34%	**2.97%**	0.30%	1.44%	**1.19%**	0.15%	0.29	1.33	0.99
			4		18973			3.26%			1.17%			0.34	1.58	0.99
			5		16192			2.73%			1.11%			0.29	1.35	0.99
			1		21408			5.12%			1.55%			1.44	7.15	1.00
	Octanol		2		18376	19389		5.23%	**5.19%**	0.05%	1.91%	**1.78%**	0.16%	0.33	1.55	0.99
			3		18382			5.22%			1.89%			0.56	1.29	0.84
		395 nm	1		12023			5.08%			2.50%			0.91	3.67	1.07
	EtOH		2		11733	11732		4.95%	**4.94%**	0.12%	2.61%	**2.58%**	0.06%	0.74	3.01	1.07
			3		11440			4.79%			2.63%			0.77	3.08	1.07
			1		14990			1.70%			0.76%			1.22	4.48	1.05
MM9	POPC	19:82	2	25339	14520	14695	9.67E-05	1.53%	**1.59%**	0.08%	0.68%	**0.71%**	0.04%	1.22	4.51	1.05
			3		14576			1.53%			0.68%			1.22	4.52	1.05
			1		11403			1.88%			1.03%			1.74	6.89	1.07
	Octanol		2		11132	10986		2.35%	**2.03%**	0.23%	1.28%	**1.15%**	0.11%	0.79	3.18	1.07
			3		10422			1.87%			1.14%			0.51	2.04	1.07

Table S5. Quantum yield measurements of molecular motors **1** to **9** in EtOH, Octanol and Lipid solutions.

f. Eyring analysis

Solutions of the stable state of motors **1** to **9** in the studied environments at a concentration of 50 µM were prepared in a 10 mm quartz cuvette and irradiated with the appropriate LED until PSS. Eyring plot analysis of the thermal isomerization processes in different environments was performed by monitoring the decrease in absorption of a UV-Vis sample over time in three different temperatures. Rate constants, (k), as changes of absorbance over time were determined by fitting a first-order decay and plotted to determine the thermodynamic parameters of the thermal helix inversions using Origin 2023 software[13] and a least squares analysis was performed on the Eyring equation to retrieve the $\Delta G^{\ddagger}$. The activation parameters at 25 °C for the metastable → stable process could be determined and are displayed Eyring plots and half-lives times at 25 °C for the studied environments are shown in Figure S13.

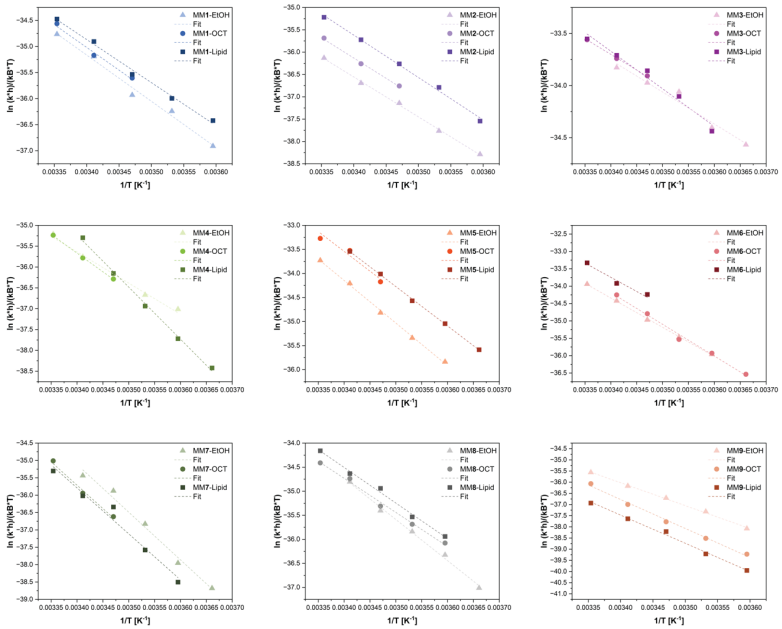

Figure S13. Eyring plot analysis of motors **1** to **9** monitoring the decrease in absorption at 405 or 475 nm at different temperatures.

8. Imaging giant unilamelar vesicles

a. Fluorescence microscopy

Fluorescence imaging was performed on a Zeiss Elyra 7 system, using 405 and 641 nm laser lines. For the image capture alpha Plan-Apochromat 63x/1.46 Oil Korr M27 Var2 (Carl Zeiss, Germany) oil objective was used. The images were acquired on pco.edge sCMOS cameras (pco.edge 4.2 CLHS) at 100ms exposure time.

For the analysis of the reaction time dilute solutions of GUVs containing saturation concentrations of MM**1-9** were imaged under 405 nm laser exposure (at 5% intensity for motor activation) and 641 nm laser exposure (at 0.15% intensity for lipid imaging) during 15 to 60 min with 1 sec interval. At least 30 vesicles were analyzed for each molecular motor. Vesicles of less than 20 µM or those who showed perturbations (fluctuations, tubulin…) prior to motor irradiation were excluded from the analysis. An example of a video recorded for each of the examined conditions is given in Supplementary video S1. The start of perturbation was noted as the first visible fluctuation for each vesicle. Vesicles that did not show fluctuations during the whole imaging time were considered as non-reacted.

b. Spinning disk confocal microscopy

Spinning disk confocal imaging was performed on a Nikon/Yokogawa CSU-W1 spinning disk confocal microscope, using 405, 488, and 641 nm laser lines. The 50 µm pinhole spinning disk was used at 4000 rpm. The sample was illuminated through a Nikon Apo TIRF 60x Oil DIC N2 immersion oil objective and the images were acquired in pco.edge sCMOS cameras (pco.edge 4.2 LT USB) at 100ms exposure time. For z-stack imaging, the desired optical sectioning was set at 0.2 µm.

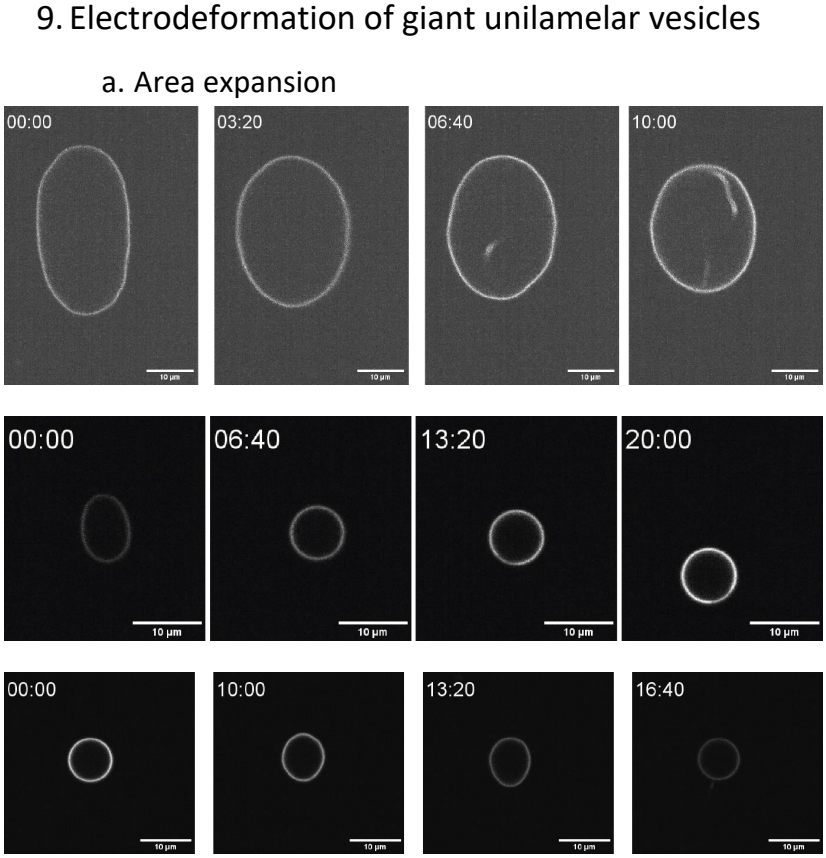

Figure S14. (top) POPC-MM7 shows excess area being sored in inward tubes upon extended irradiation (middle) POPC-MM4 displays a retraction of spherical shape upon irradiation, (bottom) POPC-MM5 shows area increase followed by expulsion of outward tubes.

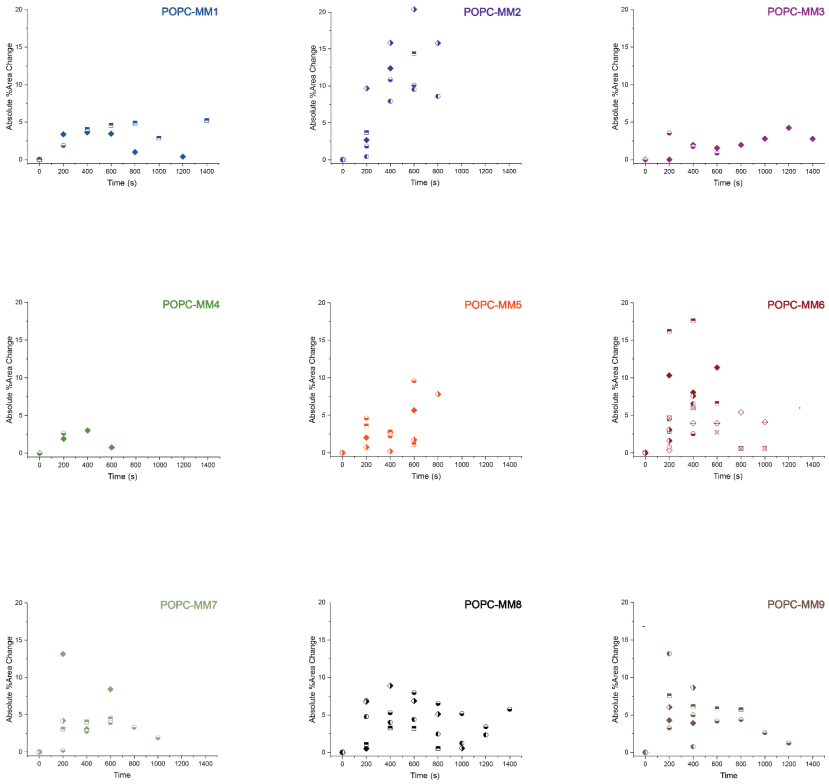

Figure S15. Absolute % Area change for vesicles containing MM1-9 upon irradiation with 405 nm laser, recorded and measured with electrodeformation.

Bibliography

1. Vicario, J., Meetsma, A. & Feringa, B. L. Controlling the speed of rotation in molecular motors. Dramatic acceleration of the rotary motion by structural modification. *Chemical Communications* 5910–5912 (2005) doi:10.1039/B507264F.
2. Vicario, J., Walko, M., Meetsma, A. & Feringa, B. L. Fine tuning of the rotary motion by structural modification in light-driven unidirectional molecular motors. *J Am Chem Soc* 128, 5127–5135 (2006).
3. Cnossen, A. *et al.* Driving unidirectional molecular rotary motors with visible light by intra- and intermolecular energy transfer from palladium porphyrin. *J Am Chem Soc* 134, 17613–17619 (2012).
4. Bao, J. *et al.* Modulation of Chirality and Intensity of Circularly Polarized Luminescence Emitting from Cholesteric Liquid Crystals Triggered by Photoresponsive Molecular Motor. *Adv Opt Mater* 10, 2101910 (2022).
5. Carroll, G. T., London, G., Landaluce, T. F., Rudolf, P. & Feringa, B. L. Adhesion of Photon-Driven Molecular Motors to Surfaces via 1,3-Dipolar Cycloadditions: Effect of Interfacial Interactions on Molecular Motion. *ACS Nano* 5, 622–630 (2011).
6. London, G. *et al.* Light-driven altitudinal molecular motors on surfaces. *Chemical Communications* 1712–1714 (2009) doi:10.1039/B821755F.
7. Wei, Y. Functionalization of molecules in confined space. (2019) doi:10.33612/DISS.108285448.
8. Lubbe, A. S., Böhmer, C., Tosi, F., Szymanski, W. & Feringa, B. L. Molecular Motors in Aqueous Environment. *Journal of Organic Chemistry* 83, 11008–11018 (2018).
9. Hou, J. *et al.* Phototriggered Complex Motion by Programmable Construction of Light-Driven Molecular Motors in Liquid Crystal Networks. *J Am Chem Soc* 144, 6851–6860 (2022).
10. Stähler, C. *et al.* Light-driven molecular motors embedded in covalent organic frameworks. *Chem Sci* 13, 8253–8264 (2022).
11. Neese, F. Software update: The ORCA program system—Version 5.0. *Wiley Interdiscip Rev Comput Mol Sci* 12, e1606 (2022).
12. Hirata, S. & Head-Gordon, M. Time-dependent density functional theory within the Tamm–Dancoff approximation. *Chem Phys Lett* 314, 291–299 (1999).
13. OriginLab Corporation, N. M. USA. Origin(Pro), Version 2023.
14. Test No. 107: Partition Coefficient (n-octanol/water): Shake Flask Method. (1995) doi:10.1787/9789264069626-EN.
15. Stranius, K. & Börjesson, K. Determining the Photoisomerization Quantum Yield of Photoswitchable Molecules in Solution and in the Solid State. *Scientific Reports 2017 7:1* 7, 1–9 (2017).
16. Montalti, M., Credi, A., Prodi, L. & Gandolfi, M. T. Handbook of Photochemistry. *Handbook of Photochemistry* (2006) doi:10.1201/9781420015195.
17. Swinehart, D. F. The Beer-Lambert Law. *J Chem Educ* 39, 333–335 (1962).

B

Appendix to Section 8.1

Supplementary Information

S1. Acetylation of D-Mannose

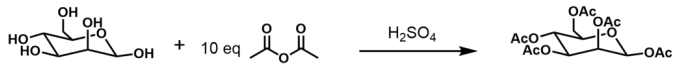

D-Mannose (20 g, 111 mmol) and acetic anhydride (105 mL, 1.11 mol) were added to a round-bottom flask and allowed to cool down. Thereafter, a minimum amount of sulfuric acid was added dropwise. The crude was extracted using ice cold water, a $NaHCO_3$ solution and distilled water. The extract was dried over $MgSO_4$, and the solvent removed by vacuum. The product (37.0 g) was obtained as a colourless and viscose oil in an 85% yield.

S2. Synthesis of Acetylated D-Mannose Acrylamide

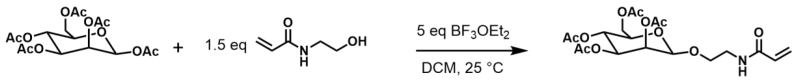

The acetylated D-mannose (18.5 g, 47.4 mmol) was dissolved in DCM (200 mL) and added to a 500 mL round-bottom flask. Subsequently, hydroxyl acrylamide (8.2 g, 71.1 mmol) was added to the flask whilst it was allowed to cool down in an ice bath. Subsequently, BF_3OEt_2 (29.3 mL, 0.24 mol) was added dropwise into the mixture which was allowed to stir overnight. Finally, the product was extracted using ice-cold water, an aqueous solution of sodium carbonate and distilled water. The extract was dried over $MgSO_4$, the solvent removed and the product purified via column chromatography (EtOAc:Hex, 7:3) to obtain a white solid (9.7 g) in 46% yield.

1H NMR (400 MHz, DMSO-d6) δ: 8.30 (1H, t, $-CH_2$-NH-(C=O)-); 6.25 (1H, dd, -(C=O)-CH=CH_2); 6.09 (1H, dd, Ha); 5.59 (1H, dd, Hb); 5.15 (2 H, m, Hc/Hd); 5.09 (1H, t, He); 4.88 (1H, s, -O-CH-O-); 4.11 (1H, dd, Hf); 3.99 (2H, dd, -O-C-O-CH_2-); 3.67 (1H, m, Hg); 3.54 (1H, m, Hh); 3.37 (2H, m, $-CH_2$-NH-(C=O)-).

13C NMR (400 MHz, DMSO-d6) δ: 170.05 (-O-(C=O)-CH_3), 169.63 (-O-(C=O)-CH_3), 169.59 (-O-(C=O)-CH_3), 169.50 (-O-(C=O)-CH_3), 164.82 ((C=O)-NH-), 131.59 (-CH=CH2), 125.19 (-CH_2=CH), 96.69 (-O-CH-O-), 68.71 (CH-CH_2-O-(C=O)-CH_3), 68.69 (CH-O-(C=O)-CH_3), 67.87 (CH-O-(C=O)-CH_3), 66.28 (CH_2-CH_2-NH), 65.44 (-CH-O-C=O)-CH_3), 61.85 (-CH_2-O-(C=O)-CH_3), 38.37 (-CH_2NH), 20.59 (-CH_3-CO), 20.46 (-CH_3-CO), 20.44 (-CH_3-CO), 20.40 (-CH_3-CO).

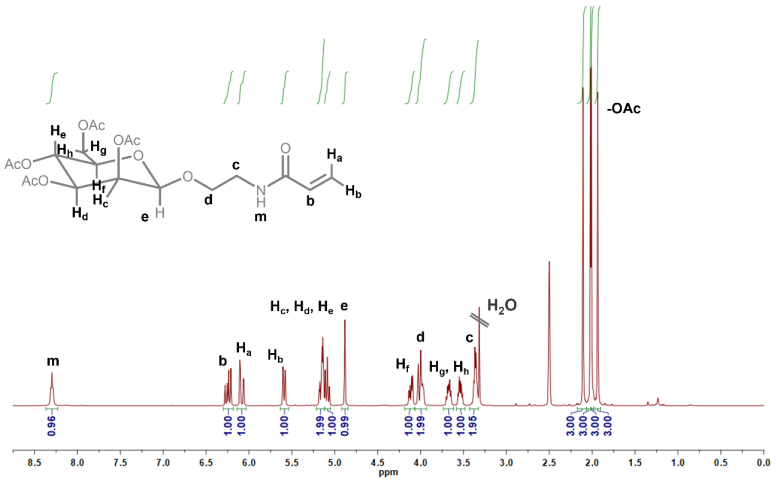

Figure S 1. ^{1}H NMR of acetylated D-mannose acrylamide in DMSO-d6.

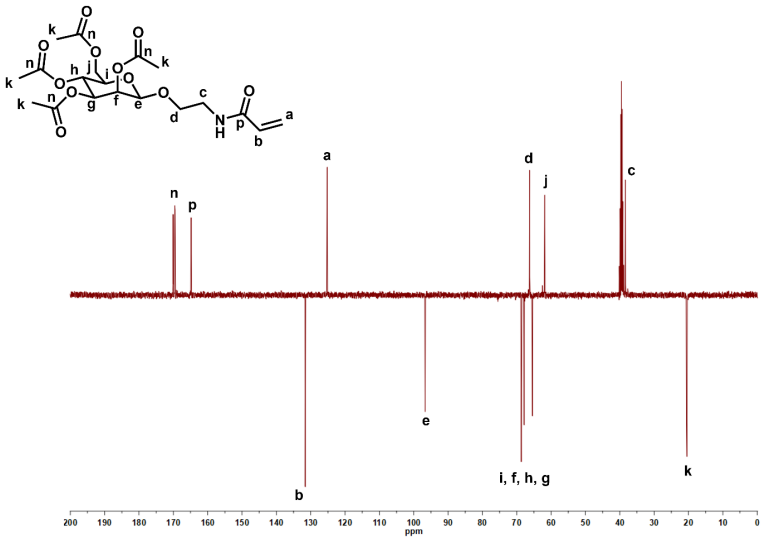

Figure S 2. ^{13}C NMR of acetylated D-mannose acrylamide in DMSO-d6.

S3. Synthesis of cholesterol CTA

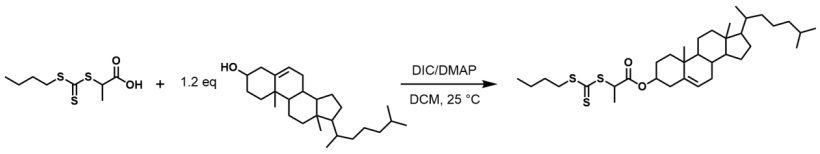

PABTC (871 mg, 3.65 mmol), cholesterol (1.7 g, 4.38 mmol) and DMAP (34.8 mg, 0.38 mmol) were dissolved in DCM (36 mL, anhydrous) and added to a 50 mL round-bottom flask. Subsequently, the reaction mixture was cooled to 0°C and a solution of DIC (488 mg, 3.83 mmol) in anhydrous DCM was added dropwise while vigorously stirring. After 2 h the reaction mixture reached room temperature and was stirred overnight. The solution was filtered, and the solvent evaporated under reduced pressure. The residual product was purified via column chromatography (Hex:EtOAc, 7:3) to obtain a yellow solid (2.1 g) in 95 % yield.

1H NMR (400 MHz, $CDCl_3$) δ: 5.37 (d; 1H; -C=CH-CH_2-); 4.76 (q, 1H, -S-(C=S)-S-CH-); 4.64 (m; 1H; -(C=O)-O-CH-CH_2-); 3.36 (t, 2H, -CH_2-S-(C=S)-S-); 2.32 (m; 2H; -(C=O)-O-CH-CH_2-C-); 2.00 (m; 2H; -C=CH-CH_2-); 1.67 (m; 2H; CH_3-CH_2-CH_2-CH_2-S-

); 1.02 (s; 3H; -(C=O)-O-CH-CH_2-CH_2-C-CH_3); 0.86 (d; 6H; -C_5H_6-CH-(CH_3)-CH_2-CH_2-CH_2-CH-(CH_3)$_2$); 0.67 (s; 3H; -C_6H_7-C-(CH_3)-C_5H_6-).

13C NMR (400 MHz, $CDCl_3$) δ: 222.32 (-S-(C=S)-S-), 170.64 (-S-(C=S)-S-CH-(C=O)-O-); 139.52 (-(C=O)-O-CH-CH_2-C=CH); 123.0 (-(C=O)-O-CH-CH_2-C=CH); 75.69 (-(C=O)-O-CH-CH_2-C=CH); 56.81 (-C_6H_4-CH-CH_2); 56.27 (-C_4H_5-CH-CH-CH_2-CH_2-CH_2-CH-(CH_3)$_2$); 50.12 (-(C=O)-O-C_6H_7-CH-CH_2-CH_2-C_5H_6-); 48.48 (-S-(C=S)-S-CH-(C=O)-O-); 42.44 (C_5H_7-C-CH_3); 39.85 (-(CH=C)-C-CH-CH_2-CH_2-C-CH_3); 39.65 (-CH_2-CH_2-CH-(CH_3)$_2$); 37.97 (-(C=O)-O-CH-CH_2-C=CH); 37.03 (-CH=C-C-CH_3); 36.71 (-(CH=C)-C-CH_2-CH_2-CH-O-(C=O)); 36.32 (-CH-CH_2-CH_2-CH_2-CH-(CH_3)$_2$); 35.93 (-CH-CH_2-CH_2-CH_2-CH-(CH_3)$_2$); 32.04 (-CH_2-CH_2-S-(C=S)-S-CH-); 31.98 (-(C=CH)-CH_2-CH-CH-); 30.10 (-(C=CH)-CH_2-CH-); 28.36 (-(C=O)-O-CH-CH_2-CH_2-C-CH_3); 28.15 (-C_5H_6-CH-(CH_3)-CH_2-CH_2-CH_2-CH-CH_3); 27.69 (-(C=CH)-CH_2-CH-CH-CH_2-CH_2-); 24.42 (-(C=CH)-CH_2-CH-CH-CH_2-CH_2-); 23.97 (-C_5H_6-CH-(CH_3)-CH_2-CH_2-CH_2-CH-CH_3); 22.96 (-C_5H_6-CH-(CH_3)-CH_2-CH_2-CH_2-CH-CH_3); 22.70 (-C_5H_6-CH-(CH_3)-CH_2-CH_2-CH_2-CH-CH_3); 22.20 (-(CH=C)-C-CH-CH_2-CH_2); 21.17 (CH_3-CH_2-CH_2-CH_2-S-); 19.46 (-(C=O)-O-CH-CH_2-CH_2-C-CH_3); 18.85 (-C_5H_6-CH-CH-CH_3-); 17.06 (-S-(C=S)-S-CH-(CH_3)-(C=O)-O-); 13.74 (CH_3-CH_2-CH_2-CH_2-S-); 11.99(-CH_3-C-CH-CH-CH_2-(CH=C)-).

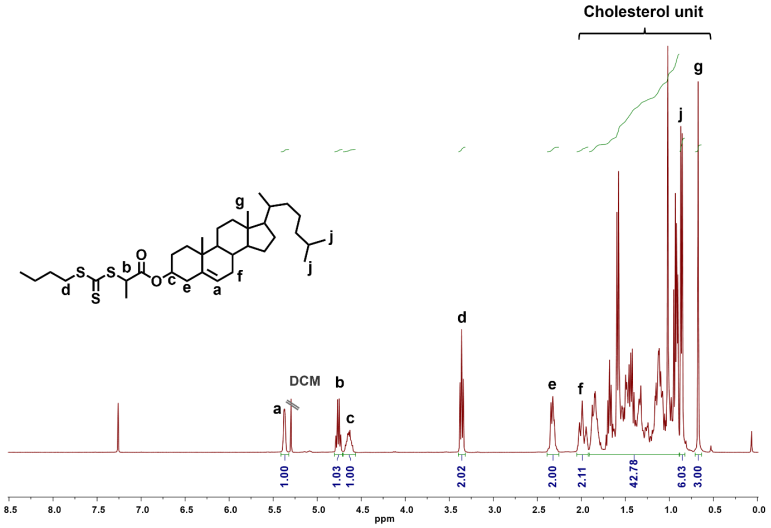

Figure S 3. ^{1}H NMR of cholesterol CTA in $CDCl_3$.

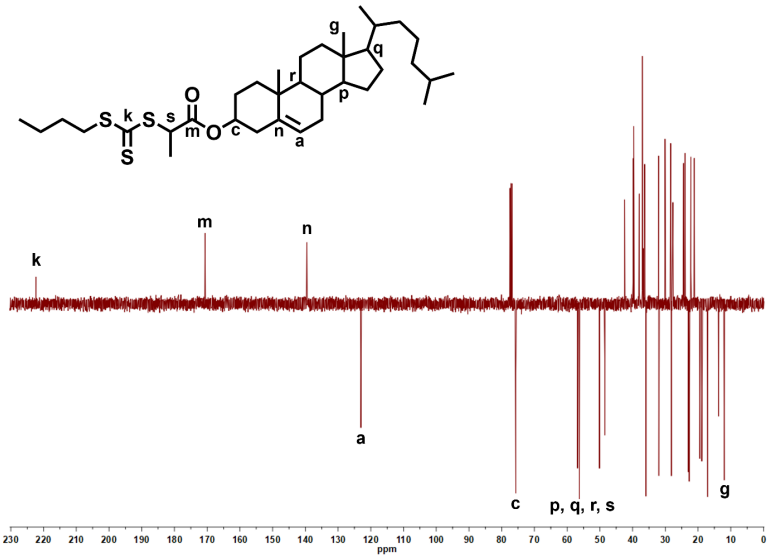

Figure S 4. ^{13}C NMR of cholesterol CTA in $CDCl_3$.

S4. ^{1}H NMR and GPC traces of the Glycopolymers

Table S 1: RAFT polymerization conditions for P1-P3, and PH3. All polymerizations were conducted in 1,4-dioxane as solvent, with Cholesterol CTA as RAFT agent, AIBN as initiator, and at 70°C. [a]Determined by ^{1}H NMR spectroscopy.

Polymer	Monomer	Time (h)	$[M]_0/[CTA]_0$	Conversion (%)[a]
P1	AcManEAA	15	10	≥ 99
P2	AcManEAA	15	20	≥ 99
P3	AcManEAA	15	30	≥ 99
PH3	AcManEAA	15	30	≥ 99

Polymer	CTA		Monomer		AIBN	
	Mass (mg)	**Moles (mmol)**	**Mass (mg)**	**Moles (mmol)**	**Mass (mg)**	**Moles (mmol)**
P1	43.1	0.071	316.2	0.71	1.15	0.0071
P2	23.3	0.038	342.2	0.77	0.62	0.0038
P3	23.3	0.038	512.8	1.15	0.62	0.0038
PH3	6.27	0.026	351.4	0.79	0.43	0.0026

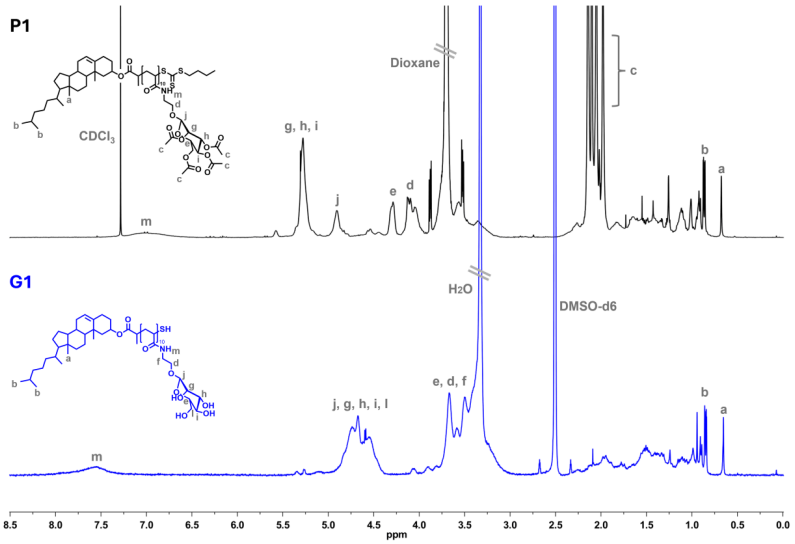

Figure S 5. ^{1}H NMR of Protected (P1) in $CDCl_3$ and Deprotected (G1) Chol Man_{10} in DMSO-d6. The disappearance of the acetyl peaks at 2 ppm (P1) and the presence of the cholesterol signals in G1 suggest a successful deprotection without affecting the cholesterol end-group.

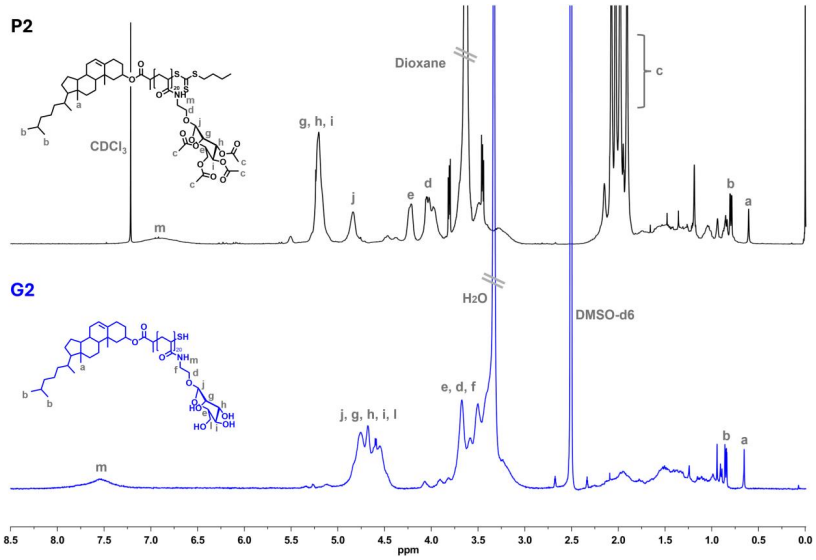

Figure S 6. ^{1}H NMR of Protected (P2) in $CDCl_3$ and Deprotected (G2) Chol Man_{10} in DMSO-d6. The disappearance of the acetyl peaks at 2 ppm (P2) and the presence of the cholesterol signals in G2 suggest a successful deprotection without affecting the cholesterol end-group.

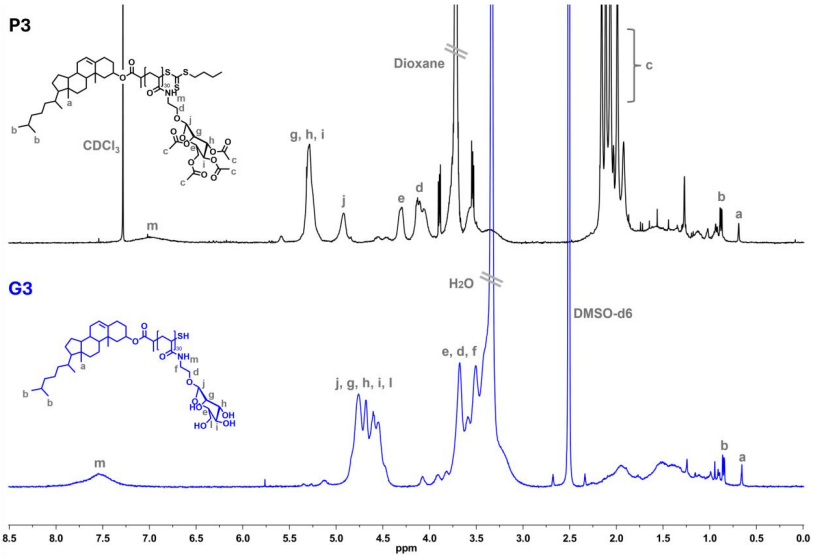

Figure S 7. ^{1}H NMR of Protected (P3) in $CDCl_3$ and Deprotected (G3) Chol Man_{10} in DMSO-d6. The disappearance of the acetyl peaks at 2 ppm (P3) and the presence of the cholesterol signals in G3 suggest a successful deprotection without affecting the cholesterol end-group.

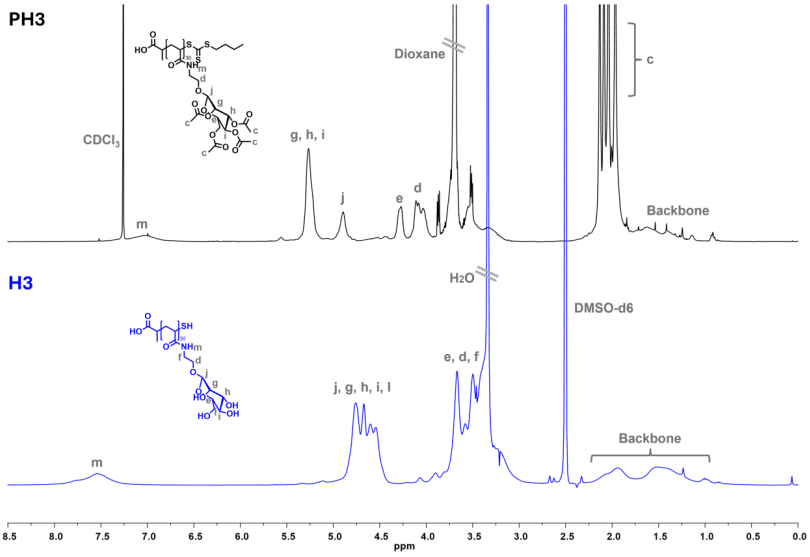

Figure S X. ^{1}H NMR of Protected (PH3) in $CDCl_3$ and Deprotected (H3) $pMan_{30}$ in DMSO-d6. The disappearance of the acetyl peaks at 2 ppm suggests a successful deprotection.

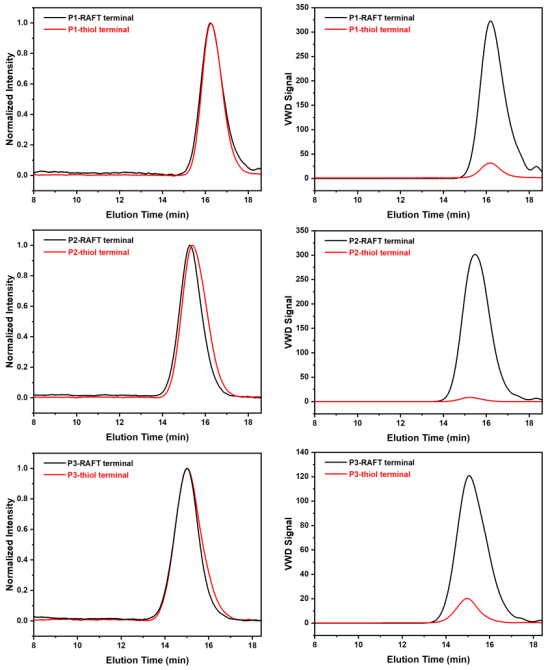

Figure S 8. DMF GPC analysis via RI and VWD detector at 309 nm before and after the reduction of the RAFT terminal group. The reduction of the RAFT agent represented 95%, 97%, and 83% for P1, P2, and P3, respectively. All samples were run at a concentration of 5 mg mL^{-1}.

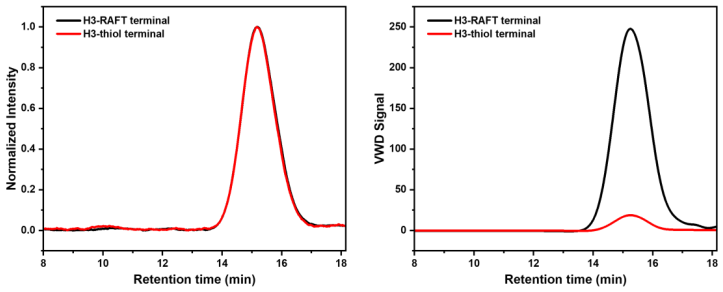

Figure S X. DMF GPC analysis via RI and VWD detector at 309 nm before and after the reduction of the RAFT terminal group. The reduction of the RAFT agent represented 92% for H3. All samples were run at a concentration of 5 mg mL^{-1}.

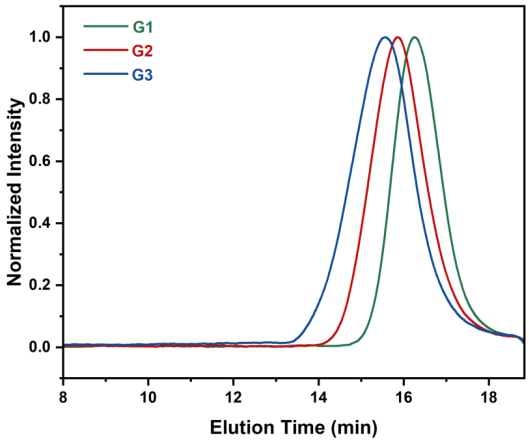

Figure S 9. DMF GPC RI traces of Deprotected Glycopolymers (G1, G2, G3).

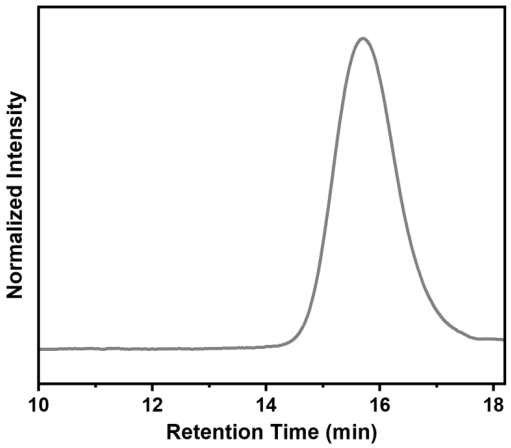

Figure S . DMF GPC RI trace of Deprotected Glycopolymer H3

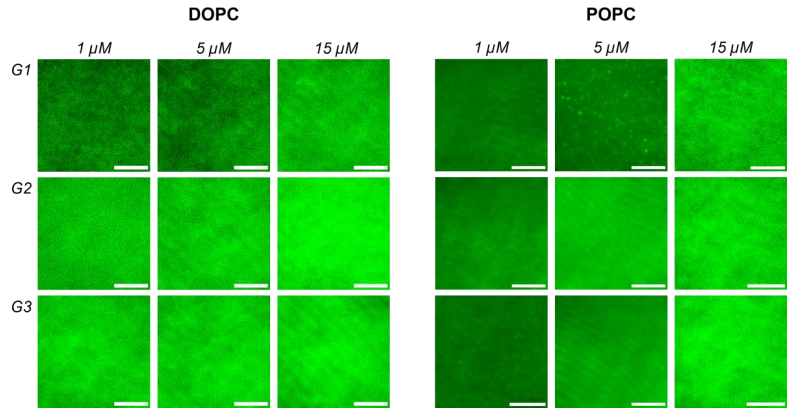

Figure S 10. Total Internal Reflection Fluorescence (TIRF) images of DOPC and POPC SLBs incubated with the glycopolymers at 1, 5, and 15 μM. Scale bar 10 μm.

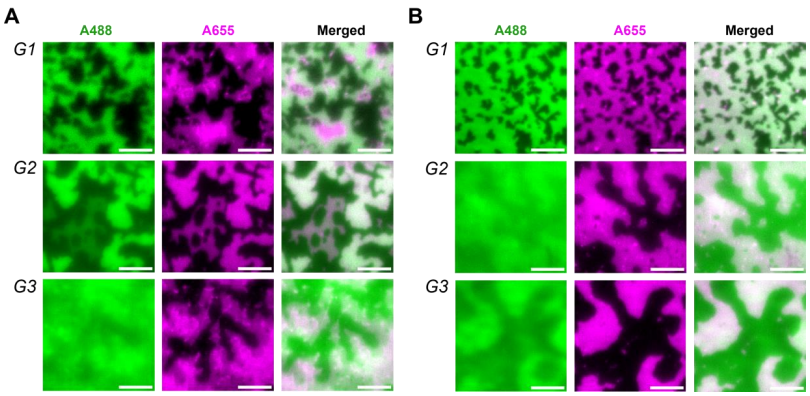

Figure S 11. (A) Total Internal Reflection Fluorescence (TIRF) images of phase-separated SLBs (35:35:30 DOPC:DSPC:Cholesterol) incubated with the glycopolymers at 1 μM, and (B) 5 μM. Scale bar 10 μm.

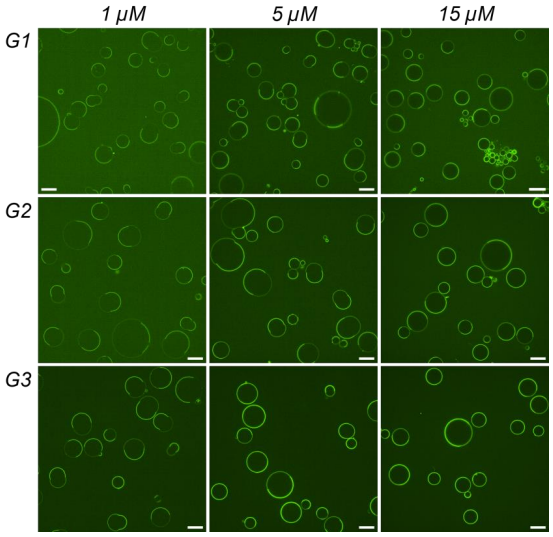

Figure S 12. Phase-separated vesicles observed by confocal laser scanning microscopy for DOPC/DSPC/Chol = 35/35/30, incubated with G1, G2, and G3, at 1, 5, and 15 μM. Scale bars are 20 μm.

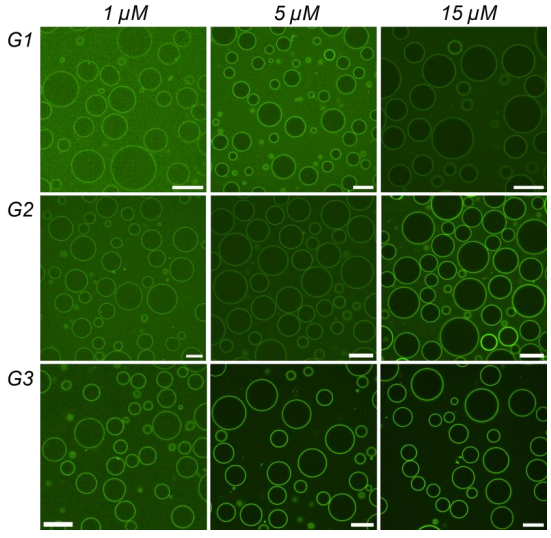

Figure S 13. DOPC GUVs observed by confocal laser scanning microscopy, incubated with G1, G2, and G3, at 1, 5, and 15 μM. Scale bars are 20 μm.

S5. Fluorescence Intensity measurements for SLBs

The average fluorescence intensity of SLBs, for each concentration, was related to the degree of labelling of each polymer. An increase in polymer concentration corresponds to an amplification in the fluorescence on the lipid bilayer (**see Figure SX**). Quantifying the average fluorescence intensity of the labelled glycopolymers, both G1 and G2 showed the same 28% increase upon increasing from 1 to 15 μM. In contrast, imaging of the SLB with G3 revealed a lower increase of 16% for the same concentration increase. A reduced increase for G3 is also observed from 5 to 15 μM, equivalent to 8%, whereas G1 and G2 both show an increase of 19%. These observations are indicative of higher carbohydrate chains resulting in a higher incorporation efficiency even at lower concentrations, and thus reaching saturation quicker. The results are in line with the glycopolymer addition to the DOPC formulated GUVs (see Figure SXX).

For SLBs formulated with purely POPC were observed in a similar manner. For increasing concentrations from 1 to 15 μM there is 44% increase for G1, 53% for G2 and 47% for G3. For the smaller rise between 5 to 15 μM in concentration, G1 registers a 35% increase in fluorescence intensity and G2, and G3 show a similar increase of around 18%. Bilayers composed of DOPC are more fluid as compared to POPC, our observations indicate that the glycopolymers in this study have a higher incorporation efficiency for more fluid membranes as we will also observe in the case of phase-separated membranes. As observed previously for DOPC SLBs, a general increase in fluorescence across the bilayer is observed upon increasing the concentration of the glycopolymers (see Figure SXX).

For phase separated SLBs with L_d/L_o co-existence composed of DOPC, DSPC and Cholesterol (35:35:30 mol%) it was observed that even for $1\,\mu M$ concentrations, glycopolymers showed some incorporation in the L_o phase. Although, the incorporation in the L_d phase remained higher, a clear indication that higher fluidity facilitated a higher incorporation. Notably, no significant increase is observed for the L_d phase in terms of fluorescence intensity. For the L_o phase, a general upward trend was observed as concentrations were increased. For G1, going from $1\,\mu M$ to $15\,\mu M$ there is a 5-fold increase and from 5 to $15\,\mu M$ there is 2-fold increase. For G2, from 1 to 15 μM there was a 2.5-fold increase in fluorescence intensity and from 5 to 15 μM only a mere 8% increase was observed. For G3, a total increase of only 8% was observed.

These results corroborate that for higher carbohydrate chain length the system reaches saturation at lower incubation concentrations, and a higher amount of surface density is achieved for higher carbohydrate chain length glycopolymers.

S6. Fluorescence Intensity measurements for GUVs

In corroboration with our previous results with SLBs, upon increasing the polymer concentrations, we observed a general rise in the fluorescence intensity of the labelled glycopolymers at the membrane. For GUVs composed of DOPC, this intensity rise corresponded to 37%, 40%, and 45% for G1, G2, and G3 respectively when the concentrations were increased from 1 μM to 15 μM. In general, free standing membranes have a higher membrane fluidity as compared to supported membranes, and thus an overall higher incorporation is observed consisted with the fluidity trend we have observed previously.

For GUVs where L_d/L_o domains co-exist, consisting of DOPC, DSPC, and Cholesterol (molar ratio of 35:35:30) a subsequent increase in fluorescence intensity corresponding to increase in concentration was observed in both the L_d and L_o domains. For G1, G2, and G3 respectively, we observed a total increase of 21%, 31%, and 38% for the disordered phase, and 15%, 25%, and 32% for the ordered phase, when the concentrations were increased from $1\mu M$ to 15 μM.

S7. Small angle X-ray scattering (SAXS) data analysis

The resultant 1D intensity vs q data are plotted in Fig. 1. At higher q values a curve in the scattering data is visible which corresponds to the scattering from the base particles in the system. There is an increase in the scattering at low q values which can occur when there is aggregation of these particles. This results in a scattering signal from this larger particle and an increase in intensity at lower q values.

The measured scattering signal has been fitted using a unified fit approach which combines a Guinier fit and a Porod fit. The Guinier region is dependent on the radius of gyration (Rg) of the particles. The Porod gradient provides information on the mass fractal dimension of the particle. A polymer coil is expected to have a gradient of 2 and decreases as the interaction between polymer chains increases giving a value of 1.66 for swollen Gaussian coils. The fit results of the samples are compared in Table 1. All fitting was done using the Irena SAXS macros running in Igor Pro.[3]

Table S2: Comparison of the determined Rg and Porod gradient.

Sample	Rg /nm	Porod gradient
G1	3.77	2.48
G2	4.23	2.03
G3	5.42	1.97
H3	2.36	1.59

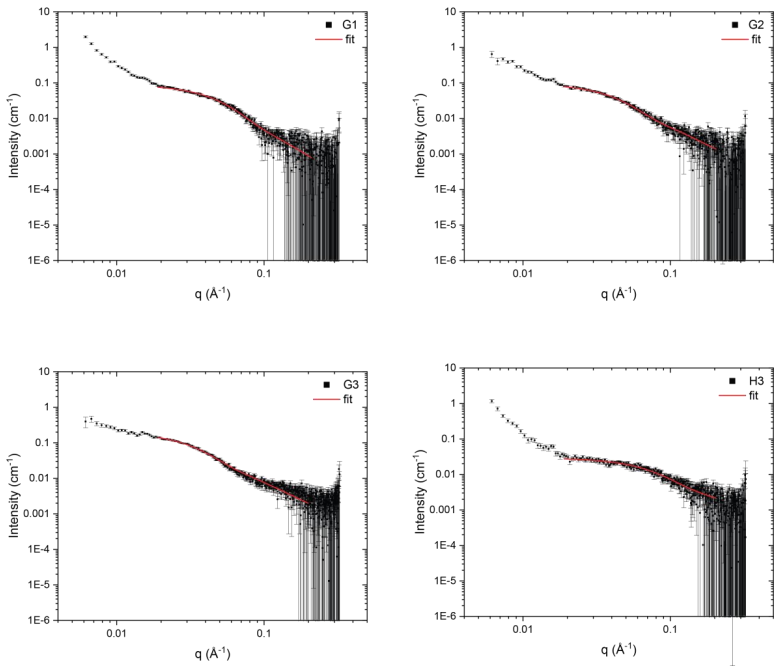

Figure S14 : Comparison of measured SAXS data along with a fit with Guiner and Porod regions utilizing the unified fit approach.

S8. Z-scan FCS with glycopolymer coated SLBs

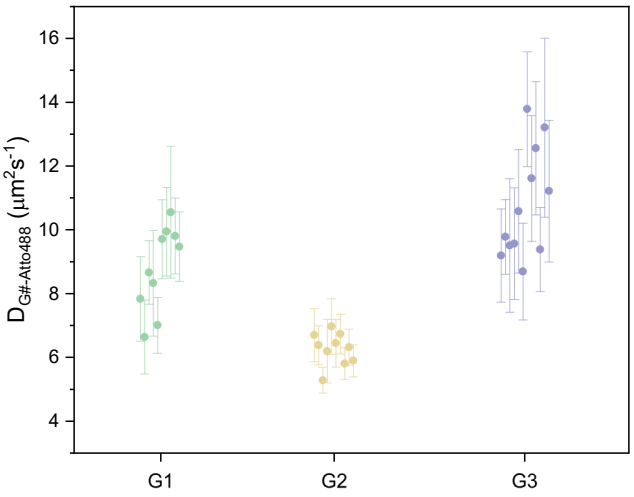

Figure S15 : Diffusion coefficients of the labelled polymer after incorporation on a supported lipid bilayer composing of POPC

Table S3: Diffusion coefficient for the glycopolymers with different carbohydrate chain length on POPC SLBs

Sample	D $[\mu m^2 s^{-1}]$
G1	8.65 ± 1.30
G2	6.17 ± 0.67
G3	10.52 ± 1.84

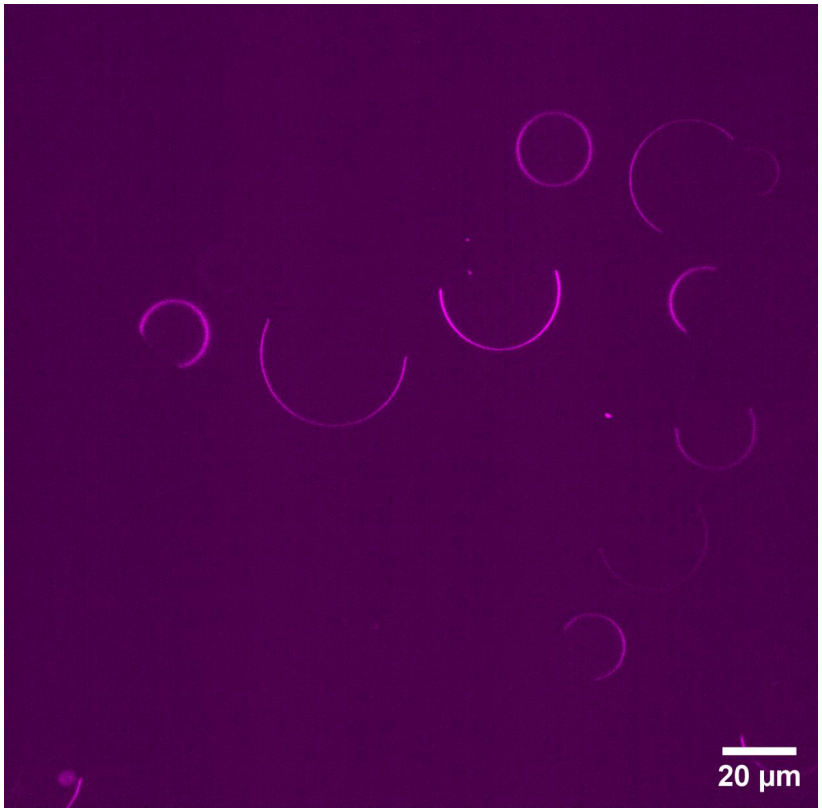

Figure S16 : Control vesicles with co-existing L_d/L_o domains consisting of DOPC, DSPC, and cholesterol (35:35:30 mol%) with 0.05 mol% A655-DOPE.

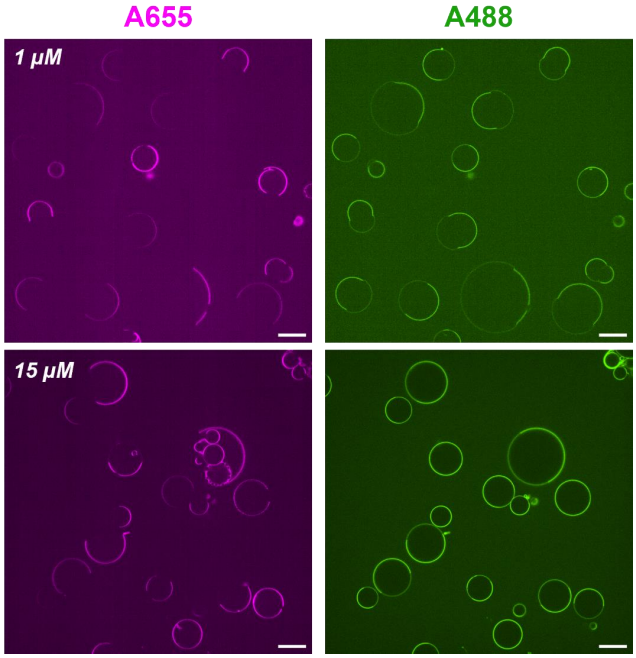

Figure S17: Phase separated vesicles incubated with G2 at 1 and 5 μM concentrations show a clear reduction in line tension along the domain boundary. Scale bar: 10 μm

S9. Estimated molar ratio of incorporated glycopolymer from surface density measured using FCS

With a calibration of the PSF from 3D FCS fitting of a dye with known diffusion coefficient, we measured the PSF radius to be $0.216\ \mu M$. This gives the total surface area of a membrane patch within the confocal volume to be $0.147\ \mu m^2$. Area per lipid for a POPC lipid has been previously reported to be $0.654\ nm^2$ which gives a total amount in the confocal volume to be ~ 224770 lipids. The weighted average surface density for G1, G2, and G3 on POPC SLBs were measured as 6364.85, 10280.71, 10671.23 μm^{-2}. This would result in a molar percentage of 2.83, 4.57, and 4.74 for the three glycopolymers respectively.

S10. Tubulation at the L_d domains upon increasing concentrations of glycopolymers

We observed that with higher incubation concentrations, the GUVs expelled tubes from the L_d domains. This tubulation is expected to be a result of the increased ΔC_{spo} with an increased

surface density σ. Additionally, since L_d domains have an overall lower bending energy as compared to the L_o domains, making it more difficult for the L_o domains to tubulate.

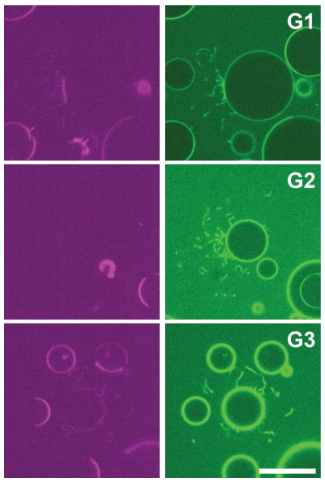

Figure S18: Phase separated vesicles incubated with 15 μM of the glycopolymers displayed outward tubulation from the L_d domains.

List of Figures

Bibliography

[1] Nägeli, C. *Pflanzenphysiologische Untersuchungen*. (1855). [cited on page 3.]

[2] Pfeffer, W. *Osmotic investigations: Studies on cell mechanics*. Van Nostrand Reinhold Company, (1985). [cited on page 3.]

[3] Traube, M. *Experimente zur Theorie der Zellenbildung und Endosmose*. (1867). [cited on page 3.]

[4] Overton, C. E. *Studies of Narcosis*. Springer Netherlands, (1991). [cited on page 4.]

[5] Overton, E. *Zeitschrift für Physikalische Chemie* **22U**(1), 189–209 February (1897). [cited on page 4.]

[6] Langmuir, I. *Journal of the American Chemical Society* **38**(11), 2221–2295 (1916). [cited on page 4.]

[7] Gorter, E. and Grendel, F. *J. Exp. Med.* **41**(4), 439–443 March (1925). [cited on page 4.]

[8] Danielli, J. F. and Davson, H. *Journal of Cellular and Comparative Physiology* **5**(4), 495–508 February (1935). [cited on page 4.]

[9] Robertson, J. D. *Biochem. Soc. Symp.* **16**, 3–43 (1959). [cited on page 4.]

[10] Lenard, J. and Singer, S. J. *Proceedings of the National Academy of Sciences* **56**(6), 1828–1835 December (1966). [cited on page 4.]

[11] Singer, S. J. and Nicolson, G. L. *Science* **175**(4023), 720–731 February (1972). [cited on page 4.]

[12] Mouritsen, O. and Bloom, M. *Biophysical Journal* **46**(2), 141–153 August (1984). [cited on page 5.]

[13] Israelachvili, J. N. *Biochimica et Biophysica Acta (BBA) - Biomembranes* **469**(2), 221–225 September (1977). [cited on page 5.]

[14] Lipowsky, R. *Journal de Physique II* **2**(10), 1825–1840 October (1992). [cited on page 5.]

[15] Jülicher, F. and Lipowsky, R. *Physical Review Letters* **70**(19), 2964–2967 May (1993). [cited on page 5.]

[16] Simons, K. and Ikonen, E. *Nature* **387**(6633), 569–572 June (1997). [cited on page 5.]

[17] Leslie, M. *Science* **334**(6059), 1046–1047 November (2011). [cited on page 5.]

[18] Devaux, P. and McConnell, H. *Journal of the American Chemical Society* **94**(13), 4475–4481 June (1972). [cited on page 5.]

[19] Kornberg, R. D. and McConnell, H. M. *Proceedings of the National Academy of Sciences* **68**(10), 2564–2568 October (1971). [cited on page 5.]

[20] Evans, E. *Biophysical Journal* **14**(12), 923–931 December (1974). [cited on page 5.]

[21] Helfrich, W. *Zeitschrift für Naturforschung C* **28**(11–12), 693–703 December (1973). [cited on page 5.]

[22] Berndl, K., Käs, J., Lipowsky, R., Sackmann, E., and Seifert, U. *Europhysics Letters (EPL)* **13**(7), 659–664 December (1990). [cited on page 5.]

[23] Seifert, U. and Lipowsky, R. *Physical Review A* **42**(8), 4768–4771 October (1990). [cited on pages 5 and 7.]

[24] Miao, L., Fourcade, B., Rao, M., Wortis, M., and Zia, R. K. P. *Physical Review A* **43**(12), 6843–6856 June (1991). [cited on page 5.]

[25] Liu, Y., Agudo-Canalejo, J., Grafmüller, A., Dimova, R., and Lipowsky, R. *ACS Nano* **10**(1), 463–474 November (2015). [cited on page 5.]

[26] Almeida, P. F., Vaz, W. L., and Thompson, T. *Biophysical Journal* **88**(6), 4434–4438 June (2005). [cited on page 5.]

[27] Schoch, R. L., Brown, F. L. H., and Haran, G. *Proceedings of the National Academy of Sciences* **118**(48) November (2021). [cited on page 5.]

[28] Nagle, J. F., Mathai, J. C., Zeidel, M. L., and Tristram-Nagle, S. *The Journal of General Physiology* **131**(1), 77–85 December (2007). [cited on page 5.]

[29] Li, Y., Lipowsky, R., and Dimova, R. *Proceedings of the National Academy of Sciences* **108**(12), 4731–4736 March (2011). [cited on page 5.]

[30] Ansell, G. B., Hawthorne, J. N., and Dawson, R. M. C. *Form and function of phospholipids*. B.B.A. library; v. 3. Elsevier Scientific Pub. Co., Amsterdam, 2d completely rev. and enl. ed edition, (1973). [cited on page 5.]

[31] Thudichum, J. L. W. *A treatise on the chemical constitution of the brain*. Bailliere, Tindall and Cox, London, (1884). [cited on page 5.]

[32] Virchow, R. *Archiv für Pathologische Anatomie und Physiologie und für Klinische Medicin* **6**(4), 562–572 December (1854). [cited on page 5.]

[33] Papahadjopoulos, D. and Watkins, J. *Biochimica et Biophysica Acta (BBA) - Biomembranes* **135**(4), 639–652 September (1967). [cited on page 5.]

[34] Akbarzadeh, A., Rezaei-Sadabady, R., Davaran, S., Joo, S. W., Zarghami, N., Hanifehpour, Y., Samiei, M., Kouhi, M., and Nejati-Koshki, K. *Nanoscale Research Letters* **8**(1) February (2013). [cited on page 5.]

[35] Lasic, D. and Papahadjopoulos, D. ii. Elsevier (1998). [cited on page 5.]

[36] Daraee, H., Etemadi, A., Kouhi, M., Alimirzalu, S., and Akbarzadeh, A. *Artificial Cells, Nanomedicine, and Biotechnology* **44**(1), 381–391 September (2014). [cited on page 5.]

[37] Walde, P., Cosentino, K., Engel, H., and Stano, P. *ChemBioChem* **11**(7), 848–865 April (2010). [cited on pages 5 and 8.]

[38] Nair, K. S. and Bajaj, H. *Advances in Colloid and Interface Science* **318**, 102935 August (2023). [cited on pages 5 and 10.]

[39] Dimova, R., Stano, P., Marques, C. M., and Walde, P. In *The Giant Vesicle Book*, 3–15. CRC Press, Boca Raton, FL : CRC Press, Taylor & Francis Group, [2020] November (2019). [cited on pages 5 and 9.]

[40] Chan, Y.-H. M. and Boxer, S. G. *Current Opinion in Chemical Biology* **11**(6), 581–587 December (2007). [cited on page 6.]

[41] García-Sáez, A. J. and Schwille, P. *Biochimica et Biophysica Acta (BBA) - Biomembranes* **1798**(4), 766–776 April (2010). [cited on page 6.]

[42] Israelachvili, J. N., Mitchell, D. J., and Ninham, B. W. *Journal of the Chemical Society, Faraday Transactions 2* **72**, 1525 (1976). [cited on page 6.]

[43] Torchilin, V. and Weissig, V., editors. *Liposomes: A Practical Approach*. Practical Approach Series. Oxford University Press, London, England, 2 edition, June (2003). [cited on page 6.]

[44] Sych, T., Schlegel, J., Barriga, H. M. G., Ojansivu, M., Hanke, L., Weber, F., Beklem Bostancioglu, R., Ezzat, K., Stangl, H., Plochberger, B., Laurencikiene, J., El Andaloussi, S., Fürth, D., Stevens, M. M., and Sezgin, E. *Nature Biotechnology* **42**(4), 587–590 June (2023). [cited on page 6.]

[45] Tanaka, T., Matsumoto, A., Klymchenko, A. S., Tsurumaki, E., Ikenouchi, J., and Konishi, G. *Advanced Science* **11**(17) March (2024). [cited on pages 6 and 9.]

[46] Weber, G. and Farris, F. J. *Biochemistry* **18**(14), 3075–3078 July (1979). [cited on page 6.]

[47] Valanciunaite, J., Kempf, E., Seki, H., Danylchuk, D. I., Peyriéras, N., Niko, Y., and Klymchenko, A. S. *Analytical Chemistry* **92**(9), 6512–6520 March (2020). [cited on page 6.]

[48] Liu, F., Danylchuk, D. I., Andreiuk, B., and Klymchenko, A. S. *Chemical Science* **13**(13), 3652–3660 (2022). [cited on page 6.]

[49] Chen, X., Bayard, F., Gonzalez-Sanchis, N., Pamungkas, K. K. P., Sakai, N., and Matile, S. *Angewandte Chemie International Edition* **62**(20) February (2023). [cited on pages 6 and 9.]

[50] Roffay, C. and Mercier, V. *Nature Reviews Molecular Cell Biology* **24**(12), 853–853 July (2023). [cited on page 6.]

[51] Colom, A., Derivery, E., Soleimanpour, S., Tomba, C., Molin, M. D., Sakai, N., González-Gaitán, M., Matile, S., and Roux, A. *Nature Chemistry* **10**(11), 1118–1125 August (2018). [cited on page 7.]

[52] Ragaller, F., Sjule, E., Urem, Y. B., Schlegel, J., El, R., Urbancic, D., Urbancic, I., Blom, H., and Sezgin, E. *The Journal of Physical Chemistry B* **128**(9), 2154–2167 February (2024). [cited on page 7.]

[53] Richter, R. P., Bérat, R., and Brisson, A. R. *Langmuir* **22**(8), 3497–3505 January (2006). [cited on page 7.]

[54] Andersson, J. and Köper, I. *Membranes* **6**(2), 30 May (2016). [cited on page 7.]

[55] Reverte-López, M., Gavrilovic, S., Merino-Salomón, A., Eto, H., Yagüe Relimpio, A., Rivas, G., and Schwille, P. *Small Methods* **7**(12) June (2023). [cited on page 7.]

[56] Dutta, D. and Kam, L. C. *Micropatterned, Multicomponent Supported Lipid Bilayers for Cellular Systems*, 53–67. Elsevier (2014). [cited on page 7.]

[57] Nair, P. M., Salaita, K., Petit, R. S., and Groves, J. T. *Nature Protocols* **6**(4), 523–539 March (2011). [cited on page 7.]

[58] El Alaoui, F., Al-Akiki, I., Ibanes, S., Lyonnais, S., Sanchez-Fuentes, D., Desgarceaux, R., Cazevieille, C., Blanchard, M.-P., Parmeggiani, A., Carretero-Genevrier, A., Piatti, S., and Picas, L. *biorxiv* March (2024). [cited on page 7.]

[59] El Alaoui, F., Casuso, I., Sanchez-Fuentes, D., Arpin-Andre, C., Rathar, R., Baecker, V., Castro, A., Lorca, T., Viaud, J., Vassilopoulos, S., Carretero-Genevrier, A., and Picas, L. *eLife* **11** January (2022). [cited on page 7.]

[60] Jackman, J. A. and Cho, N.-J. *Langmuir* **36**(6), 1387–1400 January (2020). [cited on page 7.]

[61] Binnig, G., Quate, C. F., and Gerber, C. *Physical Review Letters* **56**(9), 930–933 March (1986). [cited on page 7.]

[62] Lv, Z., Banerjee, S., Zagorski, K., and Lyubchenko, Y. L. *Supported Lipid Bilayers for Atomic Force Microscopy Studies*, 129–143. Springer New York (2018). [cited on page 7.]

[63] Alessandrini, A. and Facci, P. *Soft Matter* **10**(37), 7145–7164 (2014). [cited on page 7.]

[64] Morandat, S., Azouzi, S., Beauvais, E., Mastouri, A., and El Kirat, K. *Analytical and Bioanalytical Chemistry* **405**(5), 1445–1461 September (2012). [cited on page 7.]

[65] Nguyen, P. A., Field, C. M., Groen, A. C., Mitchison, T. J., and Loose, M. *Using supported bilayers to study the spatiotemporal organization of membrane-bound proteins*, 223–241. Elsevier (2015). [cited on page 8.]

[66] Chiantia, S., Ries, J., and Schwille, P. *Biochimica et Biophysica Acta (BBA) - Biomembranes* **1788**(1), 225–233 January (2009). [cited on pages 8, 9, and 28.]

[67] Mücksch, J., Blumhardt, P., Strauss, M. T., Petrov, E. P., Jungmann, R., and Schwille, P. *Nano Letters* **18**(5), 3185–3192 April (2018). [cited on page 8.]

[68] Stein, J., Stehr, F., Schueler, P., Blumhardt, P., Schueder, F., Mücksch, J., Jungmann, R., and Schwille, P. *Nano Letters* **19**(11), 8182–8190 September (2019). [cited on page 8.]

[69] Papahadjopoulos, D. and Kimelberg, H. K. *Progress in Surface Science* **4**, 141–232 January (1974). [cited on page 8.]

[70] Lasic, D. D. November (1999). [cited on page 8.]

[71] Horger, K. S., Estes, D. J., Capone, R., and Mayer, M. *Journal of the American Chemical Society* **131**(5), 1810–1819 January (2009). [cited on page 8.]

[72] Weinberger, A., Tsai, F.-C., Koenderink, G., Schmidt, T., Itri, R., Meier, W., Schmatko, T., Schröder, A., and Marques, C. *Biophysical Journal* **105**(1), 154–164 July (2013). [cited on page 8.]

[73] Angelova, M. I. and Dimitrov, D. S. *Faraday Discussions of the Chemical Society* **81**, 303 (1986). [cited on page 8.]

[74] Träuble, H. and Grell, E. *Neurosci. Res. Program Bull.* **9**(3), 373–380 June (1971). [cited on page 8.]

[75] Pautot, S., Frisken, B. J., and Weitz, D. A. *Langmuir* **19**(7), 2870–2879 February (2003). [cited on page 8.]

[76] Deshpande, S., Caspi, Y., Meijering, A. E. C., and Dekker, C. *Nature Communications* **7**(1) January (2016). [cited on page 8.]

[77] Blosser, M. C., Horst, B. G., and Keller, S. L. *Soft Matter* **12**(35), 7364–7371 (2016). [cited on page 8.]

[78] Bagatolli, L., Parasassi, T., and Gratton, E. *Chemistry and Physics of Lipids* **105**(2), 135–147 April (2000). [cited on page 8.]

[79] Dimova, R., Aranda, S., Bezlyepkina, N., Nikolov, V., Riske, K. A., and Lipowsky, R. *Journal of Physics: Condensed Matter* **18**(28), S1151–S1176 June (2006). [cited on page 8.]

[80] Dimova, R. *Annual Review of Biophysics* **48**(1), 93–119 May (2019). [cited on pages 8 and 9.]

[81] Faizi, H. A., Tsui, A., Dimova, R., and Vlahovska, P. M. *Langmuir* **38**(34), 10548–10557 August (2022). [cited on page 8.]

[82] Wubshet, N. H. and Liu, A. P. *Computational and Structural Biotechnology Journal* **21**, 550–562 (2023). [cited on page 9.]

[83] Betaneli, V. and Schwille, P. *Fluorescence Correlation Spectroscopy to Examine Protein–Lipid Interactions in Membranes*, 253–278. Humana Press December (2012). [cited on pages 9 and 28.]

[84] Dimova, R. *Advances in Colloid and Interface Science* **208**, 225–234 June (2014). [cited on page 9.]

[85] Moradi, S., Nowroozi, A., and Shahlaei, M. *RSC Advances* **9**(8), 4644–4658 (2019). [cited on page 9.]

[86] Schrödinger, E. *Ann. Phys.* **384**(4), 361–376 January (1926). [cited on page 9.]

[87] Adamala, K. P., Dogterom, M., Elani, Y., Schwille, P., Takinoue, M., and Tang, T.-Y. D. *Nat. Rev. Mol. Cell Biol.* **25**(3), 162–167 March (2024). [cited on page 9.]

[88] Rothschild, L. J., Averesch, N. J. H., Strychalski, E. A., Moser, F., Glass, J. I., Cruz Perez, R., Yekinni, I. O., Rothschild-Mancinelli, B., Roberts Kingman, G. A., Wu, F., Waeterschoot, J., Ioannou, I. A., Jewett, M. C., Liu, A. P., Noireaux, V., Sorenson, C., and Adamala, K. P. *ACS Synth. Biol.* **13**(4), 974–997 April (2024). [cited on page 9.]

[89] Göpfrich, K., Platzman, I., and Spatz, J. P. *Trends Biotechnol.* **36**(9), 938–951 September (2018). [cited on page 9.]

[90] Hirschi, S., Ward, T. R., Meier, W. P., Müller, D. J., and Fotiadis, D. *Chem. Rev.* **122**(21), 16294–16328 November (2022). [cited on page 9.]

[91] Van de Cauter, L., van Buren, L., Koenderink, G. H., and Ganzinger, K. A. *Small Methods* **7**(12) July (2023). [cited on page 10.]

[92] Kohyama, S., Merino-Salomón, A., and Schwille, P. *Nat. Commun.* **13**(1), 6098 October (2022). [cited on page 10.]

[93] Fink, A., Doll, C. R., Yagüe Relimpio, A., Dreher, Y., Spatz, J. P., Göpfrich, K., and Cavalcanti-Adam, E. A. *ACS Synth. Biol.* **12**(2), 369–374 February (2023). [cited on page 10.]

[94] Zhan, P., Jahnke, K., Liu, N., and Göpfrich, K. *Nature Chemistry* **14**(8), 958–963 June (2022). [cited on page 10.]

[95] Gavrilović, S., Brüggenthies, G. A., Weck, J. M., Heuer-Jungemann, A., and Schwille, P. *Small* **20**(24) January (2024). [cited on pages 10 and 86.]

[96] Seo, H. and Lee, H. *Nature Communications* **13**(1) September (2022). [cited on page 10.]

[97] Wagner, A. M., Eto, H., Joseph, A., Kohyama, S., Haraszti, T., Zamora, R. A., Vorobii, M., Giannotti, M. I., Schwille, P., and Rodriguez-Emmenegger, C. *Advanced Materials* **34**(28) June (2022). [cited on page 10.]

[98] Jahnke, K., Pavlovic, M., Xu, W., Chen, A., Knowles, T. P. J., Arriaga, L. R., and Weitz, D. A. *Proceedings of the National Academy of Sciences* **121**(22) May (2024). [cited on pages 10 and 20.]

[99] Vogele, K., Frank, T., Gasser, L., Goetzfried, M. A., Hackl, M. W., Sieber, S. A., Simmel, F. C., and Pirzer, T. *Nature Communications* **9**(1) September (2018). [cited on page 10.]

[100] Guinart, A., Korpidou, M., Doellerer, D., Pacella, G., Stuart, M. C. A., Dinu, I. A., Portale, G., Palivan, C., and Feringa, B. L. *Proceedings of the National Academy of Sciences* **120**(27) June (2023). [cited on page 10.]

[101] Mouritsen, O. G. *Cold Spring Harbor Perspectives in Biology* **3**(9), a004622–a004622 May (2011). [cited on page 11.]

[102] Roux, A., Cappello, G., Cartaud, J., Prost, J., Goud, B., and Bassereau, P. *Proceedings of the National Academy of Sciences* **99**(8), 5394–5399 April (2002). [cited on page 11.]

[103] Hasson, T. and Mooseker, M. S. *Current Opinion in Cell Biology* **7**(4), 587–594 January (1995). [cited on page 11.]

[104] Allan, V. J. and Schroert, T. A. *Current Opinion in Cell Biology* **11**(4), 476–482 August (1999). [cited on page 11.]

[105] Gopaldass, N., Chen, K.-E., Collins, B., and Mayer, A. *Nature Reviews Molecular Cell Biology* **25**(10), 765–783 June (2024). [cited on page 11.]

[106] Horn, A. and Jaiswal, J. K. *Structural and signaling role of lipids in plasma membrane repair*, 67–98. Elsevier (2019). [cited on page 11.]

[107] Lee, T.-H., Charchar, P., Separovic, F., Reid, G. E., Yarovsky, I., and Aguilar, M.-I. *Chemical Science* **15**(10), 3408–3427 (2024). [cited on page 11.]

[108] Naito, T., Yang, H., Koh, D. H. Z., Mahajan, D., Lu, L., and Saheki, Y. *Nature Communications* **14**(1) September (2023). [cited on page 11.]

[109] Wang, Y. and Kinoshita, T. *Biochemical Society Transactions* **51**(5), 1857–1869 September (2023). [cited on page 11.]

[110] Käs, J. and Sackmann, E. *Biophysical Journal* **60**(4), 825–844 October (1991). [cited on page 11.]

[111] Yanagisawa, M., Imai, M., and Taniguchi, T. *Physical Review Letters* **100**(14) April (2008). [cited on page 11.]

[112] Dimova, R., Riske, K. A., Aranda, S., Bezlyepkina, N., Knorr, R. L., and Lipowsky, R. *Soft Matter* **3**(7), 817 (2007). [cited on page 11.]

[113] Dimova, R. and Riske, K. A. *Electrodeformation, Electroporation, and Electrofusion of Giant Unilamellar Vesicles*, 1–18. Springer International Publishing (2016). [cited on page 11.]

[114] Aranda, S., Riske, K. A., Lipowsky, R., and Dimova, R. *Biophysical Journal* **95**(2), L19–L21 July (2008). [cited on page 11.]

[115] Khalifat, N., Puff, N., Bonneau, S., Fournier, J.-B., and Angelova, M. I. *Biophysical Journal* **95**(10), 4924–4933 November (2008). [cited on page 11.]

[116] Boytsov, D., Hannesschlaeger, C., Horner, A., Siligan, C., and Pohl, P. *Biotechnology Journal* **15**(7) May (2020). [cited on page 12.]

[117] Prévost, C., Tsai, F.-C., Bassereau, P., and Simunovic, M. *Journal of Visualized Experiments* (130) December (2017). [cited on page 12.]

[118] Al Nahas, K., Cama, J., Schaich, M., Hammond, K., Deshpande, S., Dekker, C., Ryadnov, M. G., and Keyser, U. F. *Lab on a Chip* **19**(5), 837–844 (2019). [cited on page 12.]

[119] Ganzinger, K. A., Merino-Salomón, A., García-Soriano, D. A., Butterfield, A. N., Litschel, T., Siedler, F., and Schwille, P. *Angewandte Chemie International Edition* **59**(48), 21372–21376 September (2020). [cited on page 12.]

[120] Hak, A., Ali, M. S., Sankaranarayanan, S. A., Shinde, V. R., and Rengan, A. K. *ACS Applied Bio Materials* **6**(2), 349–364 January (2023). [cited on page 13.]

[121] Foote, C. S. *Science* **162**(3857), 963–970 November (1968). [cited on page 12.]

[122] Itri, R., Marques, C. M., and Baptista, M. S. In *The Giant Vesicle Book*, 473–484. CRC Press, Boca Raton, FL : CRC Press, Taylor & Francis Group, [2020] November (2019). [cited on page 12.]

[123] Riske, K. A., Sudbrack, T. P., Archilha, N. L., Uchoa, A. F., Schroder, A. P., Marques, C. M., Baptista, M. S., and Itri, R. *Biophysical Journal* **97**(5), 1362–1370 September (2009). [cited on page 12.]

[124] Kerdous, R., Heuvingh, J., and Bonneau, S. *Biochimica et Biophysica Acta (BBA) - Biomembranes* **1808**(12), 2965–2972 December (2011). [cited on page 12.]

[125] Mertins, O., Bacellar, I., Thalmann, F., Marques, C., Baptista, M., and Itri, R. *Biophysical Journal* **106**(1), 162–171 January (2014). [cited on page 12.]

[126] Sankhagowit, S., Wu, S.-H., Biswas, R., Riche, C. T., Povinelli, M. L., and Malmstadt, N. *Biochimica et Biophysica Acta (BBA) - Biomembranes* **1838**(10), 2615–2624 October (2014). [cited on page 12.]

[127] Itri, R., Junqueira, H. C., Mertins, O., and Baptista, M. S. *Biophysical Reviews* **6**(1), 47–61 January (2014). [cited on page 12.]

[128] Weber, G., Charitat, T., Baptista, M. S., Uchoa, A. F., Pavani, C., Junqueira, H. C., Guo, Y., Baulin, V. A., Itri, R., Marques, C. M., and Schroder, A. P. *Soft Matter* **10**(24), 4241 (2014). [cited on page 12.]

[129] Bacellar, I. O. L., Oliveira, M. C., Dantas, L. S., Costa, E. B., Junqueira, H. C., Martins, W. K., Durantini, A. M., Cosa, G., Di Mascio, P., Wainwright, M., Miotto, R., Cordeiro, R. M., Miyamoto, S., and Baptista, M. S. *Journal of the American Chemical Society* **140**(30), 9606–9615 July (2018). [cited on page 12.]

[130] Dreher, Y., Jahnke, K., Schröter, M., and Göpfrich, K. *Nano Letters* **21**(14), 5952–5957 July (2021). [cited on page 12.]

[131] Kunitake, T., Nakashima, N., Shimomura, M., Okahata, Y., Kano, K., and Ogawa, T. *Journal of the American Chemical Society* **102**(21), 6642–6644 October (1980). [cited on page 13.]

[132] Fujiwara, H. and Yonezawa, Y. *Nature* **351**(6329), 724–726 June (1991). [cited on page 13.]

[133] DiFrancesco, M. L., Lodola, F., Colombo, E., Maragliano, L., Bramini, M., Paternò, G. M., Baldelli, P., Serra, M. D., Lunelli, L., Marchioretto, M., Grasselli, G., Cimò, S., Colella, L., Fazzi, D., Ortica, F., Vurro, V., Eleftheriou, C. G., Shmal, D., Maya-Vetencourt, J. F., Bertarelli, C., Lanzani, G., and Benfenati, F. *Nature Nanotechnology* **15**(4), 296–306 February (2020). [cited on page 13.]

[134] Hamada, T., Sato, Y. T., Yoshikawa, K., and Nagasaki, T. *Langmuir* **21**(17), 7626–7628 July (2005). [cited on page 14.]

[135] Ishii, K., Hamada, T., Hatakeyama, M., Sugimoto, R., Nagasaki, T., and Takagi, M. *ChemBioChem* **10**(2), 251–256 January (2009). [cited on page 14.]

[136] Seifert, U., Berndl, K., and Lipowsky, R. *Physical Review A* **44**(2), 1182–1202 July (1991). [cited on pages 14 and 18.]

[137] Georgiev, V. N., Grafmüller, A., Bléger, D., Hecht, S., Kunstmann, S., Barbirz, S., Lipowsky, R., and Dimova, R. *Advanced Science* **5**(8) June (2018). [cited on page 14.]

[138] Höglsperger, F., Vos, B. E., Hofemeier, A. D., Seyfried, M. D., Stövesand, B., Alavizargar, A., Topp, L., Heuer, A., Betz, T., and Ravoo, B. J. *Nature Communications* **14**(1) June (2023). [cited on page 14.]

[139] Dong, M., Babalhavaeji, A., Samanta, S., Beharry, A. A., and Woolley, G. A. *Accounts of Chemical Research* **48**(10), 2662–2670 September (2015). [cited on page 14.]

[140] Morgan, C. G., Thomas, E. W., Yianni, Y. P., and Sandhu, S. S. *Biochimica et Biophysica Acta (BBA) - Biomembranes* **820**(1), 107–114 October (1985). [cited on page 14.]

[141] Sandhu, S., Yianni, Y., Morgan, C., Taylor, D., and Zaba, B. *Biochimica et Biophysica Acta (BBA) - Biomembranes* **860**(2), 253–262 August (1986). [cited on page 14.]

[142] Morgan, C., Sandhu, S., Yianni, Y., and Dodd, N. *Biochimica et Biophysica Acta (BBA) - Biomembranes* **903**(3), 495–503 October (1987). [cited on page 14.]

[143] Pernpeintner, C., Frank, J. A., Urban, P., Roeske, C. R., Pritzl, S. D., Trauner, D., and Lohmüller, T. *Langmuir* **33**(16), 4083–4089 April (2017). [cited on page 14.]

[144] Kuiper, J. M. and Engberts, J. B. F. N. *Langmuir* **20**(4), 1152–1160 January (2004). [cited on page 14.]

[145] Urban, P., Pritzl, S. D., Ober, M. F., Dirscherl, C. F., Pernpeintner, C., Konrad, D. B., Frank, J. A., Trauner, D., Nickel, B., and Lohmueller, T. *Langmuir* **36**(10), 2629–2634 February (2020). [cited on page 14.]

[146] Aleksanyan, M., Grafmüller, A., Crea, F., Georgiev, V. N., Yandrapalli, N., Block, S., Heberle, J., and Dimova, R. *Advanced Science* **10**(31) August (2023). [cited on page 14.]

[147] Doroudgar, M., Morstein, J., Becker-Baldus, J., Trauner, D., and Glaubitz, C. *Journal of the American Chemical Society* **143**(25), 9515–9528 June (2021). [cited on page 14.]

[148] Xiong, H., Alberto, K. A., Youn, J., Taura, J., Morstein, J., Li, X., Wang, Y., Trauner, D., Slesinger, P. A., Nielsen, S. O., and Qin, Z. *Nano Research* **16**(1), 1033–1041 September (2022). [cited on page 14.]

[149] Hartrampf, N., Leitao, S. M., Winter, N., Toombs-Ruane, H., Frank, J. A., Schwille, P., Trauner, D., and Franquelim, H. G. *Biophysical Journal* **122**(11), 2325–2341 June (2023). [cited on page 14.]

[150] Reise, F., Warias, J. E., Chatterjee, K., Krekiehn, N. R., Magnussen, O., Murphy, B. M., and Lindhorst, T. K. *Chemistry – A European Journal* **24**(66), 17497–17505 November (2018). [cited on page 14.]

[151] Warias, J. E., Reise, F., Hövelmann, S. C., Giri, R. P., Röhrl, M., Kuhn, J., Jacobsen, M., Chatterjee, K., Arnold, T., Shen, C., Festersen, S., Sartori, A., Jordt, P., Magnussen, O. M., Lindhorst, T. K., and Murphy, B. M. *Scientific Reports* **13**(1) July (2023). [cited on page 14.]

[152] Kistemaker, J. C. M., Lubbe, A. S., and Feringa, B. L. *Materials Chemistry Frontiers* **5**(7), 2900–2906 (2021). [cited on page 15.]

[153] Koumura, N., Zijlstra, R. W. J., van Delden, R. A., Harada, N., and Feringa, B. L. *Nature* **401**(6749), 152–155 September (1999). [cited on page 15.]

[154] Pooler, D. R. S., Lubbe, A. S., Crespi, S., and Feringa, B. L. *Chemical Science* **12**(45), 14964–14986 (2021). [cited on page 15.]

[155] García-López, V., Chen, F., Nilewski, L. G., Duret, G., Aliyan, A., Kolomeisky, A. B., Robinson, J. T., Wang, G., Pal, R., and Tour, J. M. *Nature* **548**(7669), 567–572 August (2017). [cited on page 15.]

[156] Firsov, A. M., Pfeffermann, J., Benditkis, A. S., Rokitskaya, T. I., Kozlov, A. S., Kotova, E. A., Krasnovsky, A. A., Pohl, P., and Antonenko, Y. N. *Journal of Photochemistry and Photobiology B: Biology* **239**, 112633 February (2023). [cited on page 15.]

[157] Wallach, D. F. H. and Winzler, R. J. *Membrane "Macromolecules"*, 57–127. Springer Berlin Heidelberg (1974). [cited on page 17.]

[158] Albanese, A., Tang, P. S., and Chan, W. C. *Annual Review of Biomedical Engineering* **14**(1), 1–16 August (2012). [cited on page 17.]

[159] Clay, W. F., Katterman, F. R., and Bartels, P. G. *Proceedings of the National Academy of Sciences* **72**(8), 3134–3138 August (1975). [cited on page 17.]

[160] Thalmann, F. and Marques, C. M. In *The Giant Vesicle Book*, 230–258. CRC Press, Boca Raton, FL : CRC Press, Taylor & Francis Group, [2020] November (2019). [cited on pages 17 and 18.]

[161] de Gennes, P. G. *Macromolecules* **14**, 1637–1644 (1981). [cited on page 18.]

[162] Skau, K. and Blokhuis, E. *The European Physical Journal E* **7**(1), 13–22 January (2002). [cited on pages 18 and 19.]

[163] Brooks, J. T., Marques, C. M., and Cates, M. E. *Journal de Physique II* **1**(6), 673–690 June (1991). [cited on page 18.]

[164] Brooks, J. T., Marques, C. M., and Cates, M. E. *Europhysics Letters (EPL)* **14**(7), 713–718 April (1991). [cited on page 18.]

[165] Milner, S. T., Witten, T. A., and Cates, M. E. *Macromolecules* **21**(8), 2610–2619 August (1988). [cited on page 18.]

[166] Evans, E. and Rawicz, W. *Physical Review Letters* **79**(12), 2379–2382 September (1997). [cited on page 18.]

[167] Sakuma, Y., Kayamori, N., Tanaka, J., Haga, K., Imai, M., and Kawakatsu, T. *Biophysical Journal* **123**(4), 489–501 February (2024). [cited on page 18.]

[168] Clement, F. and Joanny, J.-F. *Journal de Physique II* **7**(7), 973–980 July (1997). [cited on page 19.]

[169] Pinho, S. S. and Reis, C. A. *Nature Reviews Cancer* **15**(9), 540–555 August (2015). [cited on page 19.]

[170] Shurer, C. R., Kuo, J. C.-H., Roberts, L. M., Gandhi, J. G., Colville, M. J., Enoki, T. A., Pan, H., Su, J., Noble, J. M., Hollander, M. J., O'Donnell, J. P., Yin, R., Pedram, K., Möckl, L., Kourkoutis, L. F., Moerner, W., Bertozzi, C. R., Feigenson, G. W., Reesink, H. L., and Paszek, M. J. *Cell* **177**(7), 1757–1770.e21 June (2019). [cited on pages 19 and 20.]

[171] Rilla, K., Pasonen-Seppänen, S., Deen, A. J., Koistinen, V. V., Wojciechowski, S., Oikari, S., Kärnä, R., Bart, G., Törrönen, K., Tammi, R. H., and Tammi, M. I. *Experimental Cell Research* **319**(13), 2006–2018 August (2013). [cited on page 19.]

[172] Rabuka, D., Forstner, M. B., Groves, J. T., and Bertozzi, C. R. *Journal of the American Chemical Society* **130**(18), 5947–5953 April (2008). [cited on pages 19 and 20.]

[173] Lasky, L. A. *Journal of Cellular Biochemistry* **45**(2), 139–146 February (1991). [cited on page 19.]

[174] Raman, R., Raguram, S., Venkataraman, G., Paulson, J. C., and Sasisekharan, R. *Nature Methods* **2**(11), 817–824 October (2005). [cited on page 19.]

[175] Paulick, M. G., Wise, A. R., Forstner, M. B., Groves, J. T., and Bertozzi, C. R. *Journal of the American Chemical Society* **129**(37), 11543–11550 August (2007). [cited on page 19.]

[176] Rabuka, D., Parthasarathy, R., Lee, G. S., Chen, X., Groves, J. T., and Bertozzi, C. R. *Journal of the American Chemical Society* **129**(17), 5462–5471 April (2007). [cited on page 19.]

[177] Godula, K., Umbel, M. L., Rabuka, D., Botyanszki, Z., Bertozzi, C. R., and Parthasarathy, R. *Journal of the American Chemical Society* **131**(29), 10263–10268 July (2009). [cited on page 19.]

[178] Blawitzki, L.-C., Bartels, N., Bonda, L., Schmidt, S., Monzel, C., and Hartmann, L. *Biomacromolecules* **25**(9), 5979–5994 August (2024). [cited on page 20.]

[179] Yu, L., Feng, R., Zhu, L., Hao, Q., Chu, J., Gu, Y., Luo, Y., Zhang, Z., Chen, G., and Chen, H. *Science Advances* **6**(47) November (2020). [cited on page 20.]

[180] Seeman, N. C. *Journal of Theoretical Biology* **99**(2), 237–247 November (1982). [cited on page 20.]

[181] Seeman, N. C. and Sleiman, H. F. *Nature Reviews Materials* **3**(1) November (2017). [cited on page 20.]

[182] Rothemund, P. W. K. *Nature* **440**(7082), 297–302 March (2006). [cited on page 20.]

[183] Schoenit, A., Cavalcanti-Adam, E. A., and Göpfrich, K. *Trends in Biotechnology* **39**(11), 1208–1220 November (2021). [cited on page 20.]

[184] Dey, S., Fan, C., Gothelf, K. V., Li, J., Lin, C., Liu, L., Liu, N., Nijenhuis, M. A. D., Saccà, B., Simmel, F. C., Yan, H., and Zhan, P. *Nature Reviews Methods Primers* **1**(1) January (2021). [cited on page 21.]

[185] Khmelinskaia, A., Mücksch, J., Petrov, E. P., Franquelim, H. G., and Schwille, P. *Langmuir* **34**(49), 14921–14931 September (2018). [cited on pages 21 and 27.]

[186] Franquelim, H. G., Khmelinskaia, A., Sobczak, J.-P., Dietz, H., and Schwille, P. *Nature Communications* **9**(1) February (2018). [cited on page 21.]

[187] Illig, M., Jahnke, K., Weise, L. P., Scheffold, M., Mersdorf, U., Drechsler, H., Zhang, Y., Diez, S., Kierfeld, J., and Göpfrich, K. *Nature Communications* **15**(1) March (2024). [cited on page 21.]

[188] Jahnke, K. and Göpfrich, K. *Interface Focus* **13**(5) August (2023). [cited on page 21.]

[189] Jahnke, K., Huth, V., Mersdorf, U., Liu, N., and Göpfrich, K. *ACS Nano* **16**(5), 7233–7241 April (2022). [cited on page 21.]

[190] Walther, T., Jahnke, K., Abele, T., and Göpfrich, K. *Advanced Functional Materials* **32**(25) March (2022). [cited on page 21.]

[191] Fragasso, A., De Franceschi, N., Stömmer, P., van der Sluis, E. O., Dietz, H., and Dekker, C. *ACS Nano* **15**(8), 12768–12779 June (2021). [cited on page 21.]

[192] Xing, Y., Dorey, A., Jayasinghe, L., and Howorka, S. *Nature Nanotechnology* **17**(7), 708–713 April (2022). [cited on page 21.]

[193] Heimstädt, O. *Zeitschrift für Wissenschaftliche Mikroskopie und für Mikroskopische Technik* **28**, 330–337 (1911). [cited on page 23.]

[194] Valeur, B. and Berberan-Santos, M. N. *Journal of Chemical Education* **88**(6), 731–738 March (2011). [cited on page 23.]

[195] *Fluorescence Microscopy: From Principles to Biological Applications*. Wiley, April (2013). [cited on pages 23 and 26.]

[196] *Principles of Fluorescence Spectroscopy*. Springer US, (2006). [cited on pages 23 and 27.]

[197] Swaminathan, S. *Nature Cell Biology* **11**(S1), S20–S20 October (2009). [cited on page 23.]

[198] Shaner, N. C., Campbell, R. E., Steinbach, P. A., Giepmans, B. N. G., Palmer, A. E., and Tsien, R. Y. *Nature Biotechnology* **22**(12), 1567–1572 November (2004). [cited on page 23.]

[199] Tokunaga, M., Imamoto, N., and Sakata-Sogawa, K. *Nature Methods* **5**(2), 159–161 January (2008). [cited on page 25.]

[200] Huang, B., Bates, M., and Zhuang, X. *Annual Review of Biochemistry* **78**(1), 993–1016 June (2009). [cited on page 25.]

[201] Axelrod, D. *The Journal of cell biology* **89**(1), 141–145 April (1981). [cited on page 25.]

[202] Ploem, J. S. *Z. Wiss. Mikrosk.* **68**(3), 129–142 November (1967). [cited on page 26.]

[203] NISHIZAWA, J.-i. *Proceedings of the Japan Academy, Series B* **85**(10), 454–465 (2009). [cited on page 26.]

[204] Betzig, E., Patterson, G. H., Sougrat, R., Lindwasser, O. W., Olenych, S., Bonifacino, J. S., Davidson, M. W., Lippincott-Schwartz, J., and Hess, H. F. *Science* **313**(5793), 1642–1645 September (2006). [cited on page 26.]

[205] Hess, S. T., Girirajan, T. P., and Mason, M. D. *Biophysical Journal* **91**(11), 4258–4272 December (2006). [cited on page 26.]

[206] Rust, M. J., Bates, M., and Zhuang, X. *Nature Methods* **3**(10), 793–796 August (2006). [cited on page 27.]

[207] Sharonov, A. and Hochstrasser, R. M. *Proceedings of the National Academy of Sciences* **103**(50), 18911–18916 December (2006). [cited on page 27.]

[208] Schnitzbauer, J., Strauss, M. T., Schlichthaerle, T., Schueder, F., and Jungmann, R. *Nature Protocols* **12**(6), 1198–1228 May (2017). [cited on page 27.]

[209] Haustein, E. and Schwille, P. *Annual Review of Biophysics and Biomolecular Structure* **36**(1), 151–169 June (2007). [cited on page 27.]

[210] Schwille, P., Meyer-Almes, F., and Rigler, R. *Biophysical Journal* **72**(4), 1878–1886 April (1997). [cited on page 27.]

[211] Medina, M. Á. and Schwille, P. *BioEssays* **24**(8), 758–764 July (2002). [cited on page 27.]

[212] Jazani, S., Sgouralis, I., Shafraz, O. M., Levitus, M., Sivasankar, S., and Pressé, S. *Nature Communications* **10**(1) August (2019). [cited on page 27.]

[213] Wahl, M., Gregor, I., Patting, M., and Enderlein, J. *Optics Express* **11**(26), 3583 December (2003). [cited on page 27.]

[214] Laurence, T. A., Fore, S., and Huser, T. *Optics Letters* **31**(6), 829 March (2006). [cited on page 27.]

[215] Elson, E. L. and Magde, D. *Biopolymers* **13**(1), 1–27 January (1974). [cited on page 27.]

[216] Sengupta, P., Garai, K., Balaji, J., Periasamy, N., and Maiti, S. *Biophysical Journal* **84**(3), 1977–1984 March (2003). [cited on page 27.]

[217] Krohn, J.-H., Babl, L., Isnel, L., Qutbuddin, Y., and Schwille, P. *Measuring Partition Coefficients of In Vitro Biomolecular Condensates Using Fluorescence Correlation Spectroscopy*, 455–475. Springer US (2024). [cited on page 27.]

[218] Deptuła, T., Buitenhuis, J., Jarzębski, M., Patkowski, A., and Gapinski, J. *Langmuir* **31**(24), 6681–6687 June (2015). [cited on page 27.]

[219] Lee, K. I., Astudillo, N., and Kang, M. *Journal of Fluorescence* **30**(3), 455–462 March (2020). [cited on page 27.]

[220] Wohland, T., Maiti, S., and Macháň, R. *An Introduction to Fluorescence Correlation Spectroscopy*. IOP Publishing, November (2020). [cited on page 27.]

[221] Sezgin, E., Schneider, F., Galiani, S., Urbančič, I., Waithe, D., Lagerholm, B. C., and Eggeling, C. *Nature Protocols* March (2019). [cited on page 28.]

[222] García-Sáez, A. J., Carrer, D. C., and Schwille, P. *Fluorescence Correlation Spectroscopy for the Study of Membrane Dynamics and Organization in Giant Unilamellar Vesicles*, 493–508. Humana Press November (2009). [cited on page 28.]

[223] Ries, J. and Schwille, P. *Physical Chemistry Chemical Physics* **10**(24), 3487 (2008). [cited on page 28.]

[224] Rusu, L., Gambhir, A., McLaughlin, S., and Rädler, J. *Biophysical Journal* **87**(2), 1044–1053 August (2004). [cited on page 28.]

[225] Qutbuddin, Y., Guinart, A., Gavrilović, S., Al Nahas, K., Feringa, B. L., and Schwille, P. *Advanced Materials* **36**(16) January (2024). [cited on page 35.]

[226] Guinart, A., Doellerer, D., Qutbuddin, Y., Zivkovic, H., Branca, C., Hrebik, D., Schwille, P., and Feringa, B. L. *Langmuir* February (2025). [cited on page 74.]

[227] Ramm, B., Goychuk, A., Khmelinskaia, A., Blumhardt, P., Eto, H., Ganzinger, K. A., Frey, E., and Schwille, P. *Nature Physics* **17**(7), 850–858 April (2021). [cited on page 85.]

[228] Kanwa, N., Gavrilovic, S., Brüggenthies, G. A., Qutbuddin, Y., and Schwille, P. *Advanced Materials Interfaces* **10**(15) April (2023). [cited on page 85.]

[229] Qutbuddin, Y., Krohn, J.-H., Brüggenthies, G. A., Stein, J., Gavrilovic, S., Stehr, F., and Schwille, P. *The Journal of Physical Chemistry B* **125**(48), 13181–13191 November (2021). [cited on page 87.]

[230] Pegoraro, C., Karpova, E., Qutbuddin, Y., Sanchis, E. M., Dimitrijevs, P., Huck-Iriart, C., Gavrilović, S., Arsenyan, P., Schwille, P., Felip-León, C., Duro-Castano, A., Conejos-Sanchez, I., and Vicent, M. J. *Advanced Materials* January (2025). [cited on page 139.]

Acknowledgements

I am eternally grateful to everyone who I have met during these last four years, they have all contributed, intentionally or otherwise, to my development as a scientist and as a person I am today. My PhD journey has been truly fascinating and as I attempt to pull the curtains, I am left without words, which many of you will appreciate as a truly rare sight.

First and foremost, Prof. Petra Schwille, thank you for giving me the opportunity to work in your group, it was truly an honor for me to have you as my boss in this scientific journey. The scientific freedom I experienced in your lab has truly shaped my entire experience of being a scientist, and even more so has given me immense strength when I consider my future endeavors. Thank you for being available even when you are not around, for being supportive even when I became the "Coal Midas" and every project I attempted failed. Thank you for the amazing hikes during our group retreats and insightful discussions during those hikes, I will always cherish them.

Thank you to Prof. Don Lamb and Prof. Jan van Hest, for accepting to be in my thesis advisory committee, and for giving me important feedback for the very many problems that I brought with me. Thank you Prof. Rumiana Dimova for letting me spend time in your lab to learn interesting and valuable techniques. Thank you Prof. Remzi Becer and Prof. Sebastian Lecommandoux for fruitful discussions and feedback on our joint works.

I am very grateful to have had amazing collaborators, without whom this PhD would not have been possible. Ainoa Guinart, thanks for deciding to come to Munich and start the "game-changer" project with me, and teaching me so many things about synthetic chemistry and photoactive compounds. Thank you for all the fun times, the bouldering sessions, and introducing me to Blender. I am happy to have found a close friend during my PhD time, and I heavily enjoyed brainstorming with you. Camilla Pegoraro and Maria Korpidou, thank you for all the craziness and happiness that you brought with you as we mutually struggled to find ways to tackle our projects. Thank you for answering all of my "OR" questions with true computer precision, and bearing me through your secondments. I am happy that our project together worked out. Thank you Roberto Terracciano for the many WhatsApp calls that entailed science, research, hobbies, gossip, and support. Thank you for teaching me so much about glycopolymers, and starting a project which pushed us to learn and discover so much about lipid membranes. Ainoa, Camilla, Roberto, without you this would not have been possible, and wouldn't have been half as fun as it ended up being. My other friends from the BIOMOLMACS consortium, I am very grateful to have met all of you and the fun times in Bologna, Valencia, Basel, Coventry, and London. Thank you Maria, Clémence, Alex, Sebastian, Adrien, Noemi, Beatriz and all the other ESRs in the BIOMOLMACS train. I am thankful for the BIOMOLMACS MSCA, and proud to be ESR-11, I have met some of my closest friends and valuable collaborators through this opportunity.

To everyone at the Schwille lab, I am grateful for the amazing atmosphere that you provided in the lab, even when experiments didn't work and projects failed, I was motivated to come to the lab purely because of the positive feelings I experienced while being around all of you. Thank you Henri for introducing me to the majority of techniques I used in my thesis. You have been my inspiration for deciding to focus my thesis on membrane biophysics. Thank you for helping me with questions with DNA origami, membranes and also for providing me guidance whenever I needed it. A special thanks to Johannes Stein and Florian Stehr for letting me start my PhD by following the two of you. Thank you Johannes for being my first mentor in the lab, showing me around, teaching me microscopy and helping me find my first project which eventually also became the first publication of my life. Thank you Jan for being the first collaborator in the lab, for showing me how to do FCS and how not to do it too. Thank you for all the restaurant suggestions and for answering my many technical

questions and queries. Thank you Nishu Kanwa, my office neighbor, for keeping up with my stupidities and occasional rants about the most inconsequential things in life. Thank you for keeping me sane during working hours. Thank you Adrian for building this great atmosphere in the lab, I will always remember the spontaneous barbecue plans, the fun coffee breaks and the many board games that I experienced with you. Thank you Svetozar for all the fun times, for planning and implementing activities, for lending an ear to my complaints, for teaching me important Serbian words, and for being *mein Bruder*. I am grateful for all the brainstorming you bring, it really helps the rusty gears in my head to keep spinning everyday, and also teaches me new things every time. Thank you Kareem for being a big brother to me, motivating me through the toughest times in my PhD. Thank you for being my friend, for being there to bounce off my ideas against, and for bringing unique questions to think about on the mundane days of work. Thank you Henry for being a dear friend during these years, for making jokes to counter-balance the stress of a PhD. Thank you for all the fun nights "downtown", as you would say it, and for accepting that it's better to call them "spectacles" rather than glasses. Thank you Maria for asking important questions, sharing real music with me and all the interesting conversations we've had. I am also grateful to Henry, Kareem, and Leon for introducing me to the kicker table. Thank you Anastasija for telling me the amazing stories of your life, your positivity has elevated many gloomy days in the lab. Thank you for all the dance lessons, and for letting me win the dance-offs against you. Thank you Aleksandra for bringing smiles early in the morning before coffee and teaching me to appreciate each day, *dobar dan*. I am certain that I will remain in contact with all of you, and will continue to be your friend.

A big thanks to all the past and present members of the group. Thank you to Zexi, Viktoriia, Adam, Leon, Hiro, Nastasja, Gereon and Béla for the pleasant atmosphere in the lab and all the fun barbecues and hangouts that we've had during this time. Thank you to Marco, Philipp, and An for taking up the mantle as the new blood in the lab, I am happy that I will be around for a while to see you all start intriguing projects in the lab.

I would like to extend special thanks to Silke, for the tremendous administrative support from even before I began my PhD. Thank you to Frank, Helge and Thomas for managing the lab, and keeping us safe and at times regulated for our own sake. Special thanks to Sigrid and Sandra for helping me with lipid preparations and maintaining the membrane lab. I am grateful to have had the opportunity to work and talk with Siggi who kept the membrane lab sunny even when the sun didn't show up in Munich. You will be fondly remembered whenever I reminisce my PhD time. Thank you Katharina, Bea, Michaela, Kerstin and Claudia for taking care of the lab and answering all of my questions.

Outside of the lab, numerous people have shaped my life during PhD. Thank you to all the friends I made in this process. Thank you Hamsa and Ramin, for the amazing dinner, movie, and board-game nights, walks through Planegg and all the summer-time weekend coffees. Thank you Jacob for going bouldering with me, having patience when I talked about science, and for bringing quirky board games to our sessions. I am also grateful to have been part of the IMPRS graduate school where I made some amazing friends and met amazing people. Thank you to all of my IMPRS buddies who are also my friends, Anja, Filip, Mariia, Leona, Maria Ciapponi, Sophie, Christina, and many more. It has been great meeting all of you. IMPRS also helped me by offering valuable courses and workshops that have greatly helped me in personal and professional development.

I would also like to thank my supervisors from the past, who helped me tremendously to apply for the PhD positions and in my previous scientific endeavors. Thank you Prof. Martin Schmeing, Prof. Hugues Nury, Prof. Amar Nath Gupta, Prof. Sayan Kar, Prof. Sugata Pratik Khastagir, and Prof. Dibyendu Samanta. You have all contributed to my interest in science and physics in particular.

I would like to thank my family and friends who have supported me in every way and who gave me enough privilege to be able to do a PhD. I am grateful to all of my friends from Jabalpur, Sparsh, Rajas, Prathmesh, Abhit, Shubham Das, Raman, and Suyash. I am

also grateful for my friends from KGP, Shubham Bansal, Vivek, Raghav, Abhineet, and Vibhav. The people who've made everything possible for me, my loving parents, Tasneem and Qutbuddin Qaizar, and my elder brother who has always been my Banyan tree, Shabbir Qutbuddin and my "sisters" Lubaina and Tasneem. My family is the greatest blessing I have, they've always supported and loved me, even when they didn't understand me, they stood by me, and for that I am forever grateful.

And then there was one, THE one in my life. I met you during my PhD journey, and you changed my life. Thank you for loving me and supporting me through the thick and thin, for being my pillar of support always, thank you for making me laugh at the end of long and tiring days, and for holding my hand as I navigated through this journey. Forever grateful to you, Rashida, and for you.